AUGUST 1960 VOLUME 8 (1960) No. 2

GREGG M. SINCLAIR LIBRARY
UNIVERSITY OF HAWAII
8-7-63

NUCLEAR INSTRUMENTS & METHODS

A JOURNAL ON ACCELERATORS, INSTRUMENTATION AND TECHNIQUES IN NUCLEAR PHYSICS

EDITOR: K. SIEGBAHN - UPPSALA

CONTENTS

C. DE VRIES and A. H. WAPSTRA, A Siegbahn-Edvarson type ironfree double focusing beta-ray spectrometer 121
R. BATCHELOR, W. B. GILBOY, A. D. PURNELL and J. H. TOWLE, Improvements in the fast neutron time of flight technique using pulse shape discrimination in an organic phosphor 146
I. BERGSTRÖM, E. C. O. BONACALZA, A. JECH, M. PEREZ and P. THIEBERGER, The oscilloscope method of measuring nuclear half-lives 151
E. M. GUNNERSEN and G. JAMES, On the efficiency of the reaction $H^3(d,n)He^4$ in titanium tritide bombarded with deuterons 173
P. MULOT, R. POUSSOT, A. P. SCHMITT et C. P. ZALESKI, Appareil automatique pour la mesure des gradients locaux du flux de neutrons dans un réacteur 185
R. J. VAN DE GRAAFF, Tandem electrostatic accelerators 195
NORMAN H. TOLK and ROBERT M. BRUGGER, Calculated shapes for neutron bursts produced by phased chopper velocity selectors 203
J. W. BUTLER, High-efficiency, long-lived vacuum cold trap 211
W. J. RAMLER, J. L. YNTEMA and M. OSELKA, Energy degrading-focusing of cyclotron beam 217

(continued on p. 3 of cover)

NORTH-HOLLAND PUBLISHING COMPANY - AMSTERDAM

NUCLEAR INSTRUMENTS AND METHODS

A journal on accelerators, instrumentation and techniques in nuclear physics

EDITOR: K. SIEGBAHN, UPPSALA

EDITORIAL BOARD:

J. B. ADAMS (CERN)
F. A. ALSINA (Buenos Aires)
E. AMALDI (Rome)
H. L. ANDERSON (Chicago)
K. T. BAINBRIDGE (Cambridge, Mass.)
P. R. BELL (Oak Ridge)
R. E. BELL (Montreal)
A. BERTHELOT (Saclay)
H. BRINKMAN (Groningen)
E. H. COOKE-YARBOROUGH (Harwell)
S. DE BENEDETTI (Pittsburgh)
M. DE HEMPTINNE (Louvain)
A. DE-SHALIT (Rehovoth)
M. DEUTSCH (Cambridge, Mass.)
S. DU TOIT (Pretoria)
B. S. DŽELEPOV (Leningrad)
W. GENTNER (Heidelberg)
P. C. GUGELOT (Amsterdam)
H. HALBAN (Paris)
O. HAXEL (Heidelberg)
P. HUBER (Basel)
S. KIKUCHI (Tokyo)
J. KOCH (Copenhagen)
M. S. KOZODAEV (Moscow)
S. LIVINGSTON (Cambridge, Mass.)
E. M. MCMILLAN (Berkeley)
M. G. MEŠČERJAKOW (Moscow)
P. B. MOON (Birmingham)
M. L. OLIPHANT (Canberra)
W. PAUL (Bonn)
A. S. RAO (Bombay)
G. SALVANI (Rome)
P. SAVIĆ (Belgrade)
P. SCHERRER (Zürich)
CH. SCHMELZER (CERN)
R. TANGEN (Oslo)
D. TAYLOR (Northampton)
V. I. VEKSLER (Moscow)
G. VON DARDEL (CERN)
O. WERNHOLM (Stockholm)
R. R. WILSON (Cornell)
S. D. WINTER (Saclay)

INSTRUCTIONS FOR CONTRIBUTORS

Contributions may be sent to the Editor, Professor K. Siegbahn, Institute of Physics, University of Uppsala, Sweden, either directly or through the intermediation of one of the members of the Editorial Board. Contributions may be written in English, French or German but should always, except for very short papers, be supplied with a brief abstract in English. Figures should be in inked original drawings or glossy prints and they should be sufficiently large. Contributors should make sure that important details in drawings and photographs will show up clearly in the diminished copy used by the publisher.

Books for review should be sent to Professor Siegbahn.

Objective and descriptive material on endeavours and product developments from the industry for the section "Spotlight on Industry" should be sent directly to the publishers, North-Holland Publishing Company, P.O. Box 103, Amsterdam.

Nuclear Instruments and Methods is published monthly. The subscription price of a volume of 360 pages is $ 17.00 (130 s), postage free.

Subscriptions should be sent to the publishers, North-Holland Publishing Company, P.O. Box 103, Amsterdam, or to any subscription-agent.

No part of this issue may be reproduced in any form, by print, photoprint, microfilm or any other means without written permission from the publisher.

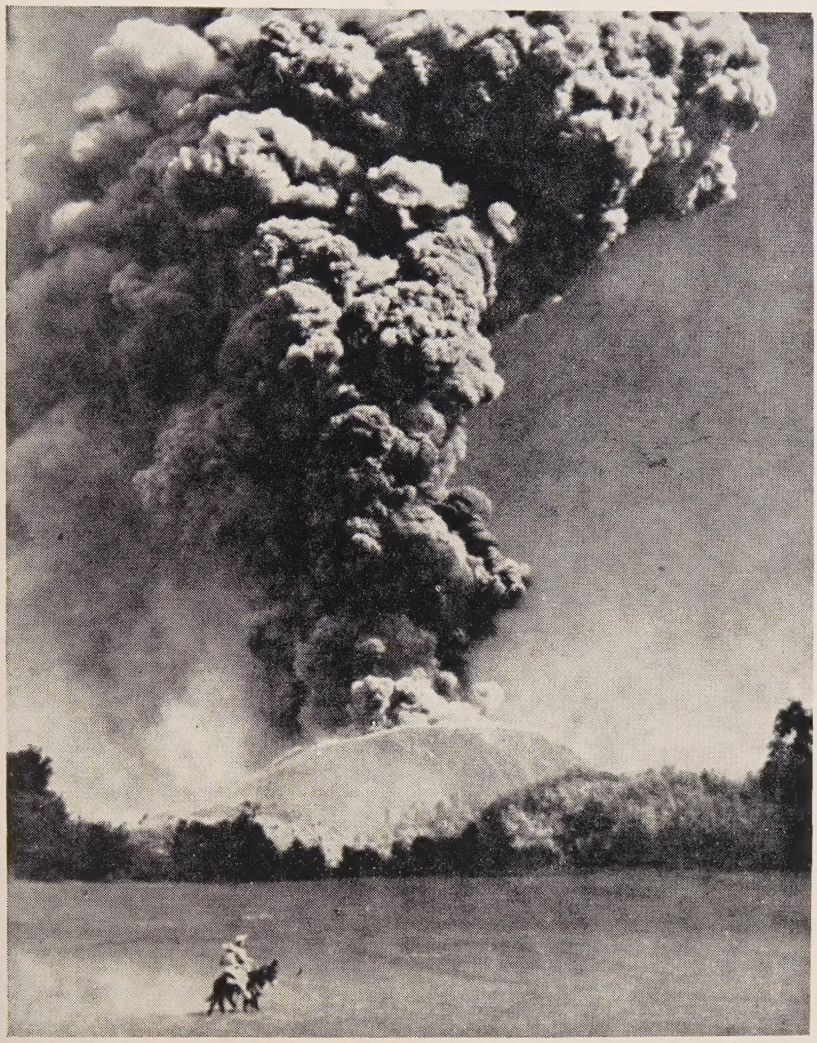

PHILIPS

Work in a nuclear reactor plant can't be compared with living beside a volcano. Workers in reactor plants, you see, are safe! They can rely all time upon monitoring instruments surrounding them - the finest and most sensitive in existence.

Philips produce indispensable and reliable equipment ranging from portable monitors and personal dosimeters to permanently monitoring, multi-channel installations such as the one designed and constructed for the Austrian Organization for Nuclear Energy Research (S.G.A.E.) at Seibersdorf near Vienna.

The equipment in use here includes channels for the measurement of both gamma-radiation and fast and slow neutrons in the experimental reactor building, and for the monitoring of water and air contamination.

no living on a volcano

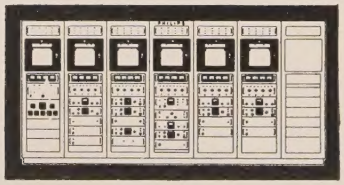

N.V. PHILIPS' GLOEILAMPENFABRIEKEN - EINDHOVEN - HOLLAND

PHILIPS
nuclear equipment

Particle accelerators ● Reactor control instrumentation ● Health protection and monitoring equipment ● Radiation measuring and detection equipment ● Geiger counter tubes ● Photomultipliers ● Radio-active isotopes ● Vacuum measuring equipment ● Air and gas liquefiers.

Eldorado

DECIMAL SCALERS
FOR THE NUCLEAR PHYSICIST

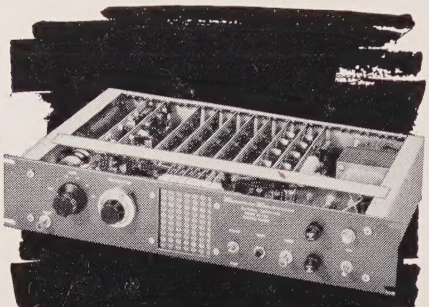

100% SOLID STATE

...and Fast

Eldorado solid state all-electronic scalers count random events at a maximum rate of over one million counts per second. Resolving time is less than 1.0 microsecond. Especially well-suited for accelerator counting room service, these compact instruments weigh just 13 pounds and use ⅓ fewer transistors than comparable models. They can be used wherever the advantages of complete transistorization are important.

Eldorado offers three standard models in the SC-750 series, each with built-in regulated power supply. Two models provide full electronic storage of 10^7 and 10^8 counts. The third has 3 decades of electronic storage and a 4-digit mechanical register. Special versions can be furnished with other counting combinations and provisions for readout to a printer or tape punch.

KEY SPECIFICATIONS

SCALER	
Resolution	Better than 1.0 microsecond
Max. Counting Rate	Greater than 1 megacycle
AMPLIFIER (optional)	
Minimum Input Signal	10 millivolts
Overload Recovery	100 X, 7 microsecond
DISCRIMINATOR TYPE	Integral
RANGE	1 to 11 volts
SIZE	19 x 3¼ x 10½ inches

Eldorado can furnish scalers and counters to fit your specific application. For more details, please address Dept. 79

Eldorado Electronics

2821 Tenth Street

Berkeley 10, California

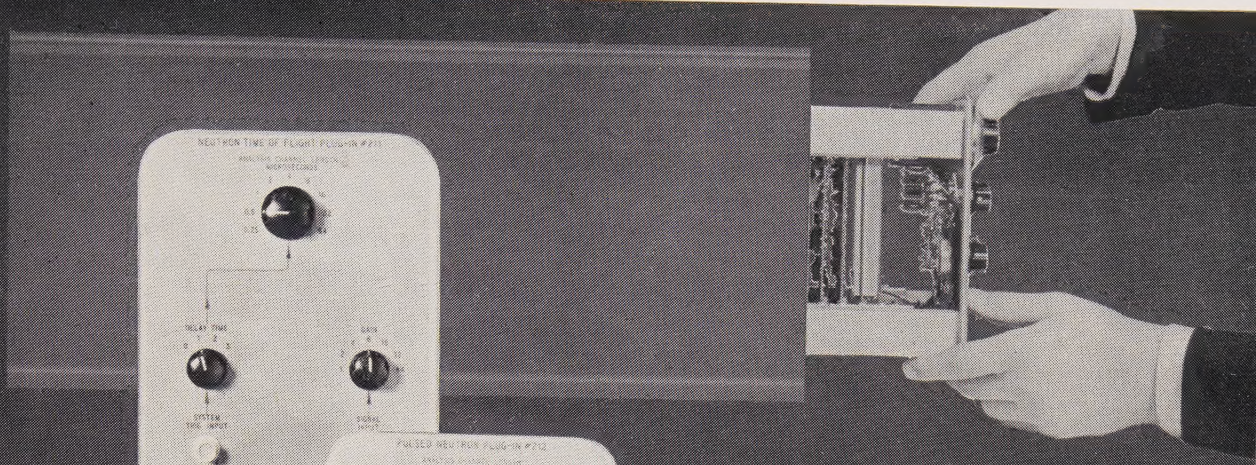

time-of-flight plug-in

pulsed neutron plug-in

PLUG-IN LOGIC

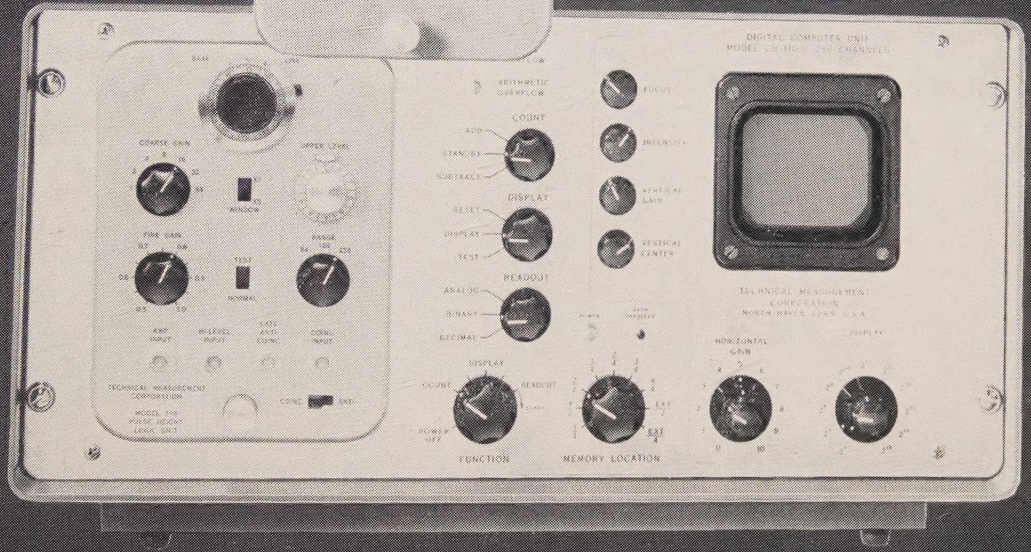

Logic is interchangeable in the TMC Model CN-110 Pulse Analyzer. Into the all-transistor, 30-pound, 256-channel digital computer you can plug Pulse Height Analysis, Pulsed Neutron, Time-of-Flight or special program units. Out of it you can get Analog, Digital or Binary data. You can carry the system and set it up almost anywhere. It is guaranteed for two years.

These instruments and all accessory units are now being delivered. Complete details of design, construction and operation are contained in a new 6-page folder available on request.

220 data handling unit

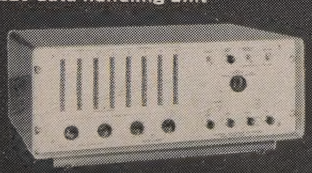

• We have excellent openings for Transistor Circuit Designers •

TMC

TECHNICAL MEASUREMENT CORPORATION

441 WASHINGTON AVENUE, NORTH HAVEN, CONN.

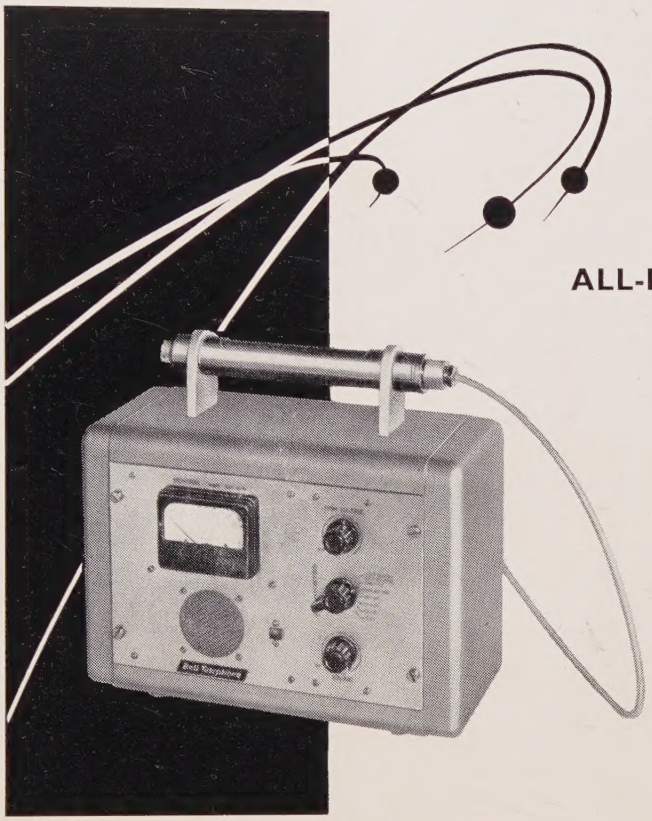

ALL-ROUND, LOW PRICED MONITOR

Typically developed as a laboratory equipment the monitor 111-A1 combines quality and high performance with low cost.

- Completely transistorized
- Designed as portable type
- Very low count rate: 0 to 5 c.p.s. full scale
- Highest count rate: 0 to 5000 c.p.s. full scale
- Equalizing accumulators
- Automatically recharged from A.C. mains
- Priced $ 410 F.O.B. Antwerp

For further information on this and other applications in the field of "Electronics for Nucleonics" ask :

AN IT&T ASSOCIATE

Bell Telephone Mfg Co

"NUCLEAR ENERGY DIVISION"
33, Berkenrodelei
HOBOKEN-Antwerp
Belgium

NORTH-HOLLAND BOOKS

Paul Ehrenfest

COLLECTED SCIENTIFIC PAPERS

XII + 632 pages

Guilders 45,00 (90s.)

This volume makes widely scattered publications readily available. All Dutch articles appear here in English; the German publications are in the original language.

Sole Agency for U.S.A.:

Interscience Publishers Inc. — New York

NORTH-HOLLAND PUBLISHING COMPANY - AMSTERDAM

MODEL 412 MERCURY RELAY

PRECISION SLIDING PULSER

for Precise Calibration of Single & Multi-Channel Pulse Height Analyzers

Determines Window Widths Using Principle of *Constant Angular Velocity*

AUTOMATICALLY
10 × more accurately
40 × faster than conventional pulsers

Incorporates Both Manual Control and Precision Motor Drive

Simulates Pulses from Scintillation, Proportional or Geiger Counters

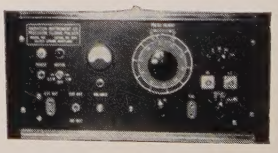

MERCURY PULSER, Model 401

Featuring Versatility and Precision

Specifically designed for the Nuclear Physics Laboratory

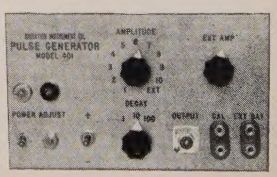

Fast rise and exponential decay simulates scintillation, proportional or geiger counter pulses for test and calibration of amplifiers, pulse height analyzers, scalers, etc.

MODEL 412 . . . $ 450.00 — MODEL 401 . . . $ 125.00

RADIATION INSTRUMENT CO.

P. O. BOX 733, SILVER SPRING, MARYLAND, U.S.A.

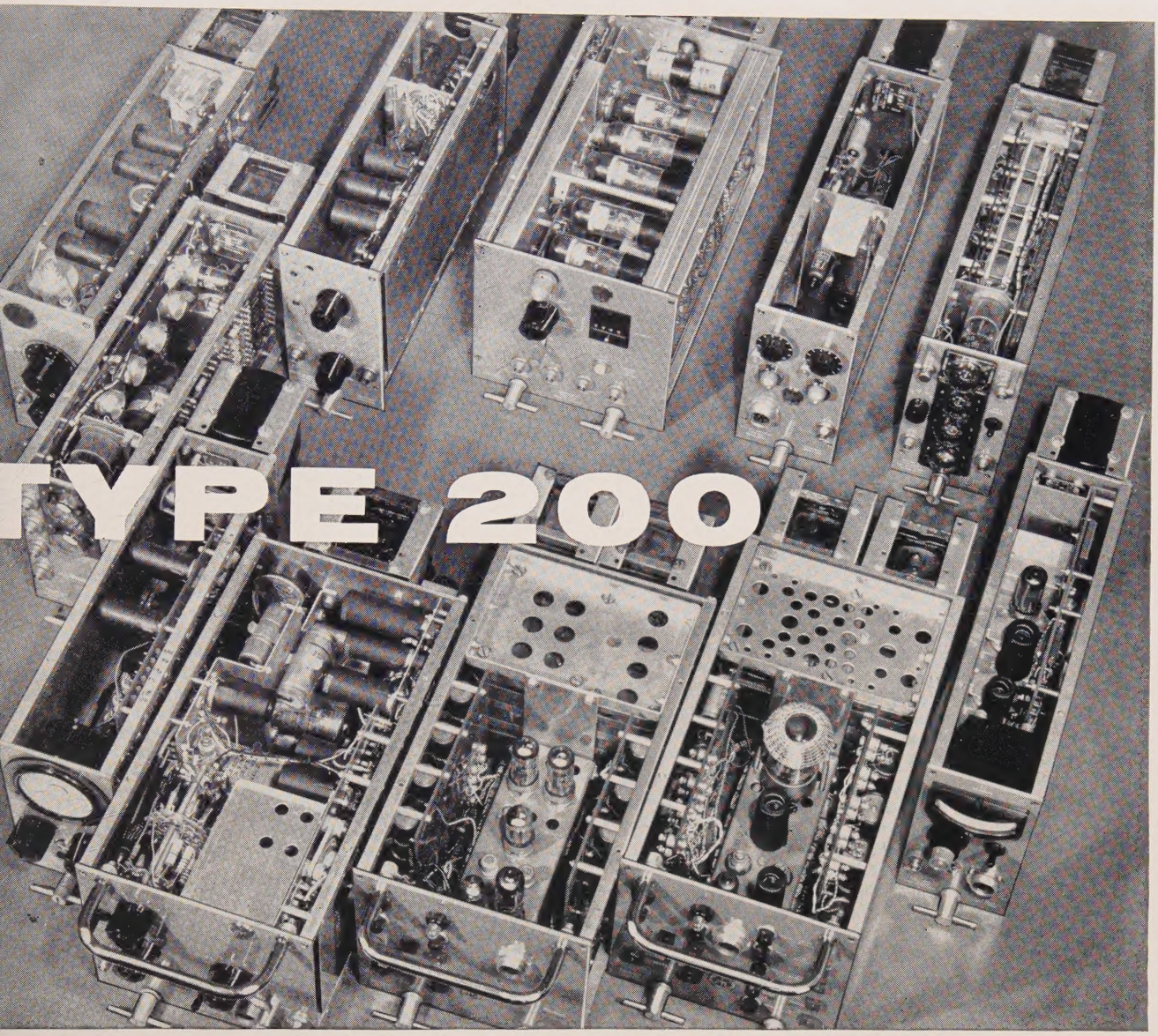

UNITIZED NUCLEONIC RANGE

The plan behind this Type 200 equipment is to offer you a Unitized Range (already 24 units and still increasing) not only to cover every type of nucleonic counting, but one that can be added to at will, so that you get only what you want, when you want.

- **Suitable for all types of nucleonic detectors.**
- **Built to a stringent specification.**
- **Designed in conjunction with A.E.R.E. Harwell.**
- **Flexible in use—a unit for every purpose.**

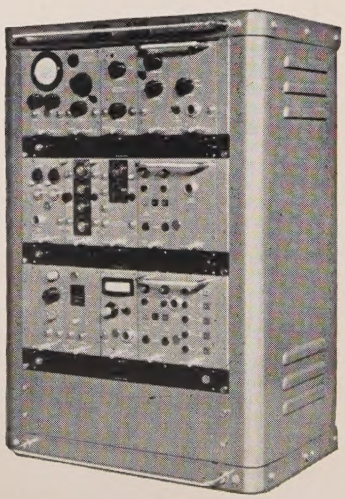

Enquiries should be addressed to:—

INSTRUMENT DIVISION

HIGH CHURCH STREET · NEW BASFORD · NOTTINGHAM

ERICSSON

CSSON TELEPHONES LIMITED · HEAD OFFICE · 22 LINCOLN'S INN FIELDS LONDON W.C.2

a Complete Scintillation Service

phosphors and counters

PLASTIC, LIQUID AND CRYSTAL PHOSPHORS

* PLASTIC PHOSPHOR NE 102, light output 65% anthracene, available in all sizes and shapes up to one ton, in thin sheet form, in fine tubes for the construction of scintillation flow counters, or as filaments for the construction of scintillation nuclear track chambers.
* BORON POLYESTER PLASTIC PHOSPHOR NE 400 and NE 401 (88% B^{10}) for neutron detection. Standard sizes from 0.5 to 5.0 inches diameter.
* SCINTILLATION CHEMICALS of highest purity P.B.D., POPOP, T.P.B., p-terphenyl, PPO, D.P.H., alpha-N.P.O., D.M.C., B.B.O., B.P.O., D.P.A., D.P.S., vinyltoluene, styrene, xylene, toluene, methyl borate, phenylcyclohexane, monoisopropylbiphenyl.
* SCINTILLATION CRYSTALS by Harshaw. Exclusive concessionaire in Great Britain for NaI(Tl), CsI(Tl), LiI(Eu), and Li^6I(Eu). NaI(Tl) available in sizes up to 9″ diameter x 9″thick, and down to 0.015″ thick with 0.005″ Be windows for X-ray counting and spectrometry. Resolution with standard sizes 7–8% on Cs^{137} line. CsI(Tl) down to 0.005″ thick for alpha and proton studies. Li^6I(Eu) in special low temperature mounts for fast neutron spectrometry.
* NEW! Photomultiplier-NaI(Tl) combinations with direct coupling of crystal to photomultiplier and giving improved resolution.
* LIGHT PIPES * SCINTILLATING GELS
* SPIRAL FLOW CELL NE 801 * LOADED LIQUID SCINTILLATORS

Write now for Bulletins and Price List

Nuclear Enterprises (G.B.) Ltd.

BANKHEAD MEDWAY, SIGHTHILL, EDINBURGH 11, SCOTLAND. (TEL. CRA 5262)

Associate Company: Nuclear Enterprises Ltd., 1750 Pembina Highway, Winnipeg, Canada.

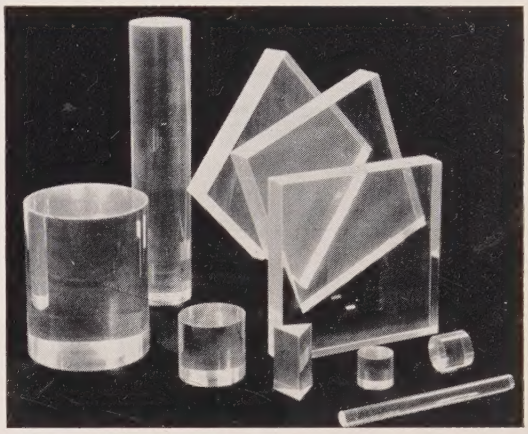

PRECISION NUCLEAR INSTRUMENTS

* Non-overloading Linear Pulse Amplifier NE 5202 of the Fairstein type.
* Pre-Amplifier and Cathode Follower NE 5202A.
* Single Channel Pulse Height Selectors NE 5102 and NE 5103.
* Shielded Scintillation Head Units NE 5501-3.
* Highly Stabilised EHT Supplies NE 5302 (1.5 kV) and NE 5303 (5kV).
* Complete assembly for C14 and tritium counting NE 8301.
* Complete Human Body Monitors and low level counting facilities.
* Ratemeter NE 5401 with six ranges and five time constants.
* Scanning scintillation spectrometer NE 8601.
* C.D.C. 100 Channel Transistorised Kicksorter

ndh 1408X

NORTH-HOLLAND BOOKS

Analytical and Canonical Formalism in Physics

by

ANDRÉ MERCIER

Head of the Department of Theoretical Physics, University of Berne

6 × 9″ VIII + 222 pages Guilders 20.00 (40 s.)

THE CONTENTS

i LAGRANGIAN FORMALISM
ii LAGRANGIAN DENSITY
iii CANONICAL FORMALISM
iv CANONICAL FORM OF ELECTRODYNAMICS
v HAMILTONIAN DENSITIES
vi TRANSFORMATIONS
vii CANONICAL FORMALISM WITH VANISHING JACOBIAN DETERMINANT

Sole Agency for U.S.A.: Interscience Publishers Inc. – New York

NORTH-HOLLAND PUBLISHING COMPANY — AMSTERDAM

"PLANNAIR" GAS CIRCULATION BLOWERS FOR NUCLEAR PROJECTS

The AGR 19 Fuel Element Cluster CO_2 circulator, here illustrated, provides for reliable and efficient cooling of nuclear reactors. The blower, with its 11,500 r.p.m. motor (200V 400 c/s supply), is sealed within a long pressure vessel at the opposite end to which the nuclear reaction occurs. CO_2 circulates through the tube at 285 p.s.i. A and 95°C. The blower output is 6300 lb./hour at 7.5 p.s.i. pressure differential. A secondary radial impeller gives a cooling gas circuit via a demineralised water heat exchanger coil which keeps the motor operating at below 75°C.

This is but one of several gas circulating blowers which Plannair have designed for various nuclear projects. These include a Leaky Cartridge Test Rig Air-Blower, a Sodium Loop-Nitrogen Circulator, a Helium Circulator, Air Circulators and a Nitrogen Circulator for R.3 Adam, CO_2 circulator for Fuel Element Cluster Irradiation Test Rig, Burst Fuel Element Test Rig Air-Blower.

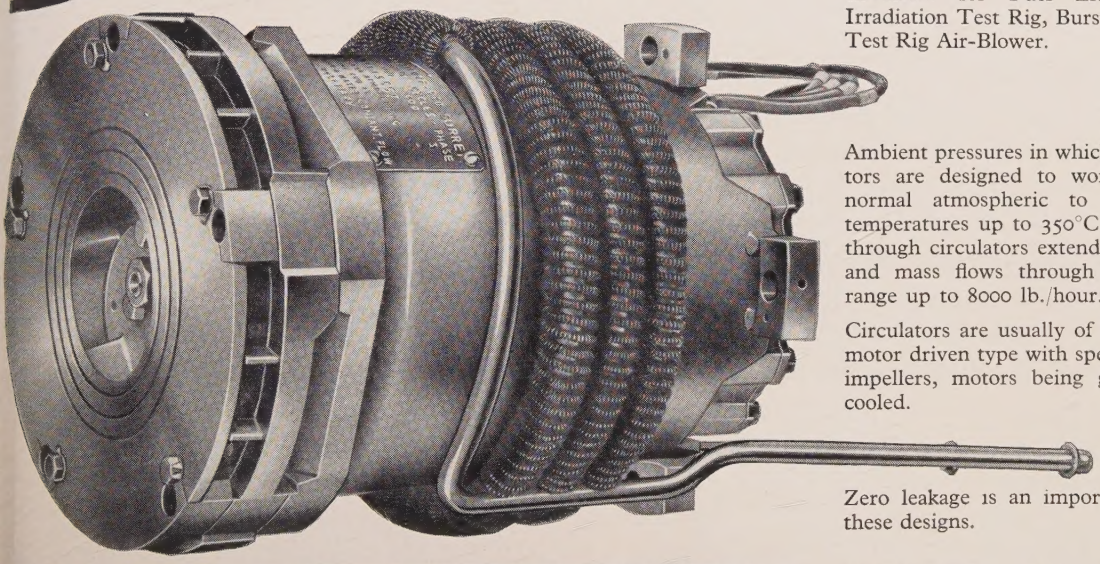

Ambient pressures in which these circulators are designed to work range from normal atmospheric to 300 p.s.i. at temperatures up to 350°C. Pressure rises through circulators extend up to 30 p.s.i. and mass flows through units cover a range up to 8000 lb./hour.

Circulators are usually of the high speed motor driven type with specially designed impellers, motors being gas and liquid cooled.

Zero leakage is an important feature of these designs.

Further details available on request.

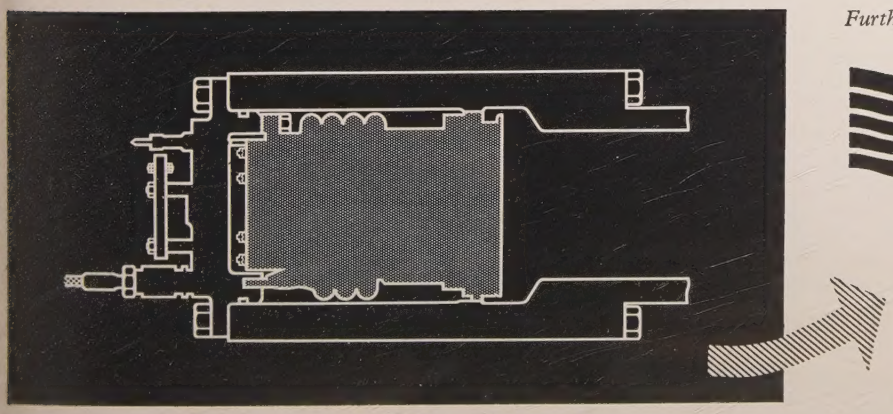

PLANNAIR

PLANNAIR LIMITED

Winfield House • Epsom Road

Leatherhead • Surrey

Tel: Leatherhead 4091/3, 2231

PLA39a

LOW COST

Van de Graaff®
NEUTRON SOURCE FOR ACTIVATION ANALYSIS

10^{10} n/sec from D-T Reaction

NEUTRON ACTIVATION is becoming of increasing importance in quantitative analysis. The extreme sensitivity of this method to trace amounts, the speed and simplicity with which samples can be analyzed, and dependence only on simple radiation counting and measuring equipment to assure accuracy, makes it suitable for microanalysis where chemical methods are inadequate or for macroanalysis with production rapidity.

THE HIGH VOLTAGE MODEL AN-400 positive-ion accelerator is the lowest-priced source of intense neutrons on the market. Operated at 400 kev, its full beam current of 150 microamperes is effective in producing neutrons from a thin tritium target. It is compact (about 10 square feet of floor area) and mobile and is designed for safety, with all high voltage fully insulated. Based on the proved designs and experience of High Voltage Engineering Corporation in building and installing more than 250 particle accelerators.

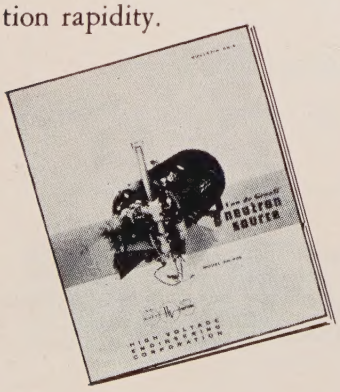

NEW BULLETIN AN-4 —Describes specifications and performance in detail. Write Technical Sales for your copy.

IN NUCLEAR ENGINEERING, the Model AN-400 is a useful experimental apparatus for studies of transient and steady-state effects in sub-critical assemblies and for teaching physics and reactor technology. May be equipped for pulsed operation or electron outputs if desired.

HIGH VOLTAGE ENGINEERING CORPORATION
BURLINGTON, MASSACHUSETTS • U.S.A.

High Voltage Engineering (Europa) N.V., Amersfoort, The Netherlands

NUCLEAR INSTRUMENTS AND METHODS **8** (1960) 121–145; NORTH-HOLLAND PUBLISHING CO.

A SIEGBAHN-EDVARSON TYPE IRONFREE DOUBLE FOCUSING BETA-RAY SPECTROMETER

C. DE VRIES and A. H. WAPSTRA

Institute of Nuclear Research, Amsterdam

Received 10 May 1960

An ironfree double focusing beta ray spectrometer with 30 cm radius for precision energy and intensity measurements has been constructed. It can be used for the focusing of electrons with an energy up to 2.6 MeV. The cooling system limits errors due to temperature effects to about one part in 10^5 in the relative $B\rho$-values of the electrons throughout the whole energy region. The long and short term stability of the coil current, delivered by a d.c. generator, is in the order of $1:10^5$. External magnetic fields are compensated; fluctuations on the most important component of these fields are automatically suppressed to less than 10^{-8} Wb/m^2. The field shape satisfies the conditions for first order focusing in the radial direction and second order focusing in the axial direction to a high degree: $\alpha = -0.500 \pm 0.003$ and $\beta = 0.39 \pm 0.02$. The maximum transmission is about 1%; the smallest linewidth obtained so far has been 0.013%.

1. Introduction

During the past few years the interest in instruments with the double focusing field shape has rapidly increased, as this field shape meets to a high extent the beta-spectroscopic requirement of a large ratio of transmission and resolution (both expressed in percentages). The additional requirement of high precision has proven to be best satisfied when this particular field shape is realized with ironfree constructions.

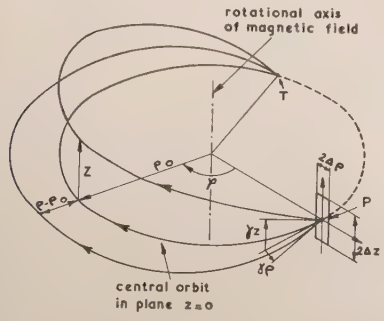

Fig. 1. Explanation of the symbols in the text.

Before discussing some existing air cored instruments we shall briefly present the focusing properties of axially symmetric magnetic fields.

Consider the trajectories of electrons of momentum p in an axially symmetric magnetic field with a plane of symmetry. A possible orbit in the symmetry plane is a circle, concentric with the axis of the field; this is called the central orbit. Cylindrical coordinates ρ, z and φ will be used (see fig. 1). The Taylor expansion of the magnetic field around the central orbit $\rho = \rho_0$ in the median plane $z = 0$ is:

$$B(\rho) = B(\rho_0)\{1 + \alpha\delta + \beta\delta^2 + \cdots\}$$

where

$$\delta = \frac{\rho - \rho_0}{\rho_0}, \quad \alpha = \frac{\rho_0}{B(\rho_0)}\left(\frac{\mathrm{d}B}{\mathrm{d}\rho}\right)_{\rho_0}$$

and

$$\beta = \frac{\rho_0^2}{2B(\rho_0)}\left(\frac{\mathrm{d}^2B}{\mathrm{d}\rho^2}\right)_{\rho_0}.$$

This series expansion and the Maxwell equations determine the entire field distribution around the central path. If only paths are considered at small angles γ_ρ and γ_z with the central path (see fig. 1), the influence of all terms of higher order than δ can be neglected.

For such first order calculation Svartholm and Siegbahn[1]) showed the equations of motion of the particles to be:

$$\begin{aligned} \delta'' &= -(1 + \alpha)\,\delta \\ z'' &= \alpha z\,. \end{aligned} \tag{1}$$

[1]) N. Svartholm and K. Siegbahn, Ark. Mat. Astr. Fys. A **33**, No. 21 (1946).

Using the boundary condition $\delta = 0$ and $z = 0$ for $\varphi = 0$, (point P in fig. 1) one finds the solution:

$$\delta = \frac{a}{\rho_0} \sin (\alpha + 1)^{\frac{1}{2}} \varphi$$
$$z = \frac{b}{\rho_0} \sin (-\alpha)^{\frac{1}{2}} \varphi . \tag{2}$$

For periodicity in ρ and z, α must lie between the values -1 and 0. If Ψ_ρ and Ψ_z are defined as the angles at which for the first time first order focusing takes place in the radial and axial direction respectively, then

$$\Psi_z = \pi (-\alpha)^{-\frac{1}{2}}$$
$$\Psi_\rho = \pi (1 + \alpha)^{-\frac{1}{2}} . \tag{3}$$

Evidently, $\alpha = -\frac{1}{2}$ gives double focusing after $\pi\sqrt{2}$ radians. Other suitable choices of α have been discussed by Lee Whiting[2]) and Mladjenović[3]). Here we will restrict ourselves to $\alpha = -\frac{1}{2}$. Then the solution for the orbit equations (2) is given by:

$$\delta = \frac{a}{\rho_0} \sin \frac{\varphi}{\sqrt{2}}$$
$$z = \frac{b}{\rho_0} \sin \frac{\varphi}{\sqrt{2}} . \tag{4}$$

This solution can also be written:

$$\rho - \rho_0 = \gamma_\rho \rho_0 \sqrt{2} \sin \frac{\varphi}{\sqrt{2}}$$
$$z = \gamma_z \rho_0 \sqrt{2} \sin \frac{\varphi}{\sqrt{2}} \tag{5}$$

which expresses the distances $(\rho - \rho_0)$ and z from the central orbit as a function of γ_ρ, γ_z and φ.

Double focusing occurs at the point φ $(\rho_0, 0, \pi\sqrt{2})$ only for electrons having a momentum $p_0 = eB(\rho_0)\rho_0$. Electrons having a slightly different $B\rho$-value focus at the point φ' $(\rho_0 \pm d, 0, \pi\sqrt{2})$ with

$$d = 4\rho_0 \left(\frac{\Delta B\rho}{B\rho} \right)_{\rho_0} .$$

Monoenergetic electrons will be measured as lines with a finite width in consequence of the spherical aberration of the focusing system and the finite dimensions of the source and the counter slit. The shape of this line will be called the spectrometer window curve. The resolution R can be defined now as the relative width at half height of the line, plotted in the $B\rho$-scale:

$$R = \frac{\Delta B\rho}{B\rho} .$$

The resolution is mostly expressed in percentages. Related quantities are the resolving power, which is the inverse of the resolution and the base line width R_0 which is the relative width at the base of the line. The ratio between R and R_0 depends on the intensity distribution within the line. In turn this intensity distribution depends on the special conditions under which the line is measured. Under simplifying assumptions the connection between R and R_0 can be given exactly[4]). In practice the following formula is a rather good approximation:

$$R \approx \tfrac{1}{2} R_0 .$$

The "energy resolution" is related with the "momentum resolution" through the relation:

$$\frac{dE}{E} = \frac{E + 2}{E + 1} \frac{dp}{p} \tag{6}$$

which formula is obtained by differentiating the relativistic relation between E and p.

For the special field under consideration the following relation holds:

$$R_0 = \frac{d}{4\rho_0} . \tag{7}$$

In discussing second order focusing the coefficient β in the Taylor expansion of the field must be considered. Shull and Dennison[5]) have shown that the image coordinates ρ^* and z^* for an electron emitted from the point $(\rho + \Delta\rho, \Delta z)$ at $\varphi = 0$, with a momentum

[2]) G. E. Lee-Whiting, Can. J. of Phys. **35** (1957) 570.
[3]) M. Mladjenović, Nucl. Instr. **7** (1960) 11.
[4]) H. Wild and O. Huber, Helv. Phys. Acta **30** (1957) 3.
[5]) F. Shull and D. Dennison, Phys. Rev. **71** (1947) 681; **72** (1947) 256.

$eB(\rho_0)\rho_0$ at the angles γ_ρ and γ_z to the tangent on the central orbit are:

$$\rho^* = \rho_0 - \Delta\rho + \frac{1}{\rho_0}\left(\tfrac{4}{3}\beta - 1\right)\Delta z^2 + \tfrac{2}{3}(1 - 8\beta)\,\rho_0\gamma_\rho^2 + \\ + 2\left(\tfrac{8}{3}\beta - 1\right)\rho_0\gamma_z^2$$

$$z^* = -\Delta z + \frac{8\beta}{\rho_0}\Delta\rho\Delta z + 4\left(\tfrac{8}{3}\beta - 1\right)\rho_0\gamma_\rho\gamma_z\,. \qquad (8)$$

From these image coordinates and eq. (7) an expression for the base resolution R_0 can be obtained as function of source dimensions $(2\Delta\rho \times 2\Delta z)$, counterslit width t, the opening angles γ_ρ and γ_z and the field coefficient β:

$$R_0 = \frac{\Delta B\rho}{B\rho} = \frac{2\Delta\rho + t}{4\rho_0} + \frac{1}{{\rho_0}^2}\,|\,\tfrac{4}{3}\beta - 1\,|\,(2\Delta z)^2 + \\ + \tfrac{1}{8}\,|\,1 - 8\beta\,|\,\gamma_\rho^2 - \tfrac{1}{2}\,|\,\tfrac{8}{3}\beta - 1\,|\,\gamma_z^2\,. \qquad (9)$$

Eq.(9) shows that the resolution R_0 is independent of the axial opening angle for $\beta = \frac{3}{8}$; then the influence of γ_ρ on the resolution goes as $\frac{1}{3}\gamma_\rho^2$. For $\beta = \frac{1}{8}$ there is no limit to γ_ρ to second order and the resolution is proportional to $\frac{1}{3}\gamma_z^2$. In this respect there is no preference for $\frac{1}{8}$ or $\frac{3}{8}$. However, there are some arguments in favour of the choice $\frac{3}{8}$. The term in eq. (9), containing the source height will be smaller for $\frac{3}{8}$ then for $\frac{1}{8}$. Due to this fact about 30% higher luminosity (defined as transmission $\times$ source area) can be obtained, if one uses the field shape with second order axial focusing instead of second order radial focusing. With the choice $\beta = \frac{3}{8}$ double focusing is obtained not only on the central orbit $\rho = \rho_0$, but also for other values of ρ, which makes possible photographic detection for an extended energy region. For the construction described below the choice $\beta = \frac{3}{8}$ is the natural one, since the radial opening angle is limited more severely then the axial one.

2. Existing Ironfree Instruments with $\alpha = -\frac{1}{2}$ and $\beta = \frac{3}{8}$

The realization of the required field shape with air coils has been obtained so far in two essentially different ways: (1) with pairs of thin coils placed symmetrically to the plane of symmetry as indicated in figs. 2a and 2b and (2) with long coaxial cylindrical coils (figure 2c). The principle shown in fig. 2a is due to Moussa and Bellicard. Fig. 2b shows a design for sixth order axial focusing as computed by Lee-Whiting and Taylor which has been realized by Graham, Ewans and coworkers in Chalk River. The construction indicated in figure 2c has been designed and built by Siegbahn and Edvarson. The relative dimensions of the above mentioned instruments can be seen from the radii of the different central orbits.

We will give now some features of these instruments.

The apparatus of Moussa and Bellicard[6]) ($\rho_0 = 210$ mm, $\beta = \frac{3}{8}$) consists of four pairs of coils placed in series for the current delivered by a high voltage supply (8 kV). The short range stability of the current is about $1:10^4$. At the maximum attainable energy of 1.3 MeV the current is about 0.5 A. The instrument is not provided with a cooling system; the temperature of the largest coils increases to about 100° C when measuring at the highest current. Therefore the instrument is mainly used at low currents. The earth magnetic field is compensated only in the direction perpendicular to the electron orbit. The instrument is provided with a G.M. counter. The maximum attainable transmission is about 1%; at this transmission a resolution of 0.9% has been reached for the ThB F-line. The highest resolution reported so far is in the order of 0.2%. Another spectrometer built along the same lines as the Moussa spectrometer is present in Nashville, [Baird[7]) and Nall[8])]. The radius of the central orbit is 300 mm, $\beta = \frac{3}{8}$, the maximum attainable energy is 1.3 MeV.

A complete description of the Chalk River machine has not yet been published. Some preliminary results have been reported by Ewan

[6]) A. Moussa and J. B. Bellicard, J. Phys. Radium **15** (1954) 85A;
J. B. Bellicard and A. Moussa, J. Phys. Radium **17** (1956) 532.
[7]) Q. L. Baird, Thesis, Nashville (1958).
[8]) J. C. Nall, Thesis, Nashville (1958).

et al.[9]). The radius of the central orbit is 1 meter and the maximum energy is 4 MeV. The transmission can be varied from 0.1 to 1% of 4π cooled with constant temperature water from a closed circuit circulating system. The coil current is measured by the voltage drop across

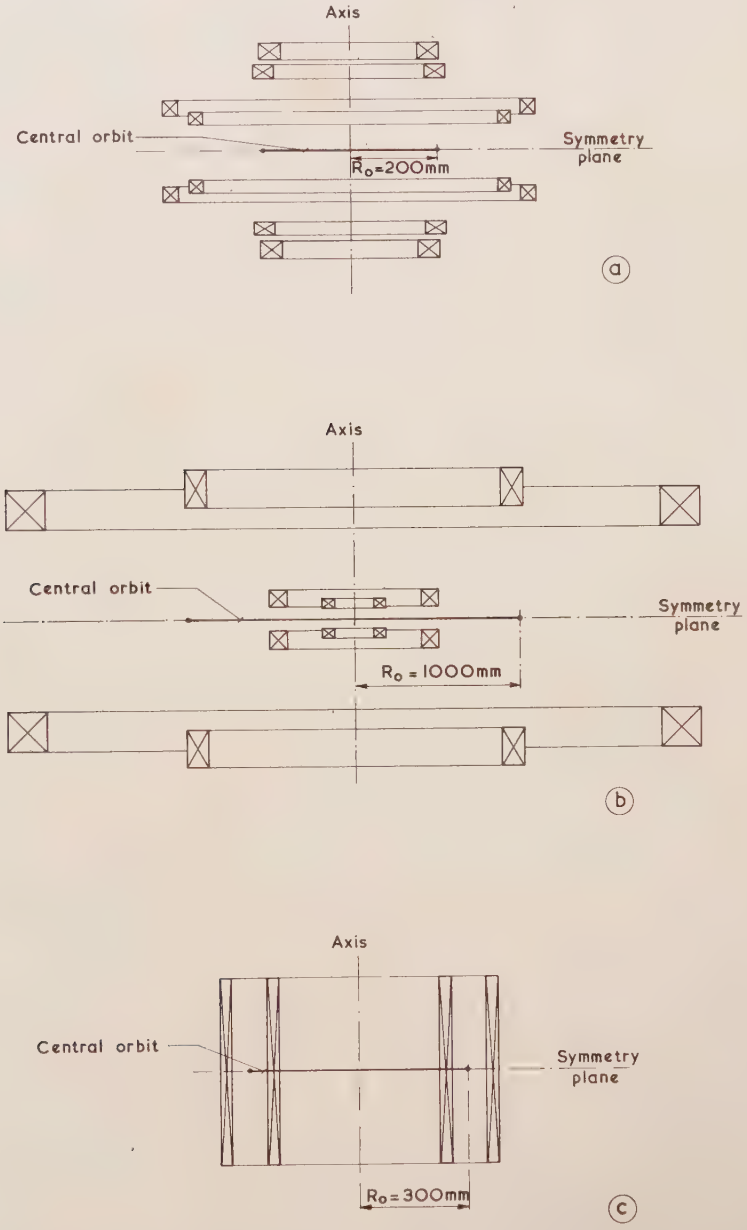

Fig. 2. Different ironfree arrangements yielding the double focusing field shape, due to (a) Moussa; (b) Lee-Whiting and Taylor; (c) Siegbahn and Edvarson.

with corresponding momentum resolution of 0.01% to 1%. The spectrometer coils are powered from a generator (600 V–50 A) and a precision standard resistor; this voltage drop is stabilized within one part in 10^5 from the reference voltage. Observed drifts in the positions of the lines of one part in 10^4 due to the temperature and external field fluctuations will

[9]) G. T. Ewan, J. S. Geiger, R. L. Graham and D. R. Mackenzie, Can. J. Phys. 37 (1959) 174.

be reduced in the future with the aid of stabilization equipment. The best momentum resolution obtained so far has been 0.013% at a transmission of 0.07%.

The instrument of Siegbahn and Edvarson[10]) ($\rho_0 = 300$ mm, $\beta = \frac{3}{8}$) consists of two coaxial counter coupled solenoids with radii of 240 mm and 360 mm and heights 500 mm. A vacuum chamber is located between the two coils in the median plane of the construction; its position can be adjusted with respect to the coils. A temperature change of 1° C in one of the coils or in the vacuum chamber is computed to cause an error in the $B\rho$-determinations of about one part in 10^5. The coils are therefore water cooled with the help of copper tubing, soldered to the inside of the copper frames; they can thus be kept constant in temperature within 1° C. The copper coils are connected in series and fed by a series of high capacity storage batteries, which guarantees the stability of the current within one part in 10^5. With small changes in the cooling system, the authors think it possible to measure beta energies up to 1 MeV while retaining the accuracy of a few parts in 10^5. This accuracy has been reached for beta energies up to 360 keV. External fields are compensated with a set of three pairs of Helmholtz coils, the currents of which are also supplied by batteries. The dimensions of the vacuum chamber allow a maximum transmission of 0.2%. The highest resolution reported so far is 0.019% at a radial opening angle of 0.01 radians.

Except for the instrument described in this thesis, the only other spectrometer of the Siegbahn type has been built by Mladjenović[3]) with a radius of the central orbit of 500 mm. The author reports a smallest linewidth of 0.018%.

From the ironfree instruments discussed, the Moussa type has in principle the advantage of a better accessibility of both the source and the counter position. The scale of the design of Moussa himself makes this advantage somewhat doubtful; it is, however, fully realized in the Chalk River instrument. The dimensions of the last instrument allow all sorts of experimental arrangements close to the source and the counter. The enormous radius of the central orbit $\rho_0 = 1000$ mm, on the other hand, requires very involved precautions against external field disturbances. As shown in section 5 these precautions are already rather involved with $\rho_0 = 300$ mm if the highest precision in the $B\rho$-determinations is desired. A definite disadvantage of the use of many coils in order to realize the desired field shape is that the degree of symmetry of the field, required for high resolution work, is only reached for a very high accuracy in the geometrical setting of these coils. In this respect the design used by Siegbahn and Edvarson is relatively simple because only two coils are involved here. These considerations and also the very good results reported by Siegbahn and Edvarson induced us to construct an instrument along the same general lines. We wished, however, to be able to measure much higher beta-energies (up to 3 MeV) with the same accuracy; the cooling of the coils had therefore to be improved considerably. Secondly, as large a transmission as possible was desired. Therefore, the instrument was designed such that the whole space between the coil tanks could be used as a vacuum chamber; the choice $\beta = \frac{3}{8}$ makes that the whole space can indeed be used since now the axial opening angle can be chosen relatively large, as is made clear in section 1. The design, made on the basis of these considerations, is described below (section 3.1).

The use of a vacuum chamber occupying the total height of the apparatus complicates the positioning of the G.M. counter and the source somewhat. The heavy constructions, needed to ensure a reproducible geometrical setting of source and counter, will be described in section 3.2, where also the special features of the counter system and the adjustable diaphragms are given.

A description of the automatically regulated cooling system, ensuring constant temperature of the coils at (25 ± 1)° C, even at the maximum power input, is given in section 3.3. The outline

[10]) K. Siegbahn and K. Edvardson, Nucl. Phys. **1** (1956) 137.

of the vacuum system is given in section 3.4.

The use of storage batteries for a current of 170 A (corresponding to 2.6 MeV electrons) is rather unpleasant; it was therefore planned to obtain the magnet current from a motor-generator set. The regulation of the current is then easy but a rather involved stabilization equipment is required in order to suppress the ripple on the d.c. voltage. The electronic device used for this purpose will be described in section 4.

A set of three pairs of Helmholtz coils is used for compensating external fields. These fields vary continuously due to various reasons: railroad traffic at 100 metre distance, automobile traffic even nearer and the influence of a cyclotron magnet at a distance of 75 meter. The most important component is therefore automatically compensated; the equipment for this will be described in section 5.

A general impression of the instrument can be obtained from the picture.

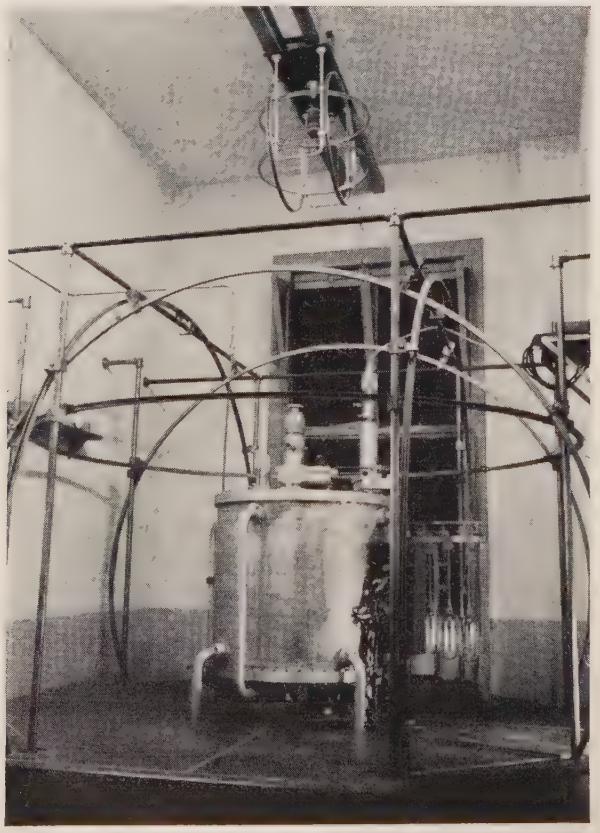

View of the ironfree double focussing spectrometer.

3. Construction of the Spectrometer

3.1. CONSTRUCTION OF COIL TANKS AND WINDING PROCEDURE

The spectrometer has been located in an old building constructed mainly out of brick walls

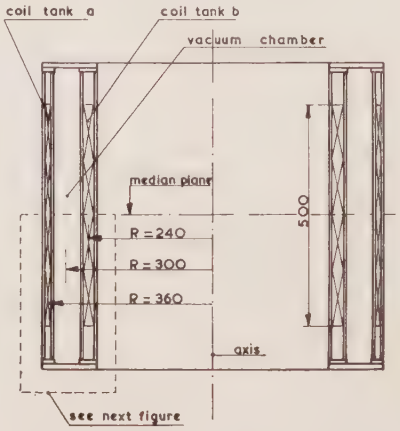

Fig. 3. Geometry of the spectrometer. The inner and outer coil are each enclosed between two cylinders. This construction allows for a cooling system, whereby each winding of the coils is brought in contact with the fluid. The coil units serve at the same time as vacuum chamber walls.

and wooden beams which is therefore suitable for housing an ironfree instrument. In addition, care has been taken to remove all obvious pieces of ferromagnetic materials from the spectrometer room and its immediate neighbourhood. The result of these precautions was found to be satisfactory.

The floor construction under the spectrometer was renewed such that the same foundation could be used for the spectrometer and for the large Helmholtz coils. A wooden platform facilitates the manipulation of the different parts of the instrument which is placed on a wooden base with three adjustable supports. These supports, made of brass, enable a final adjustment with respect to the Helmholtz coils; all the copper vacuum and cooling tubes are connected to the instrument by flexible joints.

The severe requirements on temperature stability of the coils have mainly determined the construction. Effective cooling under any working condition can best be obtained by allowing each winding to be in direct contact with the cooling medium. The use of tubes with inside cooling was not advisable; due to the fact

that the coils had to be kept thin in order to keep the space between inner and outer coils as large as possible the necessary flow of cooling liquid could then not be delivered without a very

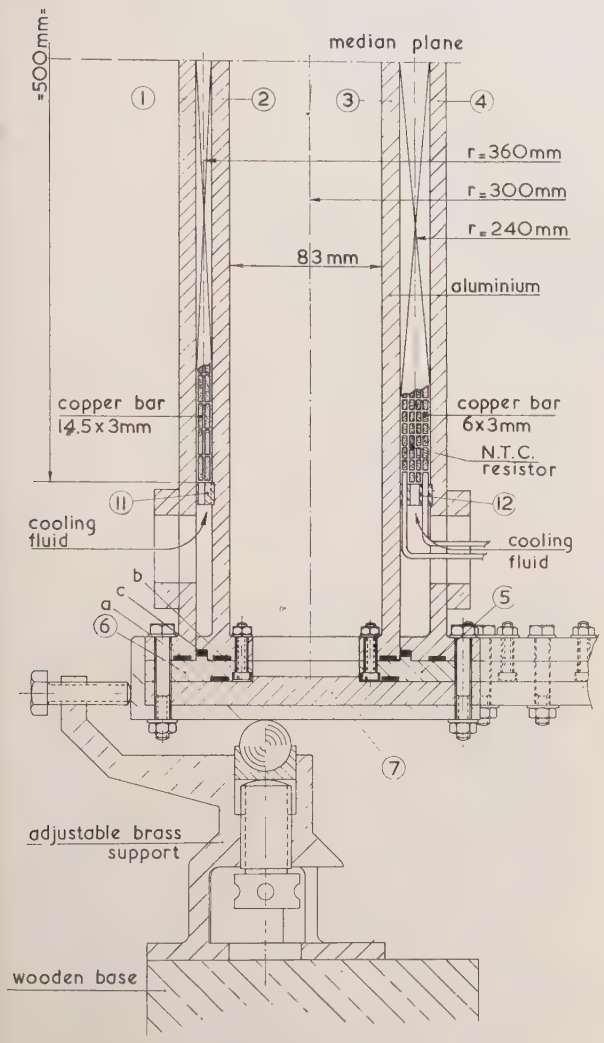

Fig. 4. Construction of the spectrometer.

high pumping pressure. Therefore, it was decided to cool the windings from the outside. Thus, the construction shown in figures 3 and 4 was chosen. Both coils are enclosed in cylindrical coil tanks which also serve as vacuum chamber walls. Each tank consists of two cylinders, made of pure aluminium (iron impurities less than 0.1%). These cylinders made of rolled sheets were welded by the argon arc process and machined to an accuracy of 0.1 mm†.

After the winding procedure, described below, the cylinders 1 and 3 are placed over the coils. The coil tanks are completed by bolting the flanges 5 and 6 on both sides to the cylinders. These flanges are sealed with polyvinilchlorid (p.v.c.) gaskets, a, b and c, in such a way that the space between the seals a and b can be evacuated if necessary. The two coil tanks are placed concentric to each other by bolting them to the flange 7 and a similar flange on the top side of the coil tanks (not shown). These flanges are machined with an accuracy of 0.1 mm to assure concentricity of the two coils. Although this construction does not allow a final adjustment of the two coils, it assures their mutual position not being disturbed. Moreover this construction gives the opportunity of using the coil tanks as vacuum chamber walls.

The dimensions of the vacuum chamber are such that a radial opening angle can be obtained of 0.09 radians; the maximum axial opening angle is fixed at 0.35 radians. The maximum solid angle is therefore 1%. Both angles can be adjusted from outside by means of movable shutters at a position schematically shown in figure 5, which is a horizontal cross section in the median plane. The figure also shows the geometrical configuration of coils, source, counter, baffles and lead shielding.

The spectrometer coils are made of electrolytical pure copper bar, the dimensions of which are indicated in fig. 4. The distances between successive windings of one layer are 1 mm for the inner coil and 2.7 mm for the outer coil (see also section 6.1). These distances are fixed by using spacers of pertinax, 20 × 1 mm and 20 × 2.7 mm, placed at distances of 50 mm. Pertinax strips, 500 × 5 × 1 mm, at distances of 20 mm, keep the layers 1 mm apart from each other and from the walls of the coil tank. These strips and the spacers are machined to an accuracy of 0.1 mm. The copper coils are thus wound with a precision of 0.1 mm with respect to cylindrical symmetry and homogeneity over the height of the coils. The coils are mounted

† We are very much indebted to N.V. Philips for carrying out perfectly this difficult work.

between two pairs of rings to fix the coil position in the vertical direction. One ring of each pair is shown in fig. 4 (11 and 12). These rings contain holes for admitting the coolant which will then

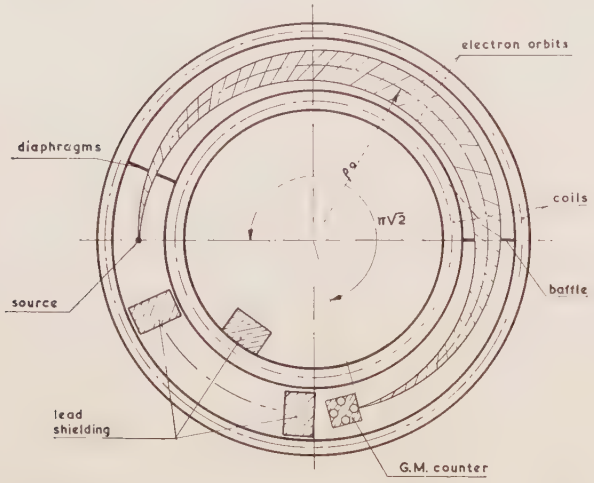

Fig. 5. Position of source, counter, diaphragms and lead shielding in the median plane of the spectrometer.

flow predominantly in the axial direction between the layers. The holes are distributed in such a way that they offer a minimum resistance to the liquid flow.

Fig. 6 gives a close up of the outer coil during the winding procedure; the figure shows also the positioning of a N.T.C. resistor between the windings. These resistors (Philips, B8 32007) with a negative temperature coefficient of the resistance of 75 Ω/° C are used to measure the temperature of the coils.

The inner coil contains 6 of these elements,

TABLE A
Geometrical and electrical data of the coils

	Outer coil	Inner coil
Number of turns	56	280
Mean radius	360 mm	240 mm
Height	500 mm	500 mm
Dimension of copper windings	3 × 14.5 mm 2 layers	3 × 6 mm 4 layers
Resistance	0.051 Ω	0.41 Ω
Maximum dissipated power	1500 W	12 000 W
Calibration constant	59×10^{-6} Wb·m^{-1}·A^{-1}	

placed in such a way that it is possible to get information about the temperature distribution in this coil. The outer coil in which the heat production is much lower, is provided with 2 N.T.C. resistances.

Table A gives both the geometrical and the electrical data of the coils.

3.2. SOURCEHOLDER, COUNTER EQUIPMENT AND DIAPHRAGMS

Special precautions are necessary to ensure the reproducibility of the positioning of the source and the counter slit in the median plane at $\rho_0 = 300$ mm. Both source and counter can be inserted through vacuum locks and have to be moved over 400 mm after passing the lock.

The position of the source in the z-direction is easily checked, but precautions had to be taken to obtain a well defined position with respect to the other degrees of freedom, ρ and φ. For that purpose, the tube supporting the sourceholder is

Fig. 6. Close-up of the outer coil during the winding procedure, showing the two layers of the coil which are separated by pertinax strips. A small N.T.C. resistor is inserted between two windings of the second layer to measure the temperature of the coil.

made of a thick, chromiumplated copper tube (ø 25 mm), which is guided by a 100 mm long akulon seal. A copper frame supporting the sourceholder can be fitted onto this tube, as may be seen in fig. 7; the sourceholder is fixed to this frame with small clamps (not shown).

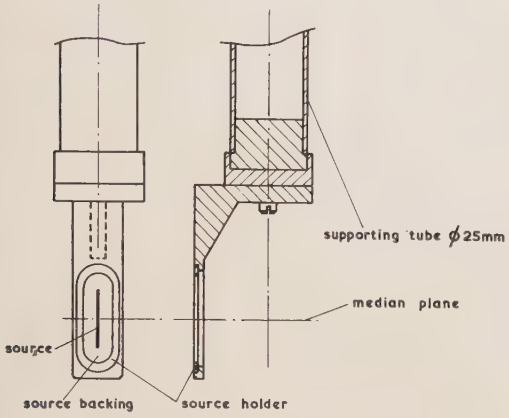

Fig. 7. Source holder.

The reproducibility of the source position in the radial direction is of the order of 0.02 mm which means better than one part in 10^4.

Instead of the frame, supporting the sourceholder, another construction can be attached which allows displacing the source in the radial as well as in the tangential direction. This construction was used for testing the focusing properties of the spectrometer by means of calibration lines (see section 6.2).

The following arguments have been considered for the counter construction:

1. According to formula (9), the resolution is dependent on the slit width; it is therefore necessary to provide for the use of different entrance slit widths to the counter. It is even possible that, during one run, different widths would be desirable: e.g. large widths for measurements of a continuous beta spectrum and narrow ones for conversion lines.

2. The counter slit and the source have to be perpendicular to the median plane of the magnetic field. This requires good reproducibility of the slit geometry.

3. It is necessary to use an extremely thin counter window to allow intensity determinations of electrons at very low energies. Use is reported of foils made of formvar as thin as 10 μg/cm^2. Such foils are rarely free from having pinholes and are easily damaged. A simple replacement procedure is required.

In connection with these considerations the

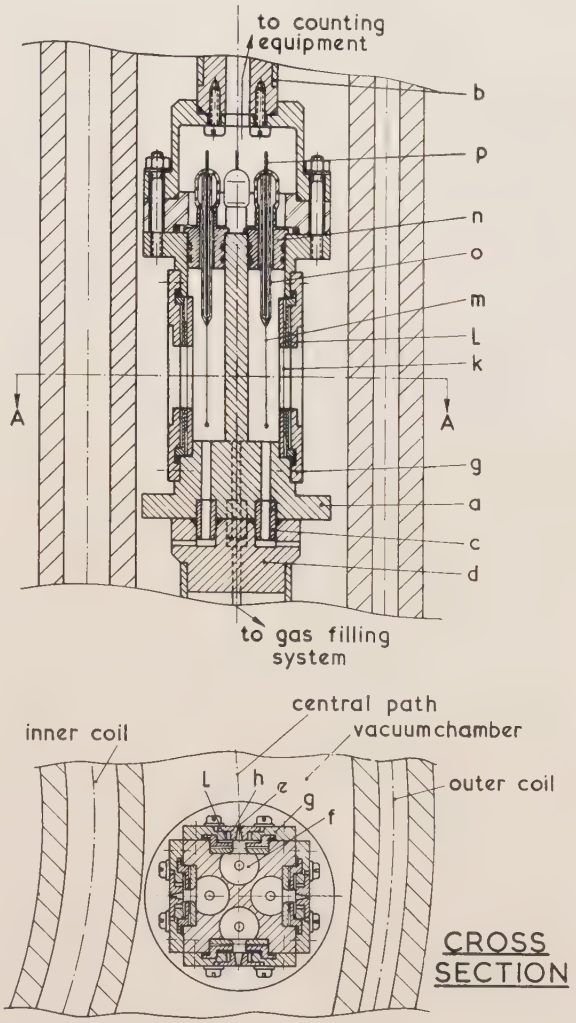

Fig. 8. Side-window Geiger-Müller counter system. For detailed explanation see text.

construction of fig. 8 was developed. This figure presents a vertical and a horizontal cross section.

A heavy copper block (a), supported by a chromium plated copper tube (b) (ø 32 mm), can be placed on a platform (d) such that its position is accurately defined by means of four studs (c). The copper block contains four similar counters; each of the counters can be

chosen as detector of the focused electrons with a simple action from outside the vacuum. Changing from one counter to another takes about half a minute.

The platform is fitted to the bottom of the vacuum chamber such that the slit (e) of the selected counter (f) is in the position required by the focusing conditions of the spectrometer. Care was taken with respect to the equivalent positioning of the different slits. The hole in the platform, in which the selected counter is placed, can be connected to a gas filling system as well as with the high vacuum side of the vacuum system. The counters not used during the measurements are kept evacuated.

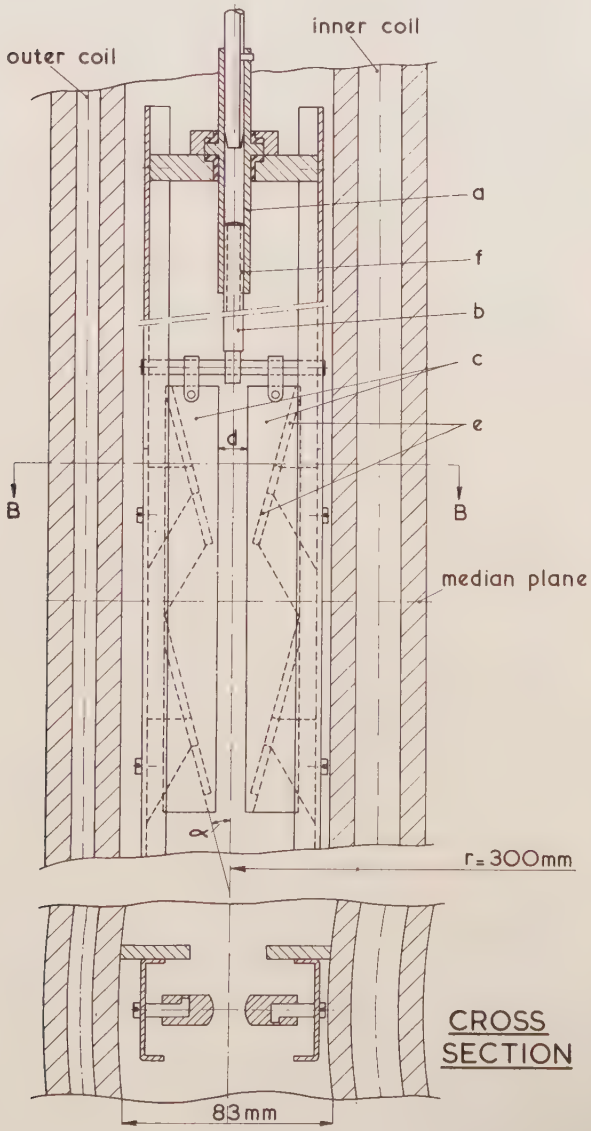

Fig. 9. Diaphragm for the radial opening angle of the electron beam.

The counter slit is defined with the aid of movable copper strips (h) fixed in a copper plate (g). They can be adjusted from 3 mm down to, say, 0.05 mm. Thus, the counter block may be provided with four different slitwidths. The counters (⌀ 15 mm, active height 50 mm) are provided with 200 μ thick tungsten cathodes. The figure shows the construction of the copper plug (n), with the glass isolation to prevent discharges. The counter window (k) is normally made of formvar ($\approx 50\ \mu g/cm^2$), supported by a nylon grid with an effective area of 95%. This grid is prepared on the copper plate (l). The foils are coated with a thin conducting layer of aluminium to avoid charging of the foil. The counter is normally filled with a 90%—10% mixture of argon-alcohol at a pressure of 6 cm Hg. The platinum thread holder (p) of the selected counter can be connected with a plug to the quenching circuit which circuit is of the type described by Den Hartog and Muller[11]; it has a fixed dead time of 0.38 milliseconds and is placed as near as possible to the Geiger counter in order to diminish the chance of external perturbations. The high voltage for the counter is provided by a Philips power supply (P.W. 4022); the counts are registered by a five decades scaler unit and a preset count/time unit (Philips P.W. 4032 and P.W. 4052). These units are placed in the control panel at about 7 meter from the spectrometer.

The system has shown to work satisfactorily. Under the conditions mentioned above, the counters have a plateau with a length of about 100 V and a slope of about three percent. The natural background is about 10 c/min. The shielding from the source allows working with rather strong activities without raising the background too much. With the formvar foils used ($\approx 50\ \mu g/cm^2$) the cut off of the counter is about 4 keV. These foils are practically free from leakages; when buffering with a one liter vessel

[11]) H. de Hartog, Thesis, Amsterdam (1948); H. de Hartog and F. A. Muller, Physica **16** (1950) 17.

the counter pressure remains constant during long periods.

Some test measurements proved that for counting rates below 15 000 c/min the efficiency is not significiently dependent on the counting rate and the results are reproducible even if intensities are determined with a time interval of several days. Above 15 000 c/min the slope of the plateau increases, thus causing comparison of line intensities to be unreliable when dealing with widely different peak counting rates. For the majority of measurements the counting rate remains below 15 000 c/min, but in order to be able to work with higher counting rates the system will be made to work as a continuous flow proportional counter; this can be done without changing the construction severely.

The diaphragms are designed such that the opening angles in both directions can be achieved without disturbing the vacuum. The problem of adjusting the radial opening angle in the median plane, at a distance of 400 mm above this plane, was solved as shown in fig. 9.

Two shutters (c) are mounted on oblique guide rails (e), so that they close the opening angle when moving downwards. This movement is controlled by turning a shaft (a) around a screw (f) on a long support (b). The radial distance (d) of the shutters depends on the pitch of the screw (f) and the angle α. Therefore, the angular displacement of the shaft (a) can be calibrated in units of radial solid angle γ_ρ, using the relation between γ_ρ and $d[= 2\ (\rho - \rho_0)]$ as given by formula (5). The angular displacement of this shaft can be read off from the outside by means of a micrometer scale. The same can be done for the axial opening angle setting. The adjustment of this opening angle is much easier to achieve and need not to be discussed. The edges of the copper shutters were machined as indicated in fig. 9. Special care was taken to assure symmetry of the slit dimensions with respect to the median plane and to the cylindrical plane $\rho = 300$ mm. As already discussed in section 3.1, the diaphragms allow a maximum solid angle of 1%.

3.3. COOLING SYSTEM

3.3.1 *Construction*

Siegbahn and Edvarson[10]) computed that a temperature rise of 1° C in one of the spectrometer coils relative to the other one, introduces an error in the $B\rho$-determination of about one part in 10^5. A temperature change in the vacuum chamber, which in their apparatus is a separate element, also effects the accuracy. They therefore maintain the temperature of their instrument constant at (18 ± 0.2)° C with the help of water cooled tubes on the inside of the coil cylinders. The maximum power dissipated in their instrument is about 350 W. The power dissipated in the coils of the present instrument at beta-energies of 2.6 MeV, however, will be about 13.5 kVA. This makes it mandatory, that the cooling system has to be very effective if, at different energies, a temperature constancy of the coils within 1° C is desired. As already discussed in section 3.1, each winding of the coils is brought in direct contact with the cooling fluid. This method of cooling requires the use of a cooling medium with a very high specific resistance in order to keep the electric leakage currents sufficiently small. Therefore, kerosine having a specific resistance of $2 \times 10^{14}\ \Omega$/m has been chosen as the coolant.

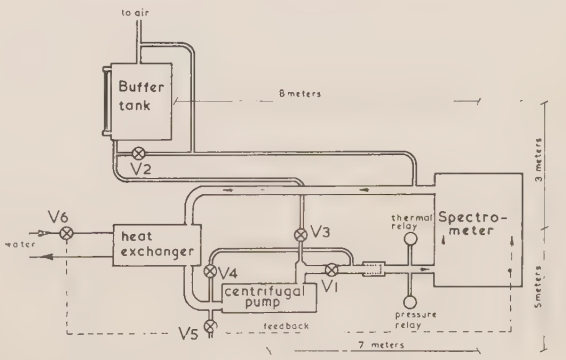

Fig. 10. Cooling system.

The rate of flow of the coolant was determined by the allowed temperature rise of the kerosine during its, mainly axial, passage through the coils. This temperature rise must be kept as small as possible to avoid large temperature gradients in the coils. The two coils are placed

in series for the coolant, which first flows through the outer coil and then through the inner one. The coolant enters both coil tanks at the bottom and leaves at the top. Homogeneity of the flow over the coils is enhanced by having four separate entry and exit ports, spaced 90° apart on the circumference of the coil tanks.

The cooling arrangement is shown schematically in fig. 10. The flow of the kerosine (400 liter per minute) is caused by a centrifugal pump (Sihi Z 8520 K/KK) working at a pressure of 1.3 atmospheres. The capacity of the heat exchanger is 10 kVA at a temperature difference of 10° C. Several filters in the main circuit prevent the entrance of electrically conducting particles which could shortcircuit the bare windings. Under working conditions, only the valves V_1, V_2 and V_6 are open. The other valves are only used if the kerosine has to be removed from the coil tanks to the buffer tank; this can be done with the help of the Sihi pump. The temperature of the coils can be kept constant at $(25 \pm 0.5)°$ C by automatically adjusting the position of the motor-driven valve V_6 in response to the signal obtained from one of the N.T.C. resistances built in the inner coil.

As safeguards, a thermo-relay and a pressure-relay are built in which are inserted electrically in the primary of the motor of the d.c. generator. The approximate distances between the iron containing parts of the system and the spectrometer are indicated in fig. 10.

3.3.2. *Performance of the cooling system*

The cooling system has worked quite satisfactorily for two years now. The coils can be kept constant in temperature within 0.5° C at an average temperature of 25° C, even at the highest occurring power input.

The N.T.C. resistor used for the stabilization system is situated in the median plane and between two layers of the inner coil. Thus, in fact the temperature of this resistor is stabilized, which means that for a discussion of the influence of the temperature distribution within the coils on the $B\rho$-determinations, one should consider the temperature difference between the coils and the N.T.C. resistor. At low currents this difference will be negligible; at high currents, however, one may expect the existence of (a) a temperature gradient in the direction of the kerosine flow and thus a difference between the average temperatures of both coils which are cooled in series and (b) a temperature jump between the inner coil and the coolant; the temperature of the resistor will lie somewhere between that of the inner coil and of the kerosine.

By means of the N.T.C. resistors inserted within the coils, we were able to investigate the temperature gradients in both coils at the maximum power input. When measuring at an energy of 2.6 MeV the power input in the inner coil is about 12 kVA, while the power input in the outer coil is then 1.5 kVA. The measurements showed that the axial gradient in the inner coil is about 1° C over the height of the coil, while the gradient in the outer coil can be neglected. These measurements also indicated that gradients in the φ-direction are not larger than 0.5° C per 180 degrees. Here we have assumed that the gradients as measured with the N.T.C. resistors are representative for those of the coils themselves. The absolute temperature of the coils at high coil current deviates from the temperature of the resistors. Therefore we decided to perform an independent measurement from which we could obtain information about the average coil temperature relative to that of the N.T.C. resistor used for the stabilization system. For this purpose we measured the resistances of the two copper coils at low as well as at high currents; during these measurements the temperature of the resistor in the median plane of the inner coil was kept constant within 0.2° C. From these measurements the difference in the average temperature of both coils at 170 A coil current was found to be about 0.9° C, whereas the average temperature of the inner coil was about 0.4° C higher than that of the resistor.

The above results are presented in fig. 11. A stream line of the kerosine is taken as the horizontal axis, while the temperature is plotted along the vertical axis. The temperatures given

are relative to that of the resistor in the median plane of the inner coil, which temperature is approximately 25° C. The dotted lines indicate the temperature of the kerosine at 170 A coil current as can be deduced from the combined knowledge of the ratio of the power inputs in both coils and of the ratio of the surfaces of the mentally (a) the effect of a temperature change of one of the coils relative to the other one and (b) the effect of an overall temperature change.

Table B presents the potentiometer reading at the top of a conversion line (ThB F-line) measured under different conditions with respect to coil temperatures. The temperature diffe-

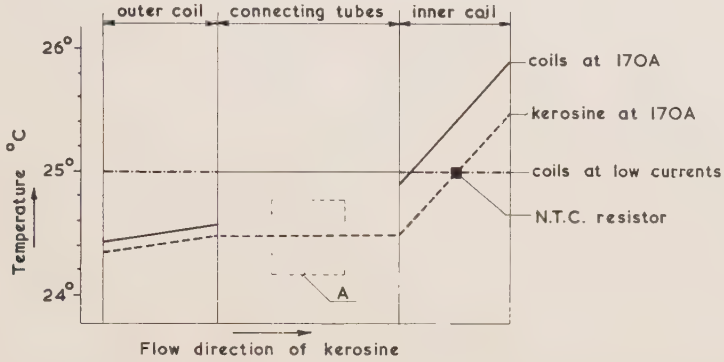

Fig. 11. Temperature distribution within the coils: – · – · – at low currents, ———— at the maximum coil current.

The figure shows that the temperature of the N.T.C. resistor, positioned in the median plane of the inner coil, follows that of the kerosine. For a discussion of the error in the $B\rho$-determination due to the temperature distribution of the coils at high currents, see text. The position of the box containing the resistors R_m (see figure 13), which box is inserted in one of the tubes connecting the inner and the outer coil for the kerosine, is indicated by the square A; thus these resistors are kept at kerosine temperature.

coils being in contact with the kerosine. Fig. 11 shows also that the manganin resistances R_m used for the bridge circuit of the magnet current device and inserted in box A, are kept constant in temperature within 1° C at any coil current.

Now we will discuss the effect on the positions of lines in consequence of (a) an overall temperature change of 1° C and (b) the temperature distribution at the maximum coil current as given in fig. 11.

Siegbahn and Edvarson[10]) have calculated the influence on the $B\rho$-determinations of a temperature change of 1° C in one of the coils or in the vacuum chamber. In our case, however, a straightforward calculation can not be given, because each copper coil is situated between two aluminium cylinders while these coil units are bolted together by aluminium flanges, the temperature distribution of which determine the position of the source- and counter construction. Therefore we preferred to determine experience between the coils during run B could be obtained by switching off the cooling pump at the end of run A; maintaining the same coil current run B could be taken after about one hour. From these measurements can be deduced that the effect on the position of the line is about 2.2 parts in 10^5 due to a temperature change of 1° C in the inner coil, while a change in temperature of 1° C in the outer coil corresponds with an effect of one part in 10^5. Both

Table B

Influence of the coil temperatures on the line position

	Potentiometer reading at the top of the F-line (halfwidth 0.04 %)	Temperature	
		inner coil	outer coil
Run A	69 390	18.2° C	18.2° C
Run B	69 412†	30.2° C	21.2° C
Run C	69 417†	30.2° C	30.2° C

† Corrected for shift in the compensation level of the external magnetic field (see section 5.3).

line shifts are in the same direction. Thus an overall temperature change of 1° C will cause an error in the $B\rho$-determinations of 3.2 parts in 10^5. The same shift is found also (a) when measuring the same line with the use of another manganin resistance R_m (see fig. 13) and (b) when measuring a line different in $B\rho$-value by a factor of 2 (ThB L-line).

The influence of the temperature distribution at high currents on the $B\rho$-determinations can be found using the above line shifts in consequence of the separate temperature changes of the two coils. We will assume here that the gradient in the inner coil will not affect the positions of the lines in first order. Then we arrive at the result that the lines measured at 2.6 MeV will be shifted with about 0.5 parts in 10^5 towards higher current readings relative to low energetic lines. If necessary, the measurements can be corrected for this error because of its systematic character.

As will be discussed in section 5.3 a temperature change of 1° C of the inner coil will also cause a deviation from the true line position due to the fact that part of the external field compensation system is dependent on this coil temperature. This line shift is about one part in 10^5 per 1° C with the same sign as the line shift discussed above.

Thus we arrive finally at the following errors in the $B\rho$-determinations due to the cooling system:

a. The error due to an overall temperature change of 1° C is 4.2 parts in 10^5.

b. The error due to the difference in temperature of both coils at higher currents is at most one part in 10^5.

3.4. VACUUM SYSTEM (Fig. 12)

The vacuum tank of the spectrometer, which has a volume of 100 liter, is exhausted by an oil diffusion pump made of brass and copper (Philips O 4), backed by a rotating pump (Edwards 1S150). The latter pump is placed at a distance of 8 meter from the spectrometer. The connecting tubes are made of copper and are 60 mm in diameter. Aluminium air locks for admission of the source and the counter can be connected to the fore vacuum or the oil diffusion pump by valves V_5, V_6, V_7 and V_8; the gas filling system of the Geiger counter can be connected to the oil diffusion pump. The pressure in the

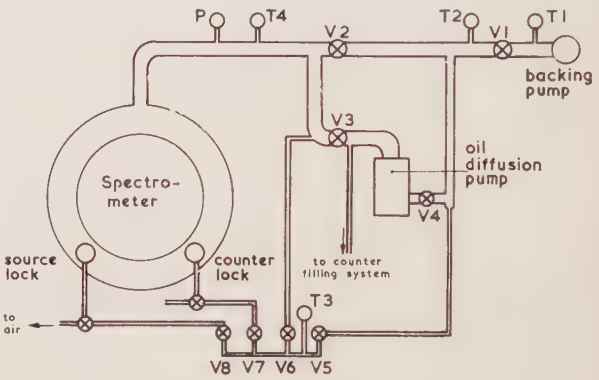

Fig. 12. Vacuum system.

different parts of the system can be read on four thermocouple manometers (T_1—T_4) (Philips Th 2), whereas in the vicinity of the tank the high vacuum can be measured with an ionization gauge (P). Most of the valves, indicated in the figure are Dikkers-Jenkins globe valves with slight modifications as described by Zilverschoon[12]) to make them useful for high vacuum work.

With this vacuum system it takes about 20 minutes to evacuate the vacuum chamber from atmospheric pressure down to about 10^{-4} mm Hg.

4. Generation, Stabilization and Regulation of the Magnet Current

4.1. INTRODUCTION

The magnet current supply of the spectrometer has been designed under the following considerations:

a. The maximum coil current must be about 170 A in order to obtain a magnetic field intensity, that will bend a beam of electrons of 2.6 MeV along a circle with a radius of 300 mm (see table A). For low energy work stabilized currents as low as a few A (5 keV $\triangleq$ 4 A) should be attainable.

[12]) C. J. Zilverschoon, Thesis, Amsterdam (1954).

b. The determination of the line position with a precision of a few parts in 10^5, as is feasible when dealing with a resolution of, say 0.02%, demands a long range stability of the field intensity of one part in 10^5 or better in the whole current range.

changed; it offers the opportunity of regulating the main current through the coils electronically with the help of an exciter for the field current of the generator. On the other hand, the ripple of any d.c. generator is orders of magnitudes larger than permitted by the above considera-

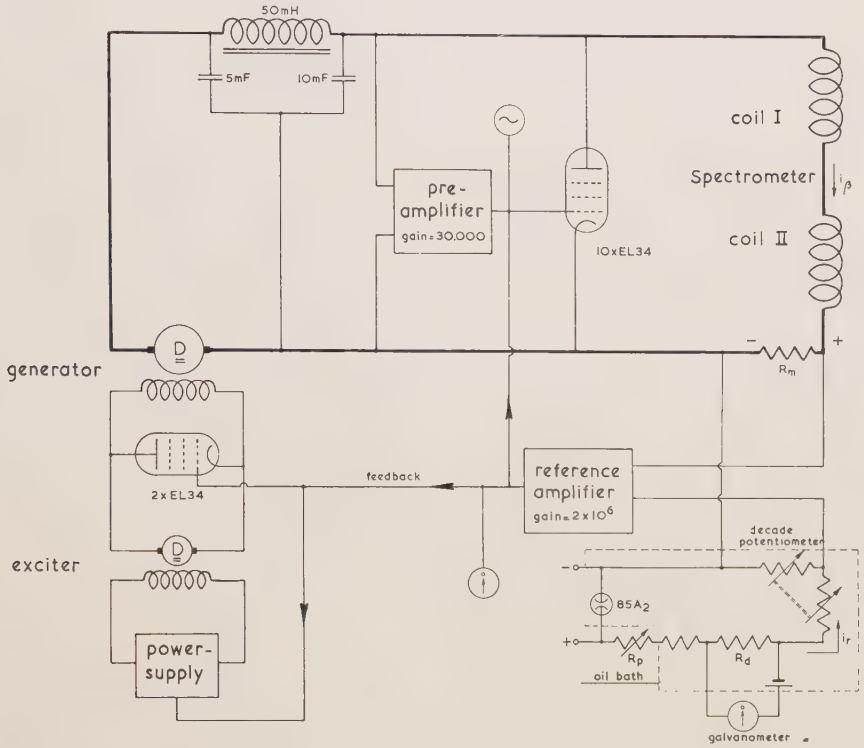

Fig. 13. Block diagram of the magnet current supply.

c. The stability of the current must be such that the line broadening due to current fluctuations is relatively small. This can be called short range stability. If we demand, that this line broadening be not more than one tenth of the intended resolution of a few parts in 10^4, the short range stability must be a few parts in 10^5 or better.

As already mentioned in section 2, the use of storage batteries for currents up to 170 A is rather unpleasant although it would be the most natural choice with respect to the stability requirements. Therefore we decided to use a motor-d.c. generator. Such a current source is very suitable for a beta-ray spectrometer where the current settings must be quickly and often

tions. Thus, a rather involved stabilization equipment had to be designed.

A convenient system has been described by Verster[13]) for the regulation of an ironfree short lens beta-ray spectrometer (long range stability better than $1:10^3$). The current through the spectrometer causes a voltage drop across a standard resistor; this voltage drop is compared with an adjustable reference voltage. The voltage difference is used as a signal for a device which adjusts the current in the main circuit. This arrangement not only keeps the spectrometer current constant, but it also allows a determination of the absolute value of this current, because the reference voltage is determined by a constant

[13]) N. F. Verster, Appl. Sci. Res. B1 (1949) 358.

current flowing through a four decade resistor.

An improved version has been developed by Schutten[14]) for the stabilization of the magnetic field of the Amsterdam isotope separator (Zilverschoon[12])). The short range stability of the magnetic field of this iron containing instrument is about $1:10^4$. The main principles of the above mentioned magnet current supplies have been used as a guide for the construction of the equipment which will be described now.

4.2. EQUIPMENT

Fig. 13 shows a block diagram of the whole system. The d.c. generator (110 V, 170 A) can be regulated electronically using an exciter, the maximum coil current of which does not exceed 170 mA. The power supply for this current, controlled by the output voltage of the bridge circuit (see below), can also deliver a current in opposite direction, sufficient to compensate the remanence field in the stator of the generator. Thus, the current through the spectrometer coils can be regulated down to zero. The field current of the generator (max. 3 A) is mainly delivered by the exciter; a parallel feeding system serving as a variable resistance supplies about 200 mA into the field coils of the generator. The grid voltage of the parallel tubes ($2 \times$ EL 34) is also controlled by the output of the bridge circuit. This parallel feeding system reduces the time delay of the exciter (≈ 1 second), because now voltage variations on the output of the bridge circuit will supply current in the generator field coils rather than voltage as would be the case if these variations were fed back via the power supply of the exciter. The parallel system is effective only for variations with a frequency lower than a few cycles per second. Higher frequencies due to (a) the instability of the position of the rotor of the generator, (b) the revolution of the rotor and (c) the collector, could not be suppressed in an effective way by this feedback system, because of the time delay in the generator itself ($\frac{1}{10}$ second). Thus, these frequencies had to be suppressed directly in the main circuit. This demands a rather elaborate set up in view of the desired stability and of the very low impedance of the air coils (600 μH, 0.5 Ω) and has been carried out as follows:

First a π-filter was placed in the main circuit, consisting of a self inductance (50 mH at a d.c. current of 100 A) and 2 capacitors, 5 and 10 mF respectively. This filter is by no means sufficient (see table C); therefore the output capacitance has been enlarged electronically. The "electronic capacitance" (impedance for 25 Hz ≈ 2 mΩ) consists in principle of 10 tubes (EL 34) parallel with the spectrometer coils. The grid voltage of these tubes is regulated with the output of a pre-amplifier (gain 3×10^4). These grids are also connected to the output of the bridge circuit as this has shown to be effective with respect to suppressing slow oscillations of the whole stabilizing equipment. The effectiveness of this quick stabilizer with respect to suppressing the ripple of the generator is roughly indicated in table C.

TABLE C

Instabilities of the voltage in the generator-spectrometer circuit as measured at different points

	Instabilities due to		
	Jumping of the rotor	Revolution of the rotor	Collector
Without stabilization	$\approx 0.1\%$	$\approx 1\%$	$\approx 1\%$
With π-filter	$\approx 0.1\%$	0.1%	$< 0.01\%$
With π-filter and quick stabilizer	0.003%	0.001%	—

The bridge circuit indicated in the block diagram will be discussed in more detail, because it partly determines the precision of the measurements. The circuit consists of a resistor R_m through which the main current i_β is flowing, a five decade potentiometer and a reference current i_r. The resistor R_m is a combination of four manganin resistors for different ranges of i_β. They are inserted in the cooling system of

[14]) J. Schutten, Appl. Sci. Res. B2 (1952) 249.

the spectrometer (see fig. 11); thus, they are kept constant at a temperature of $25 \pm 1°$ C. Their values are chosen such, that the voltage drop across them due to i_β can be read off with an accuracy of better than two parts in 10^5 by means of a five decade potentiometer,

$$10 \times (1000 + 100 + 10 + 1 + 0.1)\ \Omega\ ,$$

through which a reference current $i_r (= 0.1$ mA) is flowing. The potentiometer is manufactured by the N.V. Bleeker, Zeist, with an accuracy of about one part in 10^5. The reference current is kept constant at 0.1 mA with an accuracy better than one part in 10^5 with the aid of a stabilized neon tube (Philips 85A2) and can be checked continuously by comparing the voltage drop across a high resistance R_s (10.1874 kΩ) with the voltage of a Weston standard cell (1.01874 V) and adjusted to the correct value by means of the potentiometer R_p. The five decade potentiometer, the Weston standard cell, the neon tube and R_d are kept at a constant temperature, $25.0 \pm 0.1°$ C, with the aid of an oil bath, the temperature of which is controlled by a N.T.C. resistor (Philips, Miniature Type B8 320 05 P/330).

The output of the bridge circuit is fed to a reference amplifier. This amplifier (input impedance 100 kΩ) is of the same type as that described by Schutten[14]). The d.c. signal is first converted into an a.c. voltage by means of a modified Brown converter (400 c/sec), amplified in four stages of push pull and finally synchronously rectified by a four triode circuit. The d.c. gain of this amplifier is about 2×10^6. The output of this amplifier controls different parts of the stabilizing system as described above.

4.3. PERFORMANCE

The magnet current system has been in use for 18 months. Up till now it has worked quite satisfactorily. How far the requirements for this device have been met will be discussed now.

Any stabilized coil current can be obtained just by choosing a certain setting of the potentiometer of the bridge circuit. The time delay for steps of 0.1 A or less is negligible, whereas it takes about 1 minute to increase or decrease the coil current by 15 A.

The stability of the main current can be checked on the control desk by means of a d.c. meter, which is connected to the output of the reference amplifier and an oscilloscope, which is connected to the output of the pre-amplifier of the quick stabilizer in the primary circuit (see fig. 13). Fluctuations, in the order of a few parts in 10^6 are observable on the d.c. meter at any current. The spectrum from the oscilloscope indicates that the short range stability of the voltage across the coils is in the order of one part in 10^5. At rather low currents say less than 15 A, the short range stability is somewhat less good, up to about one part in 10^4, because some very slow fluctuations seem to be independent of the d.c. level of the generator voltage. The short range stability of the field intensity in consequence of that of the voltage across the coils is not known, although it may be expected to be somewhat better due to the coil tanks, which form short-circuited windings in the generated field. An experimental indication that the short range stability meets the ultimate requirements has been obtained from calibration measurements, during which a resolution has been reached of 0.013% for a conversion line with an energy of 222 keV (corresponding to a coil current of about 30 A).

The long range stability of the average d.c. level of the current could be checked during measurements stretched out over several days; shifts in the positions of the different lines did not exceed a few parts in 10^5.

As the reading of the potentiometer of the bridge system is used for the determination of the coil current we will discuss now possible sources of error in the current determinations:

a. Leakage currents from the coils through the cooling fluid to the coil tanks, causing the coil current to be different from the current through R_m (see fig. 13). From section 3.3.1 we may conclude that leakage currents are orders of magnitudes lower than one part in 10^5 of the coil current.

b. Temperature changes in the different parts

of the bridge circuit. As described in section 4.2 all essential parts are kept at a constant temperature such that no temperature changes can occur which will affect the precision of one part in 10^5.

d. Other sources of error, e.g. contact potentials and leakage currents in the bridge circuit. Special attention has been paid to these sources of errors. Although nothing could be found

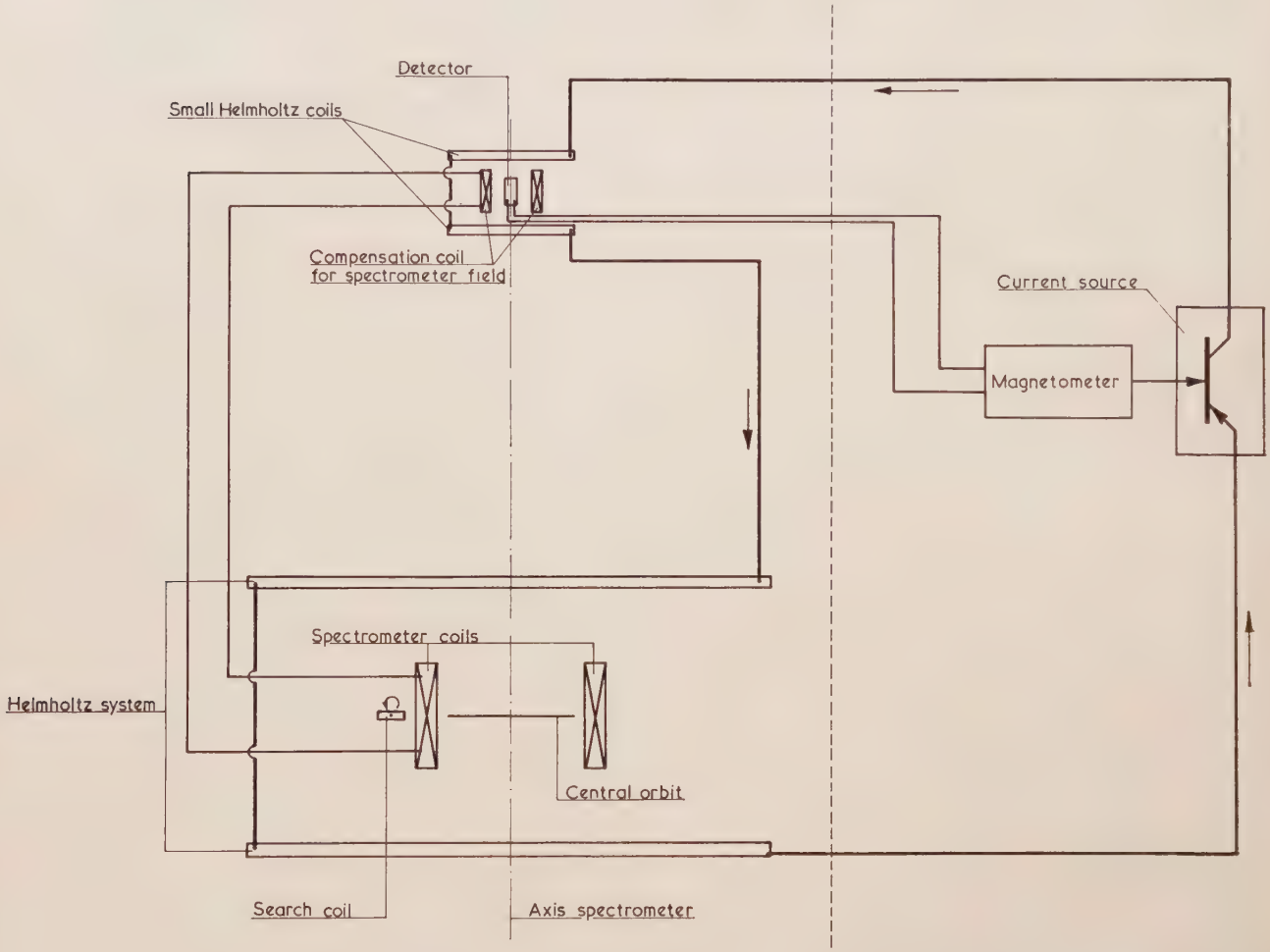

Fig. 14. Block diagram of the automatic compensation of the external magnetic field.

c. Deviation of the potentiometer reading from the true value. Each current reading is corrected for the zero resistance of this potentiometer. In addition, the true resistance can deviate from that indicated by the reading due to errors in the calibration of this element. The calibration has been carried out with an accuracy of one part in 10^5 by N.V. Bleeker at Zeist, Holland. This calibration procedure has been repeated after a time interval of about one year; no deviations have been found larger than two parts in 10^5.

which could affect the precision of one part in 10^5, it is felt that this measuring device need to be checked with precision compensating bridges if the highest possible accuracy is desired. The combined uncertainty due to the last two sources of error is assumed to be two parts in 10^5 for any current reading.

5. External Field Compensation

5.1. INTRODUCTION

The magnetic field intensity in an ironfree instrument is linearly proportional to the

current through the coils if no external fields are present. This fact makes it possible to use coil current readings as a measure for the momentum of the focused electrons. A known constant external field can be corrected for in computing electron momenta from current readings. The field gradient

$$\alpha = \frac{\rho_0}{B_0}\left(\frac{dB}{d\rho}\right)_{\rho_0},$$

however, is then dependent on the coil current. An external field of 0.45×10^{-4} Wb/m^2 (vertical component of the earth magnetic field at Amsterdam) would give a difference of 2% in the value of α at magnetic field intensities of 1 and 2×10^{-3} Wb/m^2, which means that the focusing properties would be seriously dependent on the field intensity. It is therefore necessary to compensate the external field. In addition, fluctuations of magnitudes up to 5×10^{-7} Wb/m^2 occur due to earth currents from railroad traffic at 100 meter from the instrument, while the 72″ synchrocyclotron magnet at this Institute as well as cars parking near the spectrometer building may cause field intensities of about 10^{-6} Wb/m^2; this means that the compensating system should be checked continually. The above considerations apply mainly to the vertical component of the external field; the horizontal component is less important since the electron orbits are mainly horizontal.

In order to be able to use the instrument with the intended precision of a few parts in 10^5 in the lowest previsaged energy region corresponding to a field intensity of about 10^{-3} Wb/m^2, external fields should be compensated with a precision of a few parts in 10^{-8} Wb/m^2.

5.2. COMPENSATION SYSTEM

In connection with the situation of the spectrometer room relative to the horizontal direction of the earth magnetic field, the horizontal component is compensated by means of two pairs of Helmholtz coils with their axis perpendicular to each other and with radii of 1.25 meter and 1.30 meter. The currents through these coils are delivered by power supplies which are stabilized within one part in 10^3. The values of these currents are such that the corresponding residual field at the centre of the spectrometer is less than 10^{-7} Wb/m^2. The d.c. levels of these currents can be checked by comparing the voltage drop across a precision resistance with the voltage of a standard cell. Fluctuations of the horizontal component of the external field are not compensated; an investigation of the influence of these fluctuations has shown that it is not necessary to compensate for them.

The z-component of the external field at the central orbit ($\rho_0 = 300$ mm) is compensated by means of a third pair of Helmholtz coils (radius = 1.20 meter). About 65 ampere-turns are necessary for compensating a magnetic field of 0.45×10^{-4} Wb/m^2; 340 turns are used in order to keep the necessary current conveniently low with a view towards automatic compensation of this vertical component. The compensation circuit will be described now (see fig. 14).

On the axis and 2.2 meter above the median plane of the spectrometer a magnetometer is placed within a small pair of Helmholtz coils (radius = 0.25 meter). This pair of Helmholtz coils, connected in series with the main Helmholtz coils, is designed such that it eliminates the external magnetic field at the position of the detector if the external field at the central orbit is compensated by the main Helmholtz coils. The detector is a magnetometer from the "Institut Dr. Förster", Reutlingen, Germany (type 1.103). The maximum sensitivity of this instrument is about 10^{-9} Wb/m^2. The output voltage of this instrument controls a transistorized current source for both pairs of Helmholtz coils. The overall gain of this feedback system is 4000. The detector is mounted 2.2 meter above the median plane to allow for an accurate compensation of the fringing field of the spectrometer. This compensation is performed by means of an extra coil around the detector, which coil is connected parallel to the spectrometer coils and the standard resistor R_m, as shown in fig. 16.

5.3. PERFORMANCE

The zero method system reduces the fluctuations described above to less than 10^{-8} Wb/m² at the position of the field detector. Thus, external field fluctuations equally strong at the positions of detector and central orbit, e.g. due to

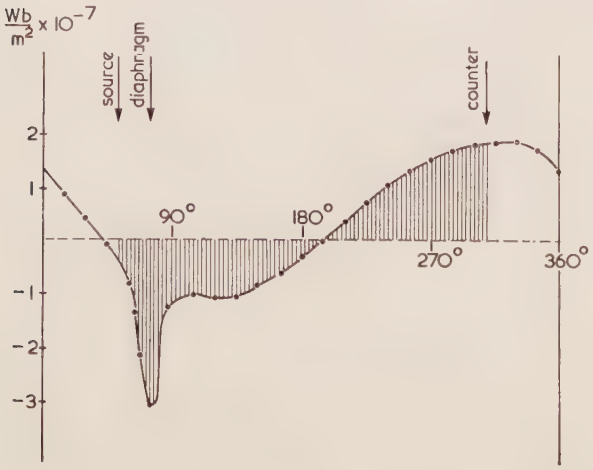

Fig. 15. Residual magnetic field along the central orbit.

changes in the intensity of the earth magnetic field, railroad traffic and the fringing field of the synchrocyclotron, will contribute less than one part in 10^5 to the spectrometer field even when measuring electron lines at an energy as low as 8 keV. Disturbances from nearby parking cars, however, still can cause a shift of 10^{-7} Wb/m² in the field intensity at the electron orbits due to the distance between the field detector and the median plane of the spectrometer. During high precision work, therefore, automobiles are not allowed to park within a radius of 20 meter. In addition, precautions have to be taken also for preventing disturbances, which might be caused by displacing iron containing equipment in the building.

The residual external field along the central orbit has been measured with a second magnetometer of the same sensitivity as the one used for the feedback system. As shown in fig. 15 the result follows a sinusoidal curve with a maximum amplitude of 1.5×10^{-7} Wb/m². The zero level, which has been adjusted by shifting the position of the detector of the feedback system in the axial direction, has been chosen such, that the integral of the intensity of the residual field over the central orbit between source and counter is nearly zero. Thus, this residual field which is probably due to imperfections of the Helmholtz system, can be neglected in most cases. Only for the very low energy region a correction to the $B\rho$-determinations has to be applied. The figure also shows that a peak near to the diaphragms is superimposed on the periodic field. This is due to iron impurities in a brass rod used for the construction of the diaphragms. Here again the influence of this disturbance can be neglected in all the usual work.

Long term drift of the adjusted compensation level may be caused by displacements of the field detector relative to the Helmholtz coils and to the spectrometer and also by a shift in the zero voltage level of the electronic equipment. The cause of a shift in the zero voltage level can be twofold (a) the d.c. level of the balanced amplifier may be out of balance, which can easily be checked and (b) the response of the field detector may become asymmetric about zero (Sokolowski[15])). To check the long term drift we attached a search coil to the spectrometer tank in the median plane and 250 mm outside the central orbit (see fig. 14). The sensitivity of this search coil is such, that a shift of 2×10^{-8} Wb/m² can be detected by means of a galvanometer equipment. During several months a long term drift of the compensation level of more than 5×10^{-8} Wb/m² has not been observed. Mainly due to the uncertainty in the difference in the field intensities at the positions of search coil and central orbit, we cannot exclude an external field contribution of 5×10^{-8} Wb/m² to the magnetic field generated by the spectrometer coils. This possible contribution means that a systematic uncertainty of 0.015×10^{-6} Wb/m in the determinations of the $B\rho$-values of electron lines should be taken into account.

Finally we will discuss the influence of the circuit used in order to compensate for the fringing field of the spectrometer at the position of the detector (fig. 16). In principle such a

[15]) E. Sokolowski, Ark. f. Fysik **15** (1959) 1.

compensation is not necessary; without it, the automatic external field compensating system will add to the spectrometer field, due to the feedback system, a homogeneous field approximately 0.2% of the spectrometer field which does not even disturb seriously the field shape in the spectrometer.

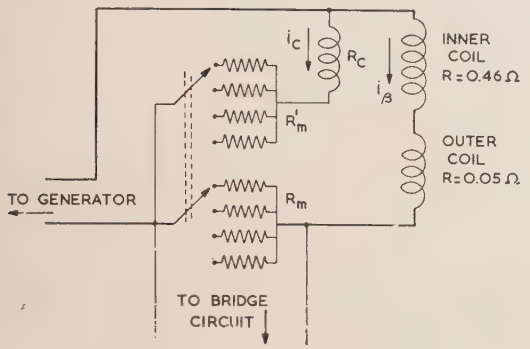

Fig. 16. The circuit to compensate the stray field of the spectrometer at the position of the field detector by means of the coil R_c.

At higher spectrometer currents, however, the intensity of the fringing field becomes larger than the earth field intensity; since it has the opposite sign, this introduces a complication in the feedback system. Therefore we decided to connect a compensation coil R_c to the spectrometer coils as indicated in fig. 16. The current ratio i_c/i_β is constant at any spectrometer current provided that (a) at each choice of R_m the corresponding resistance R'_m is chosen and (b) the resistances of R_c, the inner coil and of R'_m remain constant. The resistance of the outer coil and of R_m can be neglected in this consideration. Due to the fact that R'_m and R_c are made of constantan and manganin respectively, only temperature fluctuations of the copper inner coil can affect the constancy of the ratio i_c/i_β. The average temperature of this coil is kept constant within 1° C at all currents (see section 3.3). The temperature coefficient of the resistance of copper is 0.45% and the ratio between the spectrometer magnetic field at the central orbit and at the position of the compensating coil R_c is about 600. The influence on the $B\rho$-determinations in consequence of temperature fluctuations of the coils of 1° C is therefore about one part in 10^5. Only when measuring with the highest precision, the magnitude of this error becomes comparable with other errors; in that case it is possible to keep the temperature of the coils constant within a few tenths of one degree. We conclude therefore that the errors due to the fact that the compensating coil has been connected in parallel to the spectrometer coils can be neglected in all cases.

6. Determination of the Field Coefficients

6.1. DIRECT FIELD MEASUREMENTS

The values of the field coefficients α and β are obtained from the magnetic field distribution, which was measured using the Hall effect. The effective area of the hall plate used (Siemens and Halske, hall generator type FA 21) is 1×2 mm^2, which is sufficiently small to avoid the necessity to correct for the extension of the field measuring element. The hall voltage at 0.02 Wb/m^2 is about 1 mV when the current i_h through the plate is 75 mA; this voltage can be measured with an accuracy better than 0.1%. This precision enables one to determine α and β with sufficient accuracy. The temperature coefficient of the hall constant, which is defined as the ratio between the output voltage and the product of the field intensity and the current through the plate, is about 0.05% per °C. Since the measurements were carried out between the two spectrometer coils, which were kept at a temperature constant within 0.5° C, this temperature coefficient did not introduce serious uncertainties. The hall voltage has been measured with a null method using the bridge circuit shown in fig. 17.

The reading of the high precision decade resistor R_d at zero bridge current is taken as a measure of the hall voltage.

Since the method is relatively new, we tested its reliability. The ironfree spectrometer offers an ideal opportunity to test the linearity of the detector response; by changing the magnetic field intensity B in well defined steps (with an accuracy better than one part in 10^4) the hall voltage is measured as a function of B. The

region from (0—250) $\times 10^{-4}$ Wb/m^2 has been investigated in this way. The result, analyzed with the aid of a least square method, gave no

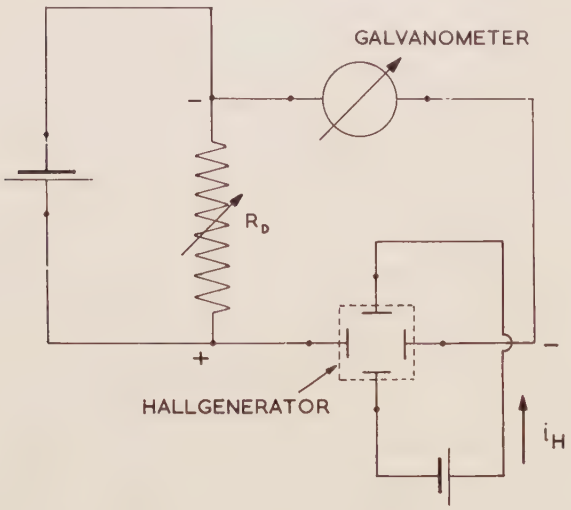

Fig. 17. The bridge circuit used to measure the output voltage of the hall generator.

departures from a straight line greater than 0.1%. In the region from (190–210) $\times 10^{-4}$ Wb/m^2, which region is of special interest because the field distribution has been measured at an average field intensity of 200 $\times 10^{-4}$ Wb/m^2, the departures from linearity were even smaller than 0.05%. The reproducibility of the measurements has been found to be about one part in 10^4.

A measurement of the axial symmetry of the spectrometer field was undertaken in the median plane at different radii: $r_1 = 300$ mm and $r_2 = 330$ mm. No aberrations larger than three parts in 10^4 could be detected over the whole circle. The field distribution was measured by shifting the detector in the radial direction over well defined distances. The result showed that the first order coefficient was about 8% lower than the desired value $\alpha = -\frac{1}{2}$. According to formula (3) this deviation will seriously spoil the transmission because the two foci will diverge then over an angle of about 0.35 radians.

The first order field coefficient α is dependent on the ampere-turns ratio of the two coils λ. A different value for α, therefore, can be obtained by shunting one of the coils or by changing the number of windings of one of the coils. We used the first method to obtain the better value of λ. Fig. 18 shows that λ had to be changed from 4.5 to 5.0 in order to obtain the correct α. This rather large change in λ means that the shunt in parallel with the outer coil should take about 10% of the coil current; rather small fluctuations in the resistance of the coil and the shunt would therefore be able to spoil precision measurements. Indeed the outer coil should be kept constant in temperature within 0.03° C to maintain the desired precision of one part in 10^5. Therefore we decided to rewind the outer coil to obtain the correct ampere-turns ratio $\lambda = 5$.

The number of turns of the outer coil has been decreased by enlarging the distance between the windings from 1 mm to 2.7 mm. The data of the number of turns of both coils as given in table A refer to the rewound outer coil.

The measurement of the field distribution of the coils at $\lambda = 5$ yielded the value -0.500 ± 0.003 for the first order coefficient α, whereas the second order coefficient β was 0.43 ± 0.04.

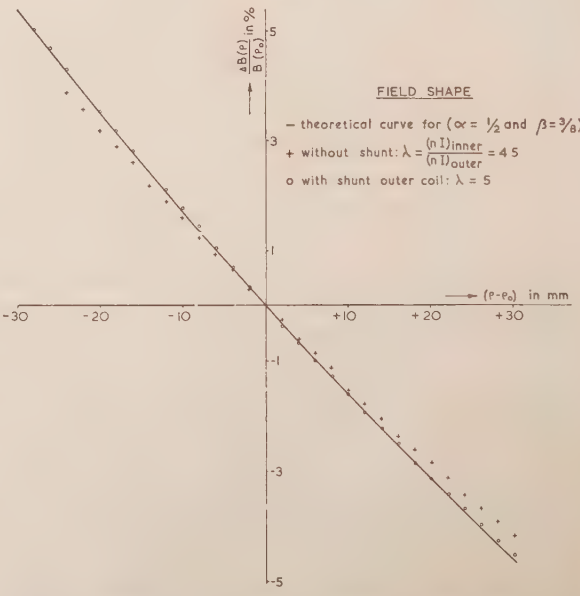

Fig. 18. Comparison between the theoretical field shape and the field shape as measured with a hall generator at two values of the ampere-turns ratio of inner and outer coil: $\lambda = 4.5$ and $\lambda = 5$.

In the next section these results will be compared with the results of the indirect test of the field coefficients by means of conversion lines.

6.2. FIELD COEFFICIENTS FROM CONVERSION LINE MEASUREMENTS

Maximum deviations of the coefficients α and β from the theoretical values $-\frac{1}{2}$ and $\frac{3}{8}$ respectively, can be found by comparing the experimentally obtained line width with that given by formula (9) which gives the base resolving power for a spectrometer with α exactly equal to $-\frac{1}{2}$ and an arbitrary value of β. For a field shape with $\alpha = -\frac{1}{2}(1+\varepsilon)$ the beam width δ_{ast} in the plane $\Psi = \pi\sqrt{2}$ will be, according to formula (3) and (5): $\delta_{ast} = \rho_0 \pi\sqrt{2}\,\gamma_\rho\,\varepsilon$.

Assuming that the base resolution R_0 is twice as large as the line width at half maximum R the following expression holds:

$$R = \frac{s+t}{8\rho_0} + \frac{|1-8\beta|}{12}\gamma_\rho^2 + \frac{|8\beta-3|}{12}\gamma_z^2 + \\ + \frac{\pi\sqrt{2}}{8}\varepsilon\gamma_\rho + \frac{|4\beta-3|}{96\rho_0^2}h^2 . \quad (10)$$

During measurements with conversion lines for calibration purposes the 222 keV L_1-line in ^{212}Bi (ThB I-line) has been measured under the following conditions:

Source width	$s = 0.07$ mm
Source height	$h = 10$ mm
Counter slit width	$t = 0.1$ mm
Radial opening angle	$\gamma_\rho = 0.013$ radians
Axial opening angle	$\gamma_z = 0.05$ radians
Resolution	$R = 0.018\%$.

The resolution R has to be corrected for contributions to the line width, which might be caused by:

a. inaccurate mutual aligning of the source and the counter slit;

b. inaccurate position of the counter slit with respect to the focusing angle $\Psi_\rho = \pi\sqrt{2}$;

c. source effects;

d. fluctuations on the magnetic field;

e. natural line width of the transition.

The method of aligning the source relative to the counter slit will be discussed elsewhere[16]). Here we will neglect a possible contribution from an inaccurate alignment of the source.

Fomula (2), which gives the relation between the radial focusing angle Ψ_ρ and the first order field coefficient α, shows that a positioning of the counter slit outside the theoretical focusing plane $\Psi = \pi\sqrt{2}$ introduces a contribution to the line width which must be either added or subtracted from the contribution due to a possible deviation in α. This fact may be even used to minimize the contribution to the line width arising when the experimental field shape deviates from that given by theory. In our case the accuracy in the geometrical setting of Ψ is about 0.003 radians. From formula (2) it follows that this possible error is equivalent with an error in α of about 0.1%. In connection with the result of the present investigation we will neglect a possible contribution to the line width due to an error in the exact position of the counter slit.

Source effects can seriously contribute to the line width. The source used for the present investigation, however, may be regarded as ideal and therefore we will not take into account a possible line broadening due to source effects.

Fluctuations on the magnetic field can be caused by (a) fluctuations on the magnet current (b) external field fluctuations and (c) temperature fluctuations of the coils which are limited to 0.2° C for this measurement. Once again for the present investigation of the maximum errors in the field coefficients we assume no line broadening due to this effect present.

The natural line width of the transition under consideration is about 10 eV. Using formula (6) we find that the momentum resolution due to the finite level width is 0.0025%. As will be justified in a forthcoming article[16]) this contribution may be added linearly to the theoretical line width as given by formula (9).

From the above considerations it follows that the corrected resolution will be 0.0145%. Inserting this value together with the above given numerical values of s, h and t into formula (10) yields:

$$\frac{|1-8\beta|}{12}\gamma_\rho^2 + \frac{|8\beta-3|}{12}\gamma_z^2 + \\ + \frac{\pi\sqrt{2}}{8}\varepsilon\gamma_\rho = 7\times 10^{-5} . \quad (11)$$

[16]) C. de Vries, Nucl. Phys. 18 (1960) 428.

First it will be assumed that β equals the theoretical value $\frac{3}{8}$ which eliminates the influence of the axial opening angle to the second order. Then we find for ε:

$$\varepsilon = \pm 0.0058$$

from which follows

$$\alpha = -0.500 \pm 0.003 .$$

If we assume on the other hand that α has exactly the value $-\frac{1}{2}$, then equation (11) yields

$$\beta = 0.375 \pm 0.025 .$$

These results agree with those of the direct measurements, as shown in table D.

TABLE D

	Field coefficients	
	α	β
Theoretical	$-\frac{1}{2}$	$\frac{3}{8}$
Hall generator measurements	-0.500 ± 0.003	0.43 ± 0.04
Conversion line measurements	-0.500 ± 0.003	0.375 ± 0.025
Combined results	-0.500 ± 0.002	0.39 ± 0.02

Averaging the results of this and the preceding section yields the result also indicated in table D.

It is to be noted that the method of testing the focusing properties of the magnetic field as carried out in this section delivers only a result for the field coefficients which is an average over an extended region of the field. For the L_1-transition used above the maximum deviation of the electron paths from the central orbit is:

$$\Delta\rho = 5.5 \text{ mm}$$
$$\Delta z = 21 \text{ mm} .$$

A more extended region ($\Delta\rho = 36$ mm and $\Delta z = 150$ mm) has been used during measurements of conversion line intensity ratios. A typical set of data for the K-line of the 412 keV transition in ^{198}Hg is:

$$s = 3 \text{ mm}$$
$$h = 20 \text{ mm}$$
$$t = 3.2 \text{ mm}$$
$$\gamma_\rho = 0.085 \text{ radians}$$
$$\gamma_z = 0.35 \text{ radians}$$
$$R = 0.38\% .$$

Still under the assumption that $R = \frac{1}{2} R_0$, the calculation using these conditions yields the result that the field shape follows exactly that predicted by theory.

Summarizing we may conclude that the field shape of the present instrument agrees very well with that required by theory for first order focusing in both directions and for second order axial focusing. In practice the opening angles γ_ρ and γ_z are adjusted in such a way that $\gamma_z/\gamma_\rho = 4$; for this ratio of the opening angles the contributions of γ_ρ and γ_z to the line width resulting from spherical aberration are about the same, if the second order field coefficient equals the value 0.39 (see formula (9)).

7. Final Remarks

With the instrument presented in the preceding sections several kinds of measurements have been carried out, which will be published elsewhere[16,17,18]). Typical data with regard to resolution and luminosity used during these measurements are summarized in table E. From this table it can be concluded that the

TABLE E

Source area (mm^2)	Transmission (%)	Line width (%)
0.7	0.013	0.013
6	0.11	0.057
60	1.0	0.35
140	1.0	0.50

[17]) C. de Vries and J. H. Dijkstra, Nucl. Phys. **18** (1960) 446.

[18]) C. de Vries, E. J. Bleeker and Mrs. N. Salomons-Grobben, Nucl. Phys. **18** (1960) 454.

spectrometer is suitable for precision measurements requiring high resolution as well as for investigations on source material with a low specific activity, where a large source area has to be used. Calibration measurements[16]) with the aid of conversion lines ranging in energy from 150 keV–2.5 MeV show the linearity of the instrument to be better than one part in 10^4.

The authors wish to thank Professor P. C. Gugelot for his interest in this work. It constitutes part of the research program of the Institute for Nuclear Research, made possible by financial support from the Foundation for Fundamental Research of Matter (F.O.M.) and the Netherlands' Organization for Pure Scientific Research (Z.W.O.).

NUCLEAR INSTRUMENTS AND METHODS 8 (1960) 146–150; NORTH-HOLLAND PUBLISHING CO.

IMPROVEMENTS IN THE FAST NEUTRON TIME OF FLIGHT TECHNIQUE USING PULSE SHAPE DISCRIMINATION IN AN ORGANIC PHOSPHOR

R. BATCHELOR, W. B. GILBOY, A. D. PURNELL and J. H. TOWLE

Atomic Weapons Research Establishment, Aldermaston, Berkshire, England

Received 8 May 1960

A very simple pulse shape discriminator based upon the method suggested by Owen[1]) has been developed for the scintillation detector of a neutron time of flight apparatus. Almost complete cancellation of γ-ray pulses is obtained with the circuit adjusted to pass neutrons of energies greater than 0.4 MeV. By discriminating against γ-rays with the detector placed inside a large water shield, the random background has been reduced by a large factor. The improvement obtained is illustrated with an inelastic neutron spectrum taken with iron at 4 MeV incident neutron energy. In this case the background reduction factor is between 5 and 10.

1. Introduction

One of the principal difficulties in fast neutron spectroscopy with the time of flight technique is to obtain a sufficiently high ratio of true events to background counts. This problem is particularly acute for systems which employ post acceleration pulsing of a Van de Graaff beam, as developed by Cranberg[2]). At high beam energies considerable background is generated by the unwanted beam being swept by the deflection system, either into the deflector plates or into metal parts further down the beam pipe assembly. For some applications, particularly inelastic neutron scattering experiments, this background can become prohibitively high.

One possible method of reducing the background is, of course, to use top terminal pulsing of the generator[3,4]). However, as far as is known, this technique has not yet been used for high energy inelastic scattering, although it is likely to be actively pursued in the future.

This paper describes a second and very simple method of reducing the background. The technique is based on the recent development by Brooks[5]) and Owen[1]) of discrimination between neutron and gamma ray pulses in certain organic scintillators by their difference in shape. In a time of flight spectrometer the background radiation incident on the well-shielded neutron detector consists of neutrons and γ-rays and cosmic rays, the latter being mainly lightly ionising μ-mesons. In the shield itself, which typically consists of a mixture of paraffin wax and lithium carbonate, or perhaps water alone, many of the background neutrons are likely to be converted into γ-rays by capture and inelastic scattering events. The radiation incident on the detector is therefore likely to be composed of a large proportion of γ-rays. Normally the detector is surrounded with an inch or two of lead to attenuate these γ-rays. By applying pulse shape discrimination to the detector, it is possible to reduce considerably the effect of the remaining γ-radiation without substantially reducing the neutron detection efficiency.

A method of reducing background, based on this technique, has previously been described by

[1]) R. B. Owen, A.E.R.E., Harwell, Report No. EL/R 2712 (1958) and I.R.E. Transactions on Nuclear Science, NS — 5 No. 3 (1958) 198.

[2]) L. Cranberg, Proceedings of the International Conference on the Peaceful Uses of Atomic Energy **4** (1955) paper 577.

[3]) V. E. Parker and R. F. King, Bull. Am. Phys. Soc. (1956) 70.

[4]) C. M. Turner and S. D. Bloom, Rev. Sci. Instr. **29** (1958) 480.

[5]) F. D. Brooks, Nuclear Instruments and Methods **4** (1959) 151.

Neilson *et al.*[6]). The method we describe was conceived independently and is believed to be rather more simple than that described previously. The performance is illustrated with an inelastic neutron spectrum taken for iron at 4.06 MeV incident neutron energy.

2. Description of Apparatus

The system to be described here has been incorporated into the time of flight spectrometer used on the Aldermaston 6 MV Van de Graaff generator. Details of the spectrometer have been described previously[7]). More recently the paraffin and lithium carbonate shield originally used has been replaced by a larger water shield. The detector, surrounded with 2″ of lead, sits in the centre of a cylindrical water tank, 4 ft in diameter and of height 4 ft. A suitable collimator, 2″ in diameter, is inset into the tank to provide an absorption-free path for the "true" neutrons incident on the detector. If further attenuation

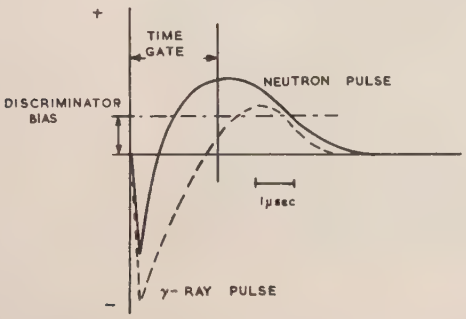

Fig. 1. Dynode pulses from the "Owen type" circuit for a 6 MeV neutron and a 2 MeV γ-ray. The positive swing of the γ-ray pulse, in this case, rises above the discriminator bias level but does not cross this level within the time gate.

of the neutrons emitted directly from the source (these of course should be eliminated in a scattering experiment) is desired, one or two smaller water shields in the form of truncated cones can be added. In order to take full advantage of the pulse shape discrimination technique, the detector used is an organic liquid scintillator type NE213†, contained in a glass cylinder 2″ diameter, 2½″ long, with flat ends. This scintillator is viewed by two photomultipliers, type RCA 6810A, connected in coincidence, and each biased well into noise. The neutron detection efficiency rises with increasing neutron energy to

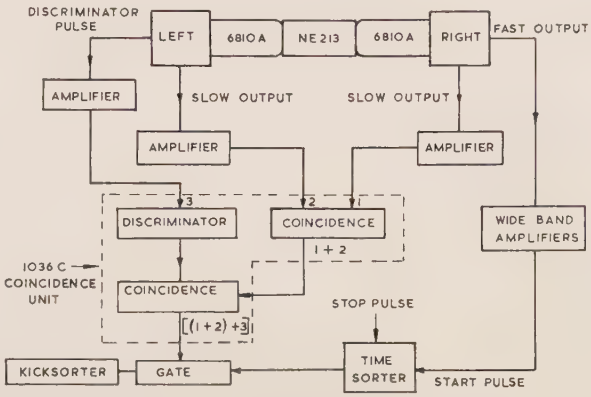

Fig. 2. Simplified block diagram of the time of flight electronic apparatus using pulse shape discrimination.

a value of about 30% at 0.8 MeV and then remains approximately constant. The value at 0.4 MeV is about 15%.

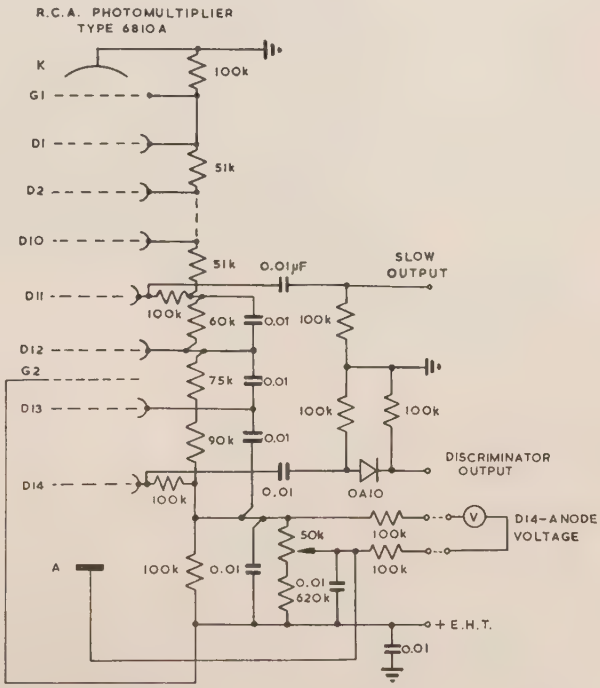

Fig. 3. Photomultiplier circuit for pulse shape discrimination.

† Supplied by Nuclear Enterprises, (G.B.) Ltd. Edinburgh.

[6]) G. C. Neilson, W. K. Dawson and F. A. Johnson, Rev. Sci. Instr. **30** (1959) 963.

[7]) R. Batchelor and J. H. Towle, A.W.R.E. (Aldermaston) Report No. NR/P-12/58 (1958); and Proc. Phys. Soc. **73** (1959) 193.

An important requirement of the n–γ discriminator is that it should not greatly impair the neutron detection efficiency over the entire energy range. At this Establishment, Souch and Redfearn[8]) have made a comparative study of the methods of pulse shape discrimination suggested by Brooks[5]) and Owen[1]) respectively. They have shown that, whereas the Brooks circuit does not permit the detection of neutrons of energies below 1 MeV, the Owen circuit can easily be set up to detect neutrons of considerably smaller energies, perhaps as low as 200 keV. against high energy γ-rays. Fig. 1 shows diagrammatically, pulses for a 6 MeV neutron and a 2 MeV γ-ray, these having approximately the same integral pulse height. As can be seen the γ-ray will, in this case be detected since the positive swing rises above the discriminator bias voltage. Note, however, that the dynode returns to positive voltage earlier in the case of the neutron pulse. The time difference is approximately 1 μsec (the value depends on the integrating time constant of the following amplifier which in this case was 0.2 μsec). Therefore, by accepting

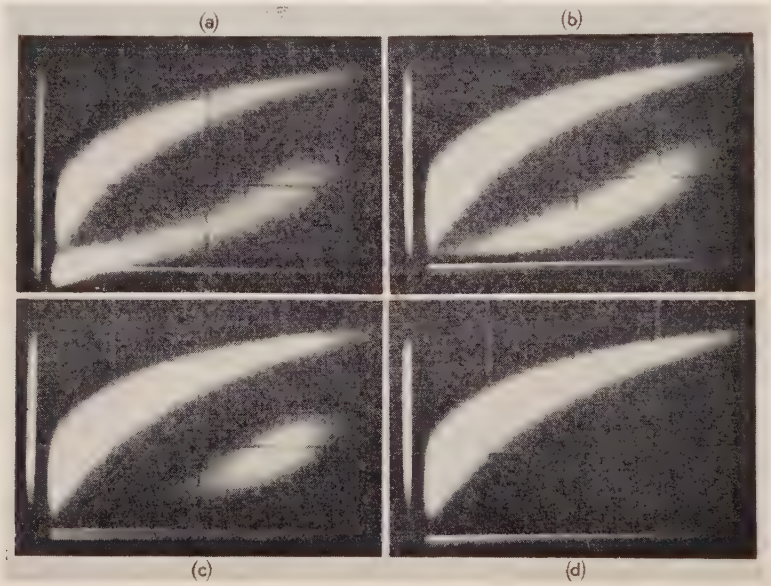

Fig 4. Oscilloscope photographs of neutron events (upper trace), and γ-ray events (lower trace), using a Po-Be source. (a) No pulse shape discrimination applied. (b) [1 + 2) + 3]. Coincidence resolving time 4 μsec, bias level adjusted to cut out low energy γ-rays and to pass 0.4 MeV neutrons. (c) [(1 + 2) + 3]. Resolving time = 2 μsec. (d) [(1 + 2) + 3]. Resolving time = 1 μsec.

Under these conditions, however, this circuit passes γ-rays of energies greater than 2 MeV although below this energy the discrimination is good. In this context it should be noted that the neutron and γ-ray energies quoted refer to the maximum recoil proton and electron energies of the respective pulse height distributions. This convention will be adopted throughout this paper.

An examination of the pulses obtained from the last dynode of a photomultiplier wired in the manner discussed by Owen[1]) suggested to us a simple method of improving the discrimination only those pulses which exceed the bias level within a time interval of one or two μsec after the start of the pulse, additional discrimination against high energy γ-rays can be obtained.

Fig. 2 shows how a scheme employing this idea is incorporated into the electronic arrangement used in the time of flight spectrometer. The left hand photomultiplier is wired, as shown in fig. 3, to give slow linear and "Owen" outputs. A crystal diode, type OA 10, is included to limit the negative swing of the last dynode pulse so that blocking effects in the following amplifier can be reduced. Otherwise the circuit

[8]) A. E. Souch and J. Redfearn, private communication.

is very similar to that originally proposed by Owen. The "Owen pulse" is amplified by a non-blocking amplifier and is then fed into the third channel of a triple coincidence unit Harwell type 1036C. Here amplitude discrimination first takes place and the resultant pulse, if any, is put into coincidence with the coincidence pulse from channels 1 and 2. Without pulse shape discrimination this (1 + 2) pulse is the one which gates the output of the time sorter through to the pulse height analyser. With pulse shape discrimination the final coincidence pulse [(1 + 2) + 3] fulfils this function, the time restriction, discussed in the previous paragraph, being obtained by reducing the resolving time of this circuit. In the 1036C unit this resolving time can be varied from 0.1 μsec to 4 μsec.

The oscilloscope photographs in fig. 4 illustrate the effect of varying this [(1 + 2) + 3] resolving time with pulses produced by a Po-Be source. The amplified "Owen pulses" and the amplified slow linear pulses were applied to the Y and X plates of the C.R.O. respectively. In fig. 4(a) the C.R.O. brightness control is switched by the coincidence (1 + 2) output to produce a spot at the extremity of the trace. The spots fall into two clear lines, the upper one representing neutrons and the lower one γ-rays. In 4(b), (c) and (d) the brightness control is switched by the [(1 + 2) + 3] coincidence output. The resolving time in (b) is 4 μsec, and the channel 3 discriminator is adjusted to cut out low energy γ-rays while still passing approximately 0.4 MeV neutrons. In (c) the resolving time is 2 μsec and in (d) 1 μsec, at which value no γ-ray events are seen.

3. Performance

Fig. 5 shows the improvement obtained with pulse shape discrimination for a typical inelastic neutron scattering experiment. Neutrons of energy 4.06 MeV, produced by bombarding a tritium gas cell with 4.95 MeV protons, are scattered by a 160 g iron sample in the form of a hollow cylinder. A long counter was used to monitor the neutron output and normalise the various runs shown in fig. 5. The lower solid

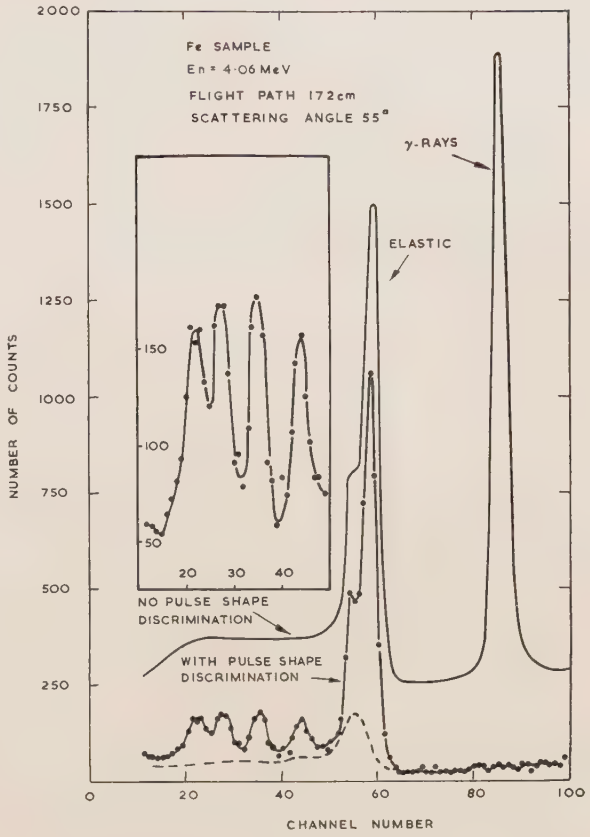

Fig. 5. Time spectra of neutrons, at 4.06 MeV incident neutron energy, scattered by iron illustrating the reduction in background obtained with pulse shape discrimination and with the scatterer removed.

curve was obtained with pulse shape discrimination applied. Each channel corresponds to 2.06 nanosec. Several inelastic peaks are observed and these are shown more clearly in the inset. These peaks are not seen in the upper curve of fig. 5 which was recorded without pulse shape discrimination, since the running time used was not sufficient to obtain the required statistical accuracy.

Another interesting feature of fig. 5 is the disappearance of the γ-ray peak in the lower curve. From the statistical accuracy of the points in this region we infer that the detection efficiency for the γ-rays observed in this experiment, which probably have a mean energy of about 1 MeV, has been reduced by a factor of at least 300. Very often the γ-ray peak is used as a calibration peak in a time of flight spectrum.

Although this is not present with the new technique it should be noted that a short run taken without pulse shape discrimination will quickly indicate its position.

The inelastic spectrum observed is very similar to that reported by Weddell *et al.*[9]), using the photographic plate technique. In fig. 5 the neutron group corresponding to scattering to the 845 keV level is seen as a bump on the side of the elastic peak. The energies of the groups shown in the inset correspond to levels in Fe^{56} at 2.16, 2.73, 3.03 and 3.18 MeV and the values agree reasonably well with the known level scheme[10]).

The system described has been tested under other conditions. In an inelastic scattering experiment with 7.5 MeV neutrons produced by the $D(d,n)He^3$ reaction, incident deuteron energy 4.3 MeV, the background was reduced by a factor 4. In the study of (He^3,n) reactions, which has formed a recent programme of work at this laboratory, reduction factors of up to 20 are observed. Using a source of $^7Li(p,n)^7Be$ neutrons, the neutron detection efficiency at 500 keV neutron energy is found to be about 90% of its former value. Above 1 MeV there is no significant decrease in the efficiency.

The application of pulse shape discrimination reduces the natural background rate from the shielded detector, (no external sources present and no accelerated beam) from 120/min to 6/min. The latter is well below that expected from cosmic rays, which would be about 20/min for this detector. The discriminator must therefore reject a large fraction of the cosmic ray pulses. This effect may be of more general interest in low level counting rate experiments.

In conclusion, this work shows that a very significant improvement in the neutron time of flight technique can be obtained by the application of pulse shape discrimination. A further improvement can be made with top terminal pulsing. This should be particularly significant for proton beams in excess of 5 MeV and deuteron beams, since in the present arrangement these beams produce very intense neutron backgrounds in the region of the deflector plates.

[9]) J. B. Weddell, B. Jennings, I. Alexoff and R. L. Mellens, Phys. Rev. **98** (1955) 582.

[10]) K. Way, R. W. King, C. L. McGinnis and R. van Lieshout, U.S.A.E.C. Report TID-5300 (1955).

NUCLEAR INSTRUMENTS AND METHODS 8 (1960) 151–172; NORTH-HOLLAND PUBLISHING CO.

THE OSCILLOSCOPE METHOD OF MEASURING NUCLEAR HALF-LIVES

I. BERGSTRÖM[a,b,c,d], E. C. O. BONACALZA[a], A. JECH[b], M. PEREZ[b] and P. THIEBERGER[a,b,c,e]

[a]*Instituto de Física, Facultad de Ciencias, Universidad de Cuyo, San Carlos de Bariloche, Argentine*

[b]*Departamento de Física, Facultad de Ciencias Exactas y Naturales, Universidad de Buenos Aires, Buenos Aires, Argentine*

[c]*Nobel Institute of Physics, Stockholm 50, Sweden*

Received 14 April 1960

It is shown that the modern fast oscilloscopes now available commercially, are very simple and powerful tools for measuring nuclear half-lives. The advantages and the limitations of the method are discussed. In order to illustrate the problems which are associated with measurements in different half-life regions, seven half-lives associated with metastable states in the following nuclei were measured: Pb^{205} (4.1ms), Pb^{206} (125 μs), Ta^{181} (17.5 μs), Rb^{85} (1.0 μs), Pb^{204} (302 mμs), Pb^{203} (55 mμs) and Ta^{181} (11.0 mμs). The half-lives measured thus cover a half-life ratio of almost 10^6:1, but it is shown that in favourable cases this ratio might be as large as 10^8:1. Thus the oscilloscope method can be used in the whole region where conventional delayed coincidence technique is applicable. It is significant for the usefulness of the method that when studying half-lives which were reasonably well known and only chosen for the purpose of investigating the oscilloscope method itself, a new half-life was discovered in one of the samples used (Pb^{203} (55 mμs)). A very great advantage of the oscilloscope is the fact that it can be very easily used as a multichannel time analyzer, by continuously photographing the events on the oscilloscope screen.

1. Introduction

The measurements of nuclear half-lives contribute in an important way to our systematic knowledge of nuclei, because in many cases they give information about the matrix elements of electromagnetic and other modes of transitions between nuclear states. In addition, the presence of delayed gamma transitions may often simplify the establishment of complicated level-schemes.

During the past ten years a considerable amount of information has been obtained about electromagnetic transitions of nuclear metastable states[1,2]). Transitions having half-lives larger than about 1 s are thus relatively well known by now. Therefore it is to be expected that many of the most interesting cases of nuclear isomerism, which will be discovered in the future will have half-lives considerably shorter than 1 s. Also in the field of alpha-spectroscopy[3]) and for the search of new elements the techniques of measuring short half-lives have become very essential. In this region delayed coincidence technique may be used and recently a considerable amount of work has been performed in order to extend the lower limit of this method. A somewhat different type of experiments used in connection with accelerators are the ones performed with pulsed beams[4]). A lot of interest has also recently been focussed onto the possibilities of developing new methods for half-lives shorter than 10^{-11} s[5,6,7]). Restricting ourselves to the region where half-lives can be relatively easily measured by delayed coincidence technique (10^{-9}–10^{-1} s),

[d] On leave of absence on a UNESCO-contract from the Royal Institute of Technology and the Nobel Institute of Physics, Stockholm, Sweden.

[e] During the later phase of this investigation working at the Nobel Institute of Physics on a scholarship from the Consejo Nacional de Investigaciones Científicas y Técnicas (Argentine).

[1]) M. Goldhaber and A. W. Sunyar, Beta and Gamma-ray Spectroscopy (North-Holland Publishing Company, 1955).

[2]) I. Bergström and G. Andersson, Arkiv för Fysik **12** (1957) 415.

[3]) P. A. Tove, Arkiv för Fysik **13** (1958) 579.

[4]) R. B. Duffield and S. H. Vegors, Phys. Rev. **112** (1958) 1958.

[5]) T. R. Gerholm, Arkiv för Fysik **11** (1956) 75.

[6]) B. Johansson and T. Alväger, Nucl. Instr. **3** (1958) 49.

[7]) A. E. Blaugrund, Phys. Rev. Letters (Sept. 1, 1959).

there are surprisingly few systematic investigations reported. Very probably one of the reasons for this is that the equipment used was often limited only to a small part of this half-life region. Obviously an instrument which covers the whole time region mentioned above would be very useful. The accuracy and flexibility of fast modern oscilloscopes, are so outstanding that we considered it worthwhile to investigate systematically, whether the oscilloscope would be such a universal instrument. The use of a cathode ray tube oscilloscope for measuring half-lives was reported for the first time already in 1947[8]) (see below), and is thus not a new method. Since then it has not been used very frequently, and as far as we know there are no systematic investigations published about the applicability and the limitations of the method.

Fast oscilloscopes and pulse height analyzers are now standard tools in most nuclear laboratories, even the smaller ones, which is usually not the case with equipment for measuring nuclear half-lives in a wide time region. One of the main advantages with this combination of equipment, is of course, that it can be rapidly put together for measuring a half-life and that the same components are immediately available for other purposes when the measurements have been finished.

2. Previous Work and the Origin of this Work

It is interesting to note that the very first delayed coincidence measurement reported already in 1934 by J. C. Jacobsen[9]) was performed in a way rather similar to the oscilloscope method. A light beam was deflected by two crossed "moving iron oscillographs" to which the pulses from two G.M. counters were fed. The deflected beam was focussed onto a moving photographic film and the delayed events could be distinguished from the prompt ones by the special shape of the picture on the film. The first successful measurement (1947) of a nuclear half-life with a cathode ray oscilloscope is due to S. Rowlands[8]). He measured the 140 μs state of RaC', which is fed by β-particles and decays by α-particle emission. A schematic drawing (fig. 1) indicates the experiment by Rowlands. Pulses originating from the detection of the β-particles released the sweep and the delayed pulses from the alpha decay were fed to the y-plates of an Ultrascope Mark 6. The delayed pulses appearing on the screen were counted visually and though the half-life obtained was considerably longer than previously reported values, Rowlands clearly showed that the method worked.

In his thesis[10]), P. Axel discusses a measurement of a half-life in Cd obtained by using the oscilloscope method. In 1948 a group at the University of Illinois tried to measure the half-life of a 70 keV state in Gd, reached in a slow neutron capture reaction[11]). In order to check the possibility of using the oscilloscope method in a case like this one, they first successfully remeasured the 0.5 μs half-life in Ge^{72}. No half-life was, however, observed in Gd. In these experiments the sweep was triggered by the capture gamma-rays and pulses due to conversion electrons of the 70 keV gamma ray were used for intensity modulation of the electron beam and also after a certain constant delay fed to the y-plates. In this way the delayed

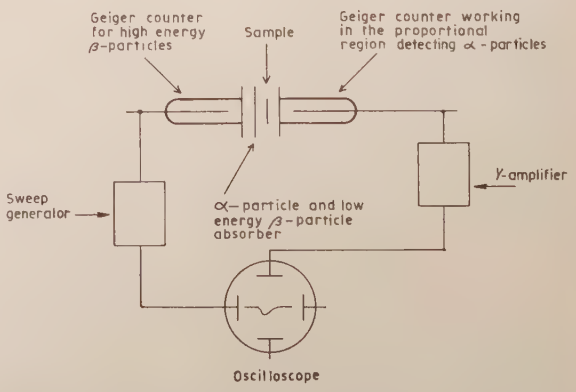

Fig. 1. Schematic drawing of the set-up used in the first measurement of a nuclear half-life (the 140 μs state of RaC') with the oscilloscope method by S. Rowlands[8]).

[8]) S. Rowlands, Nature **160** (1947) 191; Journal of Scient. Instr. **25** (1948) 218.

[9]) J. C. Jacobsen, Nature **133** (1934) 565.

[10]) P. Axel, Physics Department, University of Illinois, Thesis (1948) (unpublished).

[11]) O. Sala, P. Axel and M. Goldhaber, Phys. Rev. **74** (1948) 1249.

events appeared as "sharp knees" on the screen, which was continuously photographed. This group was thus evidently the first one which used the oscilloscope as a multichannel time analyzer.

Not until 1953 were the next measurements with this method reported. D. Alburger[12]) discovered the metastable state in Pb^{206} by letting X-rays, detected by a NaI crystal, trigger a Tektronix 511 AD and observing the delayed γ-pulses fed to the γ-plates, through a movable 1.5 cm slit in front of the screen. The light from the delayed events seen through this slit was optically focussed onto a photomultiplier and by changing the slit position and counting the light pulses a half-life of 145 ± 15 μs was obtained. This half-life was remeasured by B. Åström[13]) in 1957 with a rather different method. The cathode ray tube of a Tektronix 535 was used only for inspection purposes and the oscilloscope worked essentially as a delayed-pulse generator. Åström obtained a value of 128 ± 5 μs.

For the sake of completeness it should also be mentioned that R. Ballini[14]) in 1953 suggested a method in which not a commercial oscilloscope but rather a cathode ray tube and especially designed electronics were used. With this equipment Ballini searched for half-lives in the region 1 ms – 1 μs, but only the case of Ta^{181} ($T_{\frac{1}{2}} = 17.2$ μs) was measurable.

The oscilloscope is nowadays also frequently used in high energy physics for the determination of small time differences. An example of a life-time determination of the π^- meson is presented in a recent paper by J. Ashkin *et al.*[15]). The application of the oscilloscope in this kind of measurements is, however, somewhat different from that one used for the determination of nuclear half-lives.

[12]) D. Alburger and M. H. L. Pryce, Phys. Rev. **92** (1953) 514.

[13]) B. Åström, Arkiv för Fysik **12** (1957) 237.

[14]) R. Ballini, Annales de Physique **8** (1953) 441.

[15]) J. Ashkin, T. Fazzini, G. Fidecaro, Y. Goldschmidt-Clermont, N. H. Lipman, A. W. Merrison and H. Paul, CERN, Geneva, circulated preprint.

[16]) S. H. Vegors and R. L. Heath, Phys. Rev. (to be published) (see also Phys. Rev. Letters (Dec. 15, 1959) p. 590).

It is clear from the above that the work performed so far with the oscilloscope method concerns only a few measurements of nuclear half-lives in the region 0.5–140 μs. During a summer course in nuclear physics at the Instituto de Fisica in Bariloche, Argentine (Jan. 7–March 7, 1959), in which the authors took part, some preliminary measurements with this method were made. The outcome of this experiments was so unexpectedly successful that we felt that this method very probably was useful in a much wider half-life region than had been believed until then. Already during the summer-school in Bariloche, we confirmed the extraordinarily interesting suggestion by Vegors and Heath[16]) of a 4 ms isomeric state in Pb^{205}. This case gave us experience regarding the possible upper limit of the method. After the end of the summer-school the measurements were continued at the Physics Department of the Buenos Aires University and three half-lives of 125, 17.5 and 1.0 μs in the decay of Pb^{206}, Ta^{181} and Rb^{85}, respectively, were studied. Finally two of us (I.B. and P. T.), after coming to Sweden, continued studying the lower limit of the oscilloscope method essentially by measuring the half-lives of the first 4^+ state in Pb^{204} (302 mμs), a 55 mμs-state in Pb^{203} (discovered when measuring the half-life of Pb^{204}) and the 11.0 mμs state in Ta^{181}. The ratio between the longest and shortest half-life studied in this work is thus almost 10^6:1 but we believe that the method with favourable cases should be able to cover a ratio of about 10^8:1, which certainly is a considerable half-life region for a single instrument, the parts of which are available in most nuclear laboratories.

3. Different Ways of Applying the Oscilloscope Method

In fig. 2 an extremely simple case of nuclear isomerism is indicated. Let us assume that the half-life $T_{\frac{1}{2}}$ to be measured is due to a state B. "a" symbolizes signals telling us that nuclei in the state B have been created, and "b" are signals giving information that the same state has decayed. "a" may not only be due to

pulses from the detection of alpha- and beta-particles, conversion electrons, gamma-rays or X-rays, but in a nuclear reaction these signals may also be due to inelastically scattered

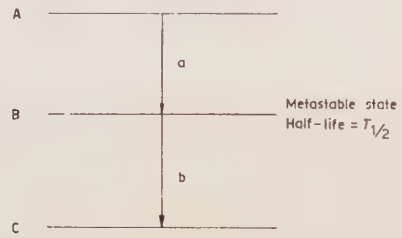

Fig. 2. Simplified schematic drawing of the level scheme corresponding to the feeding and decay of the metastable states studied. In the following the detectors accepting the photons or particles corresponding to transitions a and b and the pulses produced in them will be denoted by the same letters.

particles or pulses associated with the beam of a pulsed accelerator. However, we are not going to include these last two cases in the following discussion. "b" usually originates from pulses due to detected beta-, gamma- and X-rays and conversion electrons.

The detectors used in the experiments, when adjusted to accept the a- and b-pulses, will also detect "unwanted" pulses. The pulses may be due to cosmic ray background or to the fact that the decay scheme is much more complicated than indicated in fig. 2. The samples may also contain "impurities" of unwanted radioactive nuclei. All the pulses detected when the detectors are set to accept the a- and b-pulses will be denoted a′ and b′, respectively, in the following.

It is obvious that in cases where the half-lives studied are long compared to the time fluctuations in the detecting devices and in the oscilloscope itself, the distribution of events (corrected for random events) along the sweep direction, gives directly the decay of the metastable state studied and that thus the logarithm of the number of true, delayed events plotted as a function of the sweep time should give a straight line.

Figs. 3, 4 and 5 show some of the possibible ways of using an oscilloscope for half-life measurements. For detailed explanations the reader is referred to the figures and the figure texts. We shall return to these figures when discussing special features of the oscilloscope method. In

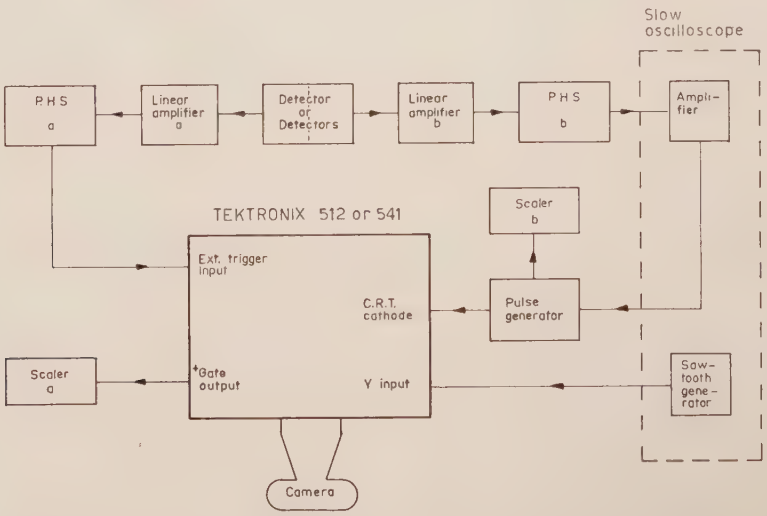

Fig. 3. Block diagram of one of the instrument combinations used for photographic recording of delayed events corresponding to half-lives between 10 μs and 5 ms. In these experiments the b′-pulses triggered a pulse generator, the output pulses of which intensity modulated the electron beam and were also counted by the scaler b. The light spots on the oscilloscope screen corresponding to the delayed events were uniformly distributed in the vertical direction of the screen by feeding the pulses from a saw-tooth generator to the y-plates of the oscilloscope and were recorded by having the camera shutter open and the film being stationary. Because of the sweep dead-time, it is advisable to count the number of released sweeps rather than the number of triggering signals from the pulse height selector. This is achieved by connecting the scaler a to the gate output of the oscilloscope.

For the measurements on Pb^{206} and Pb^{205} a single well crystal detector was used. For half-lives shorter than about 10 μs two detectors should always be used in order to avoid pile-up problems in the linear amplifiers.

most cases the a′-signals were used to trigger the oscilloscope. (There may of course exist cases where it is more favourable to trigger the oscilloscope with the b′-signal and delay the arrival of the a′-signal.) There are essentially two ways of using the b′-signals:

A. The signals may be fed to the y-plates of the oscilloscope, which, for example, was the case for the three last measurements listed in table 1.

B. In other cases the b′-signals may modulate the electron beam intensity in such a way that the delayed events may appear as a point on the oscilloscope screen (cf. figs. 6 and 9). The four longest half-lives measured in this work were obtained by using this method.

The b′-events appearing on the oscilloscope screen may be detected in the following ways:

a. Visual detection. This method is associated with the same difficulties as the first scintillation measurements of the Rutherford school. The measurements are slow and are associated with personal systematic errors of the observer, and should only be used in exceptional cases. Nevertheless if the equipment needed for the methods 3.b and 3.c discussed below is not available, it is certainly also possible to measure the half-life in this way, as fig. 15 shows, even if the measurements are very time-consuming because of the slowness of the human response.

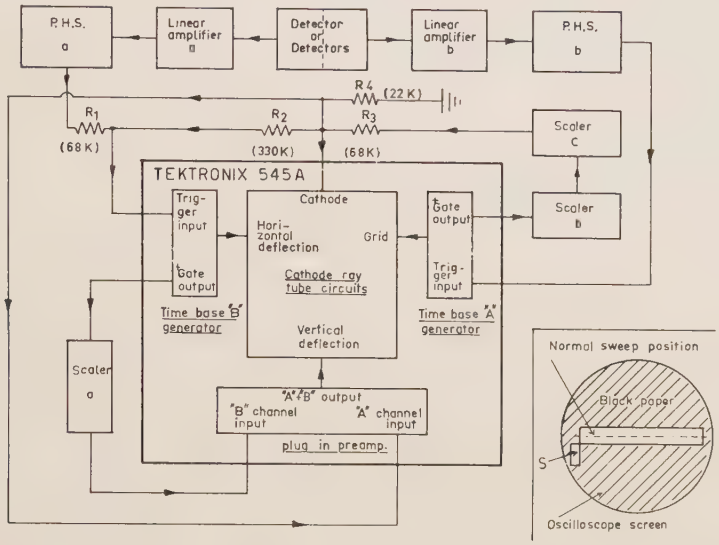

Fig. 4. Simplified block diagram showing the way in which a Tektronix 545 A was used for determining half-lives larger than about 1 μs.

Here the light spots corresponding to delayed events are produced by means of the time base "A" generator, while the time base "B" generator produces the sweeps (horizontal display switch in position "B" intensified by "A") It was found convenient to disable one of the sections of the lockout multivibrator in the time base "A" generator in order to make allowance for the possibility of more than one sweep "A" to occur for each sweep "B". In cases where the number of random events is small, the probability of having more than one b′-event per sweep is negligible and thus this precaution is not necessary.

The measurements were completely automatized by using a camera with a motor driven film. Thus, the normal sweep position was stationary and vertical deflections produced from the scalers a and c could be used in order to produce information about the counting rates in both the channels, which is needed in order to calculate the number of random events. For the a-pulse this is simply done by shifting the sweep from its normal position upwards in such a way that the light spots are hidden for a certain number of counts as explained in the text. The counting rate corresponding to the b-signals was controlled by recording light spots appearing in the slit S each 6400 b-events. In order to achieve this the number of b-events was scaled down by a suitable factor by means of scalers b and c. In order to obtain the wanted light spot in S, pulses from the scaler c have to be fed simultaneously to the cathode for intensity modulation of the electron beam, to the sweep B trigger input in order to release sweep b and thus unblank the beam and finally to the y-plates in order to deflect the sweep position downwards. This was done by means of R_1, R_2, R_3, R_4 which were chosen so as to give the right pulse heights and to decouple to a certain extent the output of the pulse height selector a from the cathode.

b. Photographic recording. For half-lives longer than about 1 μs the sensitivity of the fastest commercial films now available allowed photographic recording of the delayed events on the screen with the equipment used in this work. The great advantage of this method is, of course, that the oscilloscope can be used as a multichannel time analyzer. The films used in this work were 25 DIN Kodak 3 X and 29 DIN AGFA Isopan Record. The points on the film obtained by letting the b'-pulses intensity modulate the electron beam were counted by projecting the film on a piece of white paper with a magnification of about 30 (see fig. 6). A centimeter scale of the oscilloscope was also photographed and projected onto the same paper, thus providing a suitable time scale. Since the points representing the delayed events on the screen had a diameter of about 0.5 mm, it was not considered worth-while to divide the sweep interval into more than 10 "channels". The photographic method is especially useful in the ms-region, where the long measuring-times involved in the use of one-channel methods make the measurements almost impossible. There are simple ways of continuously obtaining the information necessary for the calculation of the random events on the same film used for the delayed events and this will be discussed further in 4.1. Figs. 12, 13 and 14 show the half-lives of metastable states in Pb^{205}, Pb^{206} and Ta^{181} obtained by using photographic recording.

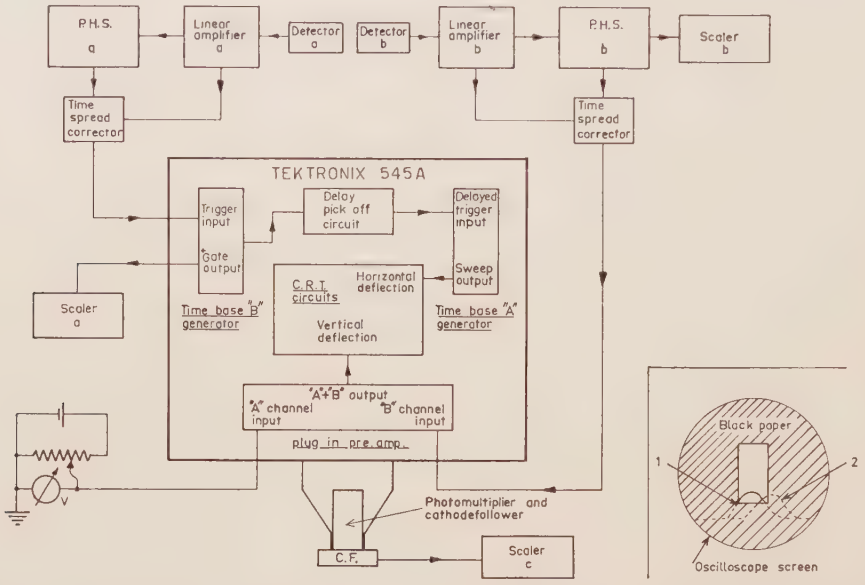

Fig. 5. Simplified block diagram of the set-up used for measuring half-lives from 10 mμs to about 1 μs and also for obtaining the resolution curves of fig. 10.

The horizontal display switch was in this case set at the position "A" delayed by "B". In this way the release of sweep "A" can be delayed by a well known, and continuously variable amount and the various points of the coincidence curve obtained without changing the position of the slit in front of the oscilloscope screen. However, for the shortest half-life (10 mμs), the steps between successive delay values needed were so small that it was necessary to set the delay control to a constant position and to change instead the horizontal position of the sweep, the corresponding potentiometer having been calibrated accurately in centimeters beforehand. To obtain the electronic resolution curve" of fig. 10 I, a third method had to be used because of the much smaller delay changes needed. The potentiometer and the voltmeter shown in this figure were used for this purpose. The reader is referred to fig. 10 I and to the text for the description of this way of operation.

The short pulses from the time-spread corrector of channel b were fed to the vertical deflection system of the oscilloscope and viewed through a slit (see inset) by a photomultiplier connected to a scaler. It is quite evident that the effective time channel width depends not only on the slit width but also on the discrimination level of the scaler C, on the intensity control setting of the oscilloscope and on the amplification in the photomultiplier. Thus, on event, giving a pulse like "I" would be counted while one producing a pulse like "2" might be rejected because the amount of light reaching the photomultiplier is smaller.

c. Photomultiplier detection. There are many ways of using a photomultiplier for the detection of the b′-events, where the visual detection and photographic recording is less convenient and

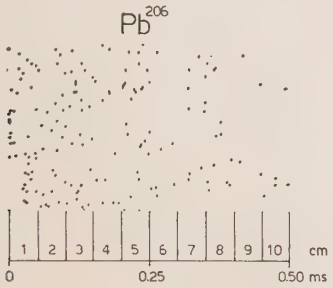

Fig. 6. The delayed events from the decay of the 7⁻ state in Pb^{206} on the oscilloscope screen photographed by a camera having the film continuously moving in the vertical direction.

below we are going to discuss only some of the most obvious ones. The screen may be uncovered or partly covered by a mask in such a way that the photomultiplier detects only those pulses which are visible through a slit in this mask.

3.1. UNCOVERED SCREEN AND VARIATION OF THE SWEEP VELOCITY

In this case the number ΔN of true delayed events on the screen detected by the photomultiplier is

$$\Delta N = \int_0^{t=\mu x} \lambda N_0 \, e^{-\lambda t} \, dt = N_0(1 - e^{-\lambda \mu x}) \qquad (1)$$

x = sweep interval
t = sweep time
μ = sweep velocity.

Thus, a straight line is obtained if the logarithm of $(N_0 - \Delta N)$ is plotted as a function of the total sweep time t. N_0 may be obtained by using extraordinarily long sweep times if this is allowed by the number of random events. In a measurement of the half-life of the 7⁻ state in Pb^{206}, the ratio between true and random coincidences was about 1.5, even at time $t = 12$ half-lives. ΔN is at this time to a very good approximation equal to N_0. Since this method thus very conveniently gives the number N_0, there are no reasons to make half-life plots in the conventional way, because for each point measured the half-life can be calculated according to (1). Fig. 7 shows as an illustration the preliminary result of a determination of the half-life of the 7⁻ state in Pb^{206} made in this way.

3.2. CONSTANT SWEEP VELOCITY AND VARIATION OF SLIT POSITION RELATIVE TO THE SWEEP ORIGIN

The slit position can obviously be changed in two different ways one of which was used by D. Alburger when he discovered the half-life of the 7⁻ state in Pb^{206} [12]). The light pulses corresponding to the delayed events were made visible through a slit in a piece of paper covering the screen and the position of this slit was mechanically changed for each "point" to be measured on the decay curve. An equivalent but simpler way is to keep the position of the slit constant on the screen and instead change the sweep origin, which in some oscilloscopes can be done with great accuracy.

3.3. CONSTANT SLIT POSITION AND VARIATION OF THE SWEEP VELOCITY

This method was used by one of us several years ago[17]) but was not considered to be reliable, because the observed and calculated numbers of random events did not agree. We now know that this must have been due to the presence of the 4 ms half-life in Pb^{205}, which at

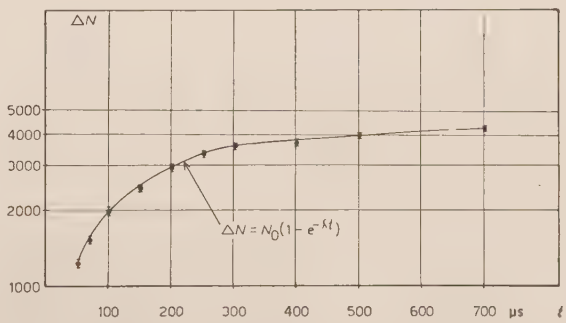

Fig. 7. The number of delayed coincidences as a function of the timegate width (from time zero to time $t = x\mu$, where x is the visible part of the sweep beginning at its origin and μ the sweep velocity) using Bi^{206}-sample and the arrangement of fig. 4, but with a photomultiplier instead of a camera. For large values of t, N approaches N_0, which makes it possible to calculate the half-life for each measured point.

[17]) I. Bergström, Nobel Institute of Physics, Stockholm (unpublished measurements).

that time was not known. In this case the number ΔN of delayed events appearing in the slit and counted by the photomultiplier is

$$\Delta N = \int_{t_1}^{t_2} \lambda N_0 \, e^{-\lambda t} \, dt = N_0 \, e^{-\lambda t_1} \quad (1 - e^{-\lambda (t_2 - t_1)})$$

where

$$t_2 - t_1 = \mu (x_2 - x_1) = \mu \Delta x \quad (\Delta x = \text{slit width}) .$$

In this case $\log N/(1 - e^{-\lambda \mu \Delta x})$ plotted as a function of t_1, should give a straight line from which the half-life can be obtained. This has to be done by a procedure of successive approximations, since the ordinate in such a plot contains the unknown decay constant. The influence of this becomes less and less important for lower sweep velocities. Fig. 8 shows a measurement of the half-life of the metastable state in Pb^{206} obtained in this way. The last part of the curve ΔN plotted as a function of t_1 gives the half-life in what we may call the zero order approximation. This half-life is 189 μs and thus too large (cf. table 1). If the value of the corresponding decay constant is used in the expression above we obviously overcorrect the number of delayed events and the half-life 117 μs is obtained. This procedure was repeated and the following approximations gave the half-lives 137, 127 and 129 μs respectively. We thus see that the half-lives obtained in this way rapidly converge towards values where the deviations are small compared to the statistical errors. The final value of 128 μs is somewhat higher than the values (cf. fig. 13) we obtained by the photographic method but, because of the poorer statistics, (one channel method), the deviation is not at all significant.

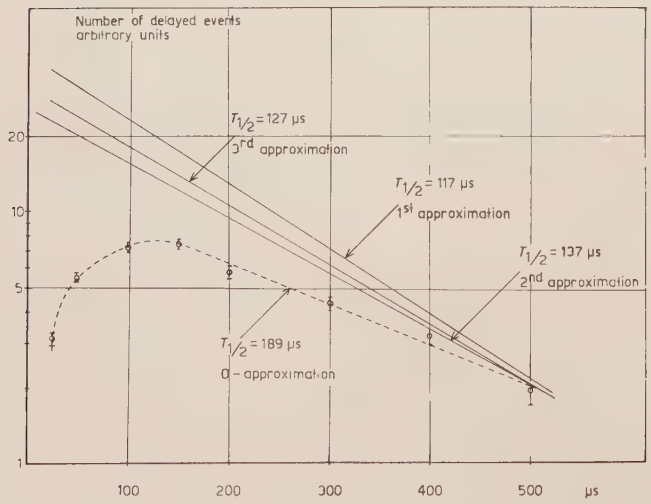

Fig. 8. The number of delayed coincidences (obtained with a constant slit width and a variable sweep velocity) as a function of the delay time which in this case was equal to the gate time. The lower curve shows the experimentally obtained result (Pb^{206}). For large values of the delay time, the slope of this curve should give a rough value of the half-life (see the text). Using a procedure of successive approximations described in the text, the upper curves are obtained and, as can be seen, the half-lives so obtained converge rather quickly towards the final value of 128 μs.

3.4. CONSTANT SLIT WIDTH AND DELAY OF THE RELEASE OF THE MAIN SWEEP

Some of the fast modern oscilloscopes, for example the Tektronix 545, are equipped in such a way that it is possible to delay the release of the main sweep by a certain time which is variable and which is well known. Letting the photomultiplier view a part of screen and varying the delay of the main sweep is a method reminding of the conventional way of measuring a half-life with a stop watch and counting during constant time intervals. This method is one of the most attractive ones. The absolute value of the slit width and the position of the sweep origin is not relevant, which indeed is important because in certain time regions the pulse width is comparable to the slit width and the effective value of the slit is dependent on the discriminator level of the scaler used to count the b′ events (cf. fig. 5). Note, for example, that in both methods described in 3.1 and 3.2 the uncertainty in the knowledge of the origin of the sweep as well as of the absolute value of the slit width contribute considerably to the final errors of the result obtained. The half-lives of the metastable states of Pb^{204}, Pb^{203} and Ta^{181} (11 mμs) were measured in this way. From the statistical point of view it is also important to use as wide time channels as possible. In the case of Pb^{204}, an 8 cm channel corresponding to approximately 160 mμs was used. When the half-life becomes comparable to the coincidence resolution curve, the slit width must, of course,

be decreased and, in the case of the measurement of Pb^{203}, it was about 40 mμs. The problems which arise when still shorter time differences are measured are discussed in 4.2.2. where we describe the special arrangement used in order to measure time differences which are only a fraction of a mμs.

4. Sources of Errors and Limitations of the Method

The measurement of a nuclear half-life with an oscilloscope is thus essentially a question of determining the number of true, delayed events as a function of the time interval corresponding to a certain part of the sweep on the oscilloscope screen. We may therefore expect that some of the limitations of the method are to be found in the oscilloscope itself and that other limitations are the same as are involved in any delayed coincidence method. Some of the most apparent quantities relevant for the discussion of errors and limitations of the oscilloscope method are thus:

1. *The number of random events.* The knowledge of the number of true, delayed events is not only limited by statistics, but also by the imperfect knowledge of the time channel Δt used. In both these respects the random events play an important role. Below we shall discuss a way of continuously controlling the number of random events which is useful for the oscilloscope method and which is especially suitable for determinations of long half-lives.

2. *Sweep properties* like the accuracy of the sweep time, the sweep linearity and the sweep stability.

3. *The background* from cosmic rays and unwanted radiation from the nuclide studied or from other nuclides present in the sample used. These problems, which are especially important in measurements of long half-lives, will be discussed in detail below in section 4.4.

4.1. DETERMINATION OF THE NUMBER OF RANDOM EVENTS

The number of true, delayed events are, of course, obtained by subtracting the random events from the total number of detected events. The number of random events N_r is

$$N_r = \frac{N_{a'} N_{b'} \Delta t}{T} \quad \text{where} \quad t = \Delta x \mu$$

T = total measuring time.
$N_{a'}$ = the total number of sweeps counted by a separate scaler (see figs. 3, 4 and 5).
$N_{b'}$ = the total number of b′-signals.
μ = sweep velocity
Δx = efficient sweep interval used, in some cases depending on the discrimination level of the scaler registering the photomultiplier pulses (cf. section 3.4).

In all half-life regions in which we have worked, there was a very satisfactory agreement between the number of measured and calculated random events. It is, of course, very important that the measured random events in the case of a constant time channel be independent of the delay time, otherwise unknown systematic errors might give rise to a distribution of events which could be incorrectly interpreted as a half-life. Especially in the ms-region, where the number of true events may be considerably smaller than the number of random events, it is advisable to check that a "horizontal line" is obtained if the a′- and b′-signals are coming from independent sources (cf. fig. 11).

As has already been pointed out, in the ms-region we photographically recorded the delayed events on the oscilloscope screen. Since many exposures lasted 18 hours continuously, it was not considered to be satisfactory to calculate the random events from the integrated number of events $N_{a'}$ and $N_{b'}$ measured during this long time-interval, because of possible drift in the electronical equipment. For this reason special signals were fed to the y-plates of the oscilloscope from the scalers counting the number $N_{a'}$ and $N_{b'}$ of the a′- and b′-signals, respectively. These signals were regularly registered by the photographic film in the following way. For each 9000^{th} a′ event a signal was fed from the fourth Decatron tube of the scaler used, to the y-plates and the sweep postion was hereby changed in such a way that the points on the

oscilloscope screen representing the delayed events were hidden behind a strip of black paper (cf. fig. 4). The sweep returned to its normal position when the Decatron reached

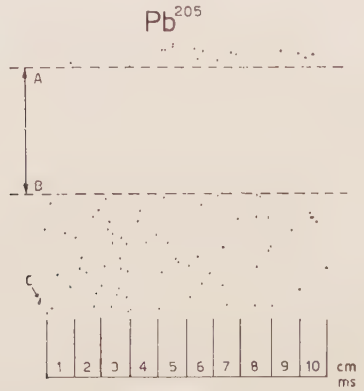

Fig. 9. The delayed events from a Bi^{205}-sample obtained in the same way as was the case for the Bi^{206}-sample (cf. fig. 6). The region A–B and the point C are related to the number of sweeps and events detected by counter b in a way discussed in 4.1, thus providing the necessary information for calculating the number of random events.

$N_{a'} = 10\,000$ and had this position for the next 9000 $N_{a'}$-events. The distance A–B on fig. 9 corresponds to the time interval in which no delayed events were seen by the film. Thus, the events on the film will be distributed into groups, each group corresponding to $N_{a'} = 9000$. In a similar way, a pulse is fed from another scaler to the y-plates each time $N_{b'} = 6400$. The sweep origin was in this case shifted about 1 cm and was made visible for the film through a narrow vertical slit in the black paper in front of the screen. Such a pulse registered by the film is seen at C in fig. 9. The distance between two such points in the film thus corresponds to $N_{b'} = 6400$.

4.2. SWEEP PROPERTIES

4.2.1. *Accuracy and linearity*

In order to obtain information of the absolute accuracy of the sweep velocity and the sweep linearity, calibrations were performed for the sweep velocities used in the measurements, by displaying on the oscilloscope screen periodical signals of known frequencies. For the Tektronix 545 used the deviations in the linearity and the sweep velocities given by the factory, were in all cases less than 0.7%. This high accuracy of modern oscilloscopes makes them very convenient for half-life-measurements.

4.2.2. *Jitter in triggering time and sweep stability*

These properties were checked by replacing the pulses from the detectors by pulses from a pulse generator, which were fed in parallel to both channels. In this way we obtain what may be called an electronic coincidence resolution curve, which does not include the time spread of the detecting devices but only that due to the oscilloscope itself and the electronics used. The electronic resolution curve presented in fig. 10 I was obtained by using the delayed sweep operation and having the photomultiplier viewing the screen through a slit of the size 1×10 mm^2 in the black paper covering the screen (cf. fig. 5). The pulse was amplified so much that within the field of view of the screen it was linear and the slit was placed parallel to the linearly rising part of the pulse. It was not possible with the oscilloscope used (Tektronix 545) to change the delay of the main sweep by sufficiently small time intervals and for this reason we had to use another method. By means of a potentiometer connected to the "A"-input of the preamplifier of the oscilloscope, a small variable D.C.-voltage was superimposed on the pulse fed in through the "A"-input and thus the vertical position of the pulse on the screen could be slightly varied (cf. fig. 5). This produces an effect equivalent to a horizontal shift of the pulse. The amount of this shift can be calculated from the knowledge of the D.C.-voltage, the amplification for the "A"-input and the slope of the pulse on the screen.

The very steep edges of the resolution curve as well as the 100% efficiency, are remarkable. According to this result, it seems in principle possible, and not at all difficult, to measure time differences as small as one or a few tenths of a mμs, even with an oscilloscope like the Tektronix 545 used in most of our experiments, which is not the fastest one commercially available.

4.3. LIMITATIONS FOR SHORT HALF-LIVES

Going back to fig. 10 I it is now justified to state that the oscilloscope itself will not set a lower limit for half-life measurements. The b-signals have still lower energies (75 and 279 keV respectively). If the latter channel is set to accept gamma-rays of the energy 126 keV, there is a broadening and a shift in the resolution

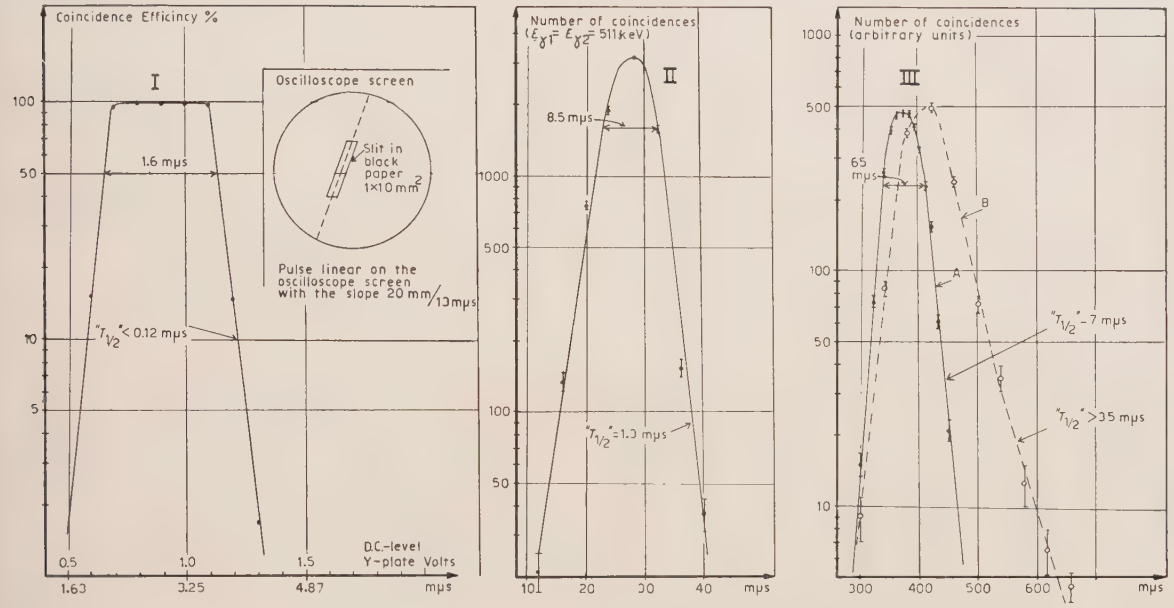

Fig. 10. Electronic coincidence resolution curve obtained by using the arrangement of fig. 5, but replacing the signals from the detectors by signals from a pulse generator. The way in which the short delay in this case was changed is described in section 4.2. II. Prompt coincidence resolution curve using the 511 keV gamma rays from the annihilation process (Na^{22}-sample). Both discriminators were set on the photopeaks. III. Prompt coincidence resolution curve when the gamma ray energies are 70 and 279 keV, respectively, and the delayed coincidence curve, obtained when the 279 keV channel is shifted to a positon corresponding to 126 keV.

This indicates the presence of a metastable state in the Pb^{203}-sample used.

widths and the slopes of the measured prompt coincidence curves will thus almost entirely be due to the time spread in the detecting devices used.

In our measurement we diminished the time spread due to pulse height spread by using a time correction circuit included in the coincidence circuit constructed by B. Johansson[18]) (used only for the shortest half-lives). Fig. 10 II shows the prompt coincidence resolution curve when the a- and b-detectors accepted the 511 keV gamma rays from the annihilation process. For a and b signals of these energies it would thus be possible to measure a half-life of a few mμs with the set-up we used. Fig. 10 III shows how the width and the slope of the resolution curve are changed when the a- and curve, which are typical for b-signals from a metastable state. The sample used in this case was Bi^{203} and fig. 18 shows a more carefully performed measurement which confirms the suggestion of a metastable state in Pb^{203}.

In fig. 19 the half-life measurement of the 615 keV-level in Ta^{181} is presented. It can be concluded from these measurements that in cases where the a- and b-signals originate from gamma rays of energies of about 150 and 500 keV detected by NaI-crystals it would be possible to estimate a half-life as short as 2 mμs by comparing the shift of the center of gravity of the delayed and prompt coincidence curves.

Thus, using NaI-crystals, under normal conditions the shortest resolution time available from the point of view of the oscilloscope could

[18]) B. Johansson, Nucl. Instr. 1 (1957) 274.

hardly be used in our measurements, and one can conclude that the difficulties and the limitations in the short half-life region for a set-up such as the one we used, are the same as for any fast arrangements of the conventional type.

It might be asked why the oscilloscope should be used at all in the short half-life region instead of a conventional coincidence circuit with delay facilities. The most apparent answers to this question are the following:

(1) If the measurement of a half-life is suddenly essential in a certain project and no fast coincidence circuits are available, the oscilloscope may save a lot of development and construction work.

(2) It is not so easy to construct a coincidence set-up in the mμs-region, with a continuously variable delay, which is the feature making the oscilloscope so convenient for delayed coincidence measurements.

4.4. LIMITATIONS FOR LONG HALF-LIVES

In this region even more than in the region of short half-lives, the sweep facilities of most oscilloscopes go far beyond those which can be used in delayed coincidence measurements. There is thus no limitation regarding the sweep possibilities.

A discussion of the limitations for long half-lives will almost be the same for any delayed coincidence method as for the oscilloscope method. Since we have not been able to find sufficiently far-reaching discussions in the literature, we have made some calculations, the main results of which will be presented here.

The statistical relative error E of a certain point on the decay curve can be written

$$E = \sqrt{\frac{N_r + N_c}{T N_c^2}} \qquad (2)$$

N_r = number of random coincidences per unit time
N_c = number of real coincidences per unit time
T = total measuring time.

Remembering that the number N_c proportional to the number of disintegrations in the source and that the number N_r is a quadratic function of the same number, one sees that E approaches a constant value E_{min} for infinitely strong sources. The statistical error can thus never be smaller than E_{min}. Substituting in (2) expressions for N_r and N_c containing parameters relevant for the error discussion we obtain:

$$E_{min} = e^{t/\tau}\left(\frac{\tau}{\Delta}\right)^{\frac{1}{2}} \sqrt{\frac{h_a h_b}{\varepsilon_a \varepsilon_b}\,\frac{\tau}{\delta T}} \quad \text{for} \quad \Delta \ll \tau \,. \qquad (3)$$

τ = the mean life of the state studied
t = the delay corresponding to a certain point on the decay curve
Δ = time channel ($\mu \Delta x$)
ε_a, ε_b = efficiences of the channels detecting the events a and b
h_a = $\frac{\text{wanted events + unwanted events from the source}}{\text{wanted events}}$ in channel a and similarly for channel b
δ = fraction of all a-transitions followed by b-transitions (obviously most decays are not so simple as indicated in fig. 2).
n_a, n_b = number of counts per unit time in counters a and b due to external background.

It can be shown that in many actual cases when reasonable source strengths are used, the value of E may differ from E_{min} by only a small amount. For instance, if the source strength is adjusted to give a ratio $N_r/N_c = 1$, and if n_a and n_b both can be neglected compared to N_a and N_b, (counts from the source), one obtains $E = \sqrt{2}\, E_{min}$.

In all cases one could, in principle, obtain a statistical error E close to E_{min} by choosing a sufficiently strong sample. As discussed in more detail below, this is in practice only possible to a certain extent due to systematic errors which become more important the higher the ratio N_r/N_c is.

From (2) we can immediately attain some conclusions which are of decisive importance when discussing the upper limit of the delayed coincidence method.

(a) For analogous conditions and for equivalent points on the decay curve, (t/τ and Δ/τ the same) the total measuring time must be proportional to the half-lives if the same value of E_{min}

is to be obtained. Thus it is evident that the half-life measurements can become too time consuming for long half-lives. The mother activity feeding the metastable state may also decay before it is possible to collect sufficient statistics. Multichannel time analyzers therefore often become indispensable in the long half-life region. As we have pointed out before, the oscilloscope itself can be used as such an instrument for half-lives larger than about 1 μs. In addition electromagnetically separated activities offer the possibility of replacing mother nuclei which have decayed, because of the small risk of introducing other longer lived nuclei increasing the number of unwanted events.

(b) For a certain case and for a wanted value of $E_{\min}$, the total time T required for the measurements is proportional to h_a and h_b and is thus a quadratic function of the impurities in the sample. From this the convenience of using electromagnetically separated activities is evident in a very striking way. There are certainly many cases where the use of electromagnetically separated radioactive samples will make possible measurements which otherwise cannot be performed. So, for example, we have frequently used sources produced in the 190 MeV Uppsala proton synchrotron. It is clear that all the activities, which are produced in nuclear reactions in which as many as 12 nucleons may be boiled off, would in many cases produce a prohibitively large number of unwanted events. The electromagnetic separation of some of the samples used in this work was performed with the 160 cm electromagnetic separator of the Nobel Institute. Figs. 12 and 13 illustrate how the efficiency of the measurements is increased when separated radioactive samples are used.

(c) The well known importance of using high efficiency of the detectors is also seen from (2).

(d) From (2) it is also clear that the branching ratio δ in many cases may set a limit to the possibility of measuring a half-life in general and that this will be especially critical for long half-lives.

Regarding the use of (2) a few comments should be made:

(1) In the short half-life region, the fulfilment of the condition $N_r/N_c = 1$ may result in such high counting rates that they cannot be used because of limitations in the detectors and pulse height analysers. On the other hand, the time T, which in such cases would result from (2), is generally so small that one can easily afford to work with much lower activities and much better ratios of N_r/N_c and to increase T correspondingly.

(2) For long half-lives, the condition $N_r/N_c = 1$ (if it is possible to fulfil it at all) leads to extremely low counting rates and the condition of negligible background might no longer be fulfilled. In these cases, if one wants to obtain a statistical error not much bigger than $E_{\min}$, one is forced to increase the source intensity and work with a poorer ratio N_r/N_c. On the other hand, since the total measuring time is proportional to the half-life measured, we see that the longer the half-life is, the less we can afford to work far from the ideal conditions. How far one can go in increasing the ratio N_r/N_c and how this depends on the coincidence set-up used, is illustrated below. First let us, in order to get an idea of the limit we are speaking about, introduce some typical values in (2) and see for this hypothetical case, which the longest measurable half-life would be. For $E_{\min} = 5\%$ and when

$$t/\tau = 2 \quad \varepsilon_a = \varepsilon_b = 0.2$$

$$t/\Delta = 5 \quad b = 1$$

$$h_a = h_b = 2 \quad T = 24 \text{ h},$$

we obtain

$$\tau_{\max} \approx 0.11 \text{ sec.}$$

The reason for the impossibility of using arbitrarily high ratios of N_r/N_c can be found in the fact that the accuracy, and mainly the stability of the time channel Δt is never perfect. Obviously an error of 1% in this resolving time will produce a change of only 1% in the number of real delayed coincidences provided the number of random coincidences is negligible. This uncertainty, however, will be 10% if $N_r/N_c = 9$. Thus, the more accurate our set-up is, the higher the ratio N_r/N_c which can be tolerated and thus

TABLE
Summarized information of th

Nucleus studied	Half-life of mother activity	Triggering signal a	a detected in	Delayed signal b
Pb^{205}	15.3 d	73 keV EC X-rays	$1\frac{3}{4}'' \times 2''$ hole NaI-crystal	mainly 987.8 keV
Pb^{206}	6.4 d	73 keV EC X-rays	$1\frac{3}{4}'' \times 2''$ hole NaI-crystal	γ-rays of energy > 100 keV
Ta^{181}	45 d	100–300 keV β-particles	3 mm anthracen crystal	133 keV γ-ray
Rb^{85}	64 d	13 keV EC X-rays	3 mm anthracen crystal	513 keV γ-ray
Pb^{204}	11.22 h	73 keV EC X-rays	$1\frac{3}{4}'' \times 2''$ NaI(Tl)-crystal	899.2 keV and 375 keV γ-rays
Pb^{203}	11.76 h	73 keV EC X-rays	$1\frac{3}{4}'' \times 2''$ NaI(Tl)-crystal	126.3 keV γ-ray
Ta^{181}	45 d	137 keV γ-ray	$1\frac{3}{4}'' \times 2''$ NaI(Tl)-crystal	482 keV, 346 keV and 136 keV γ-rays

correspondingly longer half-lives may be measured without putting impossible restrictions on the background.

The oscilloscope is by no means outstanding in this respect. The possible errors and fluctuations of the time channels, including the errors arising in the visual counting of the points, might safely be estimated as $< 1\%$, but not very much smaller, and the ratios N_r/N_c can thus not be too high; the highest value depending, of course, on the precision wanted.

Let us mention finally that in the above mentioned case if the external background $n_a = n_b = 1$ count per second and $E = \sqrt{2}\, E_{min} = 7\%$ the ratio N_r/N_c would be:

$$N_r/N_c = 11.4 .$$

For $n_a = n_b = 0.1$ count per second and the same value of the error we would have:

$$N_r/N_c = 1.64 .$$

The conclusions we can draw from this are:

(1) For a given set-up the longest measurable life time is to a great extent dependent on the counting rate due to the external background and it is not necessary to emphasize the importance of keeping this contribution as low as possible.

(2) Using high precision instruments (which should not be too difficult to construct in the 10^{-3} sec–1 sec region) one could, at least in favourable cases, cover this region of half-lives, which is often regarded as a difficult one.

5. Comments on the Measurements

In table 1 are collected the most relevant data of the measurements on the different nuclides used. In general, the main purpose was not to obtain the highest possible accuracy in each case but rather to study the method itself. For example, the half-life of the metastable state in Rb^{85} can be measured much more accurately than we did. The half-lives were chosen in such a way that they should give us experience in a wide half-life region. In some cases, however,

lf-life measurements performed

b detected in	Oscilloscope used	Type of oscilloscope detection	Total measuring time	Half-life this work (approximately least square fit)	Previous measurements
ame crystal as for a signal	Tektr. 512, 541, 545A	Photographic	110 h	4.15 ± 0.15 ms	4.8 ± 1.5 ms[16])
ame crystal as for a signal	Tektr. 512, 541, 545A	Photographic	79 min	123 ± 3 μs	123 ± 3 μs[21]) 128 ± 5 μs[13])
$\frac{1}{2}''$ × 2″NaI(Tl) crystal	Tektr. 541	Photographic	99 min	17.5 ± 0.8 μs	17.2 μs[14]) 18.8 μs 18.1 μs 22 μs 20 μs [22])
$1\frac{1}{2}''$ × 2″ NaI(Tl)-crystal	Tektr. 541	Visual	170 min	1.0 ± 0.1 μs	0.90 ± 0.04 μs[23])
$1\frac{3}{4}''$ × 2″ NaI(Tl)-crystal	Tektr. 545A	Photo multiplier	280 min	316 ± 6 mμs	260 mμs 300 mμs [22])
$\frac{3}{4}''$ × 2″ NaI(Tl)-crystal	Tektr. 545A	Photo multiplier	9 h	55 ± 5 mμs	previously not know
$\frac{3}{4}''$ × 1″ NaI(Tl)-crystal	Tektr. 545A	Photo multiplier	70 min	11.0 ± 0.4 mμs	10.6 mμs 10.4 mμs 11.0 mμs [22])

there were special reasons to be more careful. A critical analysis of "irregularities" in the half-life curve of the known metastable state in Pb^{204} led to the discovery of a hitherto unknown case of nuclear isomerism in Pb^{203} (55 mμs).

Pb^{205}:

The first Bi^{205}-samples used in Bariloche were obtained by irradiating natural lead in the Buenos Aires synchro-cyclotron with 29 MeV deuterons. The measurements were started about 2 months after the end of the irradiation. The source used was thus the Bi-activity trapped in the metallic lead. In addition to Bi^{205}, there was also Bi^{206} and Bi^{207} present. Because of these impurities and the relatively high cosmic ray background (altitude about 800 meters) the true, delayed events were only 20% of the total number of events counted during the first ms. Under such circumstances, we would never have been able to observe the 4 ms half-life reported by Vegors and Heath[16]) if the oscilloscope method could not be used in this case as a multichannel time analyzer. The experimental set-up used in these first measurements is shown in fig. 3. The b′-signals (Pb K X-rays) were used for intensity modulation of the electron beam in the way described previously. In addition, a saw-tooth voltage was fed to the y-plates which distributed the delayed events (points) in the vertical direction (4 cm) of the oscilloscope screen (cf. fig. 3). After having obtained a suitable point density in the first time channel (1 ms corresponding to the first 1 cm on the screen) the film was manually moved before the next exposure. The random coincidence rate was obtained by simultaneously counting the number of released sweeps (a′-signals) and the number of b′-signals. Even if the statistics in these first measurements were poor, they unambiguously confirm the conclusions drawn by Vegors and Heath of the existence of a 4 ms metastable state in Pb^{205}. Note, for example, that the number of delayed events decays with

the same half-life as Bi^{205}, which supports the assumption that the 4 ms half-life is due to a metastable state in Pb^{205} (see fig. 11). This was and the detector arrangements do not give rise to a distribution of events, which may be wrongly interpreted as a half-life. In order to

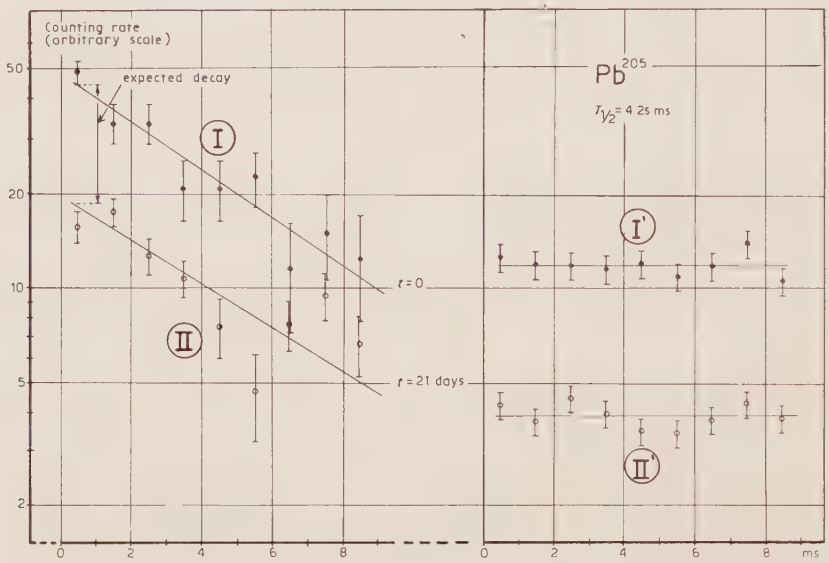

Fig. 11. First measurements of the 4 ms half-life of the $i_{13/2}$-state in Pb^{205} using the arrangement of fig. 3. Curves I and II show that the mother activity decays with the same half-life as Bi^{205}. Curves I′ and II′ were obtained by using two independent sources and detectors, thus showing that curves I and II are due to a nuclear decay.

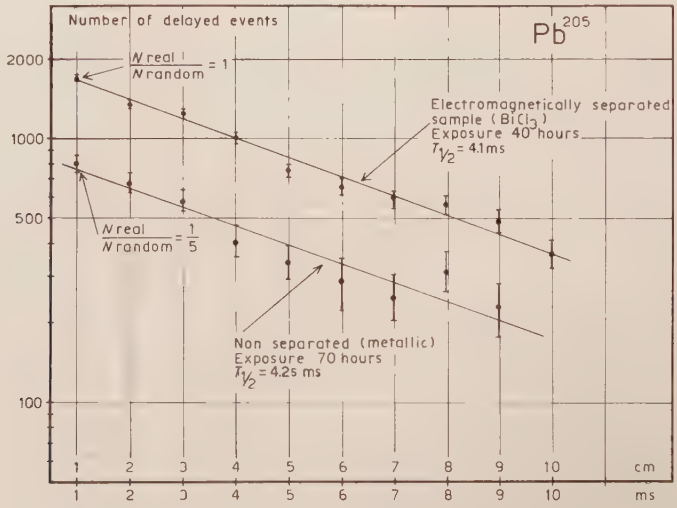

Fig. 12. Decay curves of the $i_{13/2}$ state in Pb^{205} showing the advantage of using electromagnetically separated radio-active samples in delayed coincidence measurements. The upper curve was obtained with the arrangement shown in fig. 4 and the lower curve with that shown in fig. 3.

definitely proved in later experiments in which we used electromagnetically separated Bi^{205}.

When the ratio of real to random coincidences is as poor as it was in these experiments, it is necessary to be sure that the oscilloscope itself prove that we really observed a nuclear decay we used in separate experiments independent sources for the a′- and b′-signals. As can be seen at the right of fig. 11, we obtained in this case horizontal lines within the experimental

errors. The sum of the two Bariloche measurements is presented in fig. 12. Since the value of the half-life obtained was shorter than that reported by Vegors and Heath two of us (I. B. and P. T.) repeated these experiments in Stockholm. The experimental conditions were

Recent measurements by R. Stockendal[19]) and by D. Alburger[20]) have in a very beautiful way solved the problem of the "missing" $i_{13/2}$-state in Pb^{205}. Combining the experiments by Stockendal, Alburger those performed by Vegors and Heath and our results one concludes that

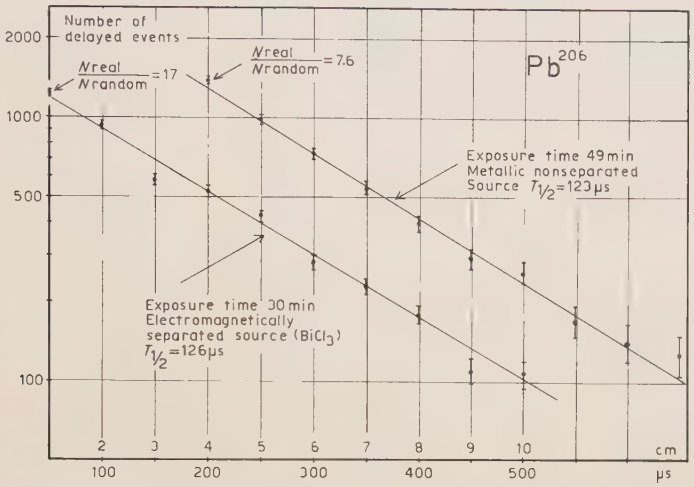

Fig. 13. Half-life curves of the decay of the 7⁻ state in Pb^{206}. The upper curve was obtained by using the arrangement of fig. 3 and the lower curve with that shown in fig. 4. Notice the advantage of using electromagnetically separated samples.

now better. For example the use of electromagnetically separated Bi^{205} greatly increased the efficiency of the measurements (cf. formula (2), section 4.4). In addition, the measurements were simplified by using a motor driven film in the camera continuously registering the events on the oscilloscope screen. In section 4.1 we have also described how the random events were continuously controlled. Thus, the complete automatization of the measurements also contributed to the better statistics obtained in the Stockholm measurements. The sum of the first three Stockholm measurements is also shown in fig. 12. In later experiments with better statistics a "tail" appeared at the end of the half-life curve which may be the explanation of the longer half-life reported by Vegors and Heath. We checked carefully that the tail was not due to an instrumental effect. It is not clear at the moment whether this tail ("half-life" about 10 ms) is due to another metastable state in Pb^{205} or whether it is due to some unknown systematic error.

the 4 ms half-life should be due to the $i_{13/2}$-state which decays by the following transitions: 26.22 keV (M2), 310.5 keV (E3) and 1014.0 keV (M4). This is certainly one of the most interesting cases of nuclear isomerism that has been reported.

Pb^{206}:

The half-life of the famous 7⁻ state in Pb^{206} has been measured by several workers and was especially suitable for checking the properties of our method in the 100-μs region. The first measurement was performed with a fresh metallic non separated sample obtained after irradiating natural lead with 29 MeV deuterons for 30 minutes in the Buenos Aires synchrocyclotron. Later we repeated this experiment in Stockholm with an electromagnetically separated sample, because the 4 ms half-life in Pb^{205},

[19]) R. Stockendal, Nobel Institute of Physics, Stockholm, Phys. Rev. **118** (1960) 1074, and Arkiv för Fysik **17** (1960) 553.

[20]) D. Alburger, Brookhaven National Laboratory, Phys. Rev. **118** (1960) 1076.

which was not well established when the previous measurements were performed, may have contributed to uncertainties in the coincidence background. The results are shown in fig. 13 and as can be seen, the half-life values are in good agreement with those obtained by Tove[21]) and Åström[13]) (cf. table 1). Note that also in this case the electromagnetically separated samples considerably increase the efficiency of the measurements. In addition there is a guarantee of no contribution to the coincidence background from half-lives associated with neighbouring mass numbers.

Ta^{181}:

The metastable state studied is in this case fed by 450 keV beta-particles from the ground state of 45 d Hf^{181} and decays by the emission of several gamma-rays, the strongest of which have the energies 136 and 133 keV. Thus, the a-signals were beta-particles, which were detected by a 3 mm anthracene crystal and the discriminator setting chosen was such that the ratio of the beta-particles and the gamma-rays detected by this crystal was an optimum. The result of this measurements, which was performed in Buenos Aires with a sample obtained from the Swedish R1-reactor, is shown in fig. 14 and the half-life obtained is in good agreement with one of the previously reported values[14,22]) (cf. table 1).

Rb^{85}:

The half-life was in this case too short to be measured by the photographic method with the

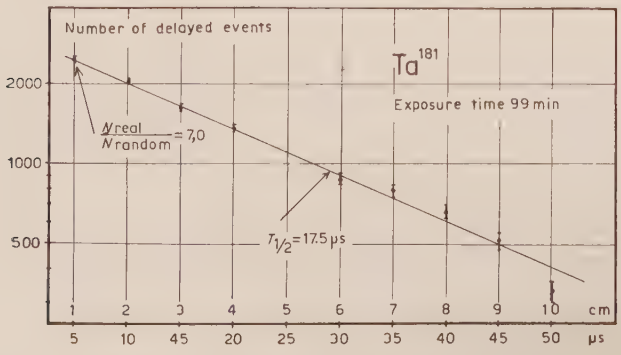
Number of delayed events
Ta181
Exposure time 99 min
Nreal / Nrandom = 7,0
T½ = 17.5 µs
2000
1000
500
1 2 3 4 5 6 7 8 9 10 cm
5 10 45 20 25 30 35 40 45 50 µs

Fig. 14. Half-life curve of the 615 keV level in Ta^{181} obtained with the arrangement of fig. 3.

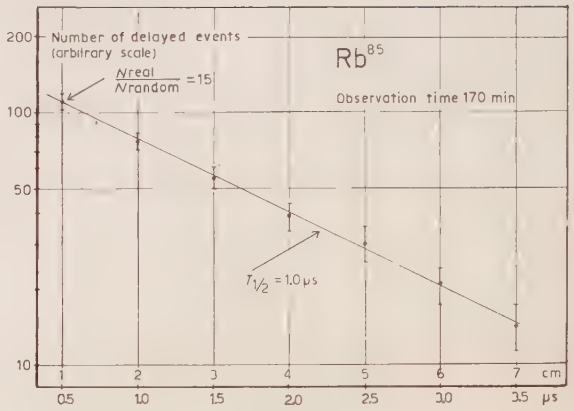

Fig. 15. Delayed coincidence curve corresponding to the decay of the 513 keV state in Rb^{85}. The light spots on the oscilloscope screen were counted visually. The arrangement of fig. 3 (without camera) was used.

equipment available to us in Buenos Aires. For this reason the delayed events on the screen were counted visually. The sample used was produced by irradiation of natural Rb in the Buenos Aires synchro-cyclotron and was neither chemically nor magnetically separated. (Note that in this case the a-signals were the 13 keV capture X-rays from Rb.) In spite of these difficulties, a half-life is obtained (see fig. 15) which, though the statistics admittedly are poor, agrees reasonably well with previous measurements[23]). By using an isotopically pure sample and by detecting the delayed events by a photomultiplier, a much more accurate value would easily be obtained.

Pb^{204}:

Bi^{204} was produced by irradiating natural lead with 50 MeV protons in the Uppsala 190 MeV synchro-cyclotron. The first source was obtained by simply dissolving part of the lead in hydrochloric acid and using part of this solution. Thus the source contained many activities, the main ones being 11.8 h Bi^{203}, its daughter 52 h Pb^{203} and 11.2 h Bi^{204}.

Fig. 16 shows the result of a measurement with such a source. In this case a 2 cm slit in

[21]) P. A. Tove, Nucl. Instr. **1** (1956) 95.
[22]) D. Strominger, I. M. Hollander and G. T. Seaborg, Rev. of Mod. Phys. **30** (1958) 585.
[23]) J. G. Siekman, Nuclear Physics **2** (1956) 254.

front of the oscilloscope screen selected the upper part of the delayed pulses in a channel of about 40 mμs. Fig. 16 shows clearly the half-life of the well known 4^+ state in Pb^{204}. However, if the contribution of the decay of this 300 mμs state is subtracted, a symmetric coincidence resolution curve is not obtained for small sweep times. The asymmetry indicates a half-life which would be considerably shorter than 300 mμs and probably longer than 33 mμs. The only way of getting a satisfactory answer was to use electromagnetically separated samples. In order to give the reader an idea of the efficiency of the separation and the weak samples required in experiments of this type, it can be mentioned that the irradiation lasted for only half an hour and that less than 0.1 % of the separated sample was used in the experiments to be discussed below.

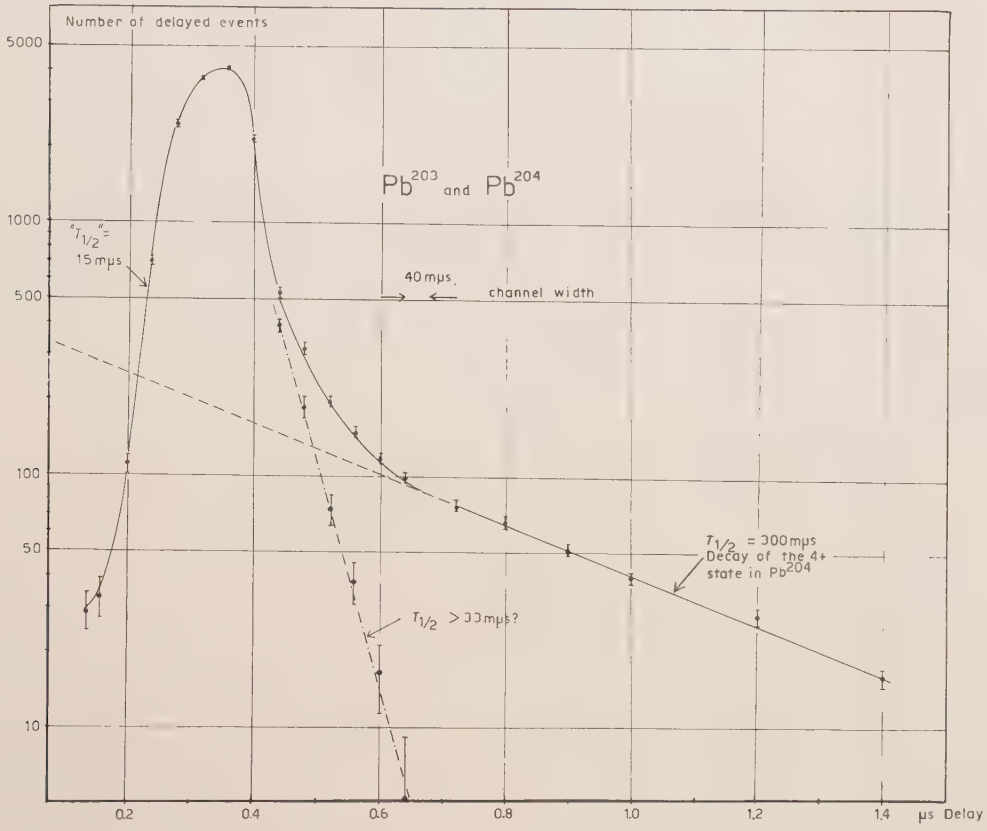

Fig. 16. Coincidence curve obtained by studying not separated Bi-activities (the main ones being Bi^{203} and Bi^{204}) and using the arrangement shown in fig. 5. As can be seen, two half-lives and a considerable number of prompt coincidences are present (see also figs. 17 and 18).

Fig. 17 shows the results of two independent measurements of the activity deposited on mass number 204 (activity half-width about 1.5 mm, line distance between mass numbers 203 and 204 about 8 mm). Note the favourable ratio of random to real coincidences again due to the electromagnetically separated samples. The half-life obtained is in good agreement with one of the previously reported values (cf. table 1).

Pb^{203}:

The results obtained when using the activity deposited on mass number 203 are shown in fig. 10 III and in fig. 18. Fig. 10 III shows a quick run which indicates that the asymmetry observed in the coincidence resolution curve of the first measurements mentioned above is indeed due to a half-life in Pb^{203}. Curve A and B were obtained when the b′-signals were selected

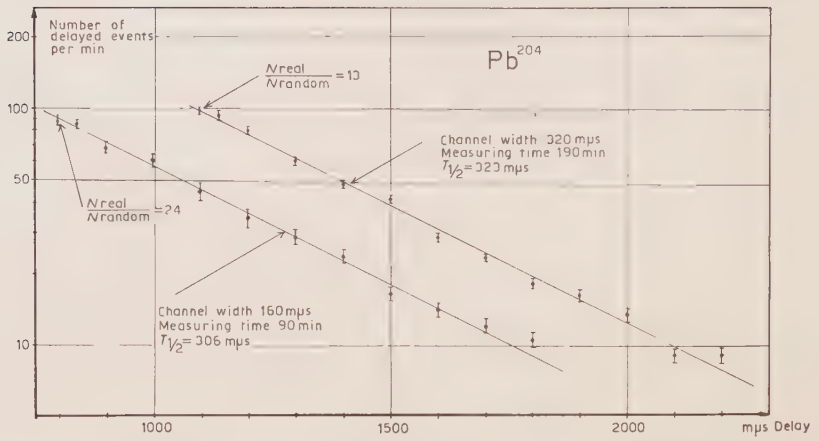

Fig. 17. Half-life curves of the first 4^+ state in Pb^{204} obtained in two independent runs with different time channel widths and using electromagnetically separated Bi^{204}. The arrangement used was that shown in fig. 5.

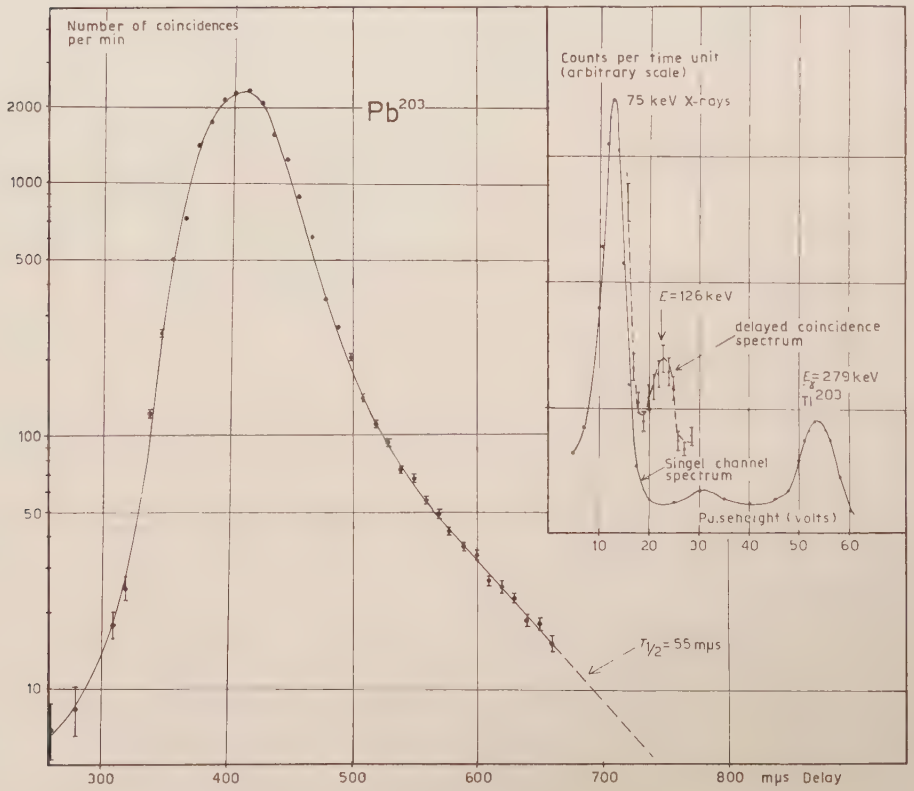

Fig. 18. Prompt and delayed coincidences obtained by using an electromagnetically separated Bi^{203}-sample and the arrangement given in fig. 5. The inset shows the one-channel spectrum of the sample used and the delayed coincidence spectrum obtained with a delay of 520 mμs and a time gate of 160 mμs. As can be seen from the figure, there is a gamma ray with an energy of 126 keV associated with the 55 mμs half-life in Pb^{203}.

with a discriminator setting corresponding to 279 and 126 keV, respectively, and the other channel selecting the K X-rays. The shift and the increase of the width of the resolution curve is typical for what is to be expected from the presence of a half-life. The discriminator setting (126 keV) was chosen because Stockendal *et al.*[24]) have reported a 126 keV gamma-ray in Pb^{203} which, according to them, should go to the groundstate of Pb^{203} and we suspected that this gamma-ray might be responsible for the observed half-life. The inset in fig. 18 shows the one channel spectrum of the sample used in the energy region discussed above. As can be seen, the 126 gamma ray is so weak that it does not show up in the one channel spectrum. The dashed curve shows the number of delayed events observed on the oscilloscope screen at the time 520 mμs with the channel width 160 mμs, as a function of the energy of the b'-signals. The coincidence curve thus obtained shows in a convincing way that the 126 keV E2 gamma ray is indeed associated with the observed half-life. The half-life was also more carefully measured (cf. fig. 18) but, as can be seen from the results obtained, there was a considerable contribution of prompt coincidences, mainly coming from the 52 h Pb^{203}-activity, which had grown in after the end of the separation. The measurements of other features of the metastable state discovered are being continued and will be reported in a separate paper[25]).

The prompt coincidence curve, which can be seen in fig. 19, was obtained by using the annihilation radiation of the positrons from a Na^{22}-sample. The energy settings of the discriminators were not changed when measuring prompt and delayed coincidences, and the low

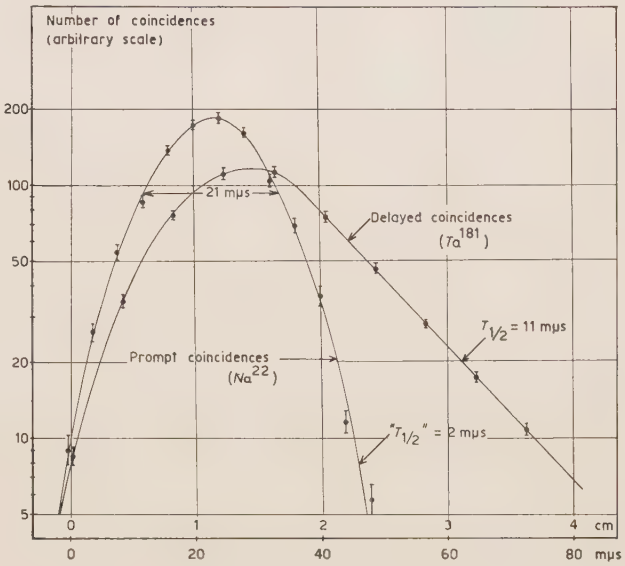

Fig. 19. Delayed coincidence curve showing the half-life of the 482 keV level in Ta^{181} and prompt coincidence curve obtained with the annihilation quanta from a Na^{22}-sample. In both cases the discriminator settings were the same and $2'' \times 1\frac{3}{4}''$ NaI(Tl) crystals were used as detectors. The slit width on the oscilloscope screen was 5 mm (10 mμs) but the effective width was smaller due to the sensitivity setting of the scaler counting the delayed events (cf. fig. 5). In order not to introduce systematic errors in the shift of the center of gravity of the coincidence curves it was necessary to use the same sweep rates in both cases.

Ta^{181} (THE 482 keV-LEVEL):

The sample used was obtained in the same way as that used in the measurements of the 615-keV level. In this case, however, the strong gamma rays with energies 147 and 482 keV (feeding and de-exciting the 482 keV level) corresponding to the a- and b-events were detected by two NaI-crystals. energy channel could thus accept only part of the Compton scattered 511 keV quanta while the other channel was wide enough to accept the 511 keV photo peak completely. According to theoretical calculations (see for example ref.[26])), the slope and the width of the prompt coincidence curve is about the best one which can be expected when using NaI-crystals for detecting gamma rays of the above mentioned energies.

The value of the half-life of the 482 keV level is in reasonably good agreement with the previous measurements[27]) (cf. table 1).

[24]) R. Stockendal, T. Novakov, B. Johansson and M. Schmorak, Arkiv för Fysik **14** (1958) 85.

[25]) I. Bergström, P. Thieberger and J. Uhler (to be published).

[26]) J. J. Peyre, Internal publication **17** (1958), Comisión Nacional de Energía Atómica, Buenos Aires, Argentina.

[27]) H. de Waard, Nucl. Instr. **2** (1958) 73.

Acknowledgements

It is a great pleasure to acknowledge the contribution of all those who helped to realize the summer school in nuclear physics in Bariloche from which this work originates. Our thanks are especially due to the head of Instituto de Física in Bariloche, prof. J. Balseiro, the Dean of the Faculty of Science in Buenos Aires, prof. R. Garcia and one of the Directors of the Argentine Atomic Energy Commission, prof. F. Alsina. The part of this work which was performed in Buenos Aires was very much stimulated by the help and sincere interest of the Head of the Physics Department, prof. J. Giambiaggi and by the equipment which was put at our disposal by Dr. J. Peyre and Dr. M. Sametband from the Argentine Atomic Energy Commission. It is also a great pleasure for us to acknowledge the importance of the equipment which was obtained from the field equipment department of UNESCO in Paris.

One of us (P. T.) also gratefully acknowledges a scholarship from the Argentine Research Council (CNICT) which made it possible for him to take part in the completion of this work in Sweden. He also wants to thank the Head of the Nobel Institute prof. Manne Siegbahn and his Swedish colleagues for their hospitality.

NUCLEAR INSTRUMENTS AND METHODS 8 (1960) 173–184; NORTH-HOLLAND PUBLISHING CO.

ON THE EFFICIENCY OF THE REACTION $H^3(d,n)He^4$ IN TITANIUM TRITIDE BOMBARDED WITH DEUTERONS

E. M. GUNNERSEN and G. JAMES

Atomic Weapons Research Establishment, Aldermaston, Berkshire

Received 10 April 1960

The lack of accurate energy loss data in metals (and particularly in titanium tritide) of deuterons of less than 100 keV has been shown to cause large uncertainties in calculations of the neutron yield produced by the $H^3(d,n)He^4$ reaction when a titanium tritide target is bombarded with low energy deuterons. Direct measurements of the energy loss in titanium hydride foils of 40–150 keV deuterons have been made, and have been used in combination with data in the literature for other metals and higher ion energies to recalculate the neutron yield from this $H^3(d,n)He^4$ reaction in titanium tritide for the deuteron energy range 9–150 keV. Using this yield curve, a technique has been described for estimating how tritium concentration varies with depth in the titanium tritide material by examing the observed variation of neutron yield with incident angle and energy of the bombarding deuteron beam. It has been found that the concentration peak is never less than 3000 Å below the surface, and that there is very little tritium contained in an upper surface layer of about 500 Å, or in the lower one-third of the titanium tritide material.

Introduction

Observed neutron yields from the $H^3(d,n)He^4$ reaction in thin titanium tritide targets bombarded with 40–150 keV deuterons are usually considerably less than the expected yields calculated from the known reaction cross-sections and from the known average tritium concentration in the target materials. This divergence may be due to inaccurate calculation of the neutron yield expected from a hypothetical thin titanium tritide target possessing constant tritium concentration throughout its thickness, or to the error introduced by assuming that the tritium concentration in the actual target examined is constant throughout its thickness.

In Part A the former cause of divergence has been investigated by examining how the available experimental data on the $H^3(d,n)He^4$ reaction cross-sections, and on the energy loss of deuterons in titanium tritide, can best be used in the calculation of neutron yield. Also in this section is described an experiment which was designed to check the validity of the available energy loss data by measuring directly the rate of energy loss of very low energy deuterons in titanium hydride foils. By using these optimum experimental data, the calculation of the neutron yield curve (i.e. neutrons/μcoulomb of deuterons, over the energy range 9–150 keV) has then been carried out for a hypothetical target ($\approx$ 15 000 Å) having a constant tritium atomic ratio of 1.5 tritium atoms per titanium atom throughout its thickness.

In Part B the actual variation with depth of the tritium concentration in the target material has been investigated experimentally by bombarding various targets with deuterons from a Cockroft-Walton accelerator over a range of incident angles and energies. This has not only yielded estimates of the contamination layer thicknesses (e.g. of titanium oxide on the titanium tritide surface), but has also yielded considerable information about the actual distribution of tritium in the lower layers of the evaporated titanium tritide material (i.e. just above the supporting nickel backing).

Some miscellaneous information on the secondary electron coefficients of titanium hydride due to H_2^+, D_1^+ and D_2^+ bombardment is presented in an appendix.

A. EXPECTED NEUTRON YIELD FROM A THIN TITANIUM TRITIDE TARGET OF UNIFORM TRITIUM ATOMIC RATIO 1.5

1. Method of Calculation

It is assumed that the tritium atomic ratio (i.e. concentration) of 1.5 tritium atoms per titanium atom is constant throughout the whole thickness of the target material ($\approx$ 15 000 Å), and that any surface contamination layer is of negligible thickness.

Since the angular dependence of the differential cross section for the reaction $H^3(d,n)He^4$ is isotopic up to at least 200 keV (Allen and Poole[1], Argo *et al.*[2]), the total yield of neutrons per incident deuteron of energy E is given by

$$Y = \int_0^E \frac{4\pi n_t \, d\sigma/d\omega}{d\varepsilon/dx} \, d\varepsilon \qquad (1)$$

where n_t is the number of tritium atoms/cm^3 (a constant), $d\sigma/d\omega$ is the differential cross-section for the $H^3(d,n)He^4$ reaction, and $d\varepsilon/dx$ is the rate of energy loss of deuterons of energy ε in the titanium tritide target.

The value of the constant n_t is obtained as follows. If the target material TiT_N contains $N = 1.5$ tritium atoms/titanium atom, then the density ρ_{TiT_N} of the target material is

$$\rho_{TiT_N} = \frac{48 + 3N}{48} \times \rho_{Ti} \times 0.85 = 4.22$$

where

$$\rho_{Ti} = 4.54 \, .$$

The factor 0.85 arises from the 15% expansion which the titanium lattice undergoes during tritiation. The number n_t of tritium atoms/cm^3 is then

$$n_t = \frac{1.5 \times \rho_{TiT_N} \times 6.02 \times 10^{23}}{A_{TiT_N}} = 7.26 \times 10^{22} \, .$$

The differential cross-sections $d\sigma/d\omega$ for the reaction $H^3(d,n)He^4$ has been measured by Conner, Bonner and Smith[3] for 10–1752 keV deuterons, and by Arnold *et al.*[4] for 7.5–120 keV deuterons. The agreement in the overlapping region is excellent. The resultant data used for $d\sigma/d\omega$ for the overall energy range 7.5–150 keV has therefore not been reproduced here, but can be obtained from the above references.

Provided the numerical evaluation of the integral in eq. (1) is accurate, the chief source of error in calculating Y over an extended energy range is the lack of reliable experimental data on the rate of energy loss $d\varepsilon/dx$ of deuterons in titanium tritide. Since the integration covers all energies of the deuterons from the incident energy E down to the point where all their energy is absorbed, the value of Y is quite as dependent on $d\varepsilon/dx$ as it is on the reaction cross-sections. There are no available experimental figures on the rate of energy loss of deuterons in either titanium tritide, titanium alone, or tritium alone for the required energy range. Moreover, most available data on the rate of energy loss of deuterons in other metals usually does not extend down to energies less than 100 keV (Allison and Warshaw[5]). Warshaw[6], however, has made some measurements on the rate of energy loss of protons in aluminium, copper, silver and gold for the proton energy range 50–350 keV, and Reynolds *et al.*[7] have published some results on the energy losses of deuterons in tritium gas for the deuteron energy range 60–700 keV. These latter agree reasonably well with some energy loss measurements made by Phillips[8] for 20–160 keV deuterons in tritium. The best approximation to use for the value of $d\varepsilon/dx$ for deuterons in TiT_N is that value obtained by assuming that Bragg's law holds (i.e. that the energy loss in a compound is the sum of the energy losses in its separate constituents).

[1]) Allen and Poole, Proc. Roy. Soc. A **204** (1951) 500.
[2]) Argo, Taschak, Agnew, Hemmendinger and Leland, Phys. Rev. **87** (1952) 612.
[3]) Conner, Bonner and Smith, Phys. Rev. **88** (1952) 468.
[4]) Arnold, Phillips, Sawyer, Stovell and Tuck, Phys. Rev. **93** (1954) 483.
[5]) Allison and Warshaw, Revs. Mod. Phys. **25** (1953) 779.
[6]) Warshaw, Phys. Rev. **76** (1945) 1759.
[7]) Reynolds, Dunbar, Wenzel and Whaling, Phys. Rev. **92** (1953) 742.
[8]) Phillips, Phys. Rev. **90** (1953) 532.

$$\frac{d\varepsilon}{dx} = \frac{48}{48 + 3N}\left(\frac{dE}{dx}\right)_{Ti} + \frac{3N}{48 + 3N}\left(\frac{dE}{dx}\right)_{T_2},$$

$$= 0.914\left(\frac{dE}{dx}\right)_{Ti} + 0.086\left(\frac{dE}{dx}\right)_{T_2} \text{ for } N = 1.5\,. \quad (2)$$

There is evidence that this law holds sufficiently accurately for those compounds in which it has been investigated provided the incident energy is not too low (Segrè[9], Phillips[8], Reynolds *et al.*[7], Dalgarno and Griffing[10]). Just how low in deuteron energy it is possible to go before the law deviates for titanium tritide is uncertain.

The values used in eq. (2) of $(dE/dx)_{Ti}$ for deuterons are obtained by interpolating with respect to $A^{-\frac{1}{3}}$ between Warshaw's two experimental curves for protons in aluminium and in copper. This curve has then been extrapolated back to the origin to obtain the lower energy, energy loss values.

Since

$$(dE/dx)_{\text{protons}}(\varepsilon) = (dE/dx)_{\text{deuterons}}(2\varepsilon)\,,$$

the values for deuterons are simply obtained by doubling the energy scale. Table 1 contains this data for $(dE/dx)_{Ti}$. The values used in eq. (2) of $(dE/dx)_{T_2}$ for deuterons are obtained by combining the results of Reynolds *et al.*, with those of Phillips, and extrapolating down to lower energies. The final figures of $(dE/dx)_{T_2}$ for deuterons, and the values of $(d\varepsilon/dx)_{TiT_{1.5}}$ for deuterons calculated from eq. (2), are given in table 1.

TABLE 1

Energy loss value for deuterons in Ti, T_2 and $TiT_{1.5}$ (values are in keV/mg/cm²)

E (keV)	$(dE/dx)_{Ti}$	$(dE/dx)_{T_2}$	Estimated $(d\varepsilon/dx)_{TiT_{1.5}}$	Measured $d\varepsilon/dx$ in TiH foils
10	59	≈ 490	96.0	—
15	88	≈ 600	132.0	—
20	108	≈ 704	159.4	—
25	132	802	189.6	—
30	149	890	212.6	—
35	163	960	231.6	—
40	177	1023	249.8	278
45	187	1081	263.8	289
50	193	1128	273.3	298
60	210	1183	294.0	315
70	223	1238	309.9	327
80	233	1268	321.7	336
90	242	1281	331.4	343
100	252	1290	341.9	346
110	260	1294	348.9	348
120	265	1295	353.5	350
130	269	1288	356.7	—
140	273	1281	359.0	—
150	276	1270	361.2	—
160	278	1251	361.3	—
170	280	1231	362.0	—

The numerical evaluation of the integral (1) for incident deuteron energies 9–150 keV has been carried out by plotting the integrand graphically, and carrying out the numerical integrations by square counting up to each incident deuteron energy E. The resultant yield curve of neutrons/μcoulomb of deuterons, is shown in fig. 1.

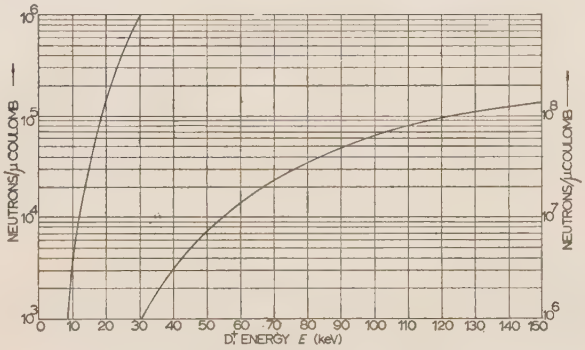

Fig. 1. Yield curve for $TiT_{1.5}$

Saker and Wood[11] of S.E.R.L. Baldock, using the same method and similar cross-section and energy loss data, later repeated the above calculation for the atomic ratio 1.5, and extended it to cover other atomic ratios ranging between 0.2 and 2.3. Their yield curve for the atomic ratio 1.5 fits the curve in fig. 1. within the thickness of the line over the whole energy range. Most of the inaccuracy in these calculations arises from uncertainty in the energy loss figures for deuterons in titanium tritide. Because of the extrapolation involved at low energies, it would be unjustifiable to claim an accuracy

[9]) Segrè, Experimental Nuclear Physics, Vol. 1 (Wiley & Sons, 1953), p. 205.

[10]) Dalgarno and Griffing, Proc. Roy. Soc. A **232** (1955) 423.

[11]) Saker and Wood, S.E.R.L., Baldock. Tech. Memo. No. 413 (1958).

greater than 10%, and it may be very much worse than this for $E < 20$ keV. It is important to note, however, that above 20 keV, the general shape of the yield curve is far more likely to be correct than the absolute position of the curve on the ordinate scale.

The results were consistent with the assumption that the D_1^+ beam contained not more than $\frac{1}{2}$% of H_2^+.

After analysis, the beam was collimated by stops E_1, E_2 (fig. 2). The annular stop E_2 was held at a negative potential of — 900 V, while

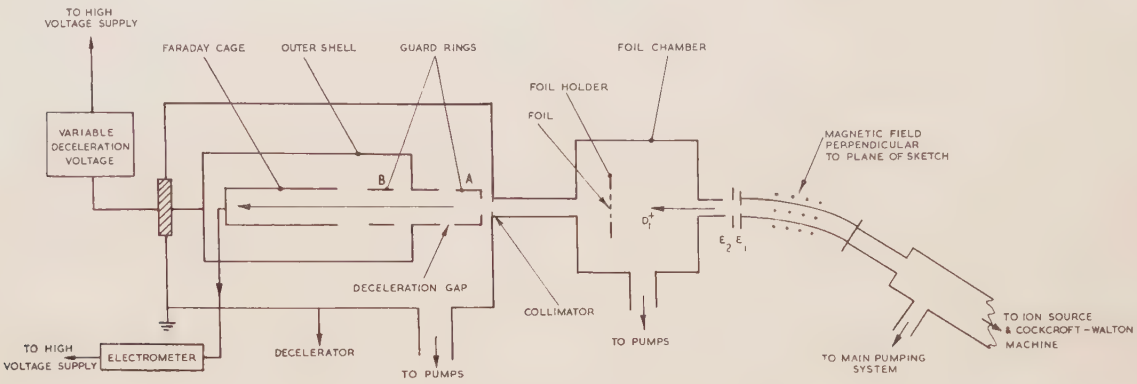

Fig. 2. Schematic layout of energy loss apparatus.

2. Measurement of the Rate of Energy Loss of Deuterons in Titanium Hydride Foils

Because of the uncertainty in the above energy loss data, it was judged necessary to carry out some direct energy loss measurements in some self-supporting titanium hydride foils. The method adopted was similar to that used by Phillips in his measurements on the energy loss of protons in gases[8]. A conventional Cockcroft-Walton machine fitted with an r.f. ion source was used to provide deuterons in the energy range of 40–150 keV. The ion beam from the accelerator tube was deflected by means of an electromagnet (fig. 2) in order to separate beams of different "e/m". A plot of the square of the magnet current at each peak of the spectrum against the appropriate "e/m" yields the straight line shown in fig. 3. The magnet current was calibrated against "e/m" by the usual flip-coil method, and this was checked accurately at a few points by proton resonance. The contamination of the D_1^+ beam with H_2^+ was roughly estimated by two methods:

(a) By chemical analysis of the deuterium gas;

(b) By measuring the relative intensities of the three beams H_1^+; D_1^+, H_2^+; and D_2^+.

the stop E_1 was left at earth potential. The ion energy was determined by measuring the voltage of the set with a calibrated micro-ammeter and a calibrated oil immersed resistance column of 2.28×10^9 ohms. The probable error in the mean energy was ≈ 3%. The pressure in the main accelerator tube was usually about 5×10^{-6} mm Hg, and at the detector end, $1\text{–}5 \times 10^{-5}$ mm Hg.

To measure the energy lost in a foil of titanium hydride, due to excitation, ionisation and charge exchange (but excluding that due to nuclear scattering), a decelerator similar to that used by Phillips[8] was placed beyond stops

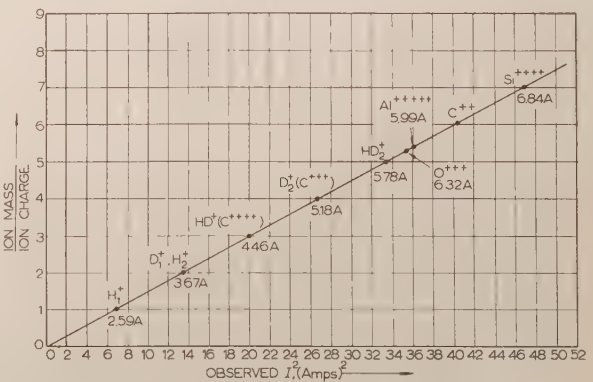

Fig. 3. Magnet calibration at 89 keV.

E_1, E_2 (fig. 2). This measured the deceleration voltage required to just bring the ions to rest. A guard ring A at — 300 V prevented secondary electrons from entering the deceleration gap (acceleration for electrons). The beam current (10^{-9}–10^{-10} A) was collected by a Faraday cage

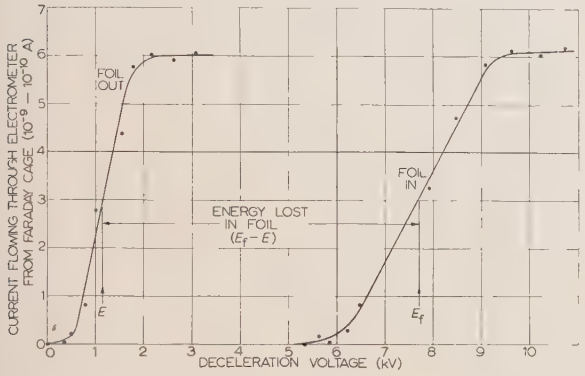

Fig. 4. Typical deceleration curves.

inside the high voltage terminal, and was measured by an electrometer. Another guard ring B, at — 300 V with respect to the Faraday cage, prevented secondaries from escaping from the Faraday cage. The outer shell was kept at about + 2000 V with respect to the Faraday cage so that any ions getting past the deceleration gap were all drawn into the Faraday cage and measured. A remotely controlled power supply at high voltage potential could vary the voltage applied across the deceleration gap. The type of plot obtained for collected beam current versus deceleration voltage is shown in fig. 4.

The energy loss in a foil of thickness x mg/cm² for each energy value $(E + E_f)/2$ is given by $E_f - E$. The inherent energy spread in the incident beam, obtained by plotting the "foil-out" deceleration curve, was usually about 2 keV. It was found to be impossible to extend the measurements below 40 keV, since (a) the energy loss (5–10 keV) in the foils became too large in proportion to the incident energy E (i.e. self-supporting foils could not be made thin enough), and (b) at less than 40 keV energy, increased scattering made it necessary to use much larger beam currents than were needed at high energies, and these larger beams tended to destroy the foils.

Self-supporting titanium hydride foils ranging in thickness from 15 to 50 μg/cm² were used. The foil thickness was estimated by weight and area determination, but even though the titanium film was always first exposed to an atmosphere of pure hydrogen after evaporation, it was very likely that a large fraction of the resultant foil material was titanium oxide. During each energy loss measurement, it was found essential to surround the foils with a surface cooled with liquid nitrogen, and also to use a subsidiary pumping system in the region of the foils. If these precautions were not taken, the energy loss $E_f - E$ was found to increase significantly after a few minutes exposure to the beam: this was probably caused by carbon deposition on the foil.

To check the accuracy of these energy loss measurements, gold and aluminium foils were examined for comparison with other figures available in the literature at about 100 keV. Within the accuracy of the experiment ($\approx 10\%$) the energy loss values obtained for 100 keV deuterons in aluminium and gold agreed with those published in Allison and Warshaw's review[5].

The measured figures for $d\varepsilon/dx$ in titanium hydride are quoted in table 1. These figures have been obtained by averaging the results for several foils of differing thicknesses. A comparison with the estimated figures for $TiT_{1.5}$ shows that the method of extrapolation and interpolation used in obtaining these $TiT_{1.5}$ figures was not greatly in error. Because of the uncertainty in the composition of the titanium hydride foils, it was decided that to seek an improvement in the accuracy of the measurements would not be worthwhile.

B. ASSESSMENT OF TITANIUM TRITIDE TARGETS

1. Apparatus and Method

A comparison with expected neutron yield can best be carried out by bombarding each target with a steady, collimated beam of magnetically analysed D_1^+ or D_2^+ ions of well defined energy (such as from a Cockcroft-Walton machine). If the incident angle which the ion beam makes with the target surface is varied, then the path length of the ions through any surface contamination layer will vary accordingly. This alters the effective incident ion energy by virtue of the energy lost in the contamination. Since the yield curve in fig. 1 is a very steep function of energy at low energies, it follows that varying the angle of incidence of the ion beam should provide a sensitive means of estimating surface contamination thickness. Actually this technique proved to be sufficiently sensitive to estimate variations in the tritium concentration in the bulk of the titanium tritide underneath the surface contamination layer.

The apparatus consisted of a Cockroft-Walton assembly similar to that described in Section A. Similar stops E_1, E_2 were used: the opening in E_2 being larger than that in E_1, so that none of the direct ion beam could strike the edges of E_2. In this way, electrons coming down the accelerator tube (e.g. secondaries from the unfocused beams striking the magnet tube), and secondary electrons produced in the target chamber beyond E_1, E_2 (see fig. 5) were not able to affect the measurements of the incident ion current entering the target chamber.

In this diagram, the ion beam is shown

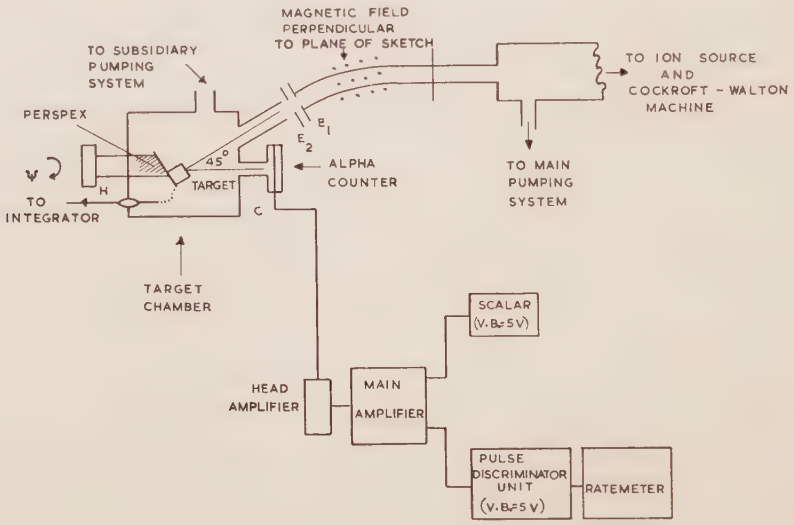

Fig. 5. Schematic layout of apparatus for target assessment.

striking the target at normal incidence. The target can, however, be rotated by turning handle H through angle ψ, and the angle θ which the beam makes with the normal to the target surface is then given by

$$2\cos\theta = 1 + \cos\psi\,.$$

The angle θ could be measured and reproduced to an accuracy of about $\frac{1}{2}°$. As the target is turned, the current distribution on the target surface will change as a result of the ion beam spot changing from circular to elliptical. However, provided none of the beam ever misses the titanium tritide surface on the target, and provided carbon deposition on the target surface is negligible, the shape of the ion beam spot is unimportant, since:

(a) The total current collected remains constant;

(b) The alpha counter window at C sees all of the target at all θ;

(c) The angle between the alpha counter axis and the ion beam direction remains constant at 45° for all θ.

The most reliable method of measuring the number of neutrons/sec produced in a titanium tritide target by the $H^3(d,n)He^4$ reaction, is to measure the number of alpha particles/sec entering a known solid angle and to convert this to neutrons/sec by means of the usual method (see ref. [12]). This alpha count rate was measured here by means of an argon flow proportional counter (fig. 5) whose mica window (≈ 1 mg/cm^2) sub-tended a solid angle of 2.44×10^{-4} steradians at the target. All the alpha particles had sufficient energy to penetrate through to the far side of the counter. The alpha count rate was usually about 200/sec and the background not more than 1/min. The charge collected by the target during a counting interval was measured by a current integrator, so that ion beam fluctuations during an alpha count were unimportant.

To prevent carbon deposition on the target surface from the ion beam, it was found necessary to connect a subsidiary pumping system direct to the target chamber, to cool the target chamber walls with liquid nitrogen, and to use a palladium leak for the ion source gas input. Heating the target to just below the dissociation temperature 230° C of titanium tritide was also tried, but was found to be unnecessary, since the preferential deposition of the carbon in the beam on to the cooled target chamber walls prevented any carbon becoming detectable on the unheated target surface until more than about 3000 μcoulombs of D_1^+ had been collected. This figure could, however, be as low as 500 μcoulombs if the beam strength were allowed to rise above about 5 μA; hence, when examining a target, the precaution was always taken of keeping the beam strength at about 2 μA and of exposing the target to this 2 μA for the minimum time necessary to get sufficient alpha count accuracy.

If we assume that the tritium distribution inside the titanium tritide is a step function (i.e. is zero concentration up to a depth d, and thereafter is finite and constant, such that the average number of tritium atoms/titanium atom over both the surface layer and the titanium tritide is 1.5), then there are two methods we may use for calculating d from the values of the neutrons/μcoulomb of deuterons, n_0, n_{ψ_1}, n_{ψ_2}, n_{ψ_3}, measured at different angles 0°, ψ_1, ψ_2, ψ_3.

Let $\rho_1 = 5$ g/cm^3 be the density of the titanium oxide contamination layer, and ρ_2 the density of titanium tritide.

Let E be the deuteron energy at the target surface, E_0 be the deuteron energy for normal incidence at the bottom of the surface layer (i.e. just before entering the titanium tritide), E_1 the same for an angle of incidence θ_1, etc.

(a) Evaluation of d by direct comparison of neutron yields at normal incidence, yielding d_N:

The observed neutrons/μcoulomb at $\psi = 0°$ will be less than it would be if $d = 0$. The difference between E and the energy E_0 (read from fig. 1) which would give the observed neutron yield, therefore is the energy lost in the contamination layer. If we assume that the figures in table 1 for $(d\varepsilon/dx)_{TiT_{1.5}}$ will suffice for this contamination layer too, we can then estimate d_N.

(b) Evaluation of d by variation of incident angle, yielding d_θ:

As ψ is increased from 0° to ψ_1, the deuterons have to go through an additional path length Δd in the surface layer, where

$$\Delta d = (\sec\theta_1 - 1)\, d\,, \quad 2\cos\theta_1 = 1 + \cos\psi_1\,.$$

By again using the calculated yield curve in fig. 1. for $TiT_{1.5}$, the value of the energy E_1 corresponding to the observed neutron yield n_{ψ_1} is obtained. The additional energy lost by the deuterons in the surface layer due to increasing the angle ψ from 0° to ψ_1 is therefore $E_0 - E_1$. We can then estimate d_θ from

$$\int_{E_0}^{E_1} \rho_2 \frac{dx}{d\varepsilon}\, d\varepsilon = \rho_1 (\sec\theta_1 - 1)\, d_\theta\,.$$

This can be repeated for other angles ψ_2, ψ_3 and the values obtained for d_θ should all be identical.

It should be emphasised that, whereas the

[12]) Benveniste and Zenger, UCRL 4266 (1954).

value of d_N is based on a single reading (viz. at $\psi = 0°$) of the neutron/μcoulomb, and depends sensitively on the absolute energy E, the value of d_θ, in contrast, is evaluated from the slope of the curve of observed neutrons/μcoulomb against ψ. The value of d_θ is therefore more reliable, and should be affected to a lesser extent by any error in the absolute value of E or by any uncertainty in the calculated yield curve for $TiT_{1.5}$.

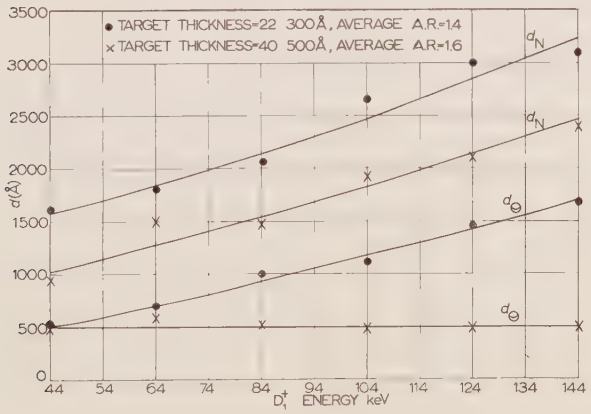

Fig. 6.
Dependence of contamination thickness on D_1^+ energy.

2. Interpretation of Results

Values of d_N and d_θ against E for a typical target are plotted in fig. 6. About one dozen titanium tritide targets, of thicknesses ranging between 10 000 Å and 25 000 Å, but manufactured under differing conditions, were examined by this technique. All the experimental data cannot be included here, but table 2 gives one typical set of readings. Also examined was a target of much greater thickness, 40 500 Å. The values obtained for d_N, d_θ for this target are also given in fig. 6.

From fig. 6, we see that for a thin target, $d_N >> d_\theta$, and both d_N and d_θ increase with E. On a much thicker target, the dependence of d_θ on E disappears. Ideally, we should expect d_θ and d_N to be equal and both independent of E. The above effects can, however, be explained qualitatively by the inadequacy of the assumption that the concentration of tritium is constant within the titanium tritide underneath the surface contamination layer.

Let us suppose that the actual tritium concentration follows a curve such as that shown in fig. 7.

When the beam is made to strike the target oblique, the neutron yield will become greater due to failure of the deuterons to reach the lower region of the target where the tritium concentration is small, and hence the difference between neutron yield at 0^0 and at θ is less than it would be if the tritium concentration were uniform below the surface layer. At a given energy this leads to a value of d_θ which should be less than the value of d_N, which is what has been observed.

Moreover, at normal incidence, the further the deuterons penetrate into the lower regions of the target where the tritium concentration is small, the smaller is the neutron yield. Thus the estimated d_N should rise with energy, and this should hold for d_θ too, but to a lesser extent. Such a dependence on energy should disappear if the target is made so thick that the deuterons cannot reach this lower concentration region. Again, this is what has been observed.

To obtain an exact measurement of the distribution of tritium inside the target material, one should ideally first guess a plausible tritium distribution curve (such as in fig. 7), divide it up into a large number of regions of effectively constant tritium concentration, and, by using the yield curves of Saker and Wood[11] for targets of tritium atomic ratio between 0.2 and 2.3, calculate the expected variation of neutron yield with E and θ. Comparison with experiment should then tell one whether the chosen distribution is correct.

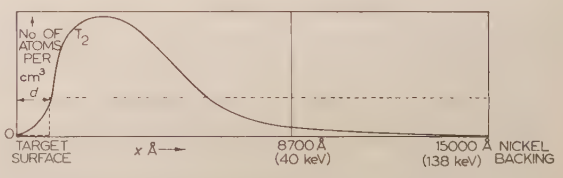

Fig. 7. Distribution of tritium inside target.

This was too tedious to carry out precisely, but one target was studied roughly by this procedure, and the tritium distribution curve in

TABLE 2

Neutron yield readings for a typical TiT target
(target thickness = 22 300 Å, Average A.R. = 1.4)

E (keV)	$\psi°$	μcoulombs of D_1^+	α's/μcoulombs	Average neutrons/μcoulomb	Expected neutrons/ μcoulomb if $d = 0$
44	0	184.6	7.62	4.61×10^5	4.51×10^6
	45	217.8	6.54	4.03×10^5	4.51×10^6
	— 45	194.7	6.97		
	— 60	195.1	6.24	3.70×10^5	4.51×10^6
	60	178.0	6.16		
	75	224.0	5.93	$3.60_5 \times 10^5$	4.51×10^6
	— 75	246.8	6.16		
	0	181.7	7.84		
64	0	184.4	44.8	2.71×10^6	1.71×10^7
	45	160.6	40.1	$2.39_5 \times 10^6$	1.71×10^7
	— 45	163.7	39.0		
	— 60	167.9	34.2	$2.10_5 \times 10^6$	1.71×10^7
	60	165.6	35.5		
	75	166.8	30.3	$1.79_5 \times 10^6$	1.71×10^7
	— 75	147.4	28.9		
	0	165.1	44.75		
84	0	76.4	143.8	8.73×10^6	4.00×10^7
	45	79.9	114.0	7.06×10^6	4.00×10^7
	— 45	78.6	114.3		
	— 60	70.5	107.0	6.56×10^6	4.00×10^7
	60	72.9	105.2		
	75	71.6	94.7	5.86×10^6	4.00×10^7
	— 75	78.1	94.8		
	0	73.4	138.5		
104	0	80.2	276.2	1.74×10^7	7.01×10^7
	45	61.7	246.0	1.54×10^7	7.01×10^7
	— 45	63.4	248.1		
	— 60	60.4	233.2	1.41×10^7	7.01×10^7
	60	61.7	218.5		
	75	61.6	188.0	1.20×10^7	7.01×10^7
	— 75	62.4	197.0		
	0	56.3	281.0		
124	0	31.65	537.0	$3.41_5 \times 10^7$	1.01×10^8
	45	31.45	487.0		
	— 45	31.15	478.0		
	— 60	31.65	450.0	$2.91_5 \times 10^7$	1.01×10^8
	60	31.75	473.0		
	75	31.75	364.0	$2.33_5 \times 10^7$	1.01×10^8
	— 75	30.60	376.1		
	0	31.20	546.0		
144	0	19.85	876.0	5.73×10^7	1.27×10^8
	45	19.80	794.0	5.08×10^7	1.27×10^8
	— 45	20.06	805.0		
	— 60	20.60	735.0	$4.61_5 \times 10^7$	1.27×10^8
	60	20.06	717.0		
	75	19.85	616.0	$3.96_5 \times 10^7$	1.27×10^8
	— 75	20.91	630.0		
	0	20.13	925.0		

fig. 7 was the result. Such a curve gave approximately the observed dependence of yield on E and θ, but the observed absolute yields were all a little lower than those calculated. The shape of the distribution is, however, substantially correct.

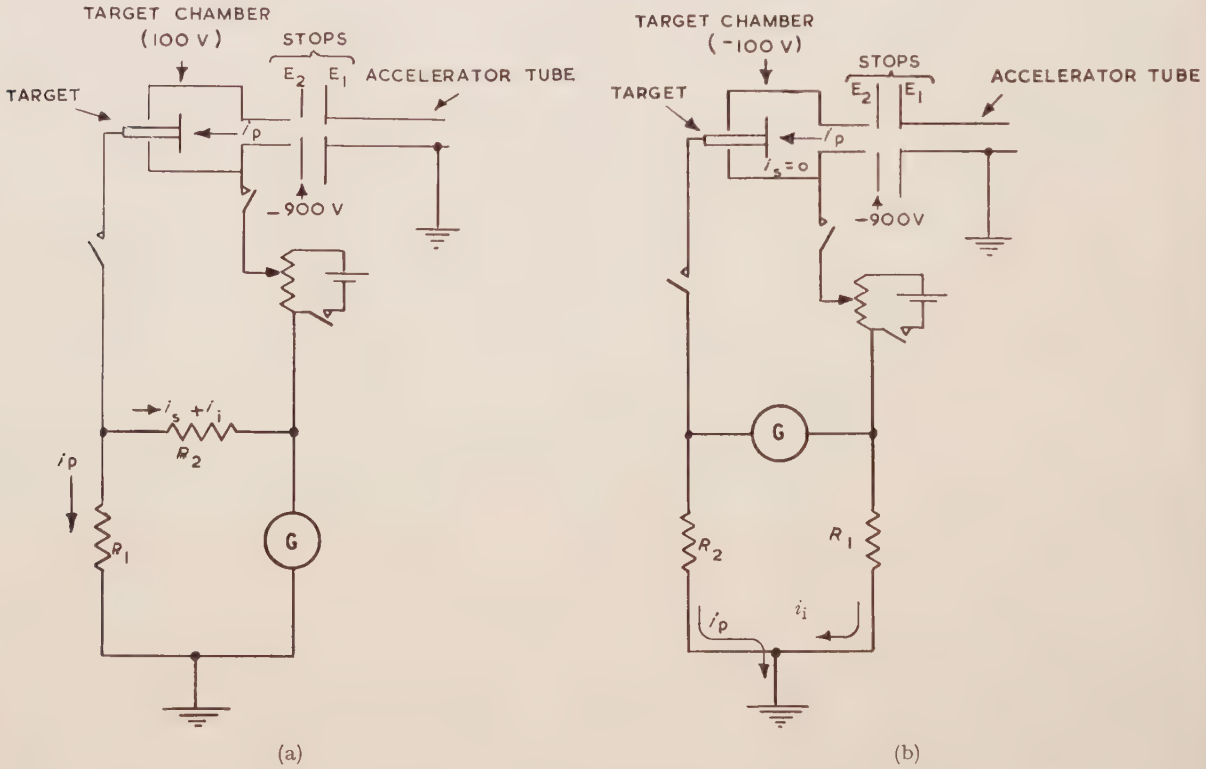

Fig. 8. (a) Bridge circuit for measuring secondary electron ratio (δ). (b) Bridge circuit for measuring i_i/i_p.

The main results of this assessment are that, in a 15 000 Å target, about the last 6 000 Å next to the backing of nickel contains very little tritium. This is supported by the method of manufacture, since the first layers of titanium vapour condensed on the nickel backing during the evaporation process are probably relatively full of gaseous "poisons" from clean-up of the evaporation vessel. Another observation is that the peak of the curve does lie a little above the atomic ratio 2.0. This means that some tritium must be in interstitial lattice positions. Again, this result is supported by the fact that in the manufacture of some targets, the titanium takes up more tritium than could go into the compound $TiT_{2.0}$. It was usual in a 15 000 Å target to observe a contamination surface layer 500–1000 Å thick, and it was found that the cleanliness and vacuum in the tritation apparatus, and the time that the target was subsequently exposed to air, greatly affected this layer thickness. A detailed account of the method of manufacture of the targets used in this investigation has been published by Cole[13].

A subsidiary, but important result of this investigation is that if higher DT neutron yields are desired (e.g. for radiation damage work), it is far better to concentrate first on maintaining a clean target surface with as much tritium as possible in the surface layers, before trying to increase the yield by increasing the incident deuteron beam. Very often, high currents give very little increase in neutron output because the target surface becomes contaminated, and the high wattage drives off a good

[13]) Cole, S.E.R.L., Baldock. Tech. Memo. No. 355 (1957).

deal of the surface tritium. If the above precautions in maintaining clean targets are observed (and this should not be difficult with a large area, cooled, rotating drum target of atomic ratio 1.6 and thickness 50 000 Å), then it should be possible to construct a relatively small and inexpensive mono-energetic fast neutron facility —small compared to a reactor. For example, under the above conditions, a beam consisting of 1 mA of D_1^+ and 1 mA of D_2^+ at 125 keV should yield a steady output slightly in excess of 10^{11} DT neutrons/sec. The wattage dissipated on the type of rotating target described above would not exceed 4 watts/cm², and this should not produce any appreciable target deterioration. The Arkansas neutron facility[14] uses a stationary target with a wattage dissipation of some hundreds of watts/cm², and yet is able to maintain a steady yield of 4×10^{10} DT neutrons/sec for long periods.

If ion currents of about 10 mA are available, and provided the clean target surface is preserved by the above recommendations with a large area rotating target, then by using a high current 125 kV power pack, it seems feasible that a facility capable of producing a steady yield of 10^{12} DT neutrons/sec could be built. It should be emphasised, however, that a Cockroft-Walton machine (which is a complex and precise instrument designed for nuclear and atomic measurements) is not suitable if such yields are required for long periods. As can be observed in fig. 1, using energies above 125 keV gives very little increase in neutron output, and merely increases the wattage dissipated in the target.

Acknowledgements

We should like to thank the techniques group in S.S.N.R. at A.W.R.E. for producing the foils used in the energy loss meaurements, and S.E.R.L., Baldock for supplying the titanium tritide targets. In particular, we should like to acknowledge the assistance of Dr. E. W. Saker and Mr. J. D. L. H. Wood, S.E.R.L., Baldock, for making available the results of their yield calculations, and also the helpful discussions with Mr. P. O. Hawkins, S.E.R.L., Baldock, who initiated the work in the first place. We are grateful to the Director of A.W.R.E. for permission to publish.

[14]) Bronner, Ehlers, Eukel, Gordon, Marker, Voelker and Fink, Nucleonics **17** (1959) 94.

Appendix

SECONDARY ELECTRON EMISSION FROM TITANIUM HYDRIDE

The apparatus used for the assessment of the tritium targets was modified and used to determine the secondary electron emission coefficients δ of some titanium hydride targets. The target chamber was used as the secondary electron collector by insulating it from the accelerator tube and by making it 100 V positive with

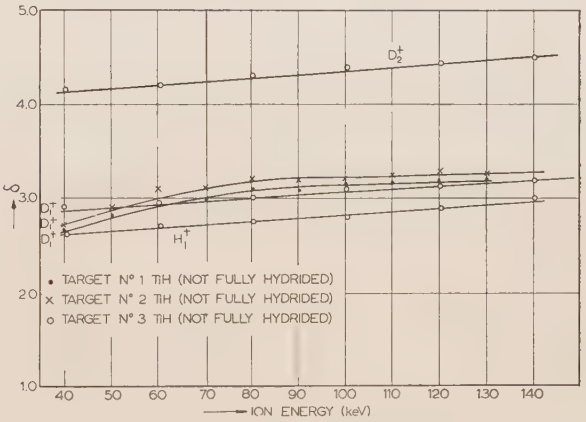

Fig. 9. Equilibrium values of δ at 5×10^{-5} mm Hg.

respect to the target. This 100 V was found to be adequate to collect all secondary electrons emitted from the target. By means of the bridge circuit in fig. 8(a), it was possible to measure the incident ion current i_p and the resultant secondary electron current i_s separately. If R_1 and R_2 in this bridge are adjusted to give a null deflection on galvanometer G, then

$$\delta = i_s/i_p = R_1/R_2 - i_i/i_p ,$$

where i_i is the current arising from ionisation of the residual gas in the target chamber. An advantage of this bridge method is that the balance point remains steady during any fluctuations in the beam. In fact, testing to see

that this balance does not alter with i_p provides a check on whether any spurious currents are being included in the measurements (e.g. leakage currents across insulators, or secondaries getting past E_2, etc.).

In order to determine the value of i_i/i_p, another bridge circuit was arranged (fig. 8(b)) in which the target chamber was made 100 V negative with respect to the target. In this way, secondary electrons from the target were repelled by the target chamber walls, so that $i_s = 0$. At balance,

$$(i_p - i_i)\, R_2 = i_i R_1 .$$

Actually, i_i/i_p turned out to be negligibly small (< 0.02) when the target chamber vacuum was better than about 1×10^{-4} mm Hg. However, at higher pressures, anomalously large values of δ will be obtained unless this correction for i_i is made.

As expected, the state of cleanliness of the titanium tritide surface was found to affect δ. If the target had previously been exposed to the atmosphere for several days, the δ measured immediately after pumping down below 5×10^{-5} mm Hg was appreciably higher than the true value. Only after hours of pumping did the measured δ settle down to a steady equilibrium value. Where the target had been stored under vacuum, the equilibrium value of δ was obtained almost immediately after pumping down in the target chamber. The values of δ presented in fig. 9 are the lowest equilibrium values obtained after hours of pumping.

NUCLEAR INSTRUMENTS AND METHODS 8 (1960) 185–194; NORTH-HOLLAND PUBLISHING CO.

APPAREIL AUTOMATIQUE POUR LA MESURE DES GRADIENTS LOCAUX DU FLUX DE NEUTRONS DANS UN REACTEUR

P. MULOT, R. POUSSOT, A. P. SCHMITT et C. P. ZALESKI

Groupe d'Etude de Piles Rapides, Département de Recherche Physique, Commissariat à l'Energie Atomique, C.E.N., Saclay, Gif-sur-Yvette (S & O)

Reçu le 9 janvier 1960

An apparatus designed to measure strong gradients of neutron fluxes as may occur in nuclear reactors is described. Strips of material to be activated are exposed to the neutron flux and the induced beta activity is measured as function of position.

Sections 2 and 3 describe the electronic and mechanical parts of the apparatus. Performance data are presented in section 4; sample data are shown in section 5.

1. Principes Généraux

La mesure de la distribution spatiale du flux des neutrons dans une pile est directement liée à la détermination de certains de ses paramètres physiques et aux études relevant de son exploitation.

En particulier, l'étude de cette distribution au niveau de certaines solutions de continuité s'est révélée intéressante pour évaluer par exemple:

les contraintes thermiques dans les éléments combustibles,

le facteur d'utilisation thermique d'un réseau hétérogène,

la déformation de la distribution du flux créé par la présence dans le réseau de corps étrangers (canal d'eau, barres de contrôle, etc.).

La mesure de telles répartitions spatiales de flux doit tenir compte des trois remarques suivantes:

(1) La présence du détecteur de neutrons ne doit pas perturber la distribution à mesurer. La méthode de détection basée sur le principe de l'activation de détecteurs métalliques semble assez bien s'adapter à cette exigence.

(2) Les distributions à mesurer peuvent présenter un gradient assez élevé. Pour les mesurer convenablement, il est nécessaire que la position relative des détecteurs soit aussi précise que possible au moment de l'irradiation. La solution consistant à utiliser un détecteur continu semble séduisante. Il faut alors posséder un appareil de mesure de l'activité de ce détecteur ayant un bon pouvoir de résolution.

(3) Souvent le flux de neutrons disponible pour de telles mesures est relativement faible; d'autre part, pour des facilités de manipulation du détecteur et de son support, il est souhaitable qu'il ne soit pas trop actif. L'appareil de détection doit donc posséder une bonne sensibilité.

L'appareil que nous allons décrire tient compte de ces remarques. Il a été étudié d'abord pour utiliser des détecteurs d'or se présentant sous la forme de bandes de 2/100 ème de mm d'épaisseur, de 6 à 7 mm de largeur et jusqu'à 30 cm de longueur†.

Après irradiation du détecteur dans un flux de neutrons de valeur moyenne convenable, on détermine l'activité relative induite le long de la bande en mesurant point par point le rayonnement β qu'elle émet. L'activité en un point correspond à l'activité moyenne d'une partie de la bande (tranche) définie par un diaphragme rectangulaire lié au système de détection du rayonnement.

Pour réaliser la mesure, la bande et son support sont placés entre deux ensembles scintillateur-photomultiplicateur, dont l'un reçoit le

† Les premières mesures décrites ici à titre d'exemple ont été effectuées avec des bandes d'or. Moyennant certaines modifications possibles du montage actuel, d'autres métaux se laminant correctement peuvent être utilisés comme détecteurs.

rayonnement total $(\beta + \gamma)$ émis par la tranche et le rayonnement du reste de la bande, l'autre ne recevant que le rayonnement γ émis par l'ensemble de la bande, le rayonnement β étant absorbé par un écran convenable.

sation de personnel et les erreurs humaines dans les relevés, cet appareil est conçu de telle sorte que tous réglages préalables étant effectués, la valeur relative de l'activité β d'une tranche à une autre tranche de largeur définie, qui sont

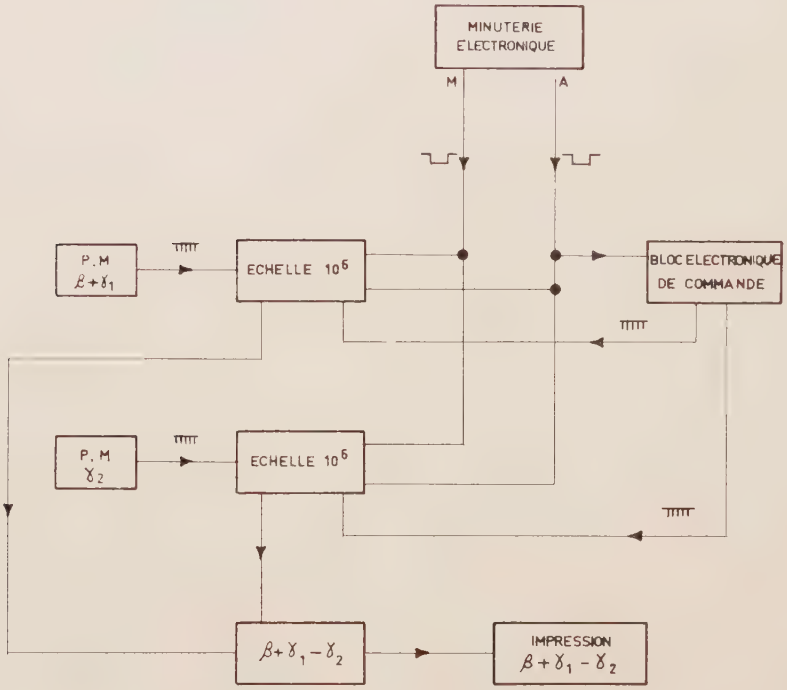

Fig. 1. Bloc diagramme sommaire.

Par soustraction des deux réponses moyennant certains ajustements préalables, nous obtenons le seul rayonnement β émis. Suivant la collimation adoptée, définissant la tranche explorée, le pouvoir de résolution est différent. La collimation réalisée par des diaphragmes interchangeables est rendue nécessaire par le compromis qui se présente entre la quantité de flux de neutrons disponible pour l'irradiation et la sensibilité liée à la résolution de l'appareil de mesure.

L'avancement de la bande irradiée devant les ensembles de détection est réalisée à l'aide d'un système mécanique de pas à pas.

Le critère de précision sur la mesure de l'activité de chaque tranche de la bande explorée conduit, compte tenu de l'irradiation maximum utilisable, à une durée de comptage par tranche souvent assez grande. Pour éviter l'immobilisation séparées par un pas déterminé, s'enregistre automatiquement sur une machine à écrire.

2. Description de la Partie Electronique

2.1. L'ENSEMBLE COMPREND

2 photo-multiplicateurs (PM) DARIO-53AVP, leurs alimentations et leurs préamplificateurs. Ils sont équipés de petits scintillateurs "plastiques" minces pour rayonnement β†.

2 échelles de comptage à grande capacité (10^6) vitesse de comptage 200—250 kHz.

1 groupe électronique de commande.

1 minuterie électronique donnant deux temps préréglés, l'un dit "temps de comptage", l'autre "temps d'arrêt".

1 décodeur électromécanique et une machine à écrire destinée à frapper les résultats.

† L'épaisseur de ces scintillateurs est ajustée sur l'énergie du rayonnement β émis par le détecteur utilisé.

2.2. FONCTIONNEMENT (fig. 1)

Cette partie électronique doit assurer l'automatisme et enregistrer le résultat du comptage $(\beta + \gamma - \gamma)$ correspondant à chaque tranche de la bande irradiée se présentant devant les PM.

Le déroulement des opérations, entièrement pendant tout ce temps. La fin du compte prédéterminé du temps de comptage est commandée par une impulsion de synchronisme délivrée par la minuterie; cette même impulsion déclenche le compte du "temps d'arrêt" et démarre le bloc électronique de commande.

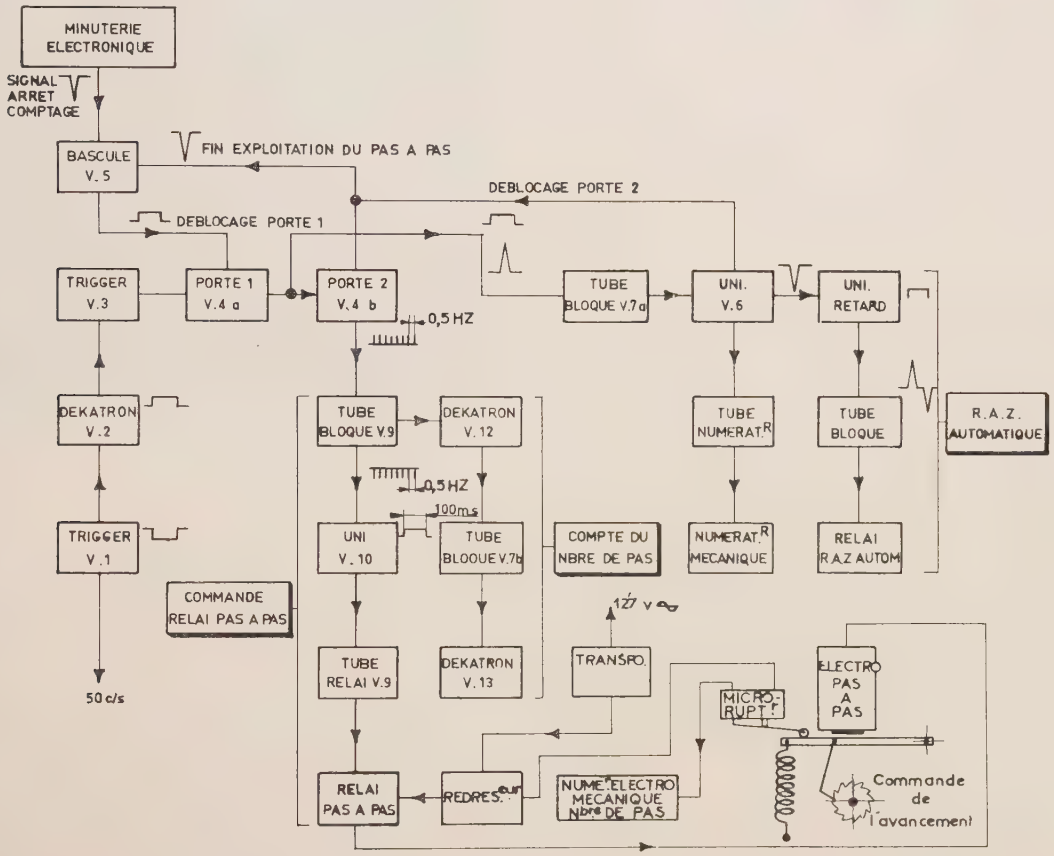

Fig. 2. Bloc diagramme, commande mécanique, compte programme.

automatique, est contrôlée par une minuterie électronique. Sur cette minuterie, deux comptes prédéterminés sont disponibles. Le premier réglant le temps de comptage, le second le temps d'arrêt.

Un oscillateur piloté par quartz sert de base de temps et, convenablement démultiplié, alimente les deux comptes de la minuterie.

Le départ de celle-ci délivre une impulsion dite de synchronisme qui commande le démarrage des échelles de comptage et du compte prédéterminé du "temps de comptage".

Les informations en provenance des deux PM vont s'accumuler sur leur échelle correspondante

Ce bloc a pour fonction:

– avance de la bande irradiée pour la placer dans la position nécessaire au comptage suivant;

– opérer la soustraction d'informations accumulées sur les 2 PM;

– imprimer le résultat de cette soustraction sur une bande de papier.

Il se divise en deux commandes:

(*a*) *Commande mécanique* (fig. 2). Elle comprend:

– l'avance de la bande irradiée par l'intermédiaire d'un pas à pas commandé par des impulsions récurrentes à 0.5 Hz.

– la notation réalisée par V_{12} et V_{13} du nombre de pas effectués pour passer d'une tranche à une autre tranche, deux tranches successives ne pouvant pas être séparées par une distance supérieure à celle correspondant à 40 pas.

– la notation du nombre de mesures effectuées, depuis le début de l'opération affichée sur le numérateur mécanique.

– pour vérification, un numérateur électromécanique affiche le nombre total de pas effectuées depuis le début de l'opération.

– la remise à zéro de l'ensemble du groupe.

(*b*) *Commande soustraction.* Elle comprend:

– l'opération de soustraction elle-même: l'impulsion servant à arrêter le comptage sur les 2 échelles est utilisée pour déclencher cette opération; cette dernière s'effectue par la méthode de complément. On utilise à cet effet des impulsions mises en forme en provenance d'un oscillateur libre (multivibrateur). Elles alimentent simultanément les échelles correspondant aux PM (donnant des réponses $\beta + \gamma$ et γ) par l'intermédiaire d'une entrée auxiliaire. Ces impulsions sont envoyées jusqu'à ce que l'échelle liée au PM γ ait atteint sa capacité maximum; elle affiche alors zéro et le signal épuisement du compte de l'échelle arrête le comptage des impulsions sur les deux échelles. Le nombre d'impulsions indiqué sur l'échelle liée au PM $(\beta + \gamma)$ correspond au résultat de la soustraction désirée.

– le décodeur automatique: le signal d'épuisement du compte de l'échelle γ est également utilisé pour commander le départ du décodeur électromécanique. Ce décodeur analyse alors le compte indiqué par l'échelle liée au PM $(\beta + \gamma)$, décade par décade et actionne le frappe sur la bande de papier.

– une remise à zéro: en fin d'impression, un signal de remise à zéro est appliqué aux deux échelles et l'ensemble complet est prêt à recevoir l'impulsion de synchronisme qui commande le démarrage des échelles de comptage et du compte prédéterminé du "temps de comptage".

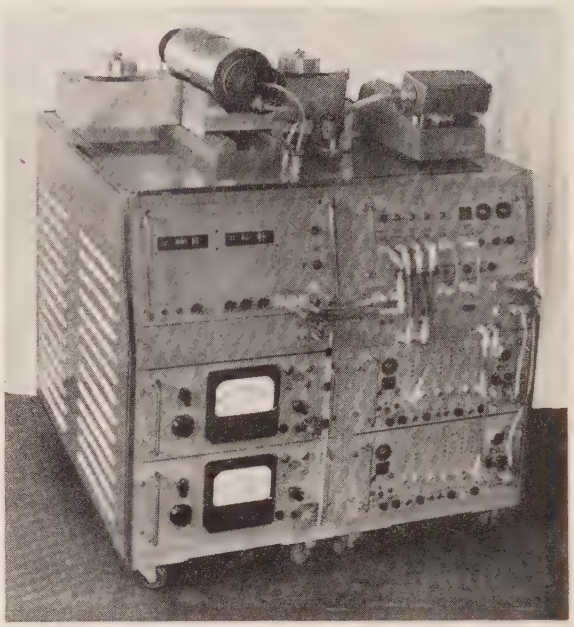

Photo No. 1. Appareil automatique pour la mesure des gradients locaux du flux de neutrons dans un réacteur. Vue d'ensemble.

3. Description de la Partie Mécanique

La valeur de l'installation dépend essentiellement de la précision de tout l'ensemble mécanique.

L'installation se présente sous forme d'un bâti mobile, en deux parties, renfernant les commandes électroniques et électriques et recevant sur son plateau supérieur les ensembles de détection et la machine à écrire qui frappe les résultats (photo No. 1).

Les ensembles de détection se composent essentiellement de deux PM placés dans un blindage cylindrique individuel. Ce blindage contre le rayonnement extérieur est en plomb, chemisé d'aluminium et gainé d'acier inox.

Leur mise en place en profondeur est assuré dans la protection de plomb par un verrouillage lié au bâti.

Les blindages reposent sur des supports en vès. Le PM γ a une position bien définie dans son blindage calé sur son support. Ce dernier comporte tout le dispositif d'avancement du ruban. L'autre PM est placé sur un support se déplaçant sur deux rails (pour des commodités de mise en place de l'ensemble de détection β).

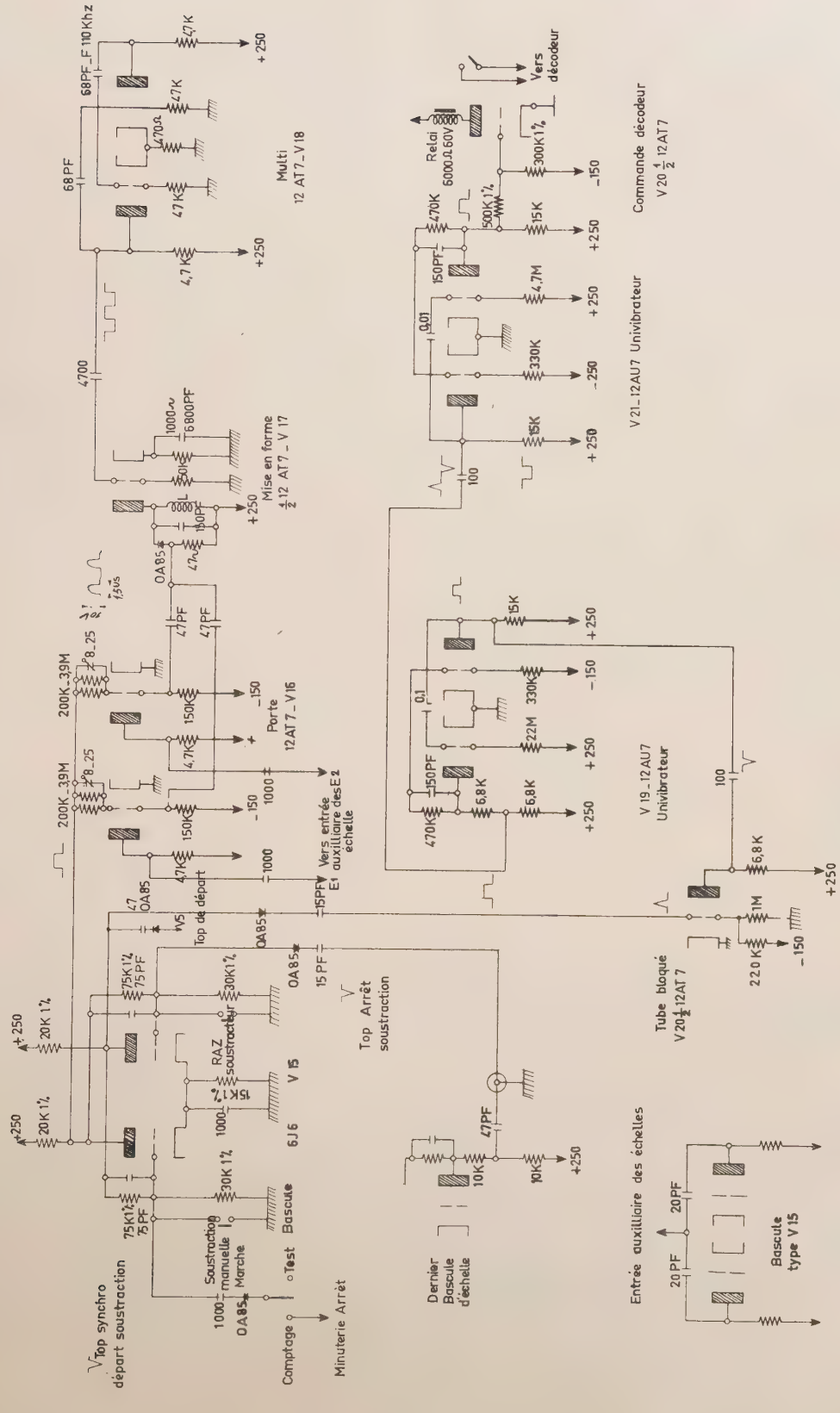

Fig. 3. Commande électronique. Soustraction. Impression des résultats.

La bande métallique irradiée à explorer est collée à l'aide d'un dispositif spécial sur un support de film de cinéma de 35 mm.

3.1. LE SYSTEME DE DETECTION (fig. 3)

Il comprend: scintillateur, porte-scintillateur, guide de film, presse-film, diaphragme, ruban à compter.

Le système actuellement réalisé, utilise des bandes d'or de 2/100 d'épaisseur, de 6 mm de largeur et de longueur maximum 300 mm.

Les dimensions des scintillateurs de forme rectangulaire ont été déterminées pour la configuration utilisée. Ces scintillateurs sont calés dans les porte-scintillateurs et appliqués contre la photo-cathode du PM à l'aide d'un joint optique approprié.

Un fraisage dans le porte-scintillateur γ permet de fixer avec précision le guide de film.

Les diaphragmes en forme de coupelles d'acier inox† sont encastrés dans l'épaisseur du guide et du presseur; ils sont interchangeables et la fenêtre est réalisée en leur centre. Leur mise en place est assurée par fixation à l'aide de deux vis (photo No. 2).

La mise en place du film et le réglage du débit de la bande se font avant la mise en place du PM mobile.

† Des coupelles en or ont été réalisées pour l'utilisation de détecteurs continus de Manganèse.

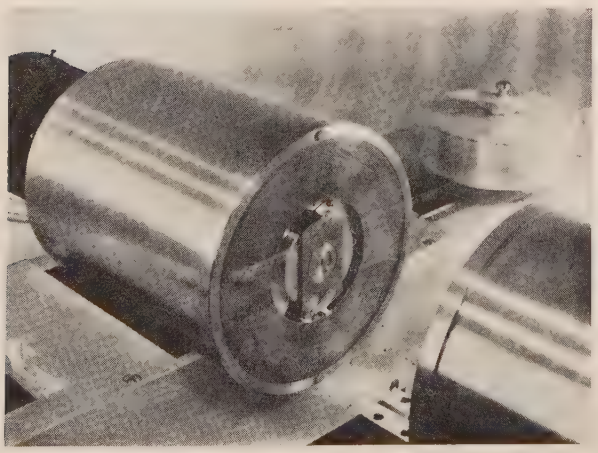

Photo No. 2. Appareil automatique pour la mesure des gradients locaux du flux de neutrons dans un réacteur. Vue du diaphragme β en position.

Au moment du comptage, les deux porte-scintillateurs emboités et le verrouillage assurent:
– un bon parallélisme des scintillateurs
– une distance équivalente du ruban aux scintillateurs
– une distance équivalente du ruban aux diaphragmes.

3.2. LE SYSTEME D'AVANCEMENT

L'ensemble du mécanisme d'avancement est monté sur le support du PM γ.

Une bobine débitrice permet de stocker le film avant la mesure. La position de cette bobine est variable par rapport à l'axe de PM et donne la possibilité de présenter un ruban de longueur 300 mm sur la partie droite du film.

La tension du film et le rattrapage des jeux sont assurés par un ressort en spirale sollicitant la bobine débitrice.

La bobine réceptrice est axée sur une glissière en queue d'aronde commandée par une vis micrométrique permettant d'ajuster le début de bande en fonction du diaphragme utilisé. Un dispositif optique permet de s'assurer de la position de la bande par rapport au diaphragme en début de mesure.

La rotation de cette bobine est obtenue par un système de pas à pas transmettant le mouvement par une démultiplication roue-vis sans fin. Un système de débrayage du pas à pas, permet un facile retour de la bande vers les points déjà mesurés.

Le pas à pas est actionné par un électro-aimant, mais possède également une commande manuelle située dans l'axe de la bobine.

Un numérateur électromécanique enregistre le nombre total de sauts effectués par le pas à pas.

3.3. LE SYSTEME DE COLLAGE

Ce système très simple permet de coller la bande irradiée à explorer suivant l'axe du film avec une précision de $\pm$ 0.2 mm (photo No. 3).

Un fraisage dans une règle en dural permet de guider le film à une extrémité. Dans l'axe de cette fraisure, une réglette reçoit le ruban tenu par un point de colle.

Après encollage de la face externe du ruban,

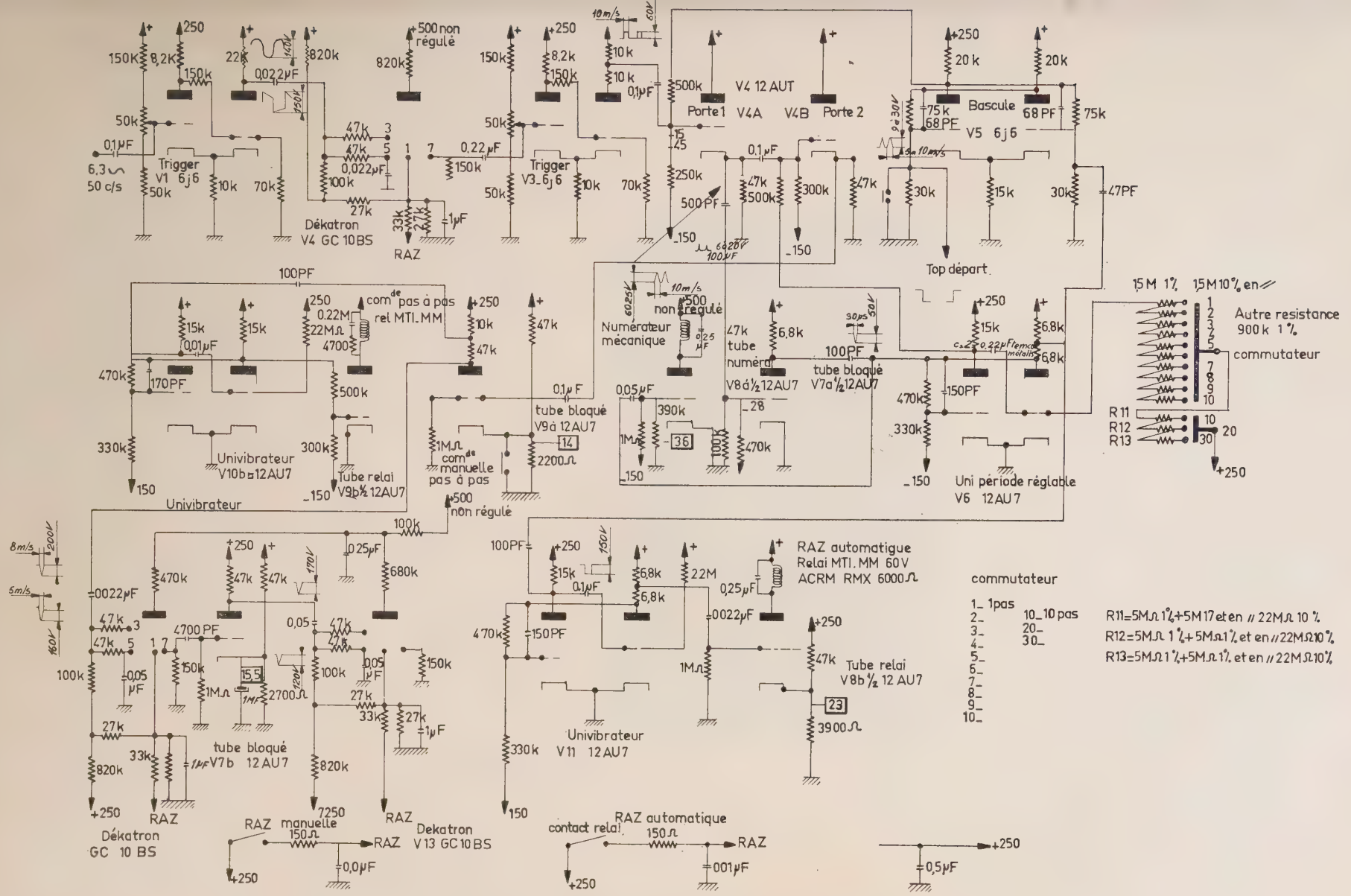

Fig. 4. Commande mécanique, compte programme.

on vient appliquer progressivement le film avec un galet caoutchouté, que précèdent deux roulettes guides de ruban.

3.4. L'ENSEMBLE AINSI REALISE PERMET:

– une bonne symétrie du système de détection,
– une coïncidence des axes des PM
– une distance minimum entre la bande irradiée et les scintillateurs,
– une mise en place rigoureuse et reproductible à chaque mesure,
– un avancement parfaitement déterminé.

les valeurs du seuil de discrimination adoptées ne correspondent pas à des valeurs réelles. A l'indication 0 volt, le bruit de fond est déjà éliminé.

Voies	Haute tension appliquée (V)	Discrimination (V)	Gain du préampli
γ	100	0.17	15
$\beta + \gamma$	1100	0	15

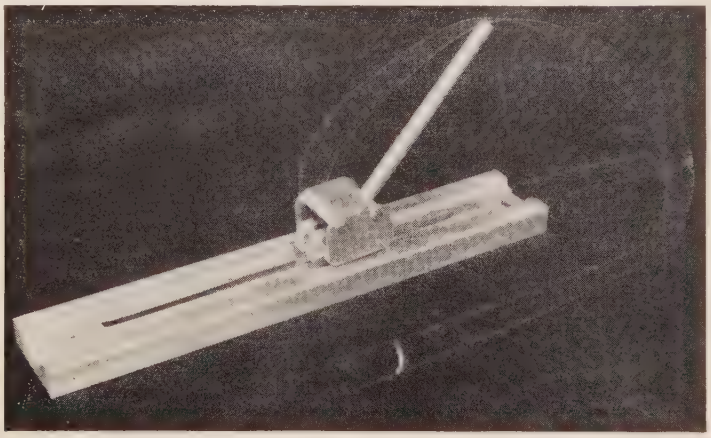

Photo No. 3. Appareil automatique pour la mesure des gradients locaux du flux de neutrons dans un réacteur. Dispositif de collage.

3.5. DEUX DISPOSITIFS SONT PREVUS:

– l'un permettant de changer les caractéristiques de l'inscription sur la machine à écrire au cas où l'exploration du ruban nécessiterait de faire varier la distance qui sépare deux tranches successives mesurées.
– l'autre permettant à l'aide d'une minuterie de couper le circuit d'alimentation au bout d'un temps prédéterminé correspondant au temps nécessaire à l'exploration du ruban.

4. Performances de l'appareil

4.1. CARACTERISTIQUES D'UTILISATION DES ENSEMBLES PHOTOMULTIPLICATEURS-SCINTILLATEURS

Toutes ces caractéristiques doivent être considérées comme nominales et attachées aux appareils actuellement en place. En particulier

Les essais ont porté essentiellement sur:

1. Etalonnage du pas à pas.

2. Résolution de l'appareil avec différents diaphragmes β.

3. Reproductibilité du système de comptage.

4. Compensation des réponses γ des deux voies.

4.2. ETALONNAGE DU PAS A PAS

Le défilement de la bande irradiée devant les ensembles de détection s'effectue à l'aide d'un système de pas à pas.

Les essais réalisés pour déterminer le déplacement de la bande correspondant au passage d'un cran au cran suivant sur le système mécanique ont conduit aux résultats suivants:

No. des essais	Nombre de pas à pas effectués	Longueur de bande débitée (mm)	Valeur sur 1 pas (mm)
1	300	150.7	0.5023
2	300	151.4	0.5046
3	300	150.8	0.5026
4	300	151.0	0.5033
5	300	151.5	0.5050
6	300	151.2	0.5040
7	300	151.2	0.5040
8	300	151.3	0.5040

Nous adopterons comme valeur élémentaire 0.504 ± 0.001 mm.

coupé perpendiculairement à son axe longitudinal et remplacé sur son support de film une des parties irradiée par une bande non active de même matière et de mêmes caractéristiques géométriques que la bande initiale.

(2) Détermination du taux de comptage β en fonction de la position devant le diaphragme de la transition entre la partie active et la partie inactive. L'avancement était réalisé dixième de mm par dixième de mm à l'aide d'une vis micrométrique associée au support en queue d'aronde de la bobine réceptrice.

La figure 4 représente une des courbes obte-

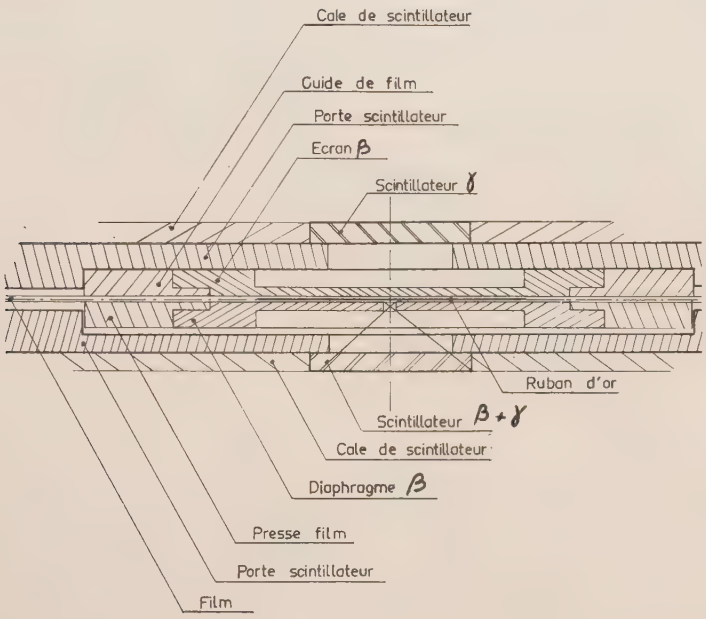

Fig. 5. Système de détection, échelle 4, coupe schématique suivant un plan horizontal dans l'axe des P–M.

4.3. ESSAIS DE RESOLUTION

Ils ont été effectués à l'aide d'une bande d'or irradiée uniformément dans un flux de neutrons de pile.

Une mesure préliminaire réalisée sur le diaphragme de 1 mm nous a permis de déterminer une région de cette bande dans laquelle l'activité induite était constante à 1% près. Cette région a été utilisée de la façon suivante pour étudier le pouvoir de résolution.

(1) Au niveau de la région retenue, nous avons nues. La largeur à mi-hauteur des courbes obtenues par différentiation des précédentes définit la résolution de l'ensemble de détection.

Les résultats sont les suivants:

Diaphragmes (mm)	Résolution mesurée (mm)
0.5	0.5 ± 0.1
1.0	1 ± 0.1
2.0	2 ± 0.1

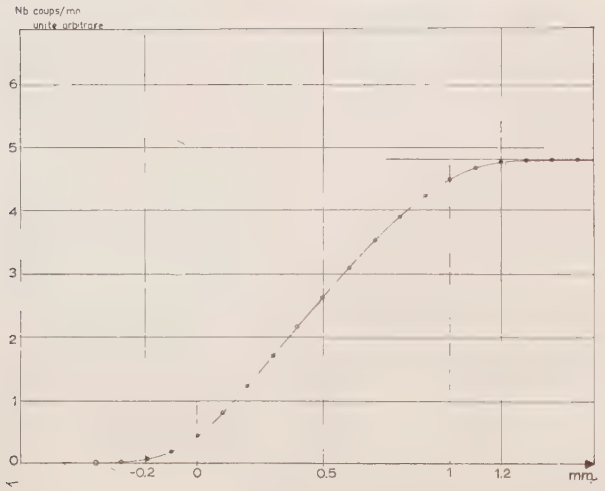

Fig. 6. Pouvoir de résolution, diaphragme de 1 mm.

4.4. ESSAIS DE REPRODUCTIBILITE

Les essais de reproductibilité du système de détection ont été réalisés en analysant la décroissance d'un échantillon d'or irradiée. Pendant une semaine, nous avons effectué chaque jour plusiers comptages sur les deux voies. L'appareil était arrêté le soir et remis en marche chaque matin. Le dépouillement des mesures nous a permis de retrouver à 1% près la période de l'or publiée dans la littérature.

4.5. ESSAIS DE COMPENSATION

Nous appelons compensation le réglage de la haute tension et de la discrimination associées à chaque ensemble de détection de manière à obtenir, dans la géométrie d'utilisation de l'appareil, la même réponse γ sur les deux voies.

Des essais ont été effectués pour vérifier que ce réglage est indépendant:

(1) de la position de la tranche analysée du ruban d'or irradié,

(2) du gradient d'activité au voisinage de la tranche.

† Nous tenons à remercier MM. Vidal et Boyer du Service de la Pile de Fontenay-aux-Roses pour l'aide efficace qu'ils ont bien voulu nous donner dans la réalisation des irradiations nécessaires.

Pour réaliser ces essais, nous avons irradié un ruban d'or sur lequel en trois endroits nous avons placé des petits disques de cadmium pour créer une dépression de flux importante.

Le résultat des mesures fait apparaître une valeur de l'écart des réponses γ des deux voies sans relation apparente avec la position du gradient de l'activité mesurée et toujours inférieure à 1% du taux de comptage β moyen obtenu†.

5. Exemple des Mesures Effectuées

La première application de cet appareil est relative à la mesure du relèvement du flux neutronique créé en intercalant entre deux barreaux d'uranium placés dans une pile un bouchon d'un matériau diffusant tel que magnésium, graphite et aluminium.

Ces mesures, effectuées à Marcoule (Pile G1) puis à Mol (pile EBR-1) (Belgique) ont permis de préciser les gradients axiaux de température dans des éléments combustibles du type G2 [1]).

La figure 7 représente une des courbes expérimentales obtenues au cours d'une expérience sur la pile BR-1 à Mol (Belgique').

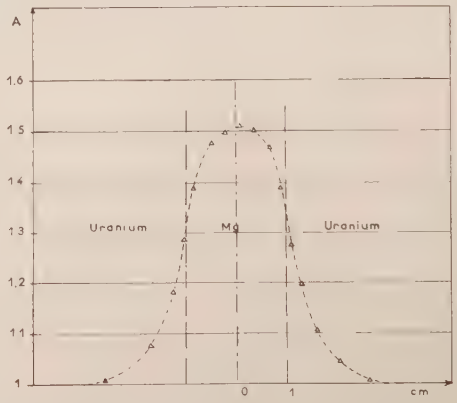

Fig. 7. Relèvement de flux au niveau d'un bouchon de magnésium 20 mm (Mol juillet 1958).

[1]) A. P. Schmitt et A. Teste du Bailler, Note No. 514, SNE/SPM, (12 Nov. 1958).

NUCLEAR INSTRUMENTS AND METHODS 8 (1960) 195–202; NORTH-HOLLAND PUBLISHING CO.

TANDEM ELECTROSTATIC ACCELERATORS

R. J. VAN DE GRAAFF

Massachusetts Institute of Technology

Received 12 August 1959

In this type of accelerator a constant potential is applied to the acceleration of the ion beam, however, not as conventionally with just one voltage application, but instead with a number of applications made in succession by means of a tandem arrangement of high voltage tubes. This number of voltage applications, which is the number of the so-called "stages" of a tandem accelerator, may be two, three, or four, depending on the design chosen. The princjples of this type of accelerator are described, and a brief account is given of the design and performance tests of a two-stage accelerator for an output rating of 10 MeV and one-half microampere of protons. Some possibilities for future development are discussed for reaching greater energies by means of three and four-stage tandem arrangements. Preliminary experimental results show the feasibility of operating these by means of the injection of a beam of neutral particles, thus retaining the use of an external ion source at ground potential, as in the present two-stage tandem accelerators.

1. Introduction

In the case of the usual type of electrostatic accelerator, positive ions are produced inside a high-voltage terminal and then accelerated to ground in one stage of acceleration. In the case of the present type of tandem accelerator, negative ions are produced at ground, and then accelerated to a high-voltage positive terminal. Within the terminal the swiftly moving negative ions are stripped of electrons, thus becoming positive ions, which then receive an additional acceleration from the terminal to ground. Thus the particle beam receives two stages of acceleration instead of one.

The principles and techniques used in tandem accelerators have been originated and developed over many years and in various laboratories. It is regretted that lack of space prevents full acknowledgements here. However, reference should at least be made to the following names:

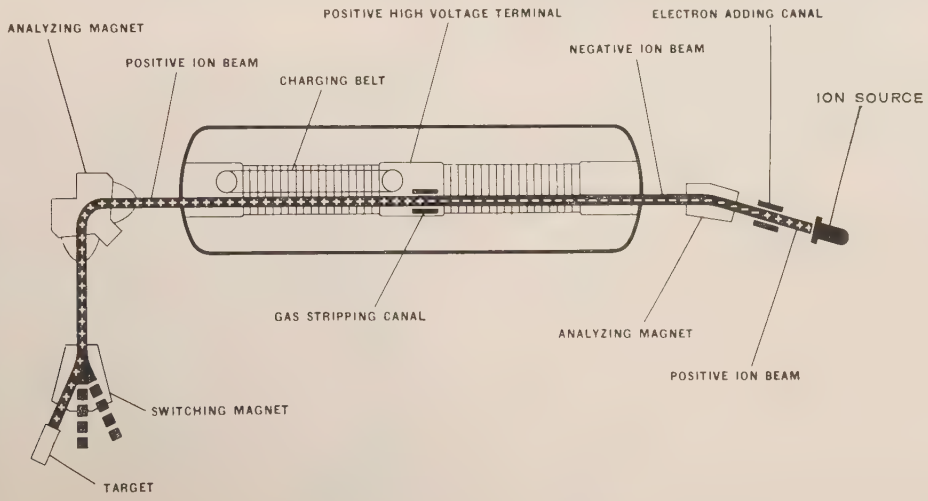

Fig. 1. Two-stage tandem accelerator.

Dempster, Bennett[1]), Kaufman, Alvarez[2]), Marshall, Woodyard, Herb, and Stier.

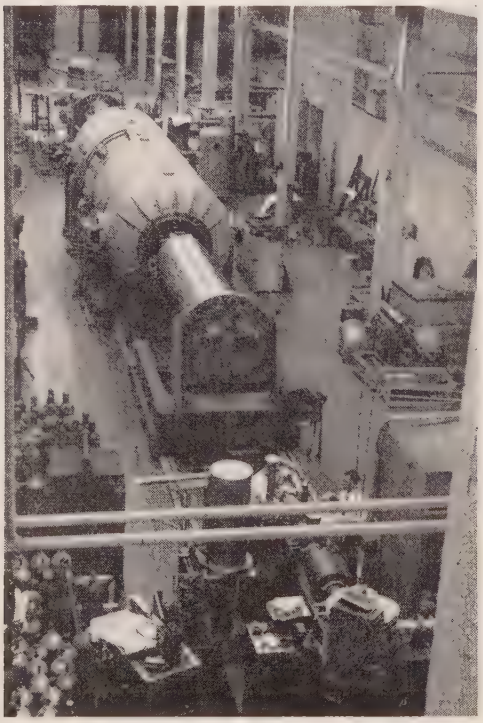

Fig. 2

of its electrons, so that it emerges as a positive-ion beam and is then given its second acceleration which brings it back to ground. The positive-ion beam is then deflected through a 90° analyzing magnet before proceeding through a switching magnet, where it can be directed to any one of three targets.

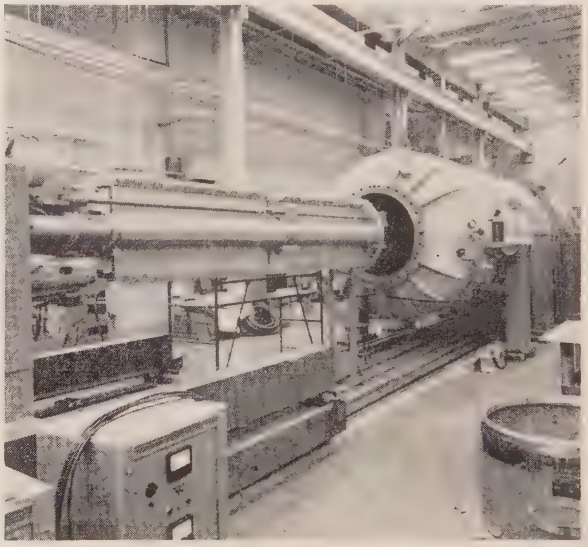

Fig. 3

The principles of operation of a two-stage tandem accelerator may be seen in more detail from the diagram in fig. 1. The positive-ion beam from the ion source at the right passes into the electron adding canal. A flow of hydrogen in this canal causes the successive attachment of two electrons to some of the positive ions, thus transforming these into negative ions. The negative-ion beam is then deflected slightly by an analyzing magnet, so that negative ions of the correct mass and energy are caused to proceed along the axis of the main vacuum tubes, and thus to be accelerated to the terminal which is at a high positive voltage. There the negative-ion beam passes into a second canal, where the presence of gas causes it to be stripped

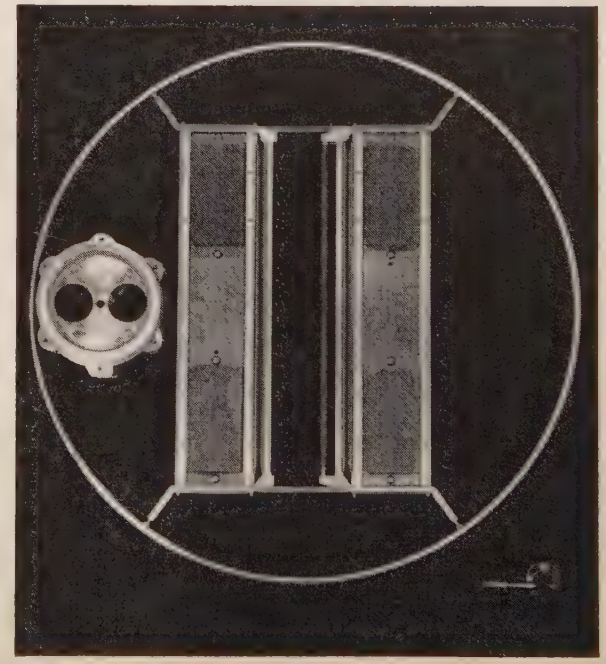

Fig. 4

[1]) W. H. Bennett and P. F. Darby, Phys. Rev. **49** (1936) 97, 422, 881;
W. H. Bennett, U. S. Patent No. 2, 206, 558 (1937);
W. H. Bennett, Rev. Sci. Instr. **24** (1952) 915.

[2]) L. W. Alvarez, Rev. Sci. Instr. **22** (1951) 705.

2. Tandem Accelerator for Chalk River

A two-stage tandem accelerator has been designed and constructed by the High Voltage Engineering Corporation for the Chalk River Laboratory of Atomic Energy of Canada, Limited. After tests in Burlington, it is now in use at Chalk River†. The next three figures are photographs showing the construction of this accelerator.

Fig. 2 shows one column rolled back from its operating position within the tank. Each column has an insulating length of 12 feet, and the tank is 8 feet in diameter and 35 feet long. Fig. 3 is a similar view, but with the equipotential rings removed, so that the acceleration tube and compression members of the column can be seen. Fig. 4 is a photograph of a "cross-section like" assembly of equipotential column parts. The outside ring is 39 inches in diameter. The four glass-block insulators can be seen at

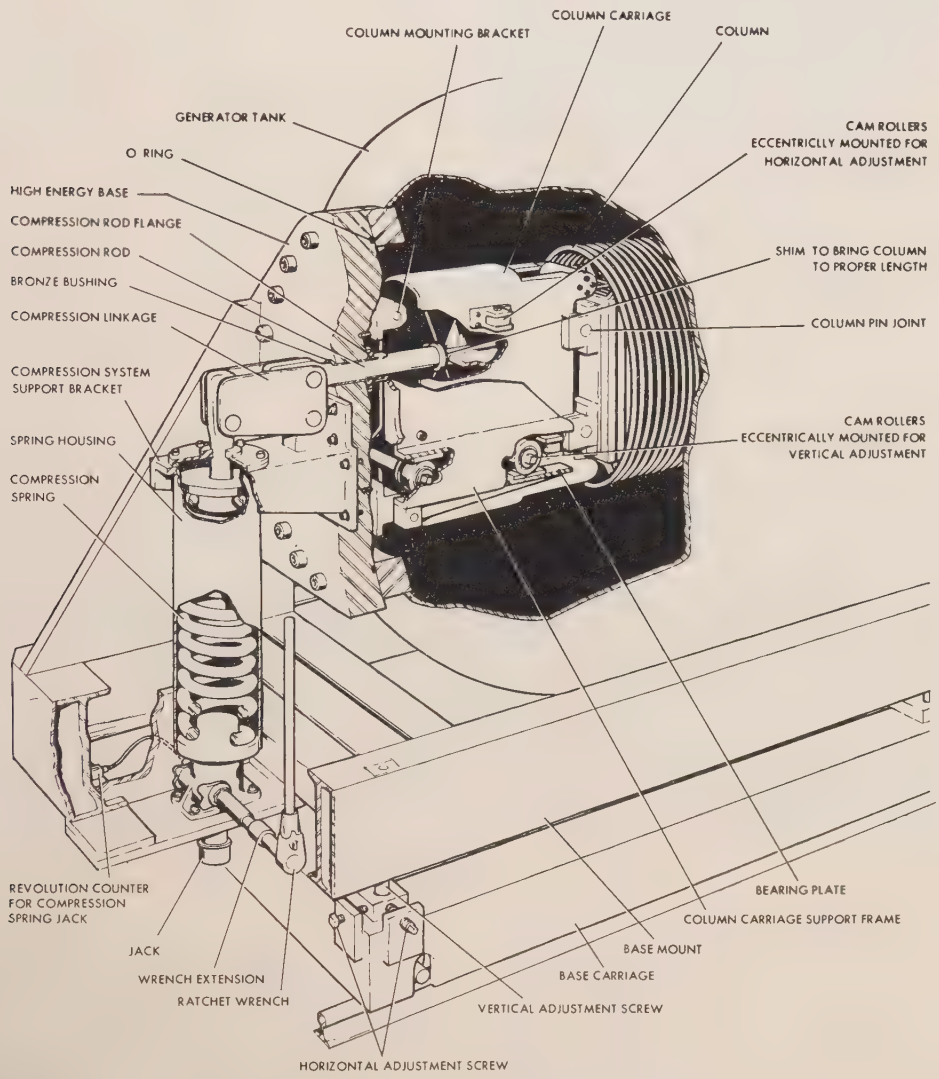

Fig. 5. Column tension adjusting mechanism.

† For additional information regarding this accelerator, reference is made to the following papers: (1) Ten MeV particle accelerator will aid nuclear research at Chalk River, by H. E. Gove, Canadian Electronics Engineering (July 1958). (2) New design makes ten MeV particle accelerator possible, by John L. Danforth, Canadian Electronics Engineering (July 1958).

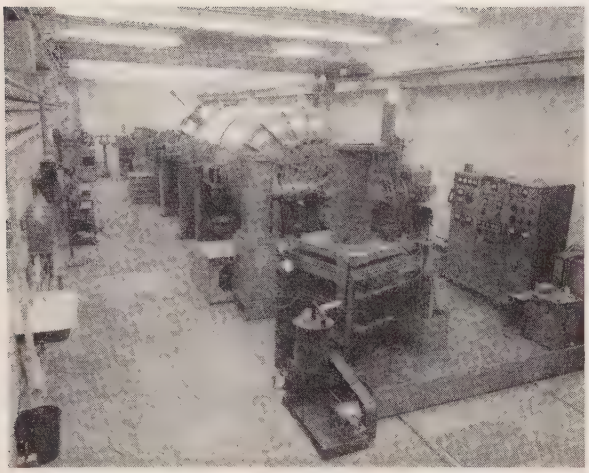

Fig. 6. Tandem accelerator of University of Wisconsin, fully installated. (Reprinted with the kind permission of the University of Wisconsin.)

the corners of the large rectangle. Space for the belt is provided in the vertical region between the four glass insulators. An acceleration-tube electrode is visible at the left.

The drawing in the next figure shows how the column is mounted on the loose plate at the end of the tank. The spring mechanism maintains a compressive force of 40 000 pounds on the ends of the column, which is sufficient to hold all of the glass insulators firmly in compression in spite of the weight of the column.

The low-energy end of the accelerator is shown in fig. 2. The ion source with its radio-frequency power supply can be seen in the mid-foreground, while a high-speed vacuum pumping system appears at the left.

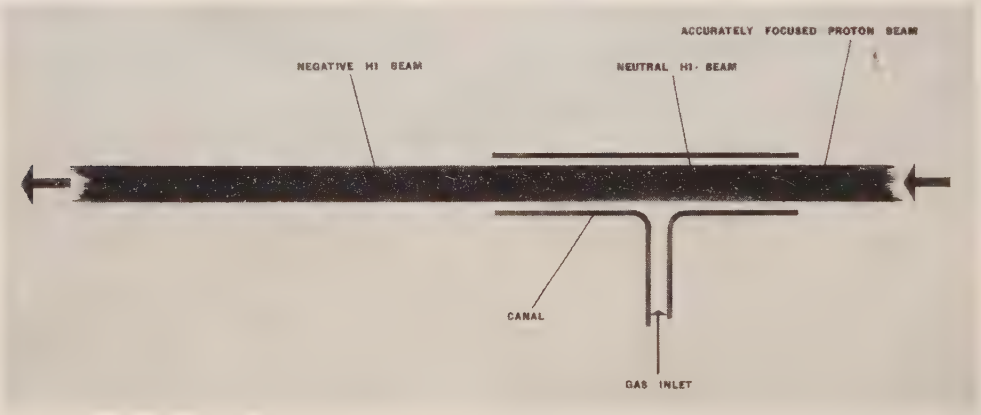

Fig. 7. Present arrangement.

TABLE 1
Neutron threshold measurements using Tandem Van De Graaff Accelerator

Reaction	Threshold energy E (MeV)	Proton resonance frequency f(Mc/sec)	$k \times 10^5$
$Li^7(p,n)$	1.8813 ± 0.0005	9.690 ± 0.010	†2021 ± 3
$B^{11}(p,n)$	3.015 ± 0.003	12.322 ± 0.003	2004 ± 3
$Na^{23}(p,n)$	5.061 ± 0.007	15.950 ± 0.020	2010 ± 4
$Al^{27}(p,n)$	5.798 ± 0.005	17.080 ± 0.010	2009 ± 4
$H^2(O^{16}+5,n)$	14.572 ± 0.030	21.555 ± 0.020	2008 ± 5
$H^2(O^{16}+4,n)$	— 14.572 ± 0.030	26.940 ± 0.020	2008 ± 6
	$E(1 + E/2Mc^2) = kf^2q^2/M$	Average of 5	2008 ± 2
			$k =$
$Ni^{60}(p,n)$	7.028 ± 0.020	18.814 ± 0.010	(2008 ± 4) ×
$Ni^{58}(p,n)$	9.459 ± 0.070	21.840 ± 0.080	10^{-5} (assumed)

† Corona Stabilizer inoperative for this run.

Fig. 7 shows the ion source, and initial accelerating electrodes, together with the electron-adding canal. A flow of hydrogen maintains this canal at sufficient pressure for charge transfer, so that about 1% of the protons in the beam emerge as negative atomic hydrogen ions.

The stripping canal is located in the terminal between the acceleration tubes. Its diameter is only 0.18 inch, which requires quite accurate beam focussing and alignment.

In the tests of the accelerator, proton beams up to 13.4 MeV were obtained, corresponding to a terminal potential of 6.7 megavolts. After 90-degree analysis, a proton beam of 1.5 microamperes was focussed on the target over a wide range of voltages. These outputs considerably exceeded the specified requirements of 10 MeV and 0.5 microampere. Measurements on the proton beam after deflection by the 90° magnet showed that it was homogeneous in energy to $\pm$ 0.02%.

In some of the tests, negative oxygen ions were injected into the accelerator when the terminal was at four megavolts. Observations at the target showed that some of these negative ions were completely stripped in passing through the terminal, thus reaching an energy of 36 MeV.

While the accelerator was still in Burlington, various tests were made in collaboration with a number of physicists from Chalk River. A number of neutron thresholds were studied and calibration measurements were made for a considerable range of particle energies. Figs. 9 and 10 have been taken from a recent paper† describing this work.

3. Some Possibilities for Future Development

An important feature of the tandem design is that the ion source and initial accelerating and focussing arrangements are situated outside the pressure tank, rather than inside the terminal and tank, as in the usual type of electrostatic accelerator. This external location will greatly facilitate the future development of improved ion sources and injection. It also affords ample space and accessibility for the possible introduction of various new injection devices, such as multiple-ion sources, apparatus for the polarization of particle beams, and equipment for beam pulsing.

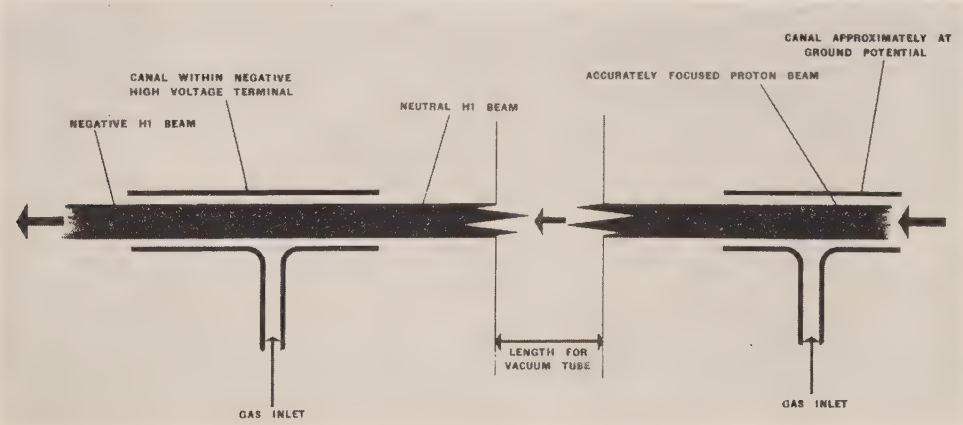

Fig. 8. Proposed arrangement,

Let us now turn to the consideration of future possibilities for the attainment of higher particle energies by tandem acceleration. Obviously, one method is by the use of higher

† Neutron threshold measurements in the proton energy range from 1.8 to 10.5 MeV using the Chalk River Tandem Van de Graaff Accelerator. This paper was read by A. J. Gale at the Vancouver Meeting (August, 1958) of the American Physical Society. Its authors were: E. Almqvist, D. A. Bromley, A. J. Ferguson, H. E. Gove, J. A. Kuehner and A. E. Litherland (Chalk River) and R. Bastide, N. Brooks, R. J. Connor, P. H. Rose (HVEC). Reprints can be obtained from High Voltage Engineering Corporation.

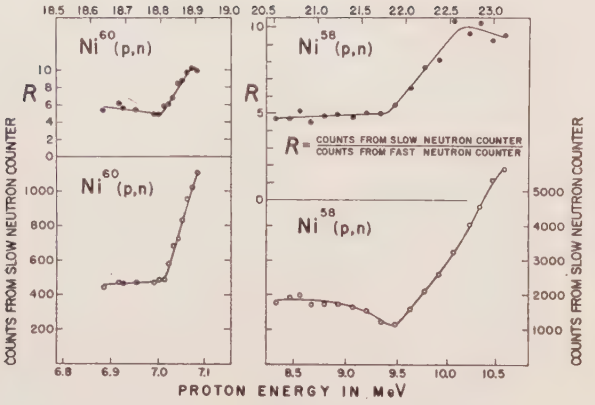
Ni 60 (p,n)
Ni 58 (p,n)
R
R = COUNTS FROM SLOW NEUTRON COUNTER / COUNTS FROM FAST NEUTRON COUNTER
COUNTS FROM SLOW NEUTRON COUNTER
PROTON ENERGY IN MeV

Fig. 9
(Reprinted with the kind permission of the Chalk River Group, Atomic Energy of Canada, Ltd.)

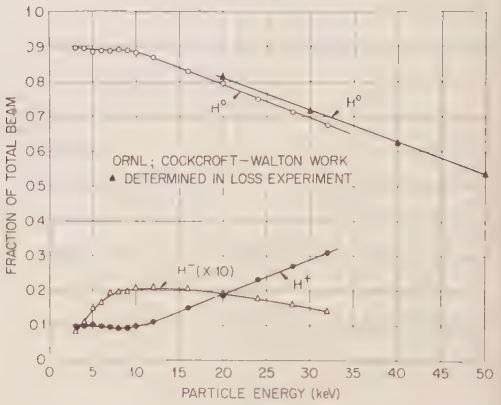

Fig. 10. Fraction of H beam in + 1.0–1 Charge states after passage through "thick" target. H in hydrogen.

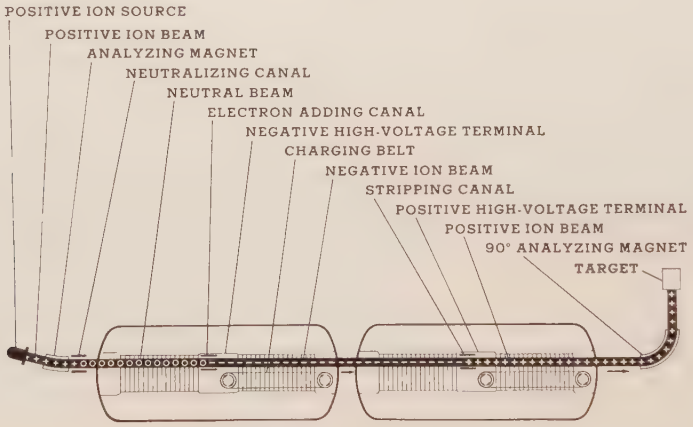

Fig. 11. Three-stage tandem accelerator.

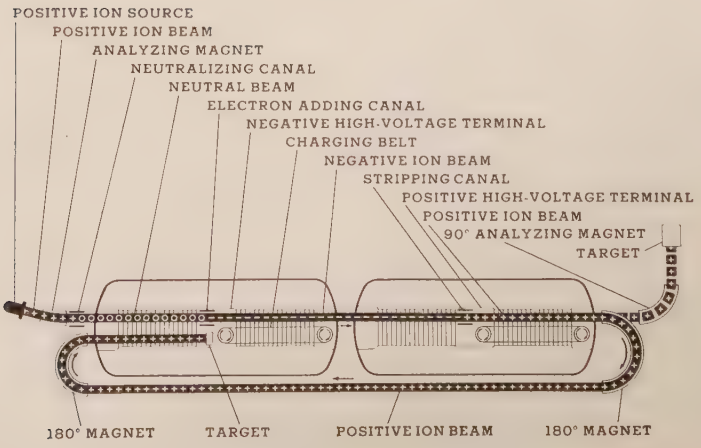

Fig. 12. Four-stage tandem accelerator

terminal potentials. At present the ceiling in this direction is represented by the ONR accelerator at M.I.T., built by J. G. Trump, and used since 1951 by W. W. Buechner for nuclear research at terminal potentials up to 10 megavolts. It is to be expected that in future accelerators there will be continuing increases in the terminal potentials attainable, due not only to growth in the size of accelerators but also to continued progress in high-voltage techniques which will make possible the insulation of still higher voltages in a given size of accelerator.

A more radical method of seeking higher tandem particle energies is by the use of more than two stages of acceleration. Fig. 11 shows a diagram of a possible arrangement for a three-stage tandem accelerator. The positive-ion beam from the ion source at the right is deflected by an analyzing magnet so that the desired positive ions are directed along the axis of the acceleration tubes. In the neutralizing canal, these positive ions encounter an amount of hydrogen which, though relatively small, is nevertheless sufficient to cause the attachment of a single electron to most of the positive ions, thus producing a beam of neutral particles which proceeds to the negative high-voltage terminal. In passing through the electron-adding canal situated in this terminal, some of the neutral particles capture and additional electron and become negative ions. These receive their first main stage of acceleration in passing from the negative terminal to ground, where they are injected into the second pressure tank as a negative-ion beam of considerable energy. In this tank, the beam receives its second and third stages of acceleration.

The operation in this tank is quite similar to that shown in the tank in fig. 1, except that in fig. 11 the injected negative ions are about 100 times more energetic and are correspondingly more homogeneous in energy, so that they can be focussed with great accuracy through the stripping canal in the positive terminal.

It is evident that an alternative arrangement for a three-stage tandem accelerator would be to have the complete apparatus for producing the negative ions installed within the negative high-voltage terminal. However, the use of a neutral particle beam, as indicated in fig. 11, appears more promising, as it would make it possible for the particle injector to be external and at ground, a situation having enormous long-run advantages, some of which have been already mentioned. Obviously such use of a neutral particle beam is practical only if the associated particle scattering is quite small. Some encouraging experimental observations in regard to the scattering effect have been made at HVEC and M.I.T.†.

TABLE 2

Positive-ion energies in MeV for certain possible arrangements of Tandem Accelerators

$V + nV$	(for two-stage tandem)
$2V + nV$	(for three-stage tandem)
$2V + 2nV$	(for four-stage tandem)

Here V = terminal potential in megavolts and n = number of electrons stripped from neutral atom.

TABLE 3

Positive-ion energies in MeV for two different arrangements of Tandem Accelerators

Positive ion	Two-stage	Three-stage
Hydrogen	13.4	20.1
Helium	20.1	26.8
Oxygen	60.3	67.0

Assumptions: Terminal potential = 6.7 megavolts. Complete stripping of positive ions.

It is hoped that some preliminary tests of actual three-stage tandem operation can be made by using the pair of two-stage tandem accelerators now under construction at HVEC.

Fig. 12 shows how a four-stage tandem accelerator could be made by the addition of two 180° deflecting magnets and an additional section of acceleration tube, the target being located inside the negative high-voltage terminal.

Table 2 gives some simple formulas for the positive-ion energies in MeV obtainable with the

† S. F. Philp, Doctorate thesis, 1958.

three different tandem arrangements which have been discussed.

The values for positive-ion energies shown in table 3 were obtained by substitution in the formulas of table 2 for hydrogen, helium and oxygen ions.

In the case of the four-stage tandem it is obvious that the inaccessibility of the target is a serious disadvantage. However, the effect of this difficulty could be much reduced by the development of special techniques and devices. It thus appears possible that four-stage tandems may later find usefulness for certain special types of research needing monoenergetic positive ions in an energy range somewhat higher than otherwise available.

NUCLEAR INSTRUMENTS AND METHODS 8 (1960) 203–210; NORTH-HOLLAND PUBLISHING CO.

CALCULATED SHAPES FOR NEUTRON BURSTS PRODUCED BY PHASED CHOPPER VELOCITY SELECTORS†

NORMAN H. TOLK and ROBERT M. BRUGGER

Phillips Petroleum Company, Atomic Energy Division, Idaho Falls, Idaho

Received 5 May 1960

The burst shapes and transmission probabilities for neutrons passing through a phased chopper neutron velocity selector of the type now being used at the Materials Testing Reactor have been calculated using an IBM-650 computer. Choppers with three types of slits (straight, parabolic, and circular) are considered and burst shapes are presented that show the operating characteristics of such velocity selectors. A function that gives a good fit to many of the burst shapes is presented. The results verify that a circular slit chopper can be used in place of the more exact parabolic slit chopper with only minor distortions in the operating ranges of interest.

1. Introduction

Several authors have considered the problem of finding the probability that a single neutron of particular velocity will pass through a rotating slit. A slit having straight parallel sides[1,2,3]) and a slit having a parabolic shape[4]) have been treated.

The present study adopts and extends this work to make possible a determination of the probability that a neutron will pass through two circular slits a set distance apart rotating with a definite phase relation, which is a geometry similar to that of the Materials Testing Reactor (MTR) phased chopper neutron velocity selector. Calculations of these probabilities for the MTR instrument are needed for a better understanding of the operating conditions, for the adjustment of experimental parameters, and for comparison with experimentally obtained results.

The methods of Marseguerra and Pauli[4]), which apply to calculation of the probability for a single chopper with a slit of parabolic shape, have been modified to fit the case of a slit of circular shape. Since calculations for a single chopper are not easily extended analytically to a double chopper arrangement, an IBM-650 computer program was developed to compute the probability $\theta(v,T)$ that a neutron of velocity v will reach at time T a given position along the beam path of the velocity selector.

The study has produced curves that show the general properties of velocity selectors having choppers with three types of slits: straight, parabolic, and circular.

2. Single Rotating Circular Slit

The procedure for circular slit choppers will be presented to illustrate the method used for all three types of choppers. Fig. 1 is a cross sectional view of the chopper to be considered. The primed coordinates are fixed in the chopper and rotate with it, while the unprimed coordinates are fixed in the laboratory system; z and z' are common to both sets of coordinates. The axis of rotation of the chopper is z. A parallel beam of polychromatic neutrons travels along x toward the right. The chopper of radius R has a slit formed by two surfaces located equal distances from and parallel to the axis of the chopper. The width of the

† Work done under the auspices of the U. S. Atomic Energy Commission.

[1]) R. S. Stone and R. E. Slovacek, Nuc. Sci. Eng. **6** (1959) 466; and KAPL–1499 (1956).

[2]) V. I. Mostovoi, M. I. Pevzner and A. P. Tsitovich, Int. Conf. Proc. Peaceful Uses Atomic Energy (Geneva) **4** (1955) 12.

[3]) P. A. Egelstaff, AERE N/R-1131 (1953); J. Nuc. Energy **1** (1954) 57.

[4]) M. Marseguerra and G. Pauli, Nuc. Instr. and Methods **4** (1959) 140.

slit is h and the chopper rotates counterclockwise with an angular velocity ω. The equations of the upper and lower surfaces that form the sides of the circular slit are

$$y'_u = + (\rho^2 - x'^2)^{\frac{1}{2}} - \rho + \tfrac{1}{2}h$$

and

$$y'_l = + (\rho^2 - x'^2)^{\frac{1}{2}} - \rho - \tfrac{1}{2}h .$$

The radius of curvature of both slit surfaces is ρ. These surfaces are assumed to be perfect absorbers.

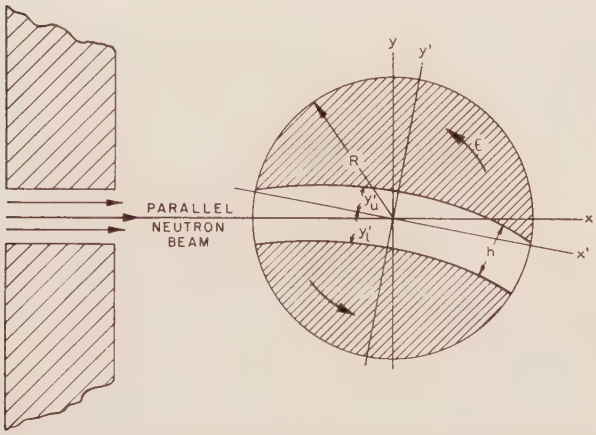

Fig. 1. Single chopper with circular slit. The primed coordinates rotate with the chopper and the unprimed coordinates are fixed in the laboratory frame of reference.

Select a time t associated with each chopper so that $t = 0$ when the rotating coordinate system coincides with the fixed system $x' = x$ and the circular slits are concave toward the negative y direction. (The case with the slit concave toward positive y will not be considered since this orientation is seldom used in curved slit neutron chopper operation.) If h is much smaller than R, and ρ is large compared to R, then the time required for the neutrons to traverse the chopper is small compared to the time for one revolution of the chopper, and it can be assumed that for pertinent values of t, $\sin \omega t = \omega t$. For the slit to be completely closed to very fast neutrons, $R^2 - 2\rho h > 0$. It follows that the equations of the upper and lower surfaces of the slit at time t in the laboratory coordinates are, to a good approximation:

$$y_u = + (\rho^2 - x^2)^{\frac{1}{2}} - \rho + \tfrac{1}{2}h + x\omega t \qquad (1)$$

$$y_l = + (\rho^2 - x^2)^{\frac{1}{2}} - \rho - \tfrac{1}{2}h + x\omega t . \qquad (2)$$

Whether or not the neutrons collide with the surfaces of the slit needs to be known to determine when neutrons are removed from the beam. Consider the front of a plane wave of neutrons traveling in the x direction with velocity v that is at $x = 0$ at time t. Eq. (1) and (2) give the positions of the surfaces of the slit. Let $x = v\tau$ be the position of the wave front when t is changed by an amount τ and the surfaces of the slit are given by eq. (1) and (2) with $t + \tau$ substituted for t. Eliminate τ, to obtain

$$y_u^* = + (\rho^2 - x^2)^{\frac{1}{2}} - \rho + \tfrac{1}{2}h + x\omega t + \omega x^2/v \qquad (3)$$

$$y_l^* = + (\rho^2 - x^2)^{\frac{1}{2}} - \rho - \tfrac{1}{2}h + x\omega t + \omega x^2/v \qquad (4)$$

where y^* gives the magnitude of y for neutrons of velocity v that intersect the upper or lower surfaces of the slit at position x. (See fig. 3 of ref.[4]) for examples of these curves for the parabolic case.) Similar equations can be written for a straight slit and for a parabolic slit[1,4]).

If the neutrons are uniformly distributed in the yz plane before entering the chopper, the greatest number that can possibly pass through the slit is proportional to a y magnitude equal to h. The number of neutrons that actually pass through the slit for a given velocity v and time t is proportional to a y magnitude, $\Delta y^*(v,t) = y_u{}^*{}_{\min} - y_l{}^*{}_{\max}$, where $y_u{}^*{}_{\min}$ is the minimum value of y_u^* for x between $-R$ and $+R$ and $y_l{}^*{}_{\max}$ is the maximum value of y_l^* for x between $-R$ and $+R$. Thus, the probability $P(v,t)$ that a neutron of velocity v that passes $x = 0$ at time t will pass through the rotating slit is

$$P(v,t) = \Delta y^*(v,t)/h . \qquad (5)$$

The quantity $P(v,t)$ represents the shape of the neutron burst in P, v, and t space that will be passed by a rotating slit. The assumption that $\sin \omega t \cong \omega t$ limits the magnitudes of h and ρ compared to R. For a single chopper, the problem is to determine the values of $y_u{}^*{}_{\min}$ and $y_l{}^*{}_{\max}$ from which the transmission probability can be obtained. The maximum probability is obtained for $t = 0$ and $v = 2\omega\rho = v'_0$. The latter is the condition that applies when a circular slit chopper is being designed to transmit neutrons of the desired velocity v'_0.

3. Burst Shape of a Phased Chopper Velocity Selector

Fig. 2 is a schematic diagram of the phased chopper velocity selector[5]) now in use at the MTR[6]). Chopper A chops the neutron beam into bursts of polychromatic neutrons that spread out in time, due to the wide range of velocities of the neutrons, as they travel to chopper B. Chopper B, which spins at exactly the same angular velocity as A and is accurately phased with it, passes only those neutrons that arrive at chopper B in one small time and velocity interval. Thus, the machine acts as a velocity selector, delivering short bursts of monochromatic neutrons.

The MTR neutron velocity selector is designed for scattering experiments[6]). The time for the neutrons to travel from a scattering sample placed 0.5 m distant from chopper B to a detector 2 m from the sample is recorded. A change in energy during scattering can thus be detected. Fig. 2 shows the case where a detector has been placed in the beam 2.5 m from chopper B to correspond in distance to the detector used in the scattering experiment.

IBM-650 programs were written to calculate the transmission probabilities and burst shapes of neutrons passing through such a velocity selector. Since the time t refers to each chopper, a time scale T is selected to relate the angular position of one chopper to the angular position of the second chopper and to determine the time that the neutrons arrive at any point along the beam path. Chopper A starts each timing cycle. Defining time $T = 0$ as the time that the y' coordinate of chopper A is parallel to the laboratory coordinate y, and defining the phase time Δ as the time T at which the y' coordinate of chopper B is parallel to y, the probability and burst shape at any point along the beam is then a function of T. The angular phase difference in degrees is $\omega\Delta 360°/2\pi$. The position of observation along the beam is determined by $D + G$ where D is the distance between choppers and G is the distance from chopper B to the detector. Thus, the position of the detector, which can be moved to any point along the beam path, is the position of the observation. All distances are measured from the centers of the choppers.

In the IBM-650 programs $P(v,t)$ is determined for a single chopper by the calculation of y_u* for a series of x's between $-R$ and $+R$ followed by the selection of the minimum value. Similarly, the maximum value of y_l* is obtained. From

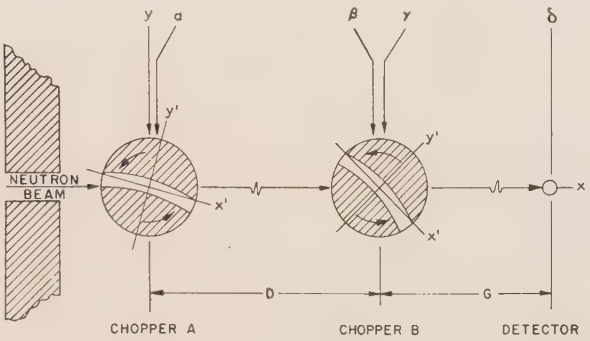

Fig. 2. Phased chopper velocity selector.

these, the probability for velocity v at a given time t can be obtained from eq. (5). The probabilities for neutrons to reach any point along the beam at time T are $P_A(v,t) = P_A(v,t - D/v - G/v)$ and $P_B(v,t) = P_B(v,T - \Delta - G/v)$, where P_A relates to chopper A and P_B to chopper B. P_B is unity for G negative; P_A is unity for D negative Also Δ is greater than or equal to zero so that the phase time is always measured in a positive sense. The probability that a neutron will pass through both choppers is the product of probabilities for the two choppers. The final products are

$$\theta(v,T) = f(v)\, P_A(v,T - D/v - G/v)\, P_B(v,T - \Delta - G/v) \quad (6)$$

and

$$\phi(T) = \int_0^\infty f(v)\, P_A(v,T - D/v - G/v)\, P_B(v,T - \Delta - G/v)\, dv \quad (7)$$

where $f(v)$ is the flux distribution in the incident beam. The quantity $\theta(v,T)$ is the probability, both velocity and time dependent, that a neutron will reach a certain position $G + D$ along the beam of the velocity selector, while $\phi(T)$,

[5]) P. A. Egelstaff, Private Communication; and R. F. Dyer, "Colloquium on Neutron Diffraction and Scattering", AERE M/R-2857 (1958).

[6]) R. M. Brugger, R. E. Schmunk, L. W. McClellan and J. E. Evans, Bul. Am. Phys. Soc. II, **4** (1959) 32.

which is only time dependent, is the quantity actually measured in an experiment, that is, the burst shape in time.

The procedure developed above permits the calculation, at any desired observation point, of the burst shape of neutrons passing through a phased chopper neutron velocity selector. For comparison of the results with experimental data, consideration must be given to the effects of angular divergence of the beam, phase uncertainty, flight path uncertainty due to finite thickness of detectors, uncertainties due to finite absorption of the walls of the chopper slits, and effects of multiple slits. No corrections for these effects are considered in this paper.

For comparison purposes, computations were made for velocity selectors having choppers with straight slits, parabolic slits, and circular slits, by means of IBM-650 programs written to cover these cases. Parameters were selected to agree with or correspond as closely as possible to those of the MTR velocity selector: the radius of the choppers R is 5.08 cm, the slit width of the choppers h is 0.08128 cm, the distance between choppers D is 0 or 2.00 m, the distance from chopper B to detector G is 0 or 2.50 m, the constant n in the Maxwellian distribution is 1.0 neutron/cm^3, and the most probable velocity v_0 of the Maxwellian distribution for a temperature 30.3° C is 2278 m/sec. Since neutron choppers and velocity selectors most often utilize the flux from a thermal reactor as the initial source of neutrons, a Maxwellian flux distribution $(4n/\sqrt{\pi})\ (v^3/v_0^3)\ \exp\ (-v^2/v_0^2)\ dv$ was selected for $f(v)$. The most probable velocity v_0 of the flux from the MTR was used and in all cases n is equal to one neutron/cm^3. This sets the initial flux in the parallel beam to be 2.58×10^5 neutrons/cm^2 sec. To obtain expected intensities from the burst shapes shown in the following figures, the ordinate must be multiplied by the number of bursts per second. To compare these calculated intensities with experimentally obtained ones, it should be remembered that reactor fluxes are quoted for isotropic angular distributions and corrections need to be made for the $1/r^2$ effect.

On several trial passes of the program through the IBM-650 machine, it was found that about twenty steps of x between $-R$ and $+R$ were sufficient; additional steps altered the curve only slightly. The velocity steps and time steps were adjusted for each case. Fig. 7 gives an idea of the number of velocity steps required.

4. Computed Probabilities and Burst Shapes

To better understand the effects of the chopping of the beam by the velocity selector as neutrons pass from chopper A to the detector, the curves shown in fig. 3 through 7 were computed. For illustration, the circular slit

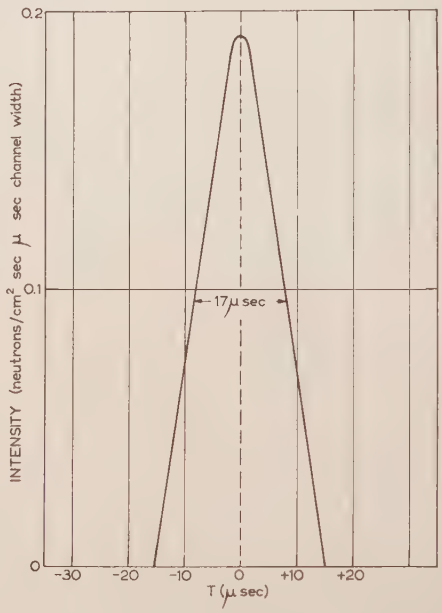

Fig. 3. Burst shape at position α immediately after neutrons are chopped by chopper A.

chopper having a radius of curvature of 211.6 cm was selected. The choppers' angular velocity was 523.6 radians/sec (5000 rpm), which gives maximum transmission for neutrons having a velocity of 2215.6 m/sec. Fig. 3 shows the burst shape $\phi(T)$ immediately after the neutrons have been chopped by chopper A. Since the program considers that the chopping occurs at the center of the choppers, the observation of these neutrons is at position α (see fig. 2) at the center of chopper A. The burst shape is almost a triangle and the base of the triangle is the time required for the periphery of the chopper to move the

width of the slit. The burst is centered at a time that corresponds to that when the circular slit is symmetrical about the y axis. Neutrons having a wide range of velocities are contained within this triangle. The total number of neutrons contained in this burst is much smaller than the initial flux of 2.58×10^5 neutrons/cm^2 sec because the burst intensity represents one burst per sec.

Fig. 4 shows the burst shape for conditions identical to those of fig. 3 except that the position of observation is at β just before the neutrons are chopped by chopper B. (In this figure the integration is over velocity for each time T: if $\theta(v,T)$ is integrated over all time T for a given velocity, and this result is compared to an unmodified Maxwellian distribution, transmission functions similar to those shown by Stone and Slovacek[1]) are obtained.) The neutrons have spread out in time, the faster ones in the Maxwellian arriving sooner than the slower ones. The shape of the Maxwellian has been modified to some extent by the transmission properties of the curved slit, the transmission at short and long times being suppressed compared to the transmission at $T = 903$ μsec ($v = 2215.6$ m/sec). The integral over time of this curve is the same as the integral of fig. 3.

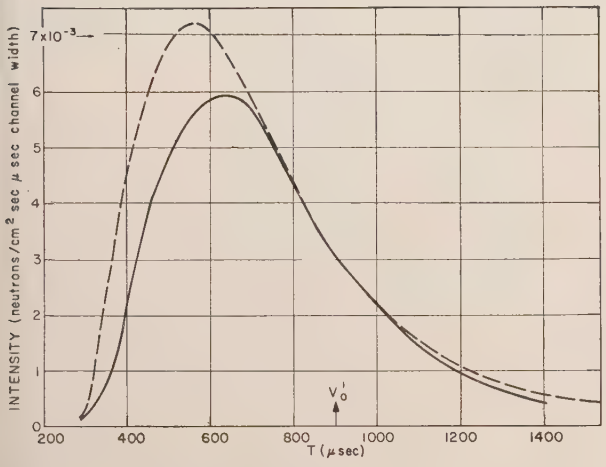

Fig. 4. Neutron distribution (solid line) at position β immediately before neutrons are chopped by chopper B. A Maxwellian distribution (dashed line) that is normalized to the solid curve at 903 μsec is shown for comparison.

Fig. 5 shows the burst shape at position γ immediately after the neutrons are chopped by chopper B. The phase time Δ was set at 700 μsec, which allows neutrons near a velocity of 2858 m/sec to pass. Again the burst shape is almost triangular with a half width of 17 μsec and a base width of 31 μsec. This chopper selects a small velocity interval and the total integrated number of neutrons has decreased accordingly.

Fig. 6 is the burst shape at position δ at the detector. The burst, no longer a triangle, has broadened due to the velocity components that passed through chopper B. While a Gaussian with its width at half maximum equal to the half width of the burst shape is a good fit to the shape near the center of the burst, it overestimates the wings. For this particular case, the function

$$f(t) = N_0 \sin^2(\pi t/2\tau)/(\pi t/2\tau)^2 \qquad (8)$$

gives a very good fit. The quantity N_0 is the peak height and τ is the full width at $0.405\,N_0$. Because the initial flux has a Maxwellian distribution, the burst shape is not exactly symmetrical about the time corresponding to the phase setting. The integral of fig. 6 is equal to the integral of fig. 5.

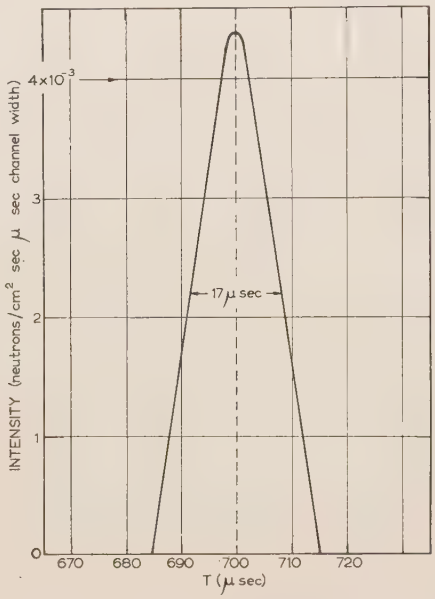

Fig. 5. Burst shape at position γ immediately after neutrons are chopped by chopper B.

Fig. 7 shows the probabilities $\theta(v,T)$ corresponding to the burst shape $\phi(T)$ of fig. 6 and shows the contributions of the different velocity intervals. Each velocity function has a shape similar to the burst shape directly after chopper B, but the half width is less than 17 μsec. These velocity components add to give the burst shape shown in fig. 6.

Fig. 8 shows a composite of several burst shapes like those of fig. 6 except the phase time Δ is different for each curve. It is seen that the intensity changes rapidly with phase time due

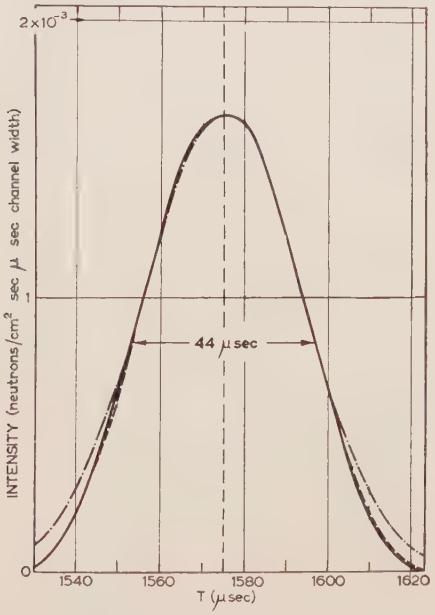

Fig. 6. Burst shape (dashed curve) at position δ at detector. The solid curve is fit of eq. (8) and the dot-dashed curve is a Gaussian distribution.

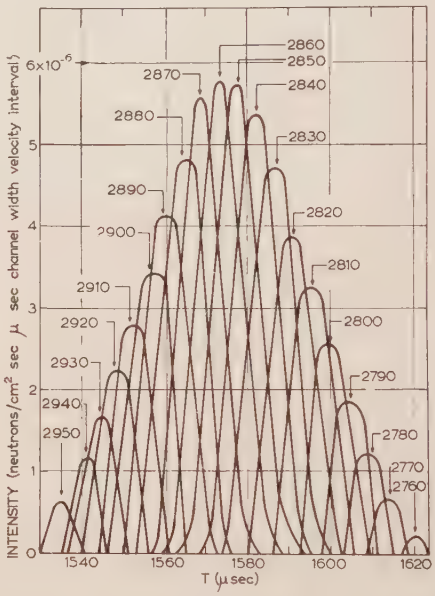

Fig. 7. The probability $\theta(v,T)$ corresponding to fig. 6. Numbers designating individual curves are velocities in m/sec.

both to the Maxwellian flux distribution and the transmission probabilities of the choppers. The program treating parabolic instead of circular slits with $v''_0 = 2\omega\rho$ (where ω and ρ are the same as those used to determine the curves of fig. 3 through 7) gives results that agree with the circular slit case of fig. 8 to better than 0.5%. The constant defining the eccentricity of the parabolic slit[4]) is v''_0/ω where v''_0 is the neutron velocity for maximum transmission.

Also in fig. 8 is shown a composite similar to that for the circular slit case for a velocity selector having straight slit choppers operating at 5000 rpm. The suppression of slower neutrons in this case is very pronounced, and it is evident that curved slits are necessary when slower neutrons are desired. With a straight slit chopper, two bursts per revolution are passed as compared with one burst per revolution for a curved slit chopper. Thus, for maximum intensities at these operating conditions, it is desirable to use the straight slit chopper for neutrons with velocities greater than 4000 m/sec ($\Delta = 500$ μsec) and the circular slit choppers for neutrons below this velocity. Also, it can be seen that the burst shape at the extremes is not symmetrical, this asymmetry being due both to the Maxwellian neutron spectrum and the transmission of the choppers. Table 1 lists some of the changes due to these modifications of the burst shape. The table shows that in some cases there is a difference between the time predicted by the phase time and the time at which the peak of the burst actually appears. For the straight slit this difference appears only at short times. The full width at half maximum is also affected by the Maxwellian flux distribution and the transmission of the choppers. For the circular case

these widths are less at extreme times and also are slightly narrowed at intermediate times. The straight slit burst shape becomes continuously narrower and more distorted at longer times.

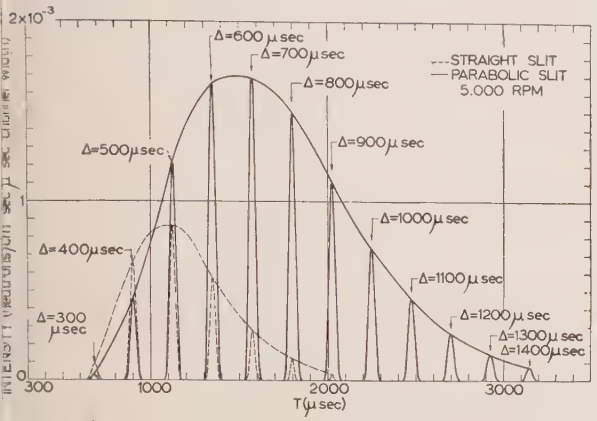

Fig. 8

A composite of burst shapes for parabolic or circular ($\rho = 211.6$ cm) and the straight slit cases at $f = 5000$ rpm. The envelopes were drawn to tie the peaks together.

burst shapes for the two cases are noticeably different, the circular slit case giving higher intensities at the lower velocity end. The total velocity range that can be covered by changing the phase

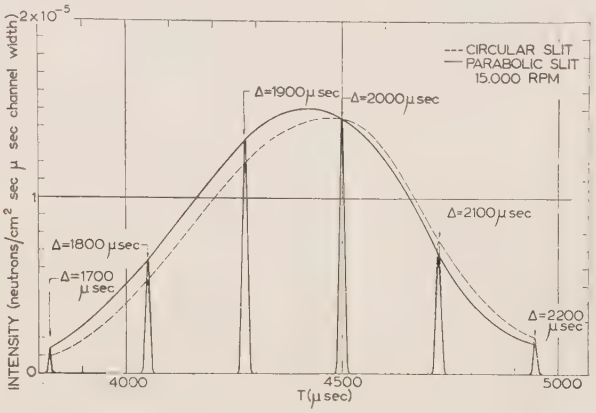

Fig. 9

A composite of burst shapes for parabolic ($v_0'' = 1007$ m/sec) and circular ($\rho = 32.05$ cm) slit cases at $f = 15\,000$ rpm. The envelopes were drawn to tie the peaks together.

To show the difference between the circular slit case and the parabolic slit case, the composite burst shapes shown in fig. 9 were computed. In this computation the frequency is 15 000 rpm and $v''_0 = 2\omega\rho = 1007$ m/sec, or ρ is 32.05 cm. This corresponds to operating conditions for cold neutrons with very good resolution. Now the is smaller than for a similar case at 5000 rpm. Here again the function of eq. (8) was found to be a very good fit to the burst shape. Table 2 gives some of the parameters obtained from these curves. The approximations of this paper will not be valid if the present treatment is applied to choppers at higher speed or with smaller ρ.

TABLE 1

Parameters of burst shapes of fig. 8 for choppers spinning at 5000 RPM

Phase time Δ (μsec)	Full width at half-height of burst shape (μsec)		ΔT (μsec)†		Velocity at peak (m/sec)		Energy at peak (eV)	
	Circular	Straight	Circular	Straight	Circular	Straight	Circular	Straight
300	35	42	+ 6.0	+ 6.0	6607	6607	0.228 182	0.228 182
400	39	42	+ 2.0	+ 2.0	4988	4988	0.130 055	0.130 055
500	43	39	+ 1.0	0	3996	4000	0.083 485	0.083 486
600	44	35	0	— 1.0	3333	3335	0.058 069	0.058 166
700	44	31	0	— 1.0	2857	2858	0.042 667	0.042 726
800	41	22	0	0	2500	2500	0.032 670	0.032 670
900	41		0		2216		0.025 670	
1000	41		— 1.0		2000		0.020 926	
1100	43		— 1.0		1818		0.017 294	
1200	44		— 1.0		1667		0.014 529	
1300	42		— 1.0		1538		0.012 379	
1400	40		— 2.0		1429		0.010 680	

† Where $T - T_0 = \Delta T$ when T is time at which peak actually occurs and T_0 is time at which phase predicts peak will occur.

TABLE 2

Parameters of burst shapes of fig. 9 for choppers spinning at 15 000 RPM

Phase time Δ (μsec)	Full width at half-height of burst shape (μsec)		ΔT (μsec)†		Velocity (m/sec)	Energy (eV)
	Parabolic	Circular	Parabolic	Circular		
1700	7.5	6.5	0	0	1176	0.007 23
1800	12.5	11.5	0	0	1111	0.006 45
1900	14.5	14.0	0	0	1052	0.005 79
2000	13.5	13.5	0	0	1000	0.005 22
2100	14.5	14.5	0	0	952	0.004 74
2200	11.5	11.5	0	0	909	0.004 31

† Where $T - T_0 = \Delta T$ when T is time at which peak actually occurs and T_0 is time at which phase predicts peak will occur.

After calculating the burst shape and probability for a particular experimental arrangement, it is possible to predict the instrument resolution broadening. As an example consider a scattering experiment. If the energy of the scattered neutrons is only slightly changed from the incident energy due to interaction with the sample, the resolution broadening due to the velocity selector is the full width at half height of the burst shape divided by the time for the neutrons to travel from the sample to the detectors. When the velocity selector has circular slit choppers spinning at 5000 rpm and the phase time is 700 μsec, the resolution broadening is $\Delta t/t = 6.3\%$. Since $\Delta t/t = \Delta\lambda/\lambda = 2\Delta E/E$, the uncertainty in the wave length λ is 6.3% and the uncertainty in energy is 12.6%. To improve this resolution the angular velocity can be increased, the distance between the sample and detectors can be increased, or the effect can be observed with colder neutrons. For example, if the angular velocity is increased to 15 000 rpm and the effect can be observed with cold neutrons, the phase time is $\Delta = 2000$ μsec and $\Delta t/t$ is 0.7%. This gives a factor of ten improvement in instrument resolution. If the energy change is large, a more extensive evaluation of the time and velocity components contributing to the probability $\theta(v,T)$ will yield the instrument resolution.

The curves presented in this paper show that the program is very useful in predicting the operating characteristic of the MTR phased chopper velocity selector. These results indicate that small changes occur in the burst widths and in $T - T_0$ that affect the settings of the experimental parameters. Also, eq. (8) is useful for resolution broadening theoretical data before comparing with experimental data. The results verify that a circular slit chopper can be used in place of the more exact parabolic slit chopper with only minor distortions in the operating ranges of interest.

Acknowledgements

The authors would like to acknowledge helpful discussions with Dr. P. D. Randolph and the computational help of Mrs. Carolyn Slayden.

NUCLEAR INSTRUMENTS AND METHODS 8 (1960) 211–216; NORTH-HOLLAND PUBLISHING CO.

HIGH-EFFICIENCY, LONG-LIVED VACUUM COLD TRAP

J. W. BUTLER

Nucleonics Division, United States Naval Research Laboratory, Washington, D.C.

Received 6 April 1960

The construction and performance of a vacuum cold trap for pump oil, "O"-ring, and other vapors are described. The trap has a capacity of 16 liters of liquid nitrogen, and lasts 5 days on one filling when clean. After a period of about 6 months to 1 year of continuous use, the lifetime has dropped to about 3 days. The trap has high pumping speed, and very high trapping efficiency, requiring a minimum of 3 successive cold-surface collisions for a molecule migrating through the trap. The principles of design include the use of very thin re-entrant tubes for mechanical support of the cold reservoir thus minimizing conduction heat transfer, an inner tube for pumping and trapping, shields for reducing radiation heat transfer, and gold-plating for opposing surfaces having different temperatures. Mercury and oil diffusion pump systems are compared.

1. Introduction

Since the liquids used in vacuum diffusion pumps have quite appreciable vapor pressures at room temperatures, the use of these pumps creates a problem of contamination of the vacuum system with the condensed vapor of the pump fluid, oil or mercury. For nuclear reaction particle accelerators, carbon is a particular nuisance because of its high cross sections for the (d,n), (d,p), (He^3,n), (He^3,p), and (He^3,α) reactions and, to some extent, the (p,γ) reaction. In the deuteron and He^3 induced reactions, some of the particle groups lead to excited states in the residual nuclei and hence to intense gamma radiation from the decay of these states. Thus carbon contamination, which is a result of oil vapor condensing on the target and being cracked by the accelerator beam, leads to background particle groups and gamma rays. Furthermore, an appreciable film of contaminant can displace the energy of a reaction resonance or neutron threshold.

Mercury does not lead to appreciable nuclear reaction yields at bombarding energies below 4 MeV (except for coulomb-excited states), but has many disadvantages (discussed below) as a vacuum system contaminant. Similarly, arguments could be made concerning oil and mercury contamination of vacuum systems used for entirely different purposes than for acceleration of charged particles, such as evaporated-target preparation systems, film depositing systems, etc. The problem is therefore to insert some type of vapor trap between the pumps and the vacuum system.

One of the most useful types of such vapor traps is a cold surface, which might be kept cold either by a recycling refrigerant, solid carbon dioxide, or liquid nitrogen. In the past, many different approaches have been used, each possessing certain advantages and disadvantages with respect to the others. In recent years, several aspects of the problem have been discussed by several authors[1]), but within the present author's knowledge, there does not exist a generally satisfactory trap design combining the features of long life, high pumping speed, and high trapping efficiency, except the one described herein. The philosophy of the present design was to obtain as high a degree of the above characteristics as feasible in an a priori manner without the investment of large amounts of time and money in an exhaustive experimental study. The trap built from this

[1]) See, for example, J. R. Ullman, Transactions, Fourth National Symposium on Vacuum Technique (1957);
N. Milleron, Transactions, Fifth National Symposium on Vacuum Technique (1958);
G. H. Miller, Rev. Sci. Instr. **24** (1953) 549; and others.

design has performed in a highly satisfactory manner for over six years. Thus, the present ideas are considered to be more of a contribution to the art of cold-trap design than to the theory.

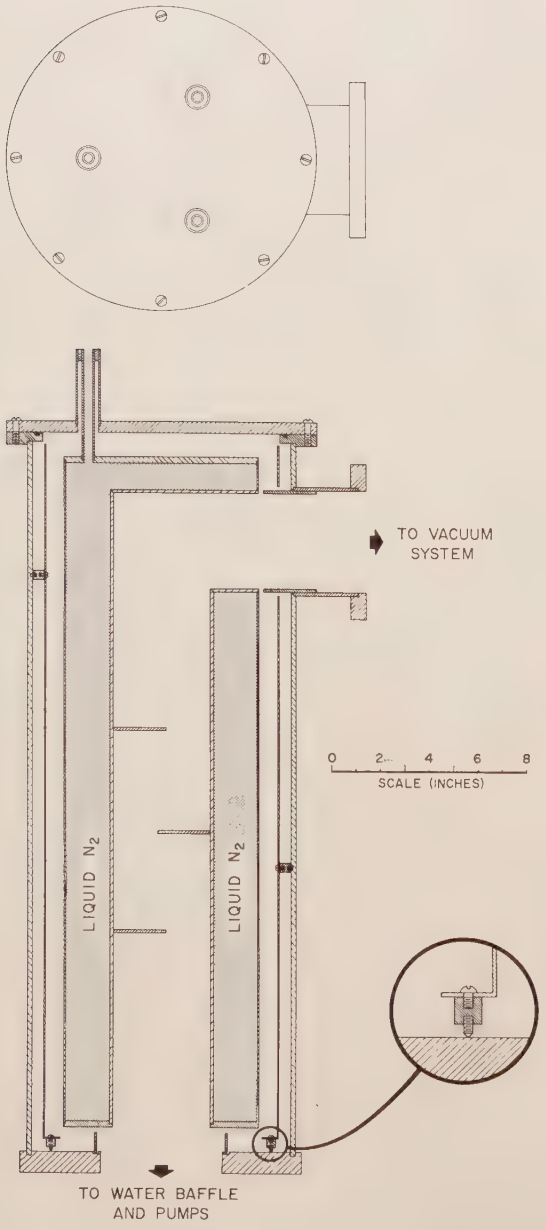

Fig. 1. Cross-section drawing of the cold trap. The shield is supported by two thin sharpened stainless steel screws and porcelain stand-off bushings. The upper two supports are approximately in the middle of the vertical dimension and are included in the drawing even though they are actually in the plane perpendicular to the plane of the drawing. For most vacuum systems, the three approximately semi-circular baffles in the pumping tube are not necessary.

Visiting physicists who have seen the installation described herein have expressed a keen interest in its design and operation. It is therefore felt that a wider dissemination of this information is desirable, and that is the goal of this paper.

2. Description of the Trap

The trap is shown in cross-section form in fig. 1. The outer can is the vacuum retaining wall. The lower flange rests on top of a water baffle, which is in turn on top of a diffusion pump. The inner can, which contains the liquid nitrogen, is supported by three thin stainless-steel tubes (0.006-in. wall) from the top flange. There are no supports on the sides or bottom. Thus the only thermal-conduction path (for practical purposes) between the liquid nitrogen and the outside container is through these thin tubes. Inconel would be slightly better from a thermal conductivity point of view, but the difference between Inconel and stainless steel is quite small. (Other vacuum cold traps which have been built at this Laboratory, smaller than the one described herein, do employ Inconel tubes.)

The tubes are re-entrant at the top in order to increase the length of heat-conduction path from "ground". These protrusions are normally covered by inverted beakers (large enough not to touch anything except the main top flange) in order to minimize heat transfer from the air, and to prevent frosting at the top of the tubes.

The thermal conductivity of a static gas (nitrogen) at atmospheric pressure in the tubes is comparable with the conductivity in the metal tubes. The emanating vapor or gas, however, requires the heat to flow "upstream" against the normal gas flow, thus reducing heat transfer due to this heat path. Moreover, since the cold nitrogen vapor inside the tubes is denser than the outside air, there is essentially no convection heat transfer through this path.

The thermal conductivity of the gas in the vacuum region is considered negligible. Radiation heat transfer between the surface of the liquid-nitrogen reservoir and the outer wall is not negligible, however, and actually constitutes

the major source of heat transfer. Several steps have therefore been taken to minimize this radiation heat transfer.

The trapping action of the system has been limited to the interior surfaces instead of the outer surfaces of the cold reservoir as used in conventional types of cold traps. That is, the pumping action through the trap is through the innermost tube, which is completely surrounded by liquid nitrogen. Thus the trapped foreign matter which coats these surface does not materially affect the radiation heat transfer to the trapping surface, because this "dirty" surface "sees" another surface at the same temperature, thus involving no heat transfer. Trapping action on the outside of the liquid-nitrogen reservoir is minimized by cylindrical baffle inserts (made of glass) at the input and output ends. These baffle inserts do not completely close off access to the outside surfaces, of course, because first, they must not touch the cold surface and thus complete a heat-conduction path to the outside, and second, it is necessary to pump out the region between the outer wall and the liquid-nitrogen can. It might be noted, however, that molecules may not migrate to this region without first striking a cold surface at least once. These baffles also serve as surface barriers in the prevention of the surface creep of the pump fluid.

A slightly modified version of this cold trap, utilizing re-entrant baffling to protect more nearly completely the outer surfaces of the liquid-nitrogen can, has been built for another vacuum system, but this re-entrant baffling appreciably increases radiation heat transfer and construction expense. Therefore, it is believed that for most fairly clean vacuum systems, the simple non-re-entrant baffle inserts are satisfactory.

In order to minimize the radiation heat transfer between the inner (0.006-in.) stainless-steel support tubes and the outer support tubes of the re-entrant sections, these adjacent areas were mechanically buffed†.

The outer wall of the liquid-nitrogen reservoir is made of 0.016-in. stainless steel so that the radiation heat transfer drops somewhat at the lower levels of reserve liquid nitrogen. Under operating conditions, this cylinder is required to stand tensile stress only (inside pressure), so the thinness of the wall is no disadvantage. Moreover, another advantage of the thin wall is the low heat capacity; not much liquid nitrogen is required to cool it from room temperature to liquid-nitrogen temperature.

The innermost tube, however, should remain at the lowest possible temperature regardless of level of reserve liquid nitrogen, because if its temperature rises, trapped vapors will begin to migrate again, and the sticking probability for new molecules striking the surface will decrease. Furthermore, the region where the warming-up would occur (the top) is adjacent to the vacuum system one wishes to protect. Therefore, the innermost tube is made of heavier material, 0.125-in. stainless steel. A simple calculation indicates that less than 2% of the total temperature difference between the liquid nitrogen and the room occurs along the trapping tube, even if the liquid-nitrogen level drops to one inch. The same type metal is used for all parts of the cold reservoir to avoid differential thermal expansion and contraction at the welded junctions. An independent reason for using thicker material for the innermost tube is that this wall has the pressure on the outside, and a very thin wall might therefore collapse. The ends of the can are of thicker (¼-in.) stainless steel because flat surfaces are under greater strain with pressure differentials than curved surfaces.

A radiation shield has been inserted between the two walls to reduce the radiation heat transfer. This radiation shield is made from 0.016-in. stainless-steel sheet, and is supported at the bottom by two thin stainless-steel screws, thermally insulated by porcelain stand-off bushings, and sharpened at the points of contact. Two further supports are near the

† For smaller traps, where mechanical buffing is not feasible, a chemical polishing method, developed by Dr. C. R. Gossett, may be used. This method, utilizing a solution of aqua regia in the inaccessible regions, leaves a bright satin-like finish on the stainless steel.

middle of the vertical dimension and are in the vertical plane perpendicular to the vertical plane containing the other two support points. These supports (shown in fig. 1 in the same plane as the other two support points in order that they be included in the drawing) are from the shield to the outer wall, and consist of screws and porcelain stand-off bushings. Thus the shield is fairly well thermally insulated, and assumes some intermediate temperature between the inner and outer cans, thus reducing the heat transfer to the inner can.

Other shields could be used to decrease further the radiation heat transfer. For example, a second coaxial shield was designed to fit between the inner can and the first shield, but it is not normally used in the installation described here. It could be supported either by the inner can or the first shield. Top and bottom shields could also be used, but their effect is rather small because of the relatively small areas involved. The supports for the shield could also be re-entrant to decrease further the conduction heat transfer from ground.

All appropriate surfaces are plated with gold to reduce heat transfer. These surfaces are the inside of the outer can and flanges, both surfaces of the shield, and the outside of the inner can. The gold was applied using a very inexpensive "paint-on" process and a silica binder†. The binder was removed by baking the parts in an oven, leaving the gold residue which was a reasonably good quality gold plate. It is not easy, however, to achieve a successful plating. It is necessary to have the surface extremely clean before application of the gold mixture.

The innermost tube (pumping tube) was made 4 inches in diameter to provide a high pumping speed. The use of the elbow bend requires a minimum of one cold-surface collision before a molecule can migrate through the trap. (It is assumed that no gas-to-gas collisions occur. At typical cold-trap pressures of a few times 10^{-7} tor, this is a reasonable assumption.) The insertion of the approximately semi-circular baffles raises the minimum number of collisions with the cold surfaces to three successive cold-surface collisions. The baffles are slightly larger than half the pumping-tube cross-sectional area in order to eliminate the possibility of a molecule just barely grazing by all of them. The baffles decrease the pumping speed by about 20%.

For most organic pump oil molecules, the sticking probability is quite high, so for most applications, the baffles shown in the pumping tube are not necessary. (Furthermore, the average number of collisions with a cold surface would be much higher than one, even without the baffles, since one is the minimum.) Most commercially available cold traps do not require even one cold-surface collision for a molecule to migrate through.

3. Experience with the Trap

The trap described has been in continuous use on the 2-MV Van de Graaff Accelerator of the Nucleonics Division at the Naval Research Laboratory since its installation in June, 1953. It is used with a water baffle, an oil diffusion pump of a nominal 500-liter/sec pumping speed, a 100-liter/sec booster pump and a 5-liter/sec forepump. The normal period between cleanings is 6 months to 1 year. When the trap is freshly cleaned, its lifetime is 5 days on one filling of liquid nitrogen. (Since the capacity is 16 liters, the evaporation rate averages slightly over 3 liters per day.) At the end of about a year's continuous use, the lifetime drops to about 3 days, or about 5 liters evaporated per day. Thus, it will normally last over even a long, holiday week end without the necessity of refilling. And no foretrap is necessary.

It is believed that the amount of oil from the diffusion pumps migrating through the cold trap is completely undetectable. When the trap is removed for cleaning, there is always an

† The material used for the gold coating was called "Liquid Bright Gold". The total cost of the plating, including labor, was about $ 50. After this work was done, other materials, using an electroless process, have appeared on the market and our new cold traps are plated with one of them. A good silver plating would also serve as a good reflector (and therefore poor radiator) of infra-red radiation, but would be much more expensive than the processes mentioned above for gold plating.

accumulation of pump oil on the bottom surface of the inner can, and some on the bottom of the two lower baffles. But there is none in the upper part of the vertical pumping tube or on the "ceiling" above the vertical pumping tube. There is also a sizable accumulation of a different type of oil at the end toward the Van de Graaff vacuum system, indicating the removal of appreciable amounts of oil from that system. This oil has a yellow hue and comes from the "○"-rings used with the flanges on the rest of the vacuum system. It is believed that the amount of pump oil migrating through the trap, even without the baffles, would be insignificant compared with the "○"-ring source of oil vapor.

The philosophy which led to the large size of the design can best be expressed in the form of a question. Why store the liquid nitrogen in a separate Dewar flask and therefore lose the liquid nitrogen by evaporation simultaneously in two different vessels when one vessel can perform both functions? Many laboratories solve the nighttime and week-end filling problems by the use of automatic filling systems operating from a supply of liquid nitrogen in a large commercial Dewar flask. Such systems are not only expensive and wasteful of liquid nitrogen, but they are sometimes unreliable. The philosophy in the current design has been therefore to use the same container for both storage and trapping. If no other uses are required for liquid nitrogen, the cold trap could be designed to have a capacity just equal to the size of a commercial Dewar delivery container multiplied by the transfer efficiency, which is fairly high, greater than 85%; and deliveries could be scheduled to coincide with filling needs. If minor, irregular uses occur for liquid nitrogen in other applications, the required amounts may be withdrawn from the trap with no particular difficulty, using a transfer tube similar to the one described below for transferring the liquid nitrogen from the delivery flask to the trap.

Since the present trap has a capacity of 16 liters of liquid nitrogen, a fifteen-liter delivery flask may be used to refill the trap with no wastage when the level of liquid nitrogen drops to the one-fifth mark. If a larger capacity trap is made, the horizontal dimension should be increased to tend to minimize the surface-to-volume ratio, and thus radiation heat transfer. The present trap was designed to fit into an existing vacuum system. Otherwise, the length would have been made somewhat shorter and the diameter somewhat larger in order to increase both pumping speed and lifetime.

Filling the cold trap is a very simple operation. The transfer device consists of a metal tube, long enough to reach to the bottom of the delivery Dewar flask, surrounded at the top by a rubber stopper, with another tube leading to a source of compressed nitrogen, and capable of supplying this pressure to the region outside the first tube, but inside the flask. Thus a pressure of about 10 psi (gage) is applied to the top surface of the liquid in the flask, forcing the liquid up through the metal tube, which has a rubber-tube extension leading through one of the three thin support tubes at the top of the trap. Constant vigilance is not required during the filling operation which takes about 10 minutes if the trap is warm at the start; only about 8 minutes are required if the trap is cold.

Although compressed air could be used for the filling operation, it is not so used at this Laboratory because of the possible hazards associated with the long operating periods of the trap. Since oxygen has a higher boiling point than nitrogen, the use of compressed air would contaminate the liquid nitrogen with oxygen, which would then distill differentially with respect to the nitrogen. That is, the oxygen would tend to accumulate as long as the trap remained cold, perhaps a year or longer. Thus, possible large concentrations of liquid oxygen could build up with possible explosive consequences.

The trap can be cleaned without disassembly, if one allows it to warm up, and torches the outer can; but this procedure is not normally used. The trap is usually disassembled for cleaning, with a small charge of liquid nitrogen still in it. The purpose of retaining the liquid

nitrogen during the disassembly is to keep the trapped material on the inner surfaces until they no longer are adjacent to the other surfaces of the trap, or vacuum system. Cleaning is normally done with standard laboratory cleaning solvents such as trichloroethylene, acetone, and ethyl alcohol.

When the trap is reassembled, it is pumped on a forevacuum (with a glass liquid-nitrogen-filled foretrap next to the forepump) for several hours before filling it. During this period, the outside can is heated to about 60° C by a hand torch. This procedure purges the inner surfaces (of the outer can) of the residue from the previous cleaning process, thus improving their reflectivity. The flanges on each end are not heated quite so much because of the "○"-ring gaskets. The low heat conductivity of the stainless-steel wall allows one to heat the wall quite close to these flanges without actually raising the flange temperature much.

For systems requiring extremely high vacua, metallic gaskets could be installed, and much higher baking-out temperatures could be used; or the system could be completely welded or soldered. Nuclear particle accelerators cannot achieve extremely high vacua because of the leak of ion source gas. Therefore the method described here is satisfactory for such systems.

4. Comparison of Oil and Mercury Systems

Since the use of the cold trap described herein obviates most of the disadvantages in the use of oil diffusion pumps, it is worthwhile to reassess the relative merits of oil diffusion pumps and mercury diffusion pumps. Some disadvantages of mercury pumps are listed, with comments significant to the present discussion.

1. Inability to pump heavy organic molecules, such as forepump oil. Since the mercury atoms (or molecules) are quite light compared with the heavy forepump oil molecules, the mercury pumps cannot prevent the migration of forepump oil through the system.

2. Extra trap required. The above situation necessitates the use of an additional trap, one between the forepump and diffusion pump to prevent this migration. This extra trap is also necessary to prevent the Hg vapor from migrating to the forepump and fouling it.

3. Inconvenience of foretraps. Since the gas pressures between the diffusion pump and forepump are quite high compared to those encountered by a high-vacuum trap, the rate of heat transfer is much higher with consequent shorter life. Thus, keeping foretraps filled over weekends is very inconvenient.

4. Inefficiency of foretraps. Because of the higher heat transfer encountered with foretraps, liquid nitrogen is seldom used. Instead, a combination of solid carbon dioxide and acetone is normally employed, with a consequent lower trapping efficiency. Thus the migration of forepump oil through the diffusion pump is still a possibility.

5. Health hazard. Mercury is a health hazard, especially in case of vacuum system accidents. Mercury is extremely difficult to remove from irregular surfaces because of its high surface tension.

6. Higher initial cost. Oil pumps are less expensive and smaller for equal pumping speeds.

7. Mercury amalgamation. Mercury dissolves many common metals used in vacuum systems. For example, it would not be possible to use gold or silver plating on a cold trap used for mercury. Also mercury dissolves silver solder and fouls ion gages.

8. Shorter cold trap life. In addition to precluding the use of high infra-red reflective coatings, such as silver and gold, on the surfaces of the trap, the mercury vapor which is trapped on the cold surfaces forms a high-heat-transfer "black-body" coating, thus increasing the liquid-nitrogen evaporation rate.

NUCLEAR INSTRUMENTS AND METHODS 8 (1960) 217–220; NORTH-HOLLAND PUBLISHING CO.

ENERGY DEGRADING-FOCUSING OF CYCLOTRON BEAM†

W. J. RAMLER, J. L. YNTEMA and M. OSELKA

Argonne National Laboratory, Argonne, Illinois

Received 24 May 1960

The ANL 60-inch cyclotron is a fixed 10.8 MeV/nucleon accelerator. To increase machine flexibility, it was desired to obtain variable energy projectiles 25—40 feet from the accelerator without severely reducing particle number and beam definition. Sacrificing energy resolution, a focused variable energy beam can be obtained by using the technique of a foil absorption system close coupled with strong focusing provided by quadrupole magnets. The system to be described can readily degrade a deuteron or alpha beam to about 2.5 MeV/nucleon with about 5% of the original particles focused a distance of 35 feet from the accelerator[1]).

1. Focusing and Degrading System

The data to be reported were obtained with the focusing system of fig. 1. Deuterons and alpha projectiles were used with 15% of the total deflected beam focused by the first quadrupole set into a 3 mm diameter concentration at the foil degrader. The beam leaving the acceleration chamber, unit 1, is astigmatic with a total horizontal and vertical divergence of 2° and 0.2°, respectively. Without activating the squeeze coil, unit 3, the cross section of the beam at the entrance to the first quadrupole set, units 5 and 6, is $\frac{1}{2} \times 2$ inches. The inside diameter of the evacuated beam tube is 2 inches and to conserve beam, the lens system first focuses the 2 inch beam dimension. The data to be reported were obtained without the use of the squeeze coil.

Positioning of the focused beam upon the foil degrader to compensate for slight shifts introduced by the machine from day to day is accomplished by unit 7, the first vertical and horizontal deflection magnet[2]). This magnet is an iron core cylinder 12 inches in length, with an I.D. of about 2 inches. Within the inner volume a uniform field whose vector direction (0–360°) and magnitude can be varied to effect beam position.

For the data obtained, the switching coil, unit 8, was not used and the particles were focused on the 0° trajectory. The foil degrader, unit 11, consists of two circular discs, remotely controlled and extensively water cooled. Each disc is independently controlled, and contains 9 apertures to provide a total of 81 absorber steps from 0 to 400 mg/cm² of aluminum. The disc aperture or foil size is one inch with a spacing of 1.5 inches between the foils of the two discs.

The degrader is closed coupled to the second quadrupole set, units 12 and 13, with a distance of $14\frac{1}{2}$ inches between centers of the degrader and unit 12. These quadrupoles function as a 2 inch diameter collecting lens for the degraded and scattered projectiles. Focus currents are adjusted to obtain slightly convergent particle trajectories into the third lens set, units 15 and 16. The dimensions of these units were chosen to be compatible with the required focal lengths and available power supplies.

The third lens set, units 15 and 16, focuses the beam into the experimental tunnel, a distance of 35 feet or more from the cyclotron. The fourth quadrupole set permits beam focusing for distances greater than 35 feet from the cyclotron.

2. Degraded-Focused Beam Currents

Using the described system, deuteron and alpha beams were degraded from 10.8 to about

† Based on work performed under the auspices of the U. S. Atomic Energy Commission.

[1]) W. J. Ramler, Nuclear Science Series Report No. 26, Sector-Focused Cyclotron, p. 266–269.

[2]) R. Benaroya and W. J. Ramler, Unpublished.

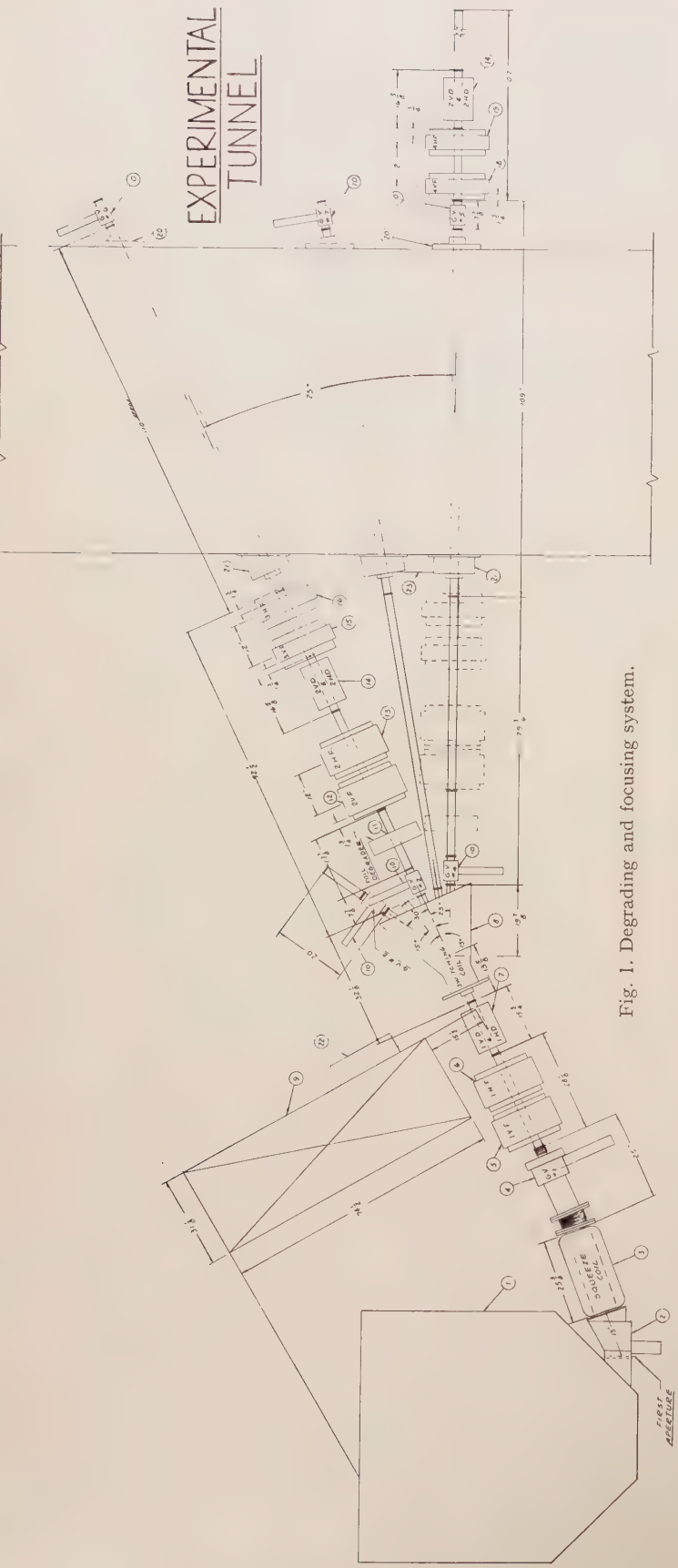

Fig. 1. Degrading and focusing system.

2.5 MeV/nucleon and focused into the experimental tunnel. The beam currents obtained in the tunnel are given by the normalized data of fig. 2. These data were obtained for an input current I_0 of 2.5 μA. Sampling checks at operating currents of $I_0 = 10\ \mu$A, showed that the given curves applied for higher operating levels.

Curve A of fig. 2 relates focused deuteron beam current and energy at a distance of about 20 feet from the degrader. These data were obtained without apertures in the 2 inch I.D. evacuated tube. Beam size was checked at the target by autoradiographing and the resultant pattern was oblong in shape. For the 21.6 MeV beam the cross sectional area was about 0.15 cm^2; 0.5 cm^2 at 15.5 MeV; and 2 cm^2 at 8.8 MeV.

The effect of collimation was determined by the use of two collimator sets, curves B and C. Each system was placed directly in front of the current collecting target. At full energy operation, the target current ratio of the systems, equals the ratio of the aperture areas; 3.5 to 1. The ratio of aperture area to the total unrestricted beam area does not compare favorably with the corresponding target currents. This discrepancy is due to the noncircular beam shape, spatial variation in the particle density, double collimator effects and possible misalignment. From past operating experience, the ratio of I_f/I_0 for the $\frac{1}{8}$ inch collimating system can equal or exceed 5% at full energy as compared to the plotted 1%. Thus, misalignment is quite possible and the plotted aperture curves are pessimistic but certainly representative of what can be obtained from day to day operation.

Alpha beam performance, fig. 2 curve D, exceeds that of deuterons, curve A, for the same geometry. Since the mean scattering angle for these two particles varies approximately with $M^{-\frac{1}{2}}$, it is to be expected that the focusing efficiency be greater for alphas than deuterons. The ratio of alpha to deuteron target current for a given E_f/E_0 compares favorably with calculations[3]) to determine the particle number,

[3]) W. C. Dickinson and D. C. Dodden, A Method for Evaluation of Multiple Scattering Effects in Charged Particle Experiments, L. A. 1182 (Dec. 1, 1950), Unpublished.

alpha or deuterons, accepted by the lens system. For example, for $E_f/E_0 = 0.4$, the ratio of target currents (curves A and D) I_α/I_D is 1.85 as compared to the calculated value of 1.9.

The limitation of the system to efficiently accept and focus low energy projectiles is shown by the break in curve D at $E_f/E_0 = 0.3$ or about 3.2 MeV/nucleon. This limitation is determined by the scattering angle, the distance between the degrader and the collecting lens set and the aperture of the lens. For the mean scattering angle of 3.5 degrees (3.2 MeV/nucleon alpha) and a 2 inch opening, this distance is computed to be about 16½ inches or the approximate distance between the degrader and the center of the unit 12 quadrupole.

The focusing system throughout the collecting of these data performed in a set pattern. The focusing power of the first quadrupole set remained fixed with the given beam focused on to the degrader. For each change in particle energy, the second and third quadrupole sets were optimized for maximum focused particle number. In general, the change of focusing current to each quadrupole was in direct proportion to the change in particle energy.

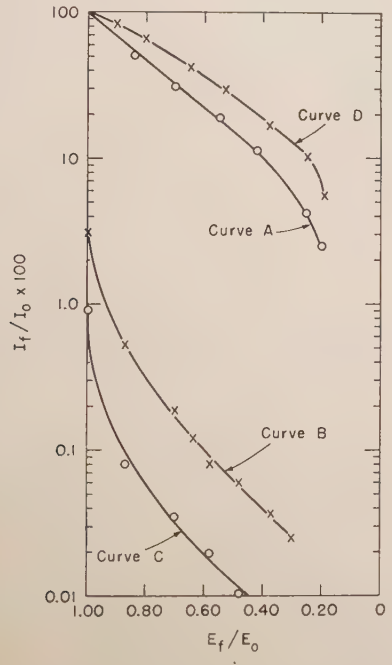

Fig. 2. Focused beam current vs. degraded beam energy. Curve A: deuterons, no collimation; B: deuterons, 2⅛ inch apertures spaced 30.5 inches apart; C: deuterons, 2 15/64 inch apertures spaced 34 inches apart; D: alphas, no collimators. I_0 and E_0 are the magnitude of current and beam energy prior to degradation. I_f and E_f are the resultant current and beam energy at the target.

3. Energy Spread

To complete the characterization of the system an analysis was performed to determine the energy spread in the degraded deuteron beam. The degraded beam entered the 60 inch scattering chamber through a collimating system of two ⅛ inch diameter apertures spaced 30.5 inches apart. The incident deuterons were scattered by a Mg target 0.0004 in. thick and the scattered particles were detected by use of a double NaI(Tl) crystal. The first (dE/dx-) crystal was about 0.008 inches thick and the second (E-) crystal was about 0.060 inches thick. Observations were made at two laboratory angles: 30° and 76°.

It is to be recognized that the pulse height distribution in the E crystal has a finite width. The factors contributing to the width are:

(a) The energy spread in the original beam E_0.

(b) The distribution introduced by the absorber in front of the E-crystal (i.e., the dE/dx-crystal).

(c) Statistical fluctuations in the E-crystal and photomultiplier.

Contributions to the distribution due to the finite subtended angle of the detector and the target thickness are negligible in the present case.

The contributions to the energy spread of the first two causes, a and b, are assumed to be constant. The inelastic lines cover a fairly wide energy region and are, in general, sufficiently spaced to be well resolved individually. The separation of the 4.122 and 4.24 MeV doublet is small compared to the observed energy spread. Observation of the deuteron spectrum of deuterons scattered by Mg shows that the line width (i.e., full width and half maximum) of the deuteron peaks is constant for all energies over a range of about 10 MeV. From this, it is concluded that the contribution to the line width of

the fluctuations in the E-crystal photomultiplier system is also a constant.

To determine the energy spread due to the degrader, a sufficient amount of scattering chamber absorber was introduced in the incident beam so that the elastic deuteron peak due to the scattering of the degraded beam coincided with one of the inelastic peaks due to the full energy beam. If the full width at half maximum in the first case is δ_1 and in the second case δ_0, the energy spread due to the absorber is

$$\delta a = \sqrt{\delta_1{}^2 - \delta_0{}^2 - 2.36\,\sigma_a}\,.$$

For lower energies of the degraded beam, 10 MeV or less, the background problem is less severe and a single crystal was used for detection. For these lower energy data, it is again assumed that the energy distribution due to the inital energy spread in E_0 and to fluctuations of the crystal-photomultiplier system are constant.

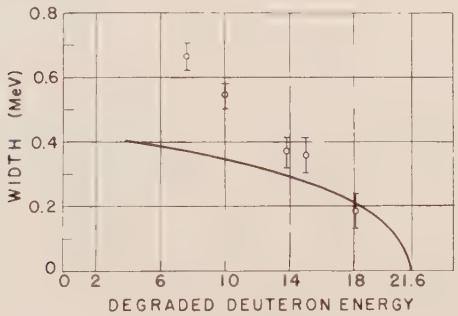

Fig. 3. Degraded deuteron beam energy spread vs. degraded beam energy. The curve has been calculated using the expression from ref. [4]).

The experimental data points given in fig. 3 were obtained by assuming that the distribution curve was normal. It should be noted that, as is to be expected, for large values of X, the distribution curve was skew. These experimental data are compared to calculated beam energy spread given by the solid curve of fig. 3. This calculated curve was obtained for the case of a monoenergetic beam of particles which has been transmitted through a thickness of absorber X. The second moment of the energy distribution of the particles is given, according to Livingston and Bethe[4])

$$(\Delta E)^2 = 4\pi e^4 Z^2 N Z X$$

where eZ is the charge of the incident particle, N the number of atoms per cm^3 of the absorber, Z the atomic number of the absorber and X the path length. This expression can be expected to give fairly good agreement with experiment for small values of X. For absorption up to 8 MeV, or an E_0/E_f of about 0.6, the calculated and experimental data are in good agreement. For larger values of absorption, the experimental points are above the calculated values.

4. Conclusion

The technique described is not limited to the reported projectiles but could be used for protons or other heavy ions. Since the mean scattering angle is approximately proportional to $M^{-\frac{1}{2}}$, the efficiency of focusing will increase with ion mass for degraded particles. The energy spread varies as $M^{\frac{1}{2}}$ and will increase with heavier ions.

The described system provides experimental flexibility to a fixed MeV/nucleon accelerator. If energy resolution is not of primary importance, it provides a quick means of obtaining energy dependent data. In addition the degraded beam can be projected many feet from the accelerator into a low background area and the cross sections of the beam can be readily controlled to maximize the efficiency of the irradiation.

Acknowledgments

The authors wish to recognize the assistance of P. Sorensen and E. Sundahl for the mechanical design of the degrader; E. Sundahl for the construction of the degrader; W. O'Neill for his work on the degrader control circuitry; and R. Benaroya for the design of many components of the external beam focusing system.

[4]) M. S. Livingston and H. A. Bethe, Rev. Mod. Phys. 9 (1937) 245.

NUCLEAR INSTRUMENTS AND METHODS 8 (1960) 221–224; NORTH-HOLLAND PUBLISHING CO.

AN INSTRUMENT FACILITATING THE MEASUREMENT OF SMALL-ANGLE SCATTERING IN NUCLEAR EMULSION

A. G. C. TENNER, B. JONGEJANS and H. WITTEVELD

Natuurkundig Laboratorium der Universiteit van Amsterdam

Received 29 May 1960

The assembly of components constituting the instrument is described. Special attention is paid to the essential features. The wiring diagrams are given. The experience obtained with the instrument in the first months of operation classifies it as a satisfactory new tool in nuclear physics. The principle underlying the instrument can be extended to bubble-chamber film.

1. Introduction

The scattering of an elementary particle by nuclei is a phenomenon of fundamental importance for gaining insight into the interaction between this particle and nuclear matter. With increasing energy of the particle scattering tends to be confined to small angles. The observation of small angles (e.g. < 2 degrees) in emulsion presents special difficulties. The instrument to be described facilitates the measurements of projected angles between 0.2 and 4 degrees. We have named the instrument "Hasem".

2. Description

The instrument consists of a microscope and a mechanical recorder. The main performances should be:

1. Possibility of observation of small kinks in nearly straight lines.

2. High operation speed enabling large quantities of information to be handled in reasonable time.

The microscope is a combination of a microscope head (Leitz Laborlux III) and a lathe bed with carriage. Being of rigid construction, this carriage easily permits coupling of the X-coordinate movement to an electric motor. The range of the X-displacement amounts to 25 cm, that of the Y-movement to 5 cm. The positions in X- and Y-direction can be read on dials with an accuracy of one micron. The position of the stage is reproducible within 5 microns. The mechanical recorder is moved in the X-direction by a direct mechanical joint. In the Y-direction the connection is made by magslips. A view of the instrument is given in fig. 1.

3. Characteristics

The most important features will be discussed now.

a. Requirements for moving the stage:

1. A high speed, resetting stage and recorder into the initial position after having finished a specific track. Stage speed: 8 mm/sec.

2. A low speed adjustable within a certain region. This region comprises an operational speed with a maximum estimated value of 0.16 mm/sec and a minimum speed value slow enough for scrutinizing difficult passages, 0.032 mm/sec.

The extreme values of the velocity are spanned by a special D.C. motor. The motor is coupled to the screw spindle of the microscope stage by means of a cardan joint and a worm gear.

b. The connection of the Y-motion of the microscope stage to the recorder is made by a set of magslips. One magslip is mechanically coupled to the Y-motion of the microscope stage, the other guides the writing lorry. The electric circuit is drawn in fig. 3.

The D.C. component of the double EL 34 ensures

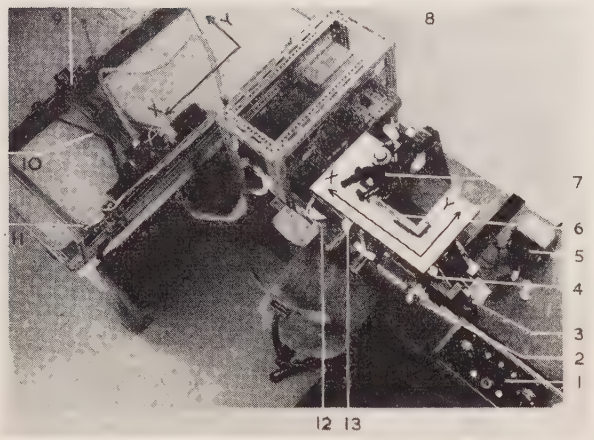

Fig. 1. View of the instrument.

1. Control panel, regulating speed and sense of the motor and locking or unlocking the writing lorry (10).

2. Knob controlling the Y-position of the microscope stage. This knob is fixed to the moving stage.

3. Calibrated disc enabling the reading of the X-position of the stage by indicating parts of the revolutions of the screw spindle.

4. Centimeter lath giving additional information regarding the X-coordinate.

5. Transformer for microscope light. The alarm bell attached to the transformer starts ringing just before the microscope stage reaches its mechanical stops.

6. Microscope stage with an emulsion plate. The plates are provided with copper strips for defining the position.

7. Microscope head. The objective is moved for focussing, the Z-position is therefore read on a dial indicator, also mounted on the head.

8. Electric motor, moving stage and recorder in X-direction. The motor is mounted independently to avoid vibrational disturbances of the microscopic field of view.

9. Recorder on table. On the right-hand side of the recorder the magslip and a 2-phase motor are visible. The latter brings the magslip into the right position.

10. Writing lorry, provided with a ball-point. The ball-point writes under a weight which can be lifted by an electromagnet.

11. One of a series of switches that interrupt the motor current when the instrument reaches the end of its range.

12. Control knob X and Z. With the aid of two hands three directions of motion must be kept under control. Two of them are combined in one hand. The principle will be clear from fig. 2.

13. Dial indicator for reading the Y-position of the stage.

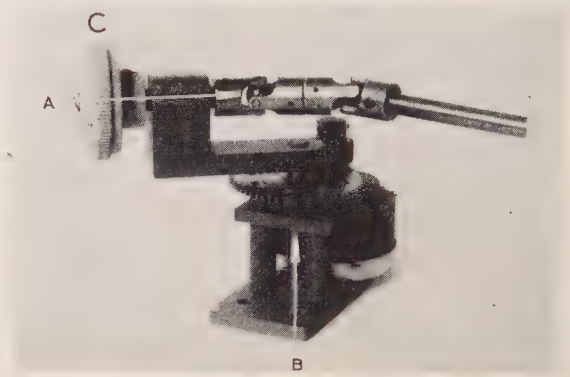

Fig. 2. Sketch of the principle of double rotation. Knob C can be rotated around its axis A; C then governs the focussing device. Knob C can also be rotated about axis B to set a potentiometer regulating the motor speed. The joint bends but still transmits rotations to the microscope.

the necessary damping of the system. The feedback with a capacitor of 0.27 μF decreases the internal resistance of the triodes. The amplification can be regulated by changing the voltage of the anodes of the output triodes. The resolution of the whole system of magslips and writing lorry amounts to 5 microns in the emulsion.

This resolution is adequate for the purpose of our angle measurements.

c. The backlash in the X-direction between the stage and the recorder amounts to 50 microns. Track-following is always done in one direction so that backlash does not occur in the result. For the Y-direction a mechanical backlash compensation is incorporated into the servosystem. Backlash in Y is not noticed on the recording sheets.

d. The angular amplification is brought in by

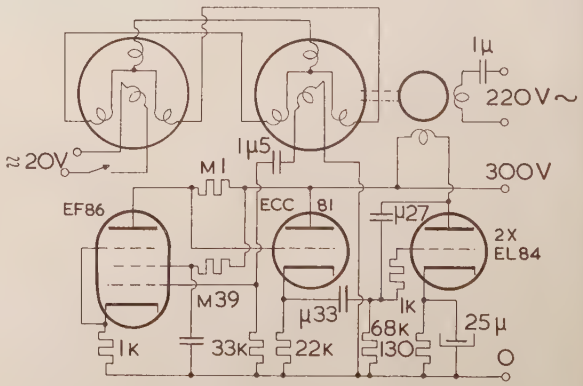

Fig. 3. Diagram of the servosystem.

amplifying the X-coordinate by 9.192 and the Y-coordinate by 97.86. Roughly speaking this amounts to an angular amplification of 10.

Exact relations between the various angles involved are easily derived. It will be clear that scattering angles smaller than 2° which up to now presented a stumbling block to emulsion

measurements[1]) are within the scope of this instrument.

4. The Electric Circuit

The diagram of the circuit is shown in fig. 4.

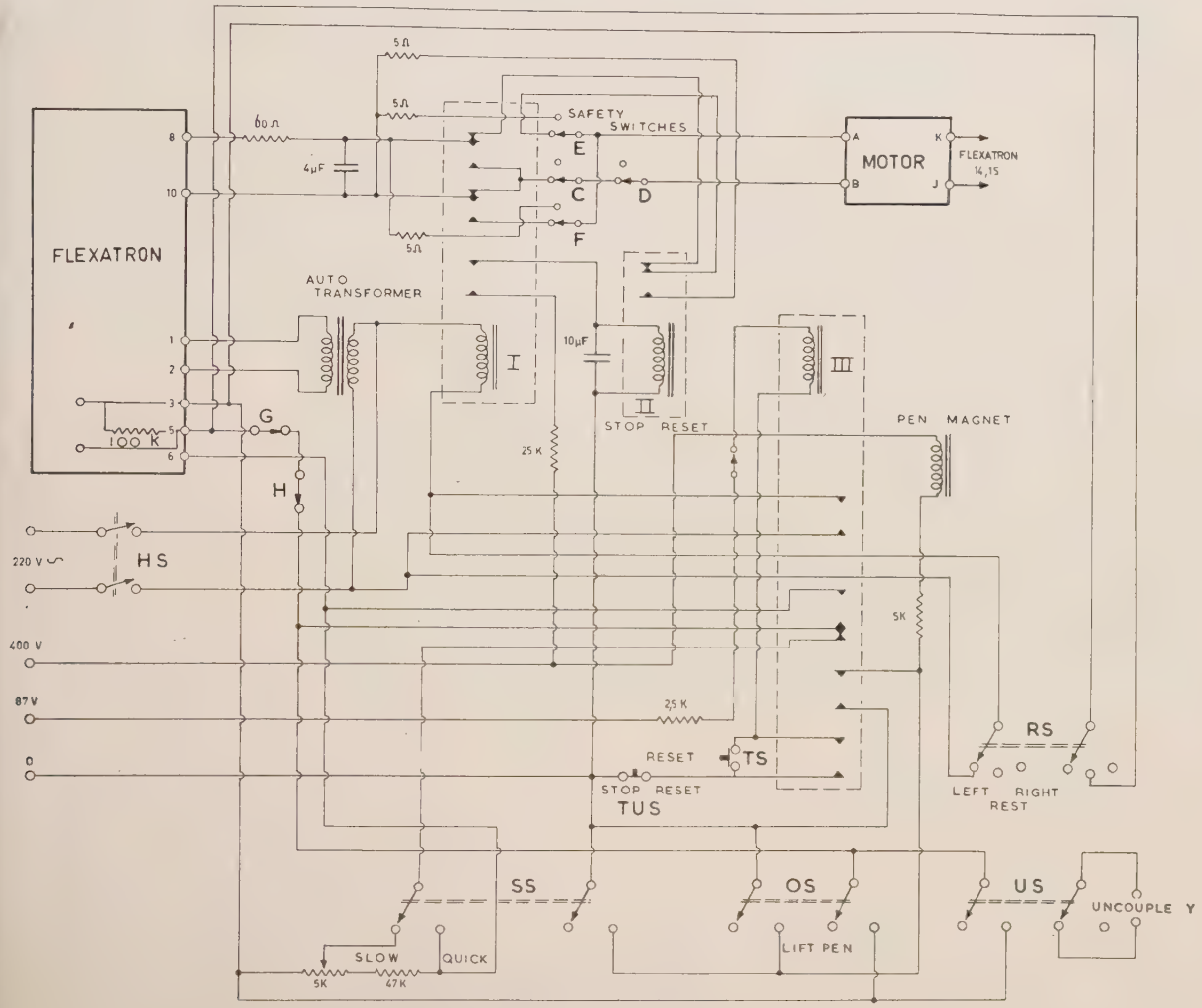

Fig. 4. Diagram of the electric circuit.

Flexatron is a trade name for the feeding unit of the motor. The *RC* circuit of 60 Ω, 4 μF is an additional element to increase speed constancy. Relay I determines the direction of the movement; switches C, D, E and F determine the end of the range of the recorder table. In the *X*-direction (E and F) the motor current is interrupted and the motor shunted for direct stopping. When either E or F is interrupted the motor can at once be operated in the opposite direction. Switches G and H are mounted on the microscope. When they are pushed in, the motor stops. They prevent mechanical damage to the microscope. Relay III operated by TS restores the instrument to the starting position. When this position has been reached, relay II shunts the motor with 5 Ω.

In addition, there are hand switches for the sense of motion (RS), for uncoupling the writing lorry (US), for lifting the ballpoint (OS), for operation at high speed (SS).

[1]) A. Barbaro *et al.*, Nuovo Cimento 9 (1958) 154.

5. Concluding Remarks

The "Hasem" has been operating for several months. Breakdown is becoming rare. The accuracy with which deflections can be measured is 0.06°. This is found by comparing the repeated values of one single measurement. The speed of operation is around 50 cm/h emulsion track. The average attainable speed of production is about 20 cm/h including refollowing tracks, searching for new tracks, making records of the starting points etc.

The tracks on the recording paper have to be scanned afterwards for recognizing deflections and determining the followed length. This amounts to $\approx 20\%$ of the tracing work.

The operation of the instrument is at present continuous over a period of two hours. After this time the observer's place is taken by another person. The operation of the instrument does not require more technical skill and ability than is necessary for ordinary microscopical work. The instrument in its present state only permits the measurements of projected angles. Now that it has been proved that the construction works adequately, the simultaneous recording of the projection of a track on the ZX plane and XY plane can be undertaken. A second version of the instrument incorporating this improvement is under construction.

The angular magnification of 10 now chosen can be easily enlarged because only simple geometrical considerations determine the magnification. The limit of magnification is determined by spurious scattering of the emulsion. We have the feeling that this effect sets in at angles smaller than 0.2°. However, no systematic search for this limit has been made.

In our opinion it seems possible to measure the diffraction scattering of particles in nuclear emulsion up to several tens of GeV with an apparatus based on the principle of the instrument described. It may be observed that the principle of angle magnification can also be used in the analysis of small-angle scattering on bubble-chamber film.

Acknowledgements

The construction of the instrument is part of the Research Program of the Foundation for Fundamental Research of Matter (F.O.M.), financially supported by the Netherlands Organization for Pure Scientific Research (Z.W.O.).

The authors are indebted to Professor G. W. Rathenau for his interest in the present work.

The criticism of our colleagues is appreciated.

NUCLEAR INSTRUMENTS AND METHODS 8 (1960) 225–229; NORTH-HOLLAND PUBLISHING CO.

NEUTRON FLUX MEASUREMENTS FROM 100 keV TO 4 MeV WITH A MODIFIED LONG COUNTER

E. TOCHILIN and R. V. ALVES

U. S. Naval Radiological Defense Laboratory, San Francisco 24, California

Received 23 May 1960

Long counter response to neutrons from a 2-MeV positive ion accelerator was investigated with three instruments which were identical except for the thermal shields within their outer cores. These shields consisted of B_2O_3, Cd, and polyethylene sleeves. For neutron energies ranging from 0.1 to 4 MeV no differences in relative response were observed for the three counters. Measurements made with indium strips placed along the axis of the counter in place of the conventional BF_3 detector showed that the foil technique could significantly extend the intensity range of the counter at no sacrifice in energy response.

1. Introduction

In the course of work at NRDL the Hanson-McKibben long counter has proved invaluable as a simple, reliable instrument for measuring neutron flux[1]). Long counter sensitivity is reasonably uniform with energy for neutrons from 0.02 to 9 MeV. A typical response curve is given in fig. 1 [2]). To measure neutron flux one needs only to reproduce the original counter assembly and to calibrate with a neutron source. With adequate care 5 percent accuracy can readily be obtained over the range from 100 keV to 5 MeV [3]).

Although the long counter has found wide use in the field of neutron physics, some of its characteristics are not well defined. These include: (1) energy response as a function of shielding material, and (2) energy response as a function of different thermal detectors. The purpose of this study was to investigate, over a range of neutron energies, the effects produced by varying these parameters. The subsequent findings show that construction of the thermal shield can be simplified and that the intensity range of the counter can be significantly extended.

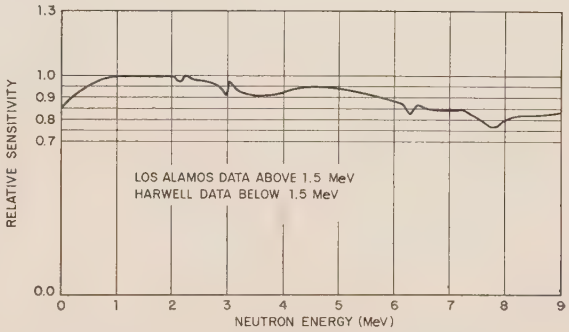

Fig. 1
Long counter efficiency as a function of neutron energy.

2. Influence of the Thermal Shield on Long Counter Response

The original long counter consists of a paraffin cylinder with a $B^{10}F_3$ detector along the axis. This central cylinder is surrounded by a B_2O_3 sleeve and is contained in an additional paraffin sleeve which lowers the response to scattered neutrons. These outer additions are referred to as the "shield". Fig. 2 shows the Precision Long Counter proposed by DePangher[3]). Construction details are similar to those of the Hansen-McKibben counter except that polyethylene rather than paraffin is used to provide better

[1]) A. C. Hanson and J. L. McKibben, Phys. Rev. **72** (1947) 673.

[2]) W. D. Allen and A. T. G. Ferguson, Proc. Phys. Soc. A **70** (1957) 639.

[3]) J. DePangher, Neutron Measurements III: Calibration of Long Counter No. 2 with Radioactive Neutron Sources, Hanford Laboratories Report HW-56199 (1958).

mechanical rigidity and a more uniform density. For calibration checks, the removable rod in the central cylinder is replaced with a PuBe neutron source.

One phase of the present study was to check the effect of the B_2O_3 shield on long counter response. This was of interest for two reasons:

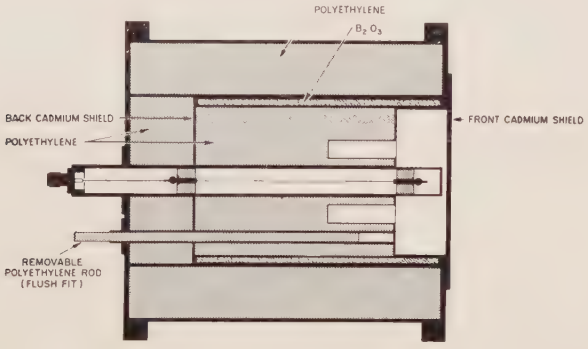

Fig. 2. Precision Long Counter.

(1) anomalous results obtained by several experimenters have been attributed to the drying out of the B_2O_3 filling, and (2) construction of the thin aluminium shell for the filling material is a delicate machining process which could be eliminated by substitution of a rigid thermal shield such as cadmium.

For this study, two long counters were constructed. One was similar to that of fig. 2 except that the outer shield contained paraffin rather than polyethylene. The B_2O_3 sleeve was removable and could be exchanged for a polyethylene sleeve of identical dimensions. The second counter had a permanent Cd sleeve, 0.020 in. thick, in place of the B_2O_3 filling.

Using the Cd-sleeved counter as a reference, comparisons were made between the B_2O_3- and polyethylene-sleeved long counters by simultaneously exposing the Cd counter and either of the other two units to monoenergetic neutrons from a 2-MeV Van de Graaff accelerator. The

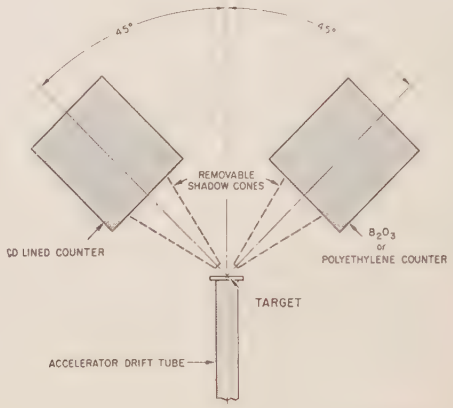

Fig. 3. General view of exposure conditions.

Table 1

Operating conditions for obtaining neutrons from the Van de Graaff accelerator

Reaction	Target material	Target thickness (μg/cm^2)	Particle energy (MeV)	Neutron energy at 45° (MeV)
$T(p,n)He^3$	Zr-T	1000	1.1–1.9	0.06–0.75
$C^{12}(d,n)He^3$	C	171	1.1–1.9	0.77–1.20
$D(d,n)N^{13}$	Zr-D	1902	0.5–1.5	3.0 –4.0

experimental arrangement is shown in fig. 3. Runs were also made with a shadow cone placed between target and inner core. These measurements determined the relative efficiency with which Cd and B shielded the detector from neutrons thermalized outside of the central core.

Monoenergetic neutrons ranging from 0.06 to 4.0 MeV were obtained by using $T(p,n)He^3$, $C^{12}(d,n)N^{13}$, and $D(d,n)He^3$ reactions. Table 1 lists the pertinent data necessary for calculating the available neutron energies. Because the targets made an angle of 45° with the beam, the effective target thickness was $\sqrt{2}$ times the thickness given in Column 3. Neutron energies as a function of laboratory angle and bombarding energies were taken from tables prepared by

Fowler and Brolley for $T(p,n)He^3$ and $D(d,n)He^3$ reactions[4]). The $C^{12}(d,n)N^{13}$ neutron energies were obtained from the data of DePangher[5]). An 80-g PuBe source was used as a neutron standard.

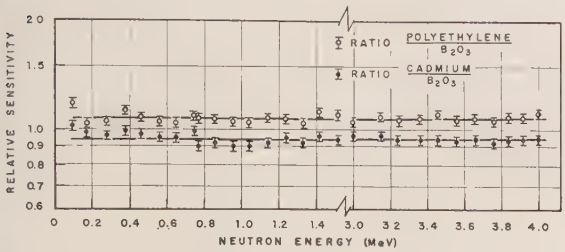

Fig. 4. Relative sensitivity of B_2O_3-, Cd-, and polyethylene-lined counters.

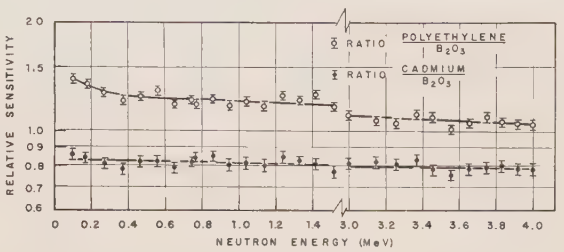

Fig. 5. Relative sensitivity of B_2O_3-, Cd-, and polyethylene-lined counters with shielded central core.

Response of the Cd- and polyethylene-lined long counters relative to the standard B_2O_3 counter is shown in fig. 4. A straight line can be drawn through both sets of data. The relative sensitivities of the Cd- and polyethylene-lined counters to the B_2O_3-lined counter are 0.94 and 1.08, respectively.

Fig. 5 is a similar comparison with the central core shielded by means of a shadow cone as indicated in fig. 3. The Cd/B "shielding" ratio remains reasonably constant at an average value of 0.8. However, the relative sensitivity of polyethylene/B varies with energy, decreasing from 1.4 at 0.1 MeV to 1.05 at 4.0 MeV. This moderate change in shielding efficiency at low energies is not significant since neutrons coming through the shield produce no more than 10 per cent of the total counts.

Table 2 gives data obtained under similar conditions with a PuBe neutron source. Given in Column 4 is the ratio of counts obtained with and without presence of the shadow cone. From 20 to 30 percent of the counter response is from neutrons originating in the outer shield of the detector. For energies from 0.1 to 1.2 MeV, 7 to 12 percent of the Cd-lined counter response was from the outer shield in contrast to 20 percent observed for PuBe neutrons. Column 5 gives the count rate obtained when the counters were rotated 90° so that the tube axis was perpendicular to the source. Column 6 gives the relative sensitivity of the counters for normal vs perpendicular incidence. Despite the impressive mass of moderator surrounding the detector, the shielding properties of the counter to stray neutrons of these energies are poor. Neither the boron nor the cadmium thermal shields had any significant effect on the amount of scattered radiation reaching the detector.

Table 2

Primary and secondary response of three long counters exposed to PuBe neutrons

Type of counter lining	Counts per minute		Ratio Cone / No cone	CPM with counter rotated 90°	Ratio Counter at 90° / Counter at 0°
	No cone	Cone			
Boron	4033	1008	0.25	2399	0.58
Cadmium	3904	801	0.20	2025	0.53
Polyethylene	4284	1287	0.30	2387	0.56

[4]) J. L. Fowler and J. E. Brolley, Revs. Mod. Phys. 28 (1956) 103.

[5]) J. DePangher, Neutron Measurement II: Operating Points for Obtaining Neutrons from the Hapo Positive Ion Accelerator, Hanford Laboratories Report HW-55085 (1958).

3. Use of Indium Detectors in the Long Counter

There are inherent limitations in the use of a proportional counter device whenever high-intensity or pulsed neutron beams are encountered. One possible method of measuring such fluxes is by activation of gold or indium foils placed along the axis of a long counter in place of the conventional BF_3 detector. However, boron is a strict $1/v$ detector while both gold and indium exhibit strong resonances in the epithermal region. We therefore decided to investigate to what degree foil detectors could reproduce the energy response of a conventional BF_3 counter.

Indium strips, 10.5 in. long, 0.5 in. wide, and 0.020 in. thick, were located in the center of an aluminum shell which simulated the BF_3 tube. This assembly was placed in the long counter so that the foil occupied essentially the same sensitive volume as the original detector. Following exposure, the foils were rolled into a spiral and counted in a 3 in. $\times$ 3 in. well-type NaI scintillation counter. A second indium exposure, made in an Al shell wrapped with 0.020 -in. Cd, was used to determine what fraction of the bare foil activity was due to epithermal neutrons. It was assumed that the indium cross section below the Cd cut-off energy of 0.4 eV would cause the foil to behave as a $1/v$ detector in this region. Use of a thick foil also favored the response to thermal neutrons owing to the self-shielding provided by the outer surface in the resonance region.

Table 3 gives the relative indium-to-BF_3 counter response obtained with 0.4-, 1.2- and 4.1-MeV neutrons and with the 80-g PuBe neutron standard. The ratios in Column 2 are for bare indium foils while those in Column 3 are for the thermal response below the Cd cut-off. All ratios are normalized to the PuBe exposures. The beam was monitored with the BF_3 counter from which the average beam level and the neutron-induced foil activity was determined. Column 4 gives the ratio of activity for bare and Cd-shielded foils. Contributions from the epithermal region are seen to be less than 10 per cent which explains why no differences with energy were found in the relative response of the bare and Cd-shielded foils. For PuBe neutrons, the sensitivity of the BF_3 counter and indium detectors were 1.8 counts per n/cm^2 and 0.042 cpm (at time zero) per n/cm^2, respectively.

Table 3

Relative $\frac{\text{Indium}}{BF_3}$ detector response in a Long Counter

Neutron energy (MeV)	Ratio $\frac{\text{Bare In}}{BF_3}$	Ratio $\frac{\text{Thermal In}}{BF_3}$	Cd ratio
0.4	1.01	1.01	11.5
1.2	0.98	0.98	12.2
4.1	0.99	0.98	13.1
PuBe	1.00	1.00	12.2

The foil technique has subsequently been used to determine fast neutron flux from the University of California 60-in. cyclotron. Earlier measurements were made by (1) measuring fast neutron flux with a sulfur threshold detector utilizing the $S^{32}(p,n)P^{32}$ reaction and (2) measuring spectrum with nuclear track plates[6]). For the simulated fission neutron spectrum obtained from 12-MeV protons and a thick Be target, it was calculated that the sulfur detector, calibrated for 14.1-MeV neutrons, measured fast neutron flux with an efficiency of 28 percent.

To check this value an independent measurement of fast neutron flux was made with a long counter incorporating a gold foil detector. Gold rather than indium was used because of the high beam intensity. Calibration was performed with a PuBe neutron standard. The same effective center and counter sensitivity was assumed for both PuBe and cyclotron neutrons. Comparative values of fast neutron flux obtained with the sulfur-track plates vs long counter measurements agreed to within 4 percent.

4. Summary and Conclusions

Long counter response to monoenergetic neutrons ranging from 0.1 to 4 MeV were observed for three counters which differed only in

[6]) E. Tochilin and G. D. Kohler, Health Physics **1** (1958) 332.

the type of thermal shield used in the outer core. No significant difference in relative response was observed for the three counters. The measurements demonstrate that counter design can be simplified either by replacing the conventional B_2O_3 loaded aluminum shell with a 0.020-in. Cd wrapper or by eliminating the thermal absorber.

Measurements at 0.4-, 1.2-, 4.1-MeV and with PuBe neutrons were also made with indium strips replacing the BF_3 counter. These results showed that foils can be substituted for the BF_3 detector with no sacrifice in energy response. The foil technique is of value whenever high intensities or a pulsed neutron beam preclude the use of proportional counting techniques.

NUCLEAR INSTRUMENTS AND METHODS 8 (1960) 230–232; NORTH-HOLLAND PUBLISHING CO.

ON THE SEPARATION OF π^+ MESONS BY A TIME OF FLIGHT METHOD

G. M. LEWIS, E. GABATHULER and R. E. AZUMA

Department of Natural Philosophy, The University, Glasgow

Received 6 April 1960

A time analysing coincidence unit of short resolving time has been employed to separate photoproduced π^+ mesons from electrons and protons by a time of flight method. The positive pions are additionally identified by their decay characteristics, so that an assessment of the method as a mass discriminator can be made.

1. Introduction

This paper refers to the possibilities of distinguishing low energy π^+ mesons over short flight paths by time of flight methods (cf. fig. 1a). In this method, the reciprocal of the velocity v, and the scintillation response S defining the energy E of the particle in flight, are correlated graphically (cf. fig. 2). The method was developed initially as an alternative to $(dE/dx,E)$ methods of separation in the low energy region, since, in principle, the front crystal need not then be thick enough to give good resolution, but only thick enough to give an indicative time pulse. Reference should be made to the work of Janes and Kraushaar[1]), in the low energy region. Recently, alternative counter methods have been reported on, for the study of low energy π^+ mesons[2,3]).

2. Method and Procedure

The detection system used here is shown schematically in fig. 1a. The evacuated flight path is defined by two plastic scintillation counters; counter 1–1.5 × 1.5 × 0.03 ins., and counter 2–3 × 2 × 1 ins., placed 60 cm apart. Pulses from the collectors of the counters 1 and 2 cut off E180F limiter valves, which generate rectangular pulses 3×10^{-8} sec long. These two pulses overlap and operate the time analysing coincidence unit, illustrated in fig. 1b; this latter unit produces a pulse whose height varies as the time delay representing the time of

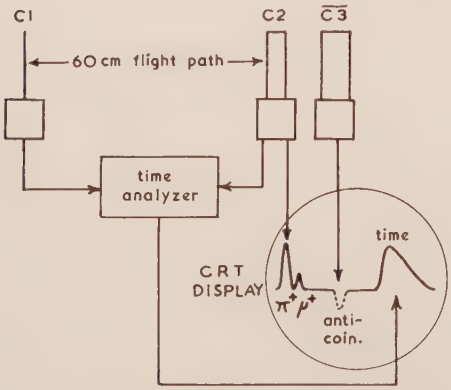

Fig. 1. (a) Detection system and mode of display.

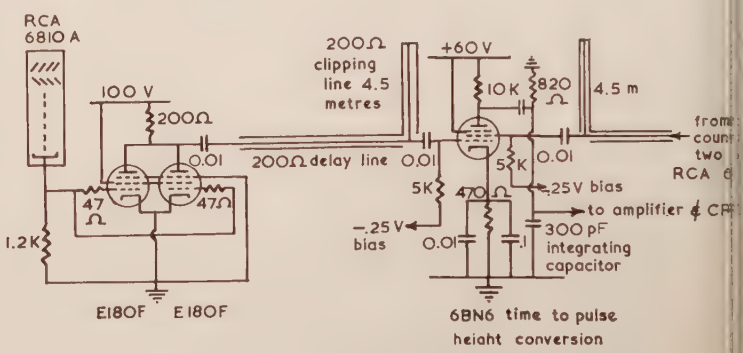

Fig. 1. (b) Time analysing circuit.

[1]) G. S. Janes and W. L. Kraushaar, Phys. Rev. **93** (1954) 900.

[2]) G. M. Lewis and R. E. Azuma, Phys. Soc. **73** (1959) 873.

[3]) J. G. Rutherglen and J. K. Walker, Nucl. Instr. and Methods **8** (1960) 239.

flight[4,5]). This time of flight pulse is used to trigger a Tektronix 517 A oscilloscope, and this pulse is also displayed on the fast time sweep, as a delayed pulse. The individual oscilloscope traces are photographed on film. On this same trace is also displayed the energy pulse from the 7th dynode of counter 2. To increase the power of the device, and to help in the assessment of the method, the dynode pulses from counter 2 lead into 100 ohm cable to give pulses approximately 10^{-8} sec wide. The π^+ particle can then be identified, and properly recorded, as both the π^+ and its 4.15 MeV μ^+ decay pulse are displayed as separate entities on the trace, provided that the particle lives longer than $\approx 10^{-8}$ sec. The time distribution of the π^+–μ^+ separation can also be made and checked with the 2.6×10^{-8} sec π^+ lifetime. Counter 3 serves as an anticoincidence counter for particles which pass right through counter 2. The pulses arising from counter 3 are appropriately delayed and displayed on the trace with inverse polarity, so that traces exhibiting such pulses can be rejected.

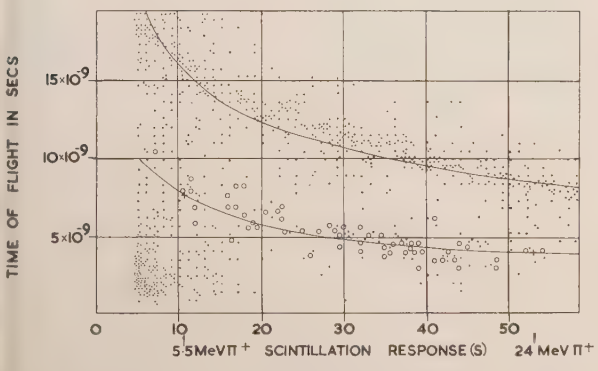

Fig. 2. Experimental results showing time of flight plotted against the scintillation response S, defining the energy E of the particle. This shows the identified π^+ mesons (o) in the meson band, the proton band, and the electron cluster ($\approx 2 \times 10^{-9}$ sec). All particles other than the identified π^+ mesons are represented by (·). + indicates the expected values for time of flight for the appropriate energy for π^+ mesons. Curves are shown of the expected time of flight v scintillator response S (cf. text) for a flight path of 60 cm for π^+ mesons and protons.

[4]) G. C. Neilson and D. B. James, Rev. Sci. Instr. 26 (1955) 1018.

[5]) R. E. Azuma and G. M. Lewis, Phil. Mag. 2 (1957) 1325.

An approximate time calibration for fig. 2 was effected with the aid of the more energetic electrons from an In^{114} β-ray source passed into the system, and inserting various lengths of delay cabling between the counters and the time analysing unit. This time calibration, however, when applied to mesons and protons could be uncertain by $\approx 10^{-9}$ sec, because of the variation in pulse rise time as a function of pulse height. A resolving time of 7×10^{-10} sec, (half-width at half-height) was obtained with the system with this indium source, when pulse height selection methods were employed. An electron energy calibration was also made for counter 2 with the 2.6 MeV γ-ray of ThC″. This provided a calibration point and a check on the electron response of the scintillator. Further energy calibrations are discussed below.

The time of flight telescope was set up at approximately 120° to the γ-ray beam of the Glasgow synchrotron, with the front crystal 8 ins. from a $\frac{1}{8}$th in. thick polythene target, viewed approximately end-on.

3. Results

The film record of the individual traces was analysed and the results plotted. The results of one of a series of runs is shown in fig. 2. From this figure it is seen that those mesons, identified positively by the presence of the decay pulses all lie on the lower band, which is distinct and apart from the upper band of particles, which are predominantly protons. The lower band will contain additionally π^+ mesons, which have decayed in such a short time that the μ^+ decay pulse is not distinct from the π^+ pulse (i.e. less than 10^{-8} sec), and also μ^+ mesons. The combined number of these can be expected to be of the same order as that of the identified π^+ mesons. Some μ^- particles will also be expected in this band.

The meson curve is to some extent self-calibrating. The π^+ mesons will have a maximum energy of 24 MeV, corresponding to their maximum range in the 1 in. scintillator. This "cut-off" therefore provides a high energy calibration point. A low energy calibration

point is then found by considering the μ^+ pulse heights which, in $\pi^+ \to \mu^+$ decays, must all be the same size. Since the π^+/μ^+ mass ratio is not very different from unity (viz. 1.33), the pulse height for a π^+ particle of energy $(4.15 \times 1.33) = 5.5$ MeV can be expected to be given by the Seitz relation (cf. Taylor *et al.*[6])) as 1.33 times that of the μ^+ particle. Thus, two energy calibration points are obtained and the times of flight associated with these meson energies calculated. These two check points are indicated in the meson band, they are consistent with the time calibration given earlier.

The scintillation response (S) of NE 102 scintillator for protons has been examined by Evans and Bellamy[7]) and by Gooding and Pugh[8]). $\mathrm{d}S/\mathrm{d}x$ follows closely a relation of form $\alpha(\mathrm{d}E/\mathrm{d}x)\ (1 + 0.01\ \mathrm{d}E/\mathrm{d}x)^{-1}$, where $\mathrm{d}E/\mathrm{d}x$ is in MeV $\mathrm{g}^{-1}\,\mathrm{cm}^2$ and α is a constant (cf. too, Birks[9])). Taking the same relation to hold for π^+ mesons, the upper curve of fig. 2 can be drawn for protons, and the lower curve for π^+ mesons. These curves are consistent with the experimental plots.

4. Discussion

Over the greater part of the energy range, the meson band stands distinct, and the results show that the method has adequate mass discrimination. Further it would seem possible to utilize a shorter flight path which would increase the solid angle subtended by the apparatus at the target. For meson detection from γ-ray machines, it is seen that the difficulties appear increasingly at the lowest energies; the random counts are evident below about 4 MeV in fig. 2. For reliable π^+ meson detection to the lowest energies, with a time of flight system identification by $\pi^+ \to \mu^+$ decay should remain incorporated as an additional criterion.

Acknowledgments

We would like to thank Dr. W. McFarlane and the synchrotron technicians for the use of the synchrotron beam, and Professor P. I. Dee for his interest in this work. We are also grateful to Miss E. Muldoon for help in the film analysis. One of us (E. G.) expresses his appreciation to the Ministry of Education, N.I., for a research grant held during the course of this work.

[6]) C. J. Taylor, W. K. Jentschke, M. E. Romley, F. S. Ely and P. G. Kruger, Phys. Rev. **84** (1951) 1034.

[7]) H. C. Evans and E. H. Bellamy, Proc. Phys. Soc. **74** (1959) 483.

[8]) T. J. Gooding and H. G. Pugh, Harwell, Private Communication.

[9]) J. B. Birks, Scintillation Counters (Pergamon Press, London, 1953).

NUCLEAR INSTRUMENTS AND METHODS 8 (1960) 233–235; NORTH-HOLLAND PUBLISHING CO.

A LOW BACKGROUND BETA COUNTER WITH A PLASTIC SCINTILLATOR ANTICOINCIDENCE SHIELD

J. R. GAT(GUTMANN)† and J. GILAT††

Israel Atomic Energy Commission Laboratories

Received 5 May 1960

The design and performance of a low background beta counter is described. The counter consists of a central gas flow proportional counter surrounded by a large plastic scintillator anticoincidence shield.

1. Introduction

The problem of counting very low beta activities often arises in health physics and in natural radioisotope work. Low background beta counters are required for this purpose. The reduction of the beta counter background to 1 c/m level is usually achieved by surrounding a conventional beta counter by an array of Geiger Mueller tubes, connected in anticoincidence with the central counter[1]). Arrangements of this kind have been applied with success[2,3,4]). Annular or bell shaped multianode shielding counters have also been developed[5,6,7,8]).

The use of a scintillation counter as anticoincidence shield offers certain advantages over the conventional G. M. umbrella:

1. It is easily adapted to different geometrical arrangements.

2. It enables spectral analysis of the background radiation to be made.

3. It eliminates the troublesome fault location so often encountered in multitube shields.

A plastic scintillator seems most suited for such a purpose. A low background counter using a scintillator shield of this type was designed, taking special care to ensure good sensitivity and light collection efficiency.

A previous attempt to use a plastic scintillator in anticoincidence shielding[9]), is reported to have given unsatisfactory results, apparently because of poor geometry and light collection efficiency.

2. Description of Counter

The counter is shown schematically in fig. 1.

An Epon, end window, gas flow counter (Tracerlab Model CE 14P), operating in the proportional region was used as central counter[10]). The anticoincidence shield was made of Nuclear Enterprises NE 102 plastic scintillator, machined to specifications and coated with a diffuse reflecting paint by the manufacturer. Its shape and dimensions were chosen to give maximum sensitivity and efficiency in light collection around the central counter. It was coupled to a 5″, DuMont 6364 photomultiplier. The sample slides and support were made of Perspex. The counters, together with their respective cathode

† Now at Isotope Department, Weizmann Institute of Science, Rehovoth.

†† The work was performed as part of an investigation by this author in partial fulfillment of the requirements for a Ph. D. thesis.

[1]) E. C. Anderson and F. N. Hayes, Ann. Rev. Nucl. Science **6** (1956) 303.

[2]) W. F. Libby, Rev. Sci. Instr. **22** (1951) 225.

[3]) J. L. Kulp and L. E. Tryon, Rev. S. Instr. **23** (1952) 296.

[4]) S. O. Softky, and R. E. Nather, Nucleonics **15**, No. 5 (1957) p. 90.

[5]) W. E. Grummit, R. M. Brown, A. J. Cruikshank and J. L. Fowler, Canadian J. Chem. **34** (1956) 206.

[6]) K. van Dureen, W. K. Hofker and J. Hermsen, Proceedings Second International Conf. on the Peaceful Uses of Atomic Energy, Vol. **14** (1958) 339.

[7]) J. Geiss, C. Gfeller, F. G. Houtermans and H. Oeschger, *ibid.*, cit. Vol. **21** (1958) 147.

[8]) W. Barendsen, *ibid.*, cit. Vol. **21** (1958) 151.

[9]) H. A. May, U.S. AEC Report. ANL 5679 (1957) p. 69.

[10]) Tracerlog No. **81** (1957); No. **92** (1958).

follower preamplifiers, and the sample slide assembly were enclosed in a light-tight brass housing. The entire arrangement was surrounded by a 10 cm thick iron brick shield.

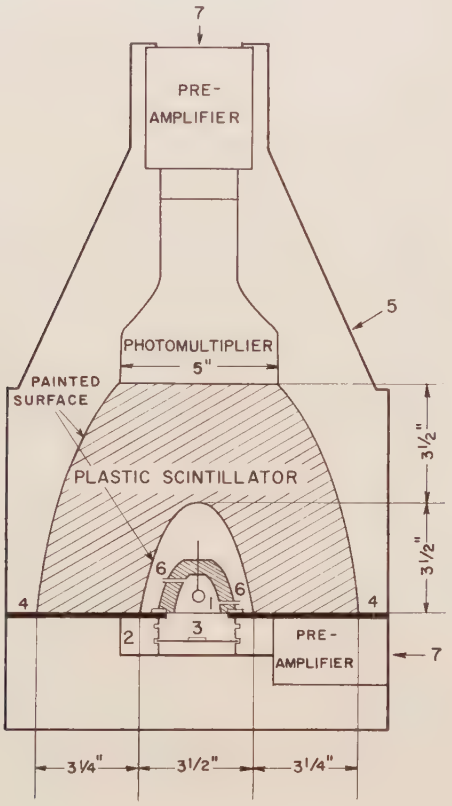

Fig. 1. A scintillator shielded low background β counter, schematic drawing (iron brick shield not shown). 1. Central gas flow counter. 2. Sample slide assembly. 3. Sample. 4. Support plate. 5. Brass housing (light-tight). 6. Gas in- and outlet. 7. Power supply and signal output.

The associated electronic circuitry is shown schematically in fig. 2†. Pulses from the scintillation counter were recorded on count recording unit A, pulses from the central counter on unit B and the coincidence and anticoincidence counts on units C and D respectively.

The relationship C + D = B was used for checking proper functioning of the equipment. For standardisation and plateau measurements with higher activity samples, the scintillation counter was disconnected, and the output of the RLI8V5 discriminator was connected to recording unit A. The dead time of the coincidence and anticoincidence gates was set at about 3 microseconds††.

3. Performance

The setup was satisfactorily operated for several months counting Sr^{90}–Y^{90} samples†††.

The performance is summarised by the following data:

Plateau: 4400–4900 volts, slope < 1%/100 volts at a 15 mV sensitivity, (i.e. gain of 2000 and 30 volts discriminator setting).

Efficiency: 40% overall efficiency for a flat 2 cm diameter Y^{90} source, at a distance of 2 mm from the window. (Determined by intercomparison with a standardized beta counter.)

Background: A. Scintillation counter background: 1800 ± 100 c/m, at 1000 volts and 10 mV sensitivity. At this rate the dead time of the instrument is entirely negligible.

B. Proportional counter background: 9.5 ± 0.3 c/m.

C. Coincidence background: 8.7 ± 0.3 c/m.

D. Anticoincidence background: 0.80 ± 0.05 c/m.

The errors indicated on A, B, C include long term variations of the background counting rate during the 6 months testing period. The error in D is the statistical counting error for an overnight count. A detailed analysis showed that the distribution of the counts follows a Poissonian curve.

Increasing the voltage or lowering the discriminator setting of the scintillation counter, caused a steep rise in the scintillation counter background, but had no appreciable effect on the anticoincidence counting rate.

Part of the residual background of 0.8 c/m may be due to scattered and terrestrial radiation

† The scintillation counter discriminator, the coincidence-anticoincidence analyser and the four count-recording units, all installed on a single chassis, were designed and built by Messrs. D. Mydansky and Z. Kamil.

†† Operation of the central counter in the Geiger region, though quite feasible, would necessitate a much longer dead time of the gates.

††† For counting samples of β–γ emitters, a suitable mercury shield should be incorporated between the proportional and the scintillation counter, to eliminate β–γ coincidences.

from below, where no anticoincidence shield was provided. (Removal of the iron bricks beneath the counter increased the anticoincidence background by about 2.5 c/m).

Summary

The feasibility of using plastic scintillators in anticoincidence shielding has been demonstrated by the performance of the counter. A smaller scintillator might possibly be used without sacrificing much of its shielding properties. This would make the entire unit more compact and comparable in price to an array of G. M. tubes.

Acknowledgement

The help of Mr. Sheinin in the assembly and maintenance of the unit is gratefully ackowledged. We would also like to thank Messrs. M. Birk, J. Wolfson and Dr. A. Nir of Nuclear Physics Dept. of the Weizmann Institute for helpful discussions.

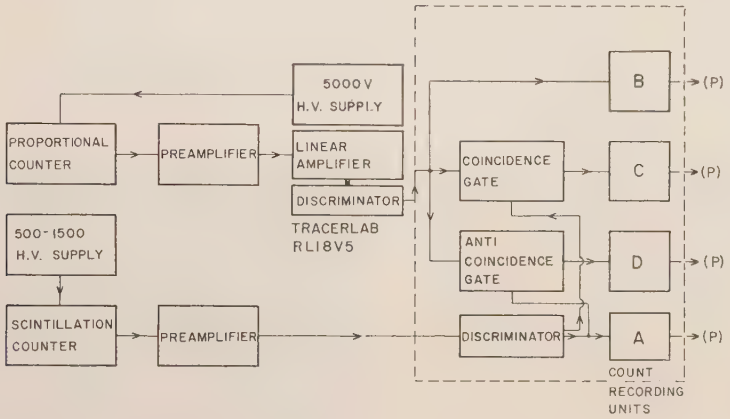

Fig. 2. Block diagram of counter and associated electronic circuits. Count recording Units: A = 2 Philips E1T scaling tubes and mechanical register; B, C, D = Mechanical registers; P = Provision for connection to printing counter.

NUCLEAR INSTRUMENTS AND METHODS 8 (1960) 236–238; NORTH-HOLLAND PUBLISHING CO.

A KILOVOLT, KILOAMPERE LOW PRESSURE SWITCH†

GEORGE J. BRUCKER

United States Signal Corps Laboratories, Fort Monmouth, New Jersey

and

KENNETH C. ROGERS

Stevens Institute of Technology, Hoboken, New Jersey

Received 9 April 1960

A low pressure switch is described that is capable of passing kiloamperes at voltages up to 30 kV. The effect of pressure and gap voltage on the switch closing time is discussed.

1. Introduction

The need for switching large currents at high voltages in thermonuclear research has lead to the development of the vacuum-gap switch[1,2]). The Megatron accelerator work at Stevens Institute requires a similar device for switching the capacitor bank current to the field coil of the Megatron. It is the purpose of this paper to present the design of a practical switch, and the experimentally determined closing time for different gap voltages and pressures.

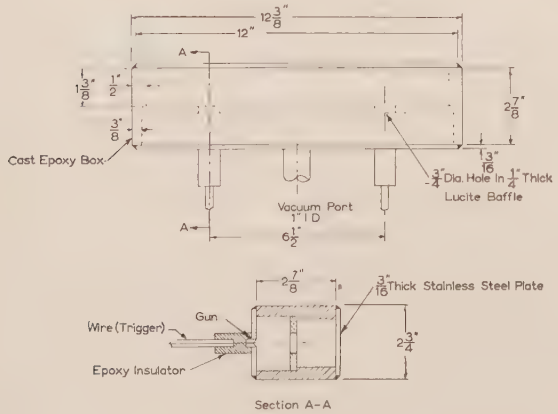

Fig. 1. Details of switch.

† Work performed under the auspices of the United States Army Signal Corps Laboratories, Fort Monmouth, New Jersey and the U.S. Atomic Energy Commission.

†† Twenty-two part of sand, ten parts of Araldite 6050, three parts of Hardener 901 by weight.

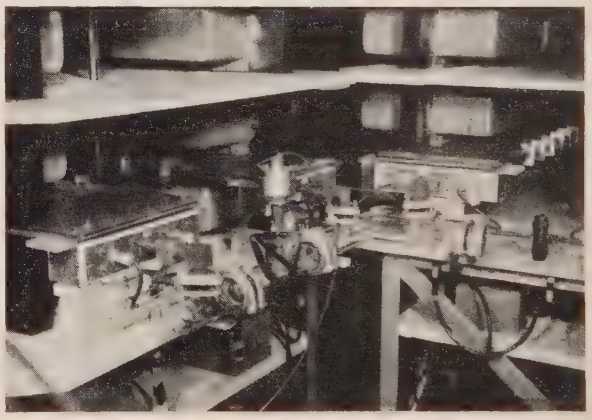

Fig. 2.
View of Stevens capacitor bank showing switches mounted on transmission lines and connected to pumping manifold.

2. Description of Switch

The design of the Stevens capacitor bank[3]) has dictated the rectangular geometry of this switch. Fig. 1 is a drawing of the switch which consists of a rectangular box cast from a mixture of epoxy and sand†† with stainless steel electrodes and a lucite baffle plate. The switch is closed by a plasma burst from a pair of coaxial plasma

[1]) D. C. Hagerman and A. H. Williams, Rev. Sci. Instr. **30** (1959) 182.

[2]) W. R. Baker, Rev. Sci. Instr. **30** (1959) 700.

[3]) K. C. Rogers *et al.*, Megatron Accelerator Progress Report, Signal Corps Contract DA36-039sc-78097 (June 3, 1958).

guns[4]). A high voltage pulse (2 kV to 10 kV) supplied by a hydrogen thyratron (5c22) and a 0.3 μF capacitor fires the guns. A view of the switches mounted on the transmission lines of the capacitor bank is shown in fig. 2.

3. Experimental Procedure

The closing delay time T_d and the "jitter" in T_d were measured for ranges of voltage across the switch V_s, and for vacua from 0.02–3.3 microns Hg. The delay time T_d, is defined to be the length of time from the inception of current flow to the plasma gun to the start of current through the switch. Both rates of current change (dI/dt) were picked up by means of Rogovsky coils, and the integrated signals were presented on a Tektronix 551 dual beam scope. The capacitor bank was prevented from ringing by a resistive load. All pressure readings were made by the same P. I. G. located close to the switch. The data are plotted in figures 3, 4 and 5. Each point is the mean of not less than five separate measurements. The polarity of the applied voltage was varied so that the gun side of the switch was either positive or negative.

4. Discussion of Results

The delay time versus voltage applied across the switch at a constant low pressure (0.02 microns) is shown in fig. 3. At this pressure it is apparent that the delay time, T_d, varies inversely with the applied voltage V_s. If electrons are responsible for closing the switch then reversing the polarity of V_s so that the gun side of the switch is positive should show a longer time delay which is independent of voltage. This is not the case at low pressure.

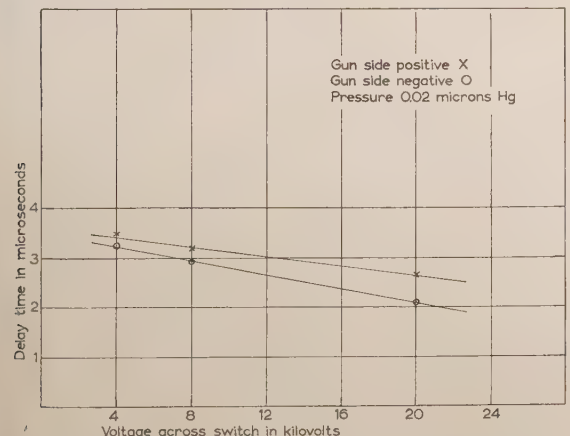

Fig. 3. Switch closing delay time versus voltage across switch for a constant pressure of 0.02 microns Hg and both positive and negative bank voltages.

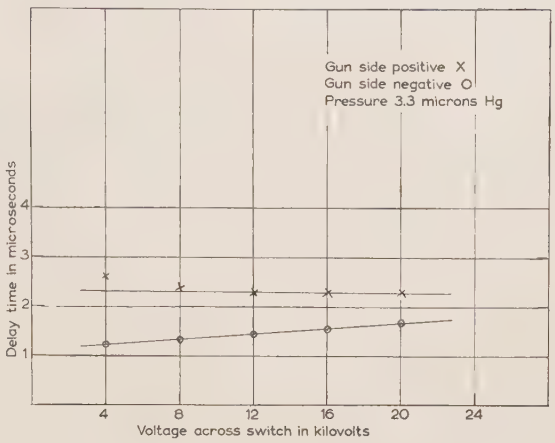

Fig. 4. Switch closing delay time versus voltage across switch for a constant pressure of 3.3 microns Hg and both positive and negative bank voltages.

The evidence in support of the theory that electrons are responsible for switch closure becomes stronger for high pressure operation. Fig. 4 displays this independence of delay time on switch voltage when the gun side of the switch is positive; in this case T_d is comparable to plasma transit time. Reversal of polarity at this pressure (3.3 microns) brings about an increase of T_d with voltage. J. A. Mather[5]), who observed this behavior in a vacuum-gap switch at Los Alamos, has suggested that the increasing delay time is due to the dependence of the electron-atomic ionization cross section $\sigma(v)$ on the applied voltage. The picture does not seem to be this simple as is indicated by fig. 5. The shape of these curves is not explicable on the basis of the ionization cross section voltage dependence, although the precision of this experiment is not sufficient to say with

[4]) K. C. Rogers *et al.*, Megatron Accelerator Progress Report, Signal Corps Contract DA36-039sc-78097 (April 1, 1959).

[5]) J. A. Mather and A. H. Williams, Rev. Sci. Instr. (to be published).

certainty that the curve of fig. 5 is the true behavior of the switch.

The mechanism responsible for switch closure should be similar to that occurring in the breakdown of an over-voltaged low pressure gap. The theory of current growth between parallel plates has been discussed in detail by Davidson[6,7,8]) and in the monograph of Llewellyn-Jones[9]). The treatment is quite complete and probably can be applied to our vacuum gap switches over the entire range of pressures. A detailed comparison with this theory is difficult because of the (unknown) effect of electrode contamination on γ, the second Townsend coefficient. By a more elementary treatment that should apply under low pressure conditions $p \ll 0.1$ microns, the time τ required for the switch to "close" is given by

$$\tau = t_+ + \frac{Mt_+}{1+M} \ln\left(\frac{2M}{M-1}\right).$$

$$M = \gamma\,(e^{\alpha d} - 1)$$

where d: electrode spacing,
α: first Towsend coefficient,
γ: second Townsend coefficient,
t_+: anode to cathode ion transit time.

If the electrodes are of steel and Fe^+ ions are responsible for (secondary) electron liberation at the cathode then for a three inch electrode gap,

$$t_+ = \frac{2.3 \times 10^{-6}}{V_s^{\frac{1}{2}}} \text{ sec},$$

V_s = gap voltage in kilovolts.

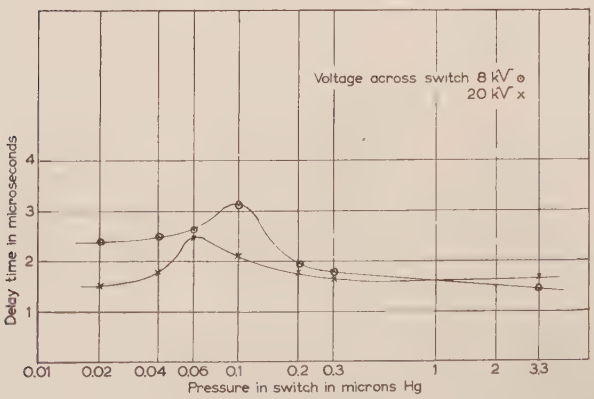

Fig. 5. Switch closing delay time versus pressure for two constant bank voltages with gun side of switch negative.

Clearly the ion transit time determines the time scale. At 20 kV and 0.02 microns pressure $t_+ = 0.5$ microsecond. This requires $M = 1 + 2\,e^{-8}$ if the above expression for τ is used. It is our belief that at all pressures switch closure is triggered by fast electrons from the "plasma gun". Metallic plasma ejected by the gun probably plays a minor role. At low pressures an avalanche is initiated by positive ions liberated from the anode. At high pressures both the anode and the gas in the gap contribute positive ions. Ion bombardment of the cathode releases secondary electrons and breakdown proceeds.

5. Conclusions

The data in fig. 5 points out the desirability of operating the switch at a pressure higher than 0.1 microns. An operating pressure of 0.3 microns would give a switch with a low value of delay time, and one which only depends to a small degree on voltage and pressure. The fluctuation (jitter) in T_d at this pressure is 0.1 μsec. This type of switch was test fired over a 1000 times at 30 kV passing a current of 30 000 amperes. The inductance and resistance of the switch is approximately 20 millimicrohenries and 0.03 ohms respectively. No special voltage conditioning is required. More development work is necessary as the switch is far from optimum, for example decrease of gap spacing will decrease the closing delay time. At this time the switch satisfies the requirements of the Megatron experiment but further development work is being conducted.

Acknowledgements

The development of this switch was initiated by several ideas and proposals of Professors David Finkelstein and Winston H. Bostick. Their assistance is gratefully appreciated. The authors also wish to express their thanks to I. Mansfield and L. Ferrari for their help in the construction and study of the switch.

[6]) P. M. Davidson, Brit. J. App. Phys. **4** (1953) 170.
[7]) P. M. Davidson, Phys. Rev. **99** (1955) 1072.
[8]) P. M. Davidson, Phys. Rev. **103** (1956) 1897.
[9]) F. Llewellyn-Jones, Ionization and Breakdown in Gases (Methuen, London, 1957).

NUCLEAR INSTRUMENTS AND METHODS 8 (1960) 239–243; NORTH-HOLLAND PUBLISHING CO.

A SCINTILLATION COUNTER SYSTEM FOR THE DETECTION OF POSITIVE AND NEGATIVE PIONS

J. G. RUTHERGLEN and J. K. WALKER

Department of Natural Philosophy, University of Glasgow

Received 21 April 1960

A three counter telescope has been developed in which pions are separated from particles of different mass by measurement of dE/dx and E. Identification of positive pions is made by means of the characteristic π^+–μ^+ decay. The arrangements for recording this information both photographically and by means of a pulse height analyser are described.

1. Introduction

The detection and identification of fast charged particles emitted from nuclear reactions is a frequent problem in nuclear physics. It is often necessary to identify particles of a particular mass among a flux of various other particles. This requires, in general, that any technique should consist of a simultaneous measurement of at least two dynamical quantities which have a different dependence on the masses of the particles.

In investigations on the production of pions from nuclei by photons it is necessary to identify pions among a large background of electrons and protons. It is also necessary to have separate identification of the positive and negative pions. The ratio of positive to negative pions is often a quantity of particular interest. For this purpose the two techniques which have been most frequently employed are the nuclear emulsion technique and the use of a magnetic spectrometer in association with a counter telescope. The emulsion technique has the advantage that the positive and negative pions are recorded simultaneously, but has the disadvantage that a large scanning time is required to obtain adequate statistics. The method of magnetic analysis is not limited in this way, but has the disadvantage that the positive and negative pions cannot be counted at the same time.

We have developed a counter telescope system which can be used to count π^+ and π^- simultaneously in a well defined solid angle and energy interval. This system was designed primarily for the measurement of π^-/π^+ ratios, but is also quite satisfactory for the measurement of absolute cross sections.

2. General Method

It can be shown[1,2] that to a good approximation

$$\frac{dE}{dx} \propto \frac{M^{0.45} Z^{1.1}}{R^{0.45}} .$$

Thus for singly charged particles with the same range R a measure of the specific ionization dE/dx distinguishes particles of different mass. This implies that for mesons, protons and deuterons of the same residual range the dE/dx are in the ratio of 0.4:1:1.3 respectively. This applies to mesons whether they are positively or negatively charged. To make use of this fact three counters were used; the first one to measure dE/dx, the second in which to stop particles and measure the resulting pulse heights E and the third to act as an anticoincidence counter. An automatic plot of dE/dx against E was performed for every particle which stopped in the second counter. The

[1]) B. Wolfe, A. Silverman and J. W. De Wire, Rev. Sci. Instr. **26** (1955) 504.

[2]) J. C. Keck, Phys. Rev. **85** (1955) 410.

resolution was sufficient to give with negligible uncertainty the total number of π^+ and π^- mesons which stopped in the second counter.

To distinguish between π^+ and π^- mesons which stopped in the second counter use was made of the characteristic decay properties of the π^+ meson. The π^+ decays into a μ^+ meson of kinetic energy 4.1 MeV with a half life of 18 mμsec. A delayed coincidence technique for the π^+–μ^+ decay has been used by several experimenters and is described in detail by Imhof *et al.*[3]). A similar system for detecting the π^+–μ^+ decay, with an efficiency of about 50%, has been developed in the present work. In order to determine the efficiency of the delayed coincidence system for detecting the μ^+ it is necessary to use hydrogen as a target from which only π^+ mesons can be photoproduced.

In the general case when there are π^- and π^+ mesons present the knowledge of the efficiency of the delayed coincidence system, together with the number of delayed coincidences recorded, yields the number of π^+ mesons which stop in the second counter. Subtraction of this number from the total number of mesons yields the number of π^- mesons. Thus a simultaneous measurement on both types of charged pion can be performed.

3. Description of Counter Telescope

The telescope consisted of three plastic scintillators (N.E. Type 101) connected by perspex light guides to R.C.A. 6810 A photomultipliers. Scintillators 1, 2 and 3 were 0.25″, 0.75″ and 0.5″ thick and 3″, 3″ and 4″ in diameter respectively. Between counters 1 and 2 there was a perspex absorber 0.25″ thick. Fig. 1 shows the telescope and the associated fast electronics, which was situated close to the counters.

Particles which stop in counter 2 register a $12\overline{3}$ coincidence-anticoincidence in a Bell type coincidence circuit which has a resolving time of 20 mμsec. When such an event occurs it is necessary to measure the pulse heights C_1 and C_2 from the collectors of photomultipliers 1 and 2. This is accomplished by means of the display unit to be described later.

We shall now consider the sequence of pulses for a π^+–μ^+ decay in counter 2. A $12\overline{3}$ event, which may be a π^+ stopping in 2, was made to operate a trigger which produced a gate pulse 80 mμsec long and rise time about 15 mμsec.

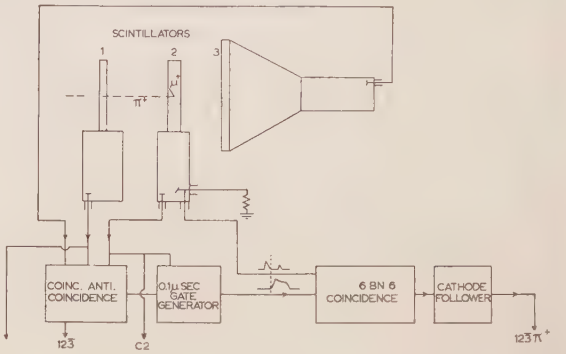

Fig. 1. The scintillation counter telescope and associated fast electronics.

In order to have a faster rise time and to minimise jitter, this pulse was mixed with the limited pulse on the anode of a limiter fed by the collector of photomultiplier 2. This resulted in a gating pulse which had a rise time of about 8 mμsec to 3 volts high and lasted for nearly 100 mμsec. The gate pulse was applied to one grid of a 6BN6 valve. The output pulse from the last dynode of photomultiplier 2 was fed directly on to the other control grid of the 6BN6. A 27″ length of 200 ohm cable was used as a clipping line on this dynode. This line was terminated with an 80 ohm resistor to minimise overshoot[4]). With this arrangement the total width of the pulse was about 15 mμsec. The object of this was to keep the π^+ and μ^+ pulses as distinct as possible. The timing of the pulses on the grids of the 6BN6 was arranged so that the dynode pulse occurred first and the gate pulse was applied to the other grid 15 mμsec later. As the half-life for the π^+–μ^+ decay is 18 mμsec it is clear that something like 50% of π^+–μ^+ decays will be recorded as delayed conincidences. The anode pulse of the 6BN6 was integrated by the stray capacity of the anode. It was found that optimum response was obtained using

[3]) W. Imhof, R. Kalibjian and V. Perez-Mendez, Rev. Sci. Instr. **29** (1958) 476.

[4]) R. Madey, Rev. Sci. Instr. **26** (1955) 971.

— 3 volts bias on both grids of the 6BN6.

The operation of the delayed coincidence circuits ($123\,\pi^+$) could be checked by measurements using the 2.6 MeV gamma ray of ThC^{11}. This was achieved by introducing sufficient 200 ohm delay cable for the dynode pulse to arrive at the grid of the 6BN6 sometime within the gate pulse. The maximum pulse height from ThC^{11} is slightly less than the equivalent light output of the 4.1 MeV μ^+ meson. Thus operation on the maximum pulses of the ThC^{11} gamma ray spectrum was considered adequate for the delayed coincidence system. This was achieved by adjusting the E.H.T. voltage on photomultiplier 2 until the delayed coincidence was just functioning. The E.H.T. voltage on counter 1 was adjusted until the gain was suitable for the display unit to be described.

4. Display Unit

The information from the telescope and its associated fast electronics was fed through 70 ohm cables to the display unit. This information consisted of the pulse heights from the collectors of photomultipliers 1 and 2 (C_1 and C_2) and the pulses from the fast coincidence circuit ($12\overline{3}$) and the delayed coincidence circuit ($12\overline{3}\ \pi^+$). The object of the display unit is to record the above pulses in such a manner as to require a minimum of subsequent analysis.

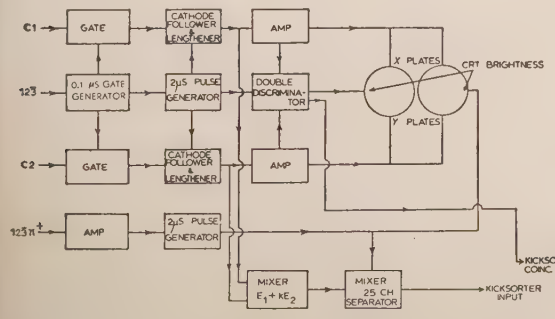

Fig. 2. A block diagram of the electronics in the display unit which records the pulse heights produced in counters 1 and 2 for all particles which stop in the second counter.

A block diagram of the electronics is shown in fig. 2. A pulse signifying a $12\overline{3}$ event was used to trigger a blocking oscillator which produced a 10 V pulse 100 mμsec long. This pulse was used to open gates through which the collector pulses C_1 and C_2 passed to lenghtening circuits, which produced 2 μsec long flat-topped pulses of amplitudes proportional to the amplitudes of the C_1 and C_2 pulses. The lengthened pulses were fed to two paraphase amplifiers whose outputs were connected to the X and Y plates respectively of a cathode ray tube (Mullard Type DB 13/2). Simultaneously the cathode of

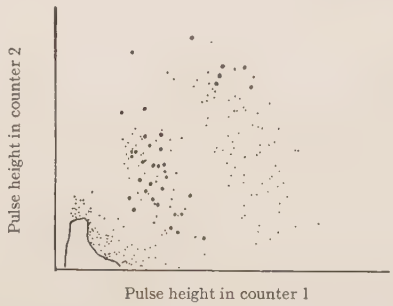

Fig. 3. A spot picture as photographed on the display unit. The target used was hydrogen from which only π^+ mesons may be produced. See text for explanation of large spots.

the C.R.T. was pulsed 40 volts negative for 2 μsec. This produced a spot on the C.R.T. whose coordinates were proportional to the pulse heights C_1 and C_2 from counters 1 and 2. A second C.R.T. whose X and Y plates were connected in parallel with the first was only brightened up when there was a delayed coincidence in counter 2. This was achieved by using the $12\overline{3}\ \pi^+$ pulse to trigger a 2 μsec pulse generator whose 40 volts negative output pulse was fed to the cathode of the second C.R.T. The two C.R.T.'s were photographed simultaneously.

Typical spot pictures are shown in fig. 3 in which the "ordinary" and "delayed coincidence" pictures have been superimposed, the latter being shown by large spots. The three different groups of spots from left to right correspond to electrons, mesons and protons. The number of spots due to electrons is very large and only the outline of the electron region is shown. These pictures were obtained using liquid hydrogen as a target, from which only π^+ mesons can be photoproduced. It is seen that about 50% of the

π^+ mesons have been detected as delayed coincidences. Protons which have produced large pulses in the second counter have produced

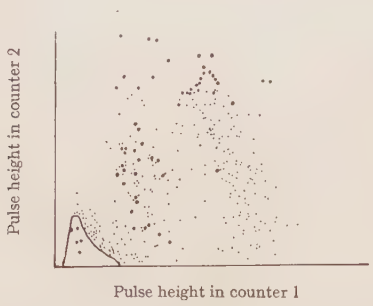

Fig. 4. A spot picture taken with deuterium as a target from which both π^+ and π^- mesons can be produced. See text for explanation of large spots.

"self delayed coincidences" due to the tail of the dynode pulse entering the delayed coincidence gate. Provided the pulse height level for the production of "self delayed coincidences" was higher than the top of the meson region in fig. 3 then no ambiguities could occur. Fig. 3 is the result of a 15 minute run with a 3 cm liquid hydrogen target exposed to a 240 MeV bremsstrahlung beam, and with the telescope about 12″ away from the centre of the target.

When a target other than hydrogen is exposed to the gamma ray beam, π^- as well as π^+ mesons are produced. Fig. 4 shows the result of a 15 minute run using a 3 cm deuterium target. The region between the mesons and protons is now occupied by a few spots. This is due to π^- mesons which stopped in the second counter and produced stars of high energy charged particles, thus increasing the pulse height from counter 2. Although the separation between mesons and protons is not quite so clearly defined as in the case of hydrogen, it was possible to obtain the total number of mesons with good accuracy from an analysis of the spot density. To reduce the probability of fast charged product particles from π^- stars entering the anti-coincidence counter and thus causing a veto, the anti-coincidence counter was situated as far away as possible from the second counter without producing a loss of anticoincidence efficiency.

5. Kicksorter Display

Although analysis of the results was normally performed by counting the spots from the photographs, it is useful in a long experiment to have some means of quickly checking the overall operation of the apparatus. Use was made of a multichannel pulse height analyser for this purpose.

The meson and proton groups on the normal $12\bar{3}$ C.R.T. display are approximately parallel straight lines. Hence if the pulses proportional to C_1 and C_2 are added to form a pulse of height $P \propto C_1 + kC_2$, the spectrum of the pulses P shows well defined peaks corresponding to mesons and protons, when the constant k is correctly adjusted. In fig. 5 such a spectrum, obtained with a liquid hydrogen target, is shown in the first 35 channels.

In order to display the events associated with a delayed coincidence separately, a step pulse of standard height, equivalent to 35 channels on the kicksorter, was added to the corresponding P pulse. The peaks corresponding to π^+ mesons and "self delayed" high energy protons can be seen in channels 40 to 60 in fig. 5.

From the point of view of the dead time of the kicksorter it was desirable to prevent the majority of the large number of electrons from

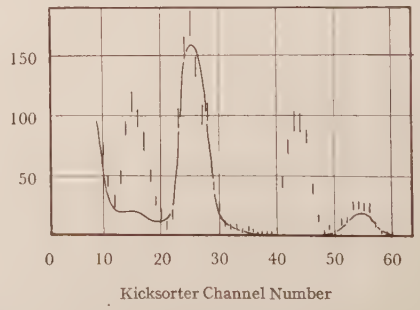

Fig. 5. Spectrum obtained on kicksorter using a liquid hydrogen target. The solid curve shows the spectrum obtained with the target empty. The two groups corresponding to π mesons are well resolved. The upper group contains mesons for which delayed coincidences have been recorded.

being counted by the kicksorter. This was achieved by gating the kicksorter by the output of a double discriminator which was fed by the C_1 and C_2 pulses.

It is seen that the kicksorter display fulfils the requirement of giving an instantaneous assessment of the results and an overall check on the operation of the apparatus at all times.

Acknowledgements

The authors wish to thank Dr. W. McFarlane and the synchrotron technicians for their co-operation, Dr. W. Hogg for use of liquid targets and Professor P. I. Dee for the interest shown in this work. One of us (J. K. W.) expresses appreciation to D.S.I.R. for a maintenance grant held during the course of this work.

Appendix

The energy interval of pions which stop in counter 2 is about 15–25 MeV. With the use of absorbers in front of the telescope, higher energy pions have been studied. However, it is of considerable theoretical interest to study photomeson production as near as possible to threshold.

To study mesons of kinetic energy 6–12 MeV, a plastic counter, 0.1 inches thick, has been added to the front of the telescope which has been described. The purpose of this counter is to measure the ionization loss of particles which stop in the previous front counter of the telescope. Thus two energy intervals of pions may be studied at the same time.

All the information is displayed in the form of spots on four cathode ray tubes which are photographed by one camera. These four displays correspond to events of the type $12\bar{3}$, $12\bar{3}\,\pi^+$, $123\bar{4}$, $123\bar{4}\,\pi^+$. For continuous monitoring the kicksorter is now used in the following manner. The first 25 channels are used to display the $12\bar{3}$ information and the $12\bar{3}\,\pi^+$ events are displayed in channels 26–50. The second 50 channels are used in a similar way for the $123\bar{4}$ system.

Successful preliminary results have been obtained with the above four counter telescope.

NUCLEAR INSTRUMENTS AND METHODS 8 (1960) 244–248; NORTH-HOLLAND PUBLISHING CO.

THE THEORY AND OPERATION OF THE ROTATING CRYSTAL SLOW NEUTRON CHOPPER

D. A. O'CONNOR

Institute of Nuclear Research, Warsaw†

Received 2 June 1960

The resolution and efficiency of the rotating crystal chopper are derived theoretically as a function of the crystal and collimator parameters. It is shown that the limiting resolution of the device is the same as that of a crystal monochromator. An experimental model chopper is described and its observed resolution compared with the theory.

1. Introduction

In studies on the inelastic scattering of slow neutrons by substances it is necessary to measure the energy distribution of neutrons scattered out of an incident monochrom atic neutron beam by a sample. This requires the use of some form of monochromator to produce the incident beam, and some form of spectrometer to measure the energy distribution of neutrons scattered by the sample through some angle. The rotating crystal chopper, together with a time of flight analyzer, is a device which serves simultaneously as a monochromator and as a spectrometer in such experiments. This device was first used and described by Brockhouse[1]).

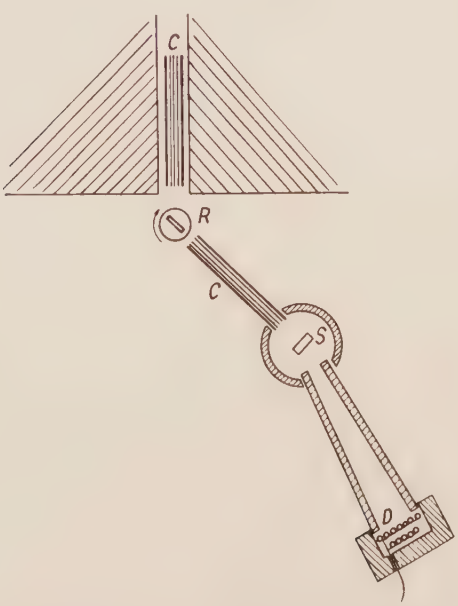

Fig. 1. Arrangement of apparat us for the measurement o the spectra of inelastically scat tered neutrons. C = colli mators, R = rotating single cryst al, S = scattering materia D = neutron d etector.

The principle of operation of the crystal chopper will be made clear by fig. 1. A single crystal, rotating continuously about an axis perpendicular to the plane of the diagram, will produce a pulse of neutrons at the collimator exit every time the crystal planes pass through the Bragg position. The mean wavelength of the neutrons will depend on the crystal plane spacing and the angle between the collimators. The energy of the scattered neutrons is found by measuring their time of flight from the sample to the detector.

2. Theory

We are interested here in computing the time duration of the neutron pulse, and the energy resolution of the device when considered as a spectrometer. The effect of the sample on the shape of the pulse will not be considered. Since the beam produced is not ideally monochromatic the pulse duration will vary with

† Present address: Department of Ph ysics, The University, Edgbaston, Birmingham 15, England.

[1]) B. N. Brockhouse, Bull Amer. Phys. Soc. Ser. II, 3 (1958) 233.

distance from the crystal as a result of the spread in neutron velocities, the pulse length being larger than that resulting from purely geometrical considerations.

Using the notation of Borst *et al.*[2]) we write for the collimator transmission functions (assumed equal) $I(\phi) = \exp - \phi^2/\alpha^2$ and for the crystal reflectivity $R(\beta) = R_0 \exp - \beta^2/2\eta^2$ where η is a measure of the mosaic spread of the crystal for the particular planes considered. Consider the moment at which the crystal has its planes at an angle γ to the Bragg position. If $\Delta\theta$ is the deviation of the angle of reflection of an individual ray of the beam from the Bragg angle θ, then we may write for the intensity of neutrons having deviations between $\Delta\theta$ and $\Delta\theta + \mathrm{d}\,\Delta\theta$:

$$P(\Delta\theta,\gamma) = \int I(\phi_1)\, R(\beta)\, I(\phi_2)\, \mathrm{d}\beta \qquad (1)$$

where

$$\phi_1 = \gamma + \beta - \Delta\theta$$

and

$$\phi_2 = \gamma + \beta + \Delta\theta\,.$$

Integration gives:

$$P(\Delta\theta,\gamma) = R_0 \pi^{\frac{1}{2}} \left(\frac{1}{\alpha^2} + \frac{1}{2\eta^2}\right)^{-\frac{1}{2}} \times$$

$$\exp - \left[\left(\frac{\Delta\theta}{\alpha}\right)^2 + \frac{\gamma^2}{\alpha^2 + 2\eta^2}\right]. \qquad (2)$$

If the crystal is rotating with angular velocity ω then the number of neutrons of wavelengths corresponding to the interval $\Delta\theta$, $\Delta\theta + \mathrm{d}\,\Delta\theta$, and emitted at times corresponding to the interval γ/ω, $\gamma/\omega + \mathrm{d}\,\gamma/\omega$, is given by:

$$\frac{1}{\omega} P(\Delta\theta,\gamma)\, \mathrm{d}\gamma\, \mathrm{d}\Delta\theta\,. \qquad (2a)$$

Neutrons of wavelength corresponding to the Bragg angle θ travel a distance L from the crystal in a time T_1 given by

$$T_1 = \frac{2dmL}{h} \sin\theta \qquad (3)$$

where the symbols have their usual meaning. Neutrons of wavelength corresponding to a Bragg angle of $\theta + \Delta\theta$ take a time:

$$T_1 - \Delta T_1 = \frac{2dmL}{h} \sin\theta - \frac{2dmL}{h} \cos\theta \cdot \Delta\theta\,.$$

It follows that the neutrons given by eq. (2) arrive at a point L from the crystal at a time:

$$T + \Delta T = T \pm \frac{\gamma}{\omega} - A\,\Delta\theta \qquad (3a)$$

where the sign of γ/ω depends on the rotation direction of the crystal and $A = (2dmL/h)\cos\theta$.

Replacing $\mathrm{d}\,\Delta\theta$ in (2) by $(1/A)\,\mathrm{d}\,\Delta T$, we obtain for the number of neutrons arriving at time $T + \Delta T$ to $T + \Delta T + \mathrm{d}\,\Delta T$:

$$P(\Delta T)\, \mathrm{d}\Delta T = \frac{\mathrm{d}\Delta T}{\omega A} \int P(\Delta\theta,\gamma)\, \mathrm{d}\gamma \qquad (4)$$

where $\Delta\theta$ from (3) is given by

$$\Delta\theta = \pm \frac{\gamma}{A\omega} - \frac{\Delta T}{A}\,. \qquad (5)$$

Substituting for $\Delta\theta$ in (4) and integrating we obtain:

$$P(\Delta T) = R_0 \pi 2^{\frac{1}{2}} \alpha^2 \eta\, [\alpha^2 (1 + A^2\omega^2) + 2\eta^2]^{-\frac{1}{2}} \times$$

$$\exp - \left[\frac{(\omega\Delta T)^2}{\alpha^2 (1 + A^2\omega^2) + 2\eta^2}\right].$$

This expression gives the shape of the pulse. The half-width of the pulse is given by:

$$\tau = 2\,(\ln 2)^{\frac{1}{2}} \left[\frac{\alpha^2 + 2\eta^2}{\omega^2} + A^2\alpha^2\right]^{\frac{1}{2}}\,. \qquad (6)$$

The total number of neutrons in one impulse is given by:

$$\int P(\Delta T)\, \mathrm{d}\Delta T = R_0 \pi^{\frac{3}{2}} 2^{\frac{1}{2}} \alpha^2 \eta\, \omega^{-1}$$

and for n impulses per revolution of the crystal the total intensity:

$$n\,(\tfrac{1}{2}\pi)^{\frac{1}{2}} \alpha^2 \eta R_0$$

In the above we have used a very idealised expression for the reflectivity of the crystal. When secondary extinction is strong the $R(\beta)$ function loses its Gaussian shape and can be approximated by an expression of the form

$$R(\beta) \sim 1\,, \qquad |\beta| \leqslant \beta_0$$

$$R(\beta) = 0\,, \qquad |\beta| > \beta_0$$

[2]) L. B. Borst and V. L. Sailor, Rev. Sci. Instr. **24** (1953) 141.

where β_0 depends on the mosaic spread of the crystal and on the reflectivity per unit volume. Using this expression we find that

$$P(\Delta T) = \pi\alpha^2[\operatorname{erf} K(\omega\Delta T - \beta_0) - \operatorname{erf} K(\omega\Delta T + \beta_0)] \quad (8)$$

where

$$K = 2^{\frac{1}{2}}[\alpha(1 + A^2\omega^2)^{\frac{1}{2}}]^{-1}.$$

If, as is often the case, β_0 is smaller than $\alpha(1 + A^2\omega^2)^{\frac{1}{2}}$ then we obtain as an approximation to (8)

$$P(\Delta T) \sim \frac{2\pi^{\frac{1}{2}}\alpha\beta_0}{(1 + A^2\omega^2)^{\frac{1}{2}}} \exp - \left[\frac{(\omega\Delta T)^2}{\alpha^2(1 + A^2\omega^2)}\right]$$

and

$$\int P(\Delta T)\, \mathrm{d}\Delta T \sim \frac{2\pi\alpha^2\beta_0}{\omega}. \quad (9)$$

The half-width of the pulse in this case is

$$\tau = 2(\ln 2)^{\frac{1}{2}}\alpha\left[\frac{1}{\omega^2} + A^2\right]^{\frac{1}{2}}. \quad (10)$$

Expression (9) can also be obtained from (7) by putting the areas of the two $R(\beta)$ functions equal and so obtaining R_0 in terms of β_0 and η.

The expressions (6) and (10) both contain two components which we shall write as

$$\tau = (\tau_a^2 + \tau_b^2)^{\frac{1}{2}}$$

where

$$\tau_a = 2(\ln 2)^{\frac{1}{2}}\frac{\delta}{\omega}$$

$$\tau_b = 2(\ln 2)^{\frac{1}{2}}\alpha A \quad (11)$$

δ will have a value somewhere between α and $(\alpha^2 + 2\eta^2)^{\frac{1}{2}}$ and represents the combined effect of the collimators and the crystal on the angular spread of the pulse. τ_a is dependent on ω as is to be expected. τ_b is independent of ω and is given by the spread in neutron velocities corresponding to the wavelength spread due to the collimator and crystal arrangement when considered as a simple monochromator. As ω increases τ converges to τ_b as a limit. The limiting resolution is given by

$$\frac{\tau_b}{L} = 2(\ln 2)^{\frac{1}{2}}\alpha B$$

where

$$B = \frac{2dm}{h}\cos\theta.$$

Putting in the appropriate constants we obtain

$$\frac{\tau_b}{L} = 8.67 \times 10^{-2}\,\alpha\, 2d\cos\theta \text{ microseconds/metre}$$

where α is in minutes of arc and $2d$ in Å. Thus, as is to be expected the limiting resolution is independent of the length of the flight path (apart, of course, from the effect of the detector thickness and the analyzer channel width).

Comparing the expressions for limiting resolution and the integrated intensity, it is seen that the intensity is inversely proportional to the square of the limiting resolution, which in turn depends on the half-width of the collimator transmission function. On the other hand the intensity is directly proportional to the mosaic spread of the crystal (through η in (7) and β_0 in (9)), which does not appear in the expression for the limiting resolution. It follows that it is desirable to use a crystal with a large mosaic spread. If the speed of the chopper is chosen so that the resolution is close to its limiting value, then the resolution required for a given experiment can be obtained by suitable choice of the collimators.

The fact that the limiting pulse width is due to the separation of neutrons with different velocities, suggests that the rotating crystal chopper could be used as a monochromator of very high resolution. The distribution in time, at the detector, of neutrons of wavelength corresponding to a deviation of $\Delta\theta$ from the Bragg angle, can be found directly from expression (2) by substituting for γ from eq. (5). This gives the number of neutrons of wavelengths between $\Delta\theta$ and $\Delta\theta + \mathrm{d}\Delta\theta$ arriving between ΔT and $\Delta T + \mathrm{d}\Delta T$:

$$R_0\pi^{\frac{1}{2}}\left(\frac{1}{\alpha^2} + \frac{1}{2\eta^2}\right)^{-\frac{1}{2}} \exp - \left[\frac{\Delta\theta}{\alpha}\right]^2 \times \exp - \left[\frac{\omega^2(\Delta T + A\Delta\theta)^2}{\alpha^2 + 2\eta^2}\right].$$

Thus neutrons of deviation from the mean of $\Delta\theta$ are distributed in time at the detector about $\Delta T = -A\Delta\theta$, and the half-width of their distribution is given by

$$\tau = 2(\ln 2)^{\frac{1}{2}}\frac{(\alpha^2 + 2\eta^2)^{\frac{1}{2}}}{\omega}.$$

This in fact corresponds to τ_a in (11). By increasing ω, τ_a can be made as small as desired compared with τ_b.

3. Experimental Chopper

A rotating crystal chopper has been built in order to test the characteristics of the device.

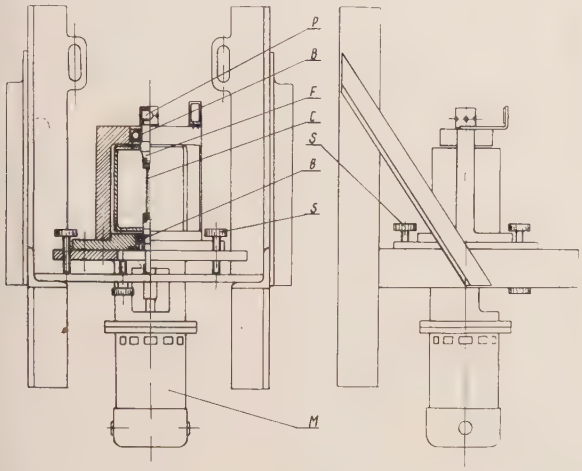

Fig. 2. Drawing of experimental model of chopper. C = single crystal, F = frame holding crystal, B = bearings, M = motor driving crystal, P = glass prisms in lucite cylinder, S = leveling screws.

The design adopted is by no means optimal but is very simple. The mechanical construction will be evident from fig. 2 and the photographs 1 and 2. The crystal in the form of a plate of dimensions 5 × 50 × 50 mm, is mounted in an aluminium frame which rotates about a vertical axis. The crystal plate is cut so that an appropriate crystallographic plane is parallel to the

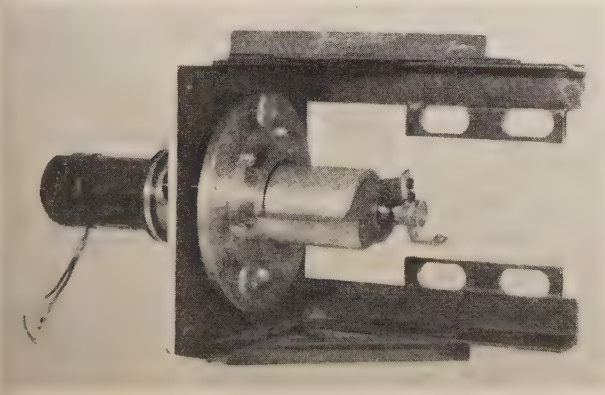

Photograph 1

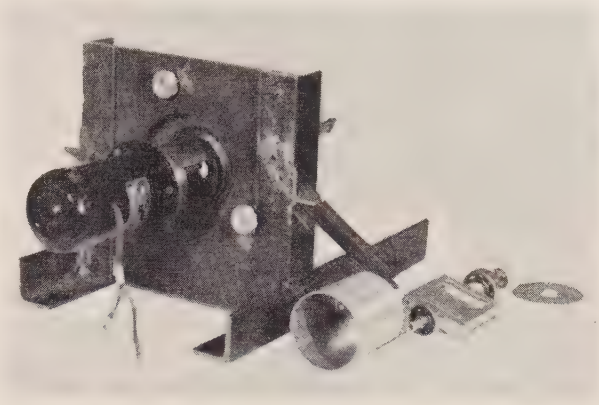

Photograph 2

larger surface of the plate. The crystal and the frame are enclosed in a thin cylindrical aluminium shield to reduce the air resistance in rotation. The crystal is driven by a 100 W series wound electric motor which gives a maximum speed of 15 000 r.p.m. The rotor together with the crystal are very light so that dynamic balancing is not required, care being taken only to ensure that the crystal is mounted symmetrically with respect to the axis.

An electrical impulse for sychronizing the time analyzer is derived from an optical arrangement with a photocell. On the upper end of the rotor axis, two small glass right-angled prisms are mounted with their larger faces pressed together. A narrow light beam when reflected through 90° by the prisms is focussed on a 1 mm slit in front of a photocell at a distance of about 50 cm from the axis. The use of two prisms pressed together ensures that the impulses are 180° apart. The crystal of course gives two neutron pulses, 180° apart, per revolution. The rise time of the light pulse is of the order of microsecond for speeds of rotation as low as 1000 r.p.m.

4. Measurements with the Experimental Chopper

The measurements described below were made at the VVRS reactor in Warsaw. Measurements were made of the width of the neutron pulse as a function of the speed of rotation. The crystal used was zinc cut with its (002) planes

parallel to the larger face. The collimators were of the Soller type with steel strips forming slits of nominal half-width 10 minutes of arc. The neutron detector consisted of a bank of BF_3 neutron counters of effective thickness about 6 cm, placed at a distance of 3.19 m from the crystal axis. A 100-channel time analyzer was used with a channel width of 5 microseconds. The interval between the synchronizing impulse and the beginning of the first channel could be be varied.

The neutron impulses were found to be approximately Gaussian in shape. The counting rate in the analyzer was 250 counts/min at the maximum, and the background counting rate was less than 1% of this value. The half-width of the observed impulses includes contributions due to the channel width and the effective detector width. Thus the total width, τ, will be given by:

$$\tau^2 = \tau_a^2 + \tau_b^2 + \tau_c^2 + \tau_d^2$$

where τ_d is the detector width and τ_c the analyzer channel width. From (11) it is seen that τ_a is proportional to $1/\omega$ so that a plot of τ^2 versus

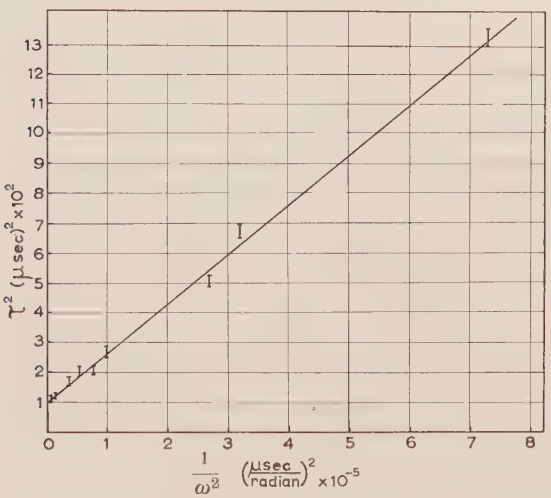

Fig. 3
Plot of τ^2 versus $1/\omega^2$ for experimental model chopper.

$1/\omega^2$ should give a straight line of slope $2\,(\ln 2)^{\frac{1}{2}}\,\delta$ and intercept at $1/\omega^2 = 0$ of $\tau^2 = \tau_b^2 + \tau_c^2 + \tau_d^2$. In fig. 3 there are plotted the observed values of τ^2 as a function of $1/\omega^2$. From the slope δ is found to have the value of 27 ± 1 minutes of arc which is a reasonable value for the collimator and crystal used. The limiting value of τ was found to be 31 ± 1 microseconds. The detector half-width was estimated, on the basis of its thickness and the average neutron velocity, to be 20 microseconds. τ_b is then found to be approximately equal to 22 microseconds which from eq. (11) gives for α the value 9.4 minutes which is in good agreement with its design value.

Since the light pulse giving the synchronizing impulse was not coincident with the neutron pulse at the crystal, the centre of the neutron pulse at the detector moved in the analyzer channels as ω was varied. Since the delay between the synchronizing pulse and the neutron pulse at the crystal depends on $1/\omega$ a plot of the channel number of the centre of the pulse at the detector versus $1/\omega$ gives a straight line, and the intercept at $1/\omega = 0$ gives the channel number of the centre of the pulse corresponding to the true time of flight of the neutrons. In this way the time of flight for the particular Bragg angle used was found to be 1005 ± 5 microseconds which corresponds to a wavelength of 1.28 A. At this wavelength the pulse of second order neutrons given by the crystal was observed to have an amplitude of 2% of the first order pulse.

5. Concluding Remarks

The rotating crystal chopper is a comparatively simple device to build. Its performance can be predicted on the basis of static measurements made on the crystal on a crystal spectrometer. Its normal limiting wavelength resolution is the same as that of a normal crystal monochromator. It is shown that under certain circumstances however, the effective wavelength resolution can be considerably increased.

Acknowledgements

The author wishes to thank K. Skoczek who was responsible for the mechanical design and S. Szafran and S. Nabywaniec for technical assistance.

NUCLEAR INSTRUMENTS AND METHODS 8 (1960) 249–254; NORTH-HOLLAND PUBLISHING CO.

ZUM EINFLUSS DER KRISTALLFORM AUF DAS ENERGETISCHE UND ZEITLICHE AUFLÖSUNGSVERMÖGEN EINER SZINTILLATIONSANORDNUNG

G. LUCK

Jena, Lasallestr. 6

Eingegangen am 25. April 1960

A decrease of the number of reflections of photons in a scintillation crystal leads to smaller fluctuations in time and pulse amplitudes of the output signal. This is possible with special forms of the scintillator. Mainly for great scintillator dimensions and high particle energies this seems of some interest. It is one of the ways to raise the energetical and time resolution of a scintillation arrangement.

1. Einleitung

Neben dem guten zeitlichen Auflösungsvermögen eines Szintillationszählers wünscht man oft ein hohes energetisches Auflösungsvermögen. Mehrere Wege wurden bereits eingeschlagen, um den Szintillationsprozess so zu beeinflussen, damit dieses Ziel erreicht wird. Man entwickelte empfindliche Fotokatoden, verbesserte die Elektronenoptik der Vervielfacher und dergleichen mehr.

Aber kein noch so gut ausgesuchter Szintillator auf der einen und kein noch so optimal gestalteter Multiplier auf der anderen Seite bringen den gewünschten Erfolg, wenn nicht beide gleichzeitig in sinnvoller Weise zum Szintillationszähler vereint werden. Alle Fotonen einer Szintillation sollen möglichst vollzählig zur Fotokatode gelangen. Praktisch entstehen aber Verluste durch die Absorption im Kristall bzw. Lichtleiter und durch die unvollständige Reflexion des umgebenden Reflektormaterials. Die Verlustrate wird umso höher ausfallen, je grösser die Zahl der Reflexionen ist. Die Form des Szintillators hat einen grossen Einfluss darauf.

2. Die Statistik des Szintillationsprozesses

Im wesentlichen besteht der Szintillationsvorgang aus sechs Einzelprozessen[1]):

1. Die Absorption der Kernstrahlung im Szintillator.

2. Die Umwandlung der Energie durch Lumineszenz in Lichtquanten.

3. Der Transport der Fotonen zur Fotokatode.

4. Die Auslösung von Fotoelektronen aus der Fotokatode.

5. Die Elektronenvervielfachung durch die Dynoden des Multipliers.

6. Die Analyse der Ladungsimpulse durch die nachfolgende elektronische Anordnung.

Alle sechs Vorgänge sind statistischer Natur. So hängt die Absorption der Strahlung im Szintillator davon ab, an welcher Stelle sie erfolgt; dasselbe gilt für die Umwandlung in Lichtquanten. Die pro Energieeinheit der einfallenden Strahlung erzeugte Fotonenzahl hängt offensichtlich von der Homogenität der Anregungszentren im Kristall ab. Optische Inhomogenitäten, Sprünge u.s.w. verursachen zusätzliche statistische Schwankungen der Ausgangsimpulse. Ein auf die Katode fallendes Foton kann entweder ein Fotoelektron auslösen oder keines. Die fotoelektrische Empfindlichkeit, die auch mit veränderlicher Fotonenenergie variiert, ist ebenfalls nicht an allen Punkten gleich. So ist diese Umwandlung durch das polychromatische Licht statistisch gesprochen ein aus vielen Einzelprozessen zusammengesetztes "Entweder–Oder" Ereignis. Dasselbe gilt vom Transport der Fotonen zur Katode. Die Chance, überhaupt zur Katode zu gelangen, hängt im wesentlichen von der Zahl der Reflexionen im Kristall und Lichtleiter ab. Nur ein durchschnittlicher Bruchteil f

[1]) Price, Nuclear Radiation Detection (McGraw-Hill, 1958).

der ursprünglichen Fotonenzahl wird ankommen. Da f von der Geometrie der Szintillatoranordnung abhängt – genau wie die einzelnen Umwandlungsgrade von Fotonen in Fotoelektronen –, so bewirkt schon eine einfache Drehung des Vervielfachers gegenüber seinem Szintillator eine veränderte statistische Verteilung der Ausgangsimpulse. Der gesamte Szintillationsvorgang ist ein komplexes statistisches Zusammenspiel aller angeführten sechs Einzelprozesse. Die statistische Durchrechnung wurde bereits weitgehend von Breitenberger[2]) durchgeführt. Daneben existieren noch viele Beiträge anderer Autoren[3–6]), die ebenfalls mehr oder weniger vollständig den gesamten Szintillationsprozess mathematisch statistisch behandelten. An dieser Stelle soll ausführlicher auf den Einfluss der Kristallform und der Verspiegelung der Szintillatorwände eingegangen werden. Es wird sich heraus-stellen, dass der Lichtüberführungsfaktor f auch durch die Form der Kristalle beeinflussbar ist.

Die statistische Behandlung der gestellten Aufgabe erfolgt mit der Methode der "Momente erzeugenden Funktionen" oder kurz "erzeugende Funktionen" (generating functions), wie sie bereits von Laplace und De Moivre eingeführt wurden. Diese Methode erlaubt eine konzentrierte mathematische Behandlung mancher statistischer Probleme.

Es ist das Ziel aller mathematischen Ausführungen, das relative Schwankungsquadrat

$$R^2 = \frac{\delta^2}{\bar{n}^2} \tag{1}$$

zu finden.
Mit der Definition der Generatorfunktion

$$G(x) = \sum_n p_n x^n$$

(x = Hilfsvariable) (2)

folgt an Stelle von (1):

$$R^2 = \frac{G''(1) + G'(1) - [G'(1)]^2}{[G'(1)]^2} \tag{3}$$

(G' = Ableitung nach x)

Für eine vorliegende Problemstellung bleibt nur übrig, die jeweilige Generatorfunktion zu finden, mit deren Hilfe sich dann das relative Schwankungsquadrat nach Formel (3) errechnen lässt.

So findet man für die Erzeugnung der Sekundärelektronen im Vervielfacher eine Generatorfunktion, die sich nur in rekursiver Form ausdrücken lässt. Die Generatorfunktion $G_2(x)$ für die zweite Elektronenkaskade ist

$$G_2(x) = G[G_1(x)] \tag{4}$$

oder allgemein

$$G_{n+1}(x) = G[G_n(x)]\,, \quad \text{mit} \tag{5}$$

$$G_1(x) = G(x) = q + px^m\,. \tag{6}$$

Die Wahrscheinlichkeit m Sekundärelektronen zu erzeugen ist p, der Fall der inaktiven Wahrscheinlichkeit ist $q = 1 - p$.

Die Zahl der Dynoden sei n.

Liegt eine Poissonverteilung (Normalverteilung) vor, so gilt wegen

$$G(x)\, e^{-\lambda(1-x)} \tag{7}$$

nach mehreren Umformungen

$$R_n^2 = \lambda^2 \frac{\bar{m}^{n-1}(\bar{m}^n - 1)}{\bar{m}^{2n}(\bar{m} - 1)} \tag{8}$$

($\bar{m}$ = mittlere Zahl der erzeugten Sekundärelektr.)

mit $\lambda^2 = R^2(X_1)$ und X_1 als Zahl der Elektronen an der ersten Dynode. Für $\bar{m} > 1$ und grössere n ($n \geq 10$) vereinfacht sich Formel (8) zu

$$R_n^2 = \frac{\lambda^2}{\bar{m}(\bar{m} - 1)}\,. \tag{9}$$

Das ist eine Beziehung, die oft im Zusammenhang mit den statistischen Schwankungen eines Szintillationszählers angegeben wird. Die relativen Schwankungen der Elektronen an der ersten Dynode erscheinen am Ausgang um den Faktor $\sqrt{\bar{m}(1/(\bar{m} - 1))}$ verkleinert.

Für grössere Werte von n sind diese Schwankungen von n selbst unabhängig. Eine Erhöhung der Stufenzahl n ändert also nichts an der

[2]) E. Breitenberger, Progress in Nuclear Physics Vol. 4 (1955).

[3]) F. J. Garlick und G. T. Wright, Brit. J. Appl. Phys. 5 (1954) 13.

[4]) G. T. Wright, Phys. Rev. **91** (1953) 1282.

[5]) G. T. Wright, J. of Sci. Instr. **31** (1954) 377.

[6]) W. Feller, Probability Theory and its Applications, (John Wiley, London, 1950).

Schwankungsbreite der Ausgangsimpulse. Es kommt nach Formel (9) nur darauf an, die Zahl der Partikel an der ersten Dynode so hoch wie möglich zu halten, damit die Ausgangsschwankungen klein bleiben. Im λ^2 stehen dann alle statistischen Änderungen verursacht durch unvollständige Lichtüberführung, inhomogen empfindliche Fotokatoden, wechselnde Szintillatorausbeute u.s.w. Um auch diese Einflüsse zu erfassen, wählte Breitenberger einen anderen Ansatz für die Generatorfunktion. Er ging aus von

$$G(x) = E(1 - f) + f \cdot V(x) \qquad (10)$$

mit $V(x)$ als Generatorfunktion der Verstärkung des Vervielfachers, $E(x)$ als Generatorfunktion der Elektronenemission und mit der durchschnittlichen Fotonenüberführungszahl $\bar{f} = \sum_i q_i f_i$.

Als Ergebnis fand er für die relative quadratische Schwankung des Ladungsstosses am Ausgang:

$$R_Q^2 = R_f^2 + \frac{1 + R_v^2}{\bar{E}\,\bar{f}}. \qquad (11)$$

Dieses Ergebnis entspricht dem bereits auf anderem Wege gefundenen Resultat von Garlick und Wright[3]). R_V ist die relative Schwankung, die durch den Verstärkervorgang im Multiplier entsteht, R_f die aus der Fotonenleitung herrührende.

Trägt man nun R_Q^2 als Funktion von $(Ef)^{-1}$ auf, so erhält man eine sehr eindringliche Darstellung (Abb. 1), wie sie bereits Hopkins 1951 vorschlug. Er fand eine Gerade, die um R_f^2 über

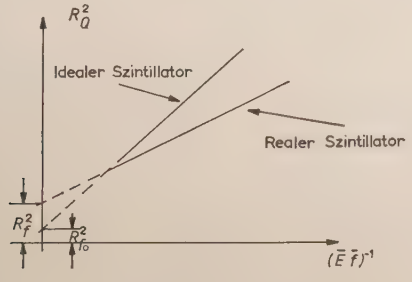

Abb. 1. R_Q^2 als Funktion von $(Ef)^{-1}$.

dem Koordinatenursprung die Ordinate schnitt, genau wie es auch Formel (11) verlangt, wenn f keine Konstante sein soll. Im Falle $f = \text{const.}$, müsste die Gerade durch den Nullpunkt laufen, so wie es sehr oft in der Literatur beschrieben ist. Die Neigung der Geraden ist ein Mass für die Katodenempfindlichkeit des Vervielfachers. Sie verläuft steiler bei grösseren Empfindlichkeiten.

Der Wert von R_f^2 ist offensichtlich davon abhängig, wieviel Schlieren oder sonstige optische

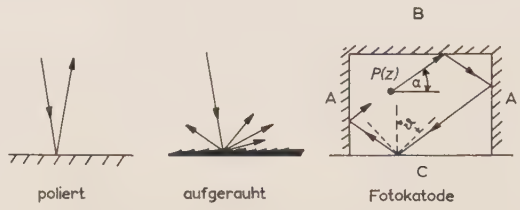

Abb. 2. Schematische Darstellung des Reflektionsvorganges in einem Szintillator. Der Winkelbereich, unter dem keine Totalreflexion auftritt, beträgt 2ϑ.

Fehlstellen der Szintillator besitzt. Jedoch selbst unter der Annahme eines optisch idealen Kristalles, bleibt eine überraschende Tatsache bestehen, dass nämlich R_f^2 mindestens noch in der Grössenordnung 10^{-3} (rel. Schwankung von 3 bis 4%) ist. Namentlich bei guten Szintillationsspektrometern und hohen Quantenenergien ist oft dieser Wert allein verantwortlich für das Gesamtauflösungsvermögen! Zum Beispiel für Gammaenergien grösser als 1 MeV kann man mit einem Szintillator aus NaJ (Tl) $\bar{E}\,\bar{f} > 10^3$ ansetzen und dann ist R_f^2 von merklichem Einfluss. Woher kommt selbst bei optisch idealen Kristallen diese "Grundschwankung" R_{f0}^2? Wie lässt sie sich beeinflussen? Die erste Frage lässt sich dahingehend beantworten, dass selbst optisch ideale Kristalle ein $R_{f0}^2 \approx 10^{-3}$ durch die statistische Zahl der Reflexionen des Lumineszenzlichtes innerhalb des Kristalles erhalten. Das mögen die folgenden Ausführungen und Abbildungen belegen (Abb. 2). Rein anschaulich leuchtet aus der rechten Darstellung der Abb. 2 ein, dass die Anzahl der Reflexionen $r(z)$ davon abhängt, an welchem Kristallort $P(z)$ die Fotonen entstehen und unter welchem Winkel von $P(z)$ gegen die Flächen A, B und C sie emittiert werden. Da das Kristallmedium als optisch sehr gut durchlässig betrachtet werden soll (gilt nicht für Polykristalle und zu kurzwelligen Licht), so tritt beim Auftreten auf die Fläche C sehr oft der Fall einer Totalreflexion ein. Erst wenn das Foton durch eine Störstelle im Szintillator bzw. durch den

Reflektor in eine andere Richtung gelenkt wird, kann es in günstige Winkelbereiche kommen und schliesslich doch zur Fotokatode gelangen. Unter Umständen hat es dabei eine recht erhebliche Zahl von Reflexionen durchgemacht. Nicht nur Kristallinhomogenitäten, sondern auch der Rauhigkeitsgrad der Reflektorwände A und B sind von grossem Einfluss. Angerauhte Wände können diese Zahl erheblich reduzieren. Mit pulverisiertem MgO statt hochpoliertem Magnesium oder Aluminium als Reflektor konnte in der Tat auch messtechnisch eine Verbesserung des Energieauflösungsvermögens erzielt werden[1]).

Durch jede Reflexion treten Verluste an Fotonen im Reflektormaterial auf. Im Endergebnis geben dann Schwankungen der Zahl der Reflexionen eine entsprechende Schwankung der Fotonenzahl. Mit wachsender Zahl der Reflexionen nimmt auch das relative Schwankungsquadrat der Fotonen zu. Vernachlässigt werden Verluste durch die Absorption im Szintillator gegenüber den Verlusten im Reflektormaterial. Quantitativ folgt so für das Quadrat der relativen "Grundschwankung" R_{f0}^2:

$$R^2_{f0} = (1 - \rho)^2 R_r^2 . \qquad (12)$$

Dabei sind ρ der Reflexionsfaktor und R_r die relative Fotonenschwankung auf Grund der Reflexionen. Um R_{f0} klein zu halten, sind ein grosses ρ und nur wenige Reflexionen anzustreben. Für MgO und die in Frage kommenden Wellenlängen um 4000 Å liegt ρ in der Grössenordnung 0.9. Das ist ein ziemlich hoher Wert, wenn man die Skala der Reflexionskoeffizienten fester Körper betrachtet.

Gelingt es nun, die Generatorfunktion des Reflexionsvorganges aufzustellen, so ist R_r^2 bestimmbar und gemäss Formel (12) auch R_{f0}^2. Für den Fall, dass gleichwahrscheinlich ein bis n-Reflexionen auftreten können, findet man als Generatorfunktion folgenden Ausdruck:

$$G_n(x) = \frac{x}{n} \frac{x^n - 1}{x - 1} . \qquad (13)$$

Treten nur einmalige bis doppelte Reflexionen auf, so wird $R_r^2 = 0.11$ und mit $\rho = 0.9$ würde $R_{f0}^2 \approx 10^{-3}$.

Das ist aber genau die Grössenordnung, wie sie bereits für den idealsten Kristall als nicht unterschreitbar angegeben wurde. Zieht man noch die Möglichkeit von Dreifachreflexionen in Betracht, so wächst R_f^2 auf den Wert 0.17 an. Für gleichwahrscheinlich auftretende Reflexionen bis $n = 20$ wirde der Verlauf von R_r^2 als Funktion von n in Abb. 3 errechnet. Man erkennt daraus deutlich, dass besonders stark in Anfangsteil der Kurve ein Anstieg von R_r^2 erfolgt. Eine Ausschaltung aller Drei- bis Mehrfachreflexionen auf nur einfache und doppelte, würde das Auflösungsvermögen um mindestens 20% verbessern.

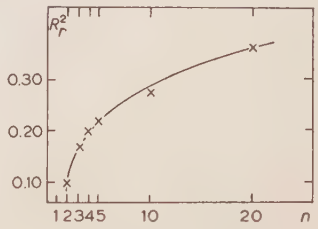

Abb. 3. Das relative Schwankungsquadrat R_r^2 als Funktion der Zahl der Reflexionen n im Szintillator.

Ein Weg dazu wurde bereits angedeutet, nämlich das umgebende Reflektormaterial anzurauhen. Eine andere Möglichkeit wäre eine geeignete Formgebung des Szintillators. Statt zylindrischer Formen sollte man besser konische verwenden. Namentlich bei grossen Flüssigkeitsszintillatoren oder plastischen Phosphoren und hochenergetischen Partikeln, für deren Nachweis ein gutes Auflösungsvermögen gewünscht wird, erscheint die konische Form vorteilhafter. Rein geometrisch kann man sich anhand der Abb. 4 klarmachen, dass mit erhöhter Neigung der Flächen A der Winkelbereich kleiner wird, unter dem eine Totalreflexion auftritt. Das führt zu weniger Reflexionen und damit zu einem kleineren R_{f0}. Natürlich sind auch andere, ähnliche Kristallformen denkbar – etwa ein konisch zugespitzter Zylinder –, bei dem sich ebenfalls die Zahl der Reflexionen herabsetzen liesse.

In der Praxis hat man keine idealen Szintillatoren und ein Teil des R_{f0}-Wertes hat auch andere Ursachen. Das können bevorzugte Lumineszenzgebiete oder durch Nachleuchten der

Kristalle verursachte unnormale Szintillationsänderungen sein. Allerdings nur unter ungünstigen Verhältnissen gewinnen diese Faktoren gegenüber dem Einfluss der Statistik des Reflexionsvorganges vergleichbar Bedeutung.

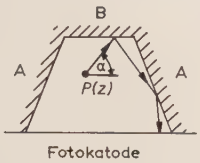

Abb. 4. Durch die konische Form wird der unter dem Winke α emittierte Lichtstrahl (vergl. Abb. 2) nicht mehr tota reflektiert.

3. Grenzen des zeitlichen Auflösungsvermogens

Das Auflösungsvermögen von Koinzidenzanordnungen für ultrakurze Zeiten, zum Beispiel von Chronotons, hängt ab von den zeitlichen Schwankungen der Anstiegszeit der Szintillationsimpulse. Das gilt auch für Koinzidenzanordnungen, die von der Impulsbreite nicht stark abhängig sind, wie die Differentialmethode von Z. Bay[7]).

Das zeitliche Auflösungsvermögen für sehr kurze Zeiten wird durch den Szintillationszähler bestimmt, nicht aber durch die Technik der Koinzidenzkreise. Drei Faktoren sind es, die für die Schwankungen der Anstiegszeit der Szintillationsimpulse verantwortlich sind:

1. Die Fotonenemission des Szintillators erfolgt statistisch.

2. Schwankungen der Sammelzeit der Fotonen durch die endliche Grösse von Szintillator und Lichtleiter.

3. Schwankungen der Fotoelektronen und Sekundärelektronen im Vervielfacher.

Beim Čerenkovzähler entfällt die erstgenannte Ursache. Anstelle dieser Schwankungen treten die Abweichungen der Flugzeit der relativistischen Partikel im Radiator.

R. F. Post und L. I. Schiff[8]) errechneten erstmalig das mittlere Schwankungsquadrat Δt_E^2 für die unter 1) angeführte Schwankungsursache. Sie fanden dafür folgenden Ausdruck:

$$\Delta t_E^2 \approx \frac{t_0^2 q}{q_0^2}\left[1 + \frac{2(q+1)}{q_0}\right]. \qquad (14)$$

Dabei sind t_0 die Abklingzeit des Phosphors, q die Zahl der Elektronen, die mit Sicherheit zur Impulsbildung beitragen und q_0 die durchschnittliche Gesamtzahl der emittierten Fotoelektronen (bei einem angenommenen Überführungsgrad der Elektronen aus der Katode zur ersten Dynode von 100%). Als Beispiel für ziemlich optimale Verhältnisse seien 1 MeV-Elektronen mit einem Umwandlungsgrad von 1% der Fotonen in Fotoelektronen für Terphenyl in Toluol ($t_0 \approx 2.5 \times 10^{-9}$ sec) angenommen. Nur das erste emittierte Elektron möge zur Impulsbildung ausgenutzt werden; also $q = 1$. Dann folgt für $\overline{\Delta t}$:

$$\sqrt{\overline{\Delta t^2}} \approx 3 \times 10^{-11}\,\text{sec}\,.$$

Für Koinzidenzmessungen ist dieser Wert noch mit $\sqrt{2}$ zu multiplizieren.

Diese Grösse von einigen 10^{-11} sec für die Schwankungen der Fotonenemission kann man als Grenzwert ansehen, wie er zur Zeit mit den gebräuchlichen Szintillatoren und Vervielfachern für ultrakurze Zeiten erreichbar ist. Wenn es durch wirksamere Fotokatoden gelänge, den Umwandlungsgrad von Fotonen in Fotoelektronen zu steigern, so würde q_0 anwachsen und man erhält für die Schwankungen der Fotonenemission noch kleinere Zeitwerte. Ein Weg in dieser Richtung stellt die Entwicklung der Multialkali-Katode dar. Sie hat eine etwa 2 bis 3-fach höhere Empfindlichkeit im Vergleich zu den üblichen Fotokatoden vom Typ Cs-Sb.

Auch die Schwankungen $\overline{\Delta t}_V$ der Elektronen der Fotokatode und Dynoden eines Vervielfachers lassen sich bereits in die Grössenordnung einiger 10^{-11} sec bringen. Normalerweise stellen sie mit konventionellen Vervielfachertypen den Hauptanteil der zeitlichen Gesamtschwankungen. Das gilt vor allem für Ausführungsformen mit Jalousie- und Netzdynoden. Speziell für die Kurzzeittechnik entwickelte und im Handel erhältliche Typen, wie zum Beispiel die sowj. Vervielfacher ФЭУ-33 und ФЭУ-36 und der amerikanische RCA 6810 A, erreichen schon Anstiegszeiten – ausgelöst von nur einem bzw.

[7]) Z. Bay, Phys. Rev. **83** (1951) 242.
[8]) R. F. Post and L. J. Schiff, Phys. Rev. **80** (1950) 1113.

weningen Fotoelektronen – von der Grössenordnung 10^{-9} sec und weniger. Der RCA 6810 A ist ein modifizierter RCA 6810, dessen ebene Fotokatode durch ein gewölbte ersetzt wurde, um die Laufzeitschwankungen von der Katode zur ersten Dynode zu verkleinern. Darüber hinaus gibt es noch eine Reihe anderer Massnahmen, um die Laufzeiten der Elektronen im Vervielfacher zu vermindern. Aus der Zahl der Möglichkeiten erwähne ich nur eine interessante Lösung, die RCA beim Typ C 7251 beschritt. Durch Spannungen von alternierendem Vorzeichen an den Dynodenstrecken erreichte man eine schnelle Anfangsbeschleunigung mit anschliessendem raschen Abbremsen der Elektronen kurz vor der nächsten Dynode. Die grossen Streuungen der Anfangsgeschwindigkeiten der Foto- und Sekundärelektronen wurden vermindert und durch das Abbremsen wurde wieder eine Geschwindigkeit hergestellt, wie sie für eine maximale Ausbeute an Sekundärelektronen notwendig ist. Durch dieses Beschleunigungs-Bremsprinzip liessen sich die zeitlichen Schwankungen auf kleiner als 10^{-10} sec herabdrücken!

Bleibt nur noch die Berechnung der Schwankungseinflüsse, wie sie von den verschiedenen Sammelzeiten der Fotonen im Szintillator und Lichtleiter entstehen. Auf Grund der Beziehung

$$\sqrt{\overline{\Delta t_{\mathrm{E}}^2}} \approx 3 n_{\mathrm{B}} \sqrt{\overline{\Delta s_{\mathrm{F}}^2}} \times 10^{-11} \text{ sec}\,, \qquad (15)$$

mit der mittleren Schwankung $\sqrt{\Delta s_{\mathrm{F}}^2}$ (in cm) des Laufweges und n_{B} als Brechzahl des Szintillators für die wirksame Fluoreszenzwellenlänge ist eine Abschätzung dieser Grösse möglich.

Je nach der Zahl der Reflexionen im Szintillator und Lichtleiter werden sich auch die Laufwege voneinander unterscheiden. Die absolute Grösse von Δs_{F}^2 hängt natürlich von der im Einzelfall benutzten Anordnung ab und ist nicht einfach mathematisch zu erfassen. R. F. Post[9]) gab in erster Näherung für einen zylindrischen Lichtleiter eine Abhängigkeit zwischen Schwankung und Länge des Lichtleiters an.

Prinzipiell steht man jedoch vor der gleichen Frage wie im Falle des energetischen Auflösungsvermögens nicht zu kleiner Partikelenergien: Wie vermindert man im statistischen Mittel die Zahl der Reflexionen? Bereits D. C. Moore[10]) bestätigte messtechnisch den Einfluss einer verbesserten optischen Koppelung zwischen Szintillator und der Fotokatode eines RCA 4646. Die Zeitauflösung wurde eindeutig besser.

Da sich die mittlere Gesamtschwankung $\overline{\Delta t_{\mathrm{G}}}$ eines Szintillationszählers nach Formel

$$\sqrt{\overline{\Delta t_{\mathrm{G}}^2}} = \sqrt{\overline{\Delta t_{\mathrm{E}}^2} + \overline{\Delta t_{\mathrm{V}}^2} + \overline{\Delta t_{\mathrm{F}}^2}} \qquad (16)$$

berechnet, und alle Summanden unter der Wurzel mit gleichem mathematischen Gewichtsfaktor auftreten, so dürften unter der Annahme optimaler Verhältnisse der Einflüsse von 1) und 3) die Schwankungen der Sammelzeit der Fotonen im Bereich der Mikromikrosekunden nicht mehr vernachlässigbar sein. So wie es für bestimmte Messungen des energetischen Auflösungsvermögens auf möglichst wenige Reflexionen ankommt, so gilt das gleiche auch für Kurzzeitmessungen. Dabei wird man in Zukunft der Form und Güte des Szintillators und des umgebenden Reflektors mehr Beachtung schenken müssen.

Zusammenfassung

Ausgehend von der Forderung nach einer kleinen relativen statistischen Schwankung der Ausgangsimpuls am Vervielfacher wird gezeigt, dass Schwankungen der Fotonenüberführungszahl eine zusätzliche Verschlechterung des energetischen Auflösungsvermögens bewirken. Dabei hat auch die Kristallform einen Einfluss. Durch günstig gewählte Formen kann man die Zahl der Reflexionen im Szintillator herabsetzen. Namentlich für hohe Teilchenenergien und grosse Szintillatoren erreicht man bessere energetische Auflösungswerte.

Auch das zeitliche Auflösungsvermögen im Bereich von Zeiten kleiner als ca 10^{-11} sec ist nicht mehr von den Schwankungen der Sammelzeit der Fotonen im Szintillator unabhängig. Eine weitgehende Verminderung der Zahl der Reflexionen erscheint dann ebenfalls angebracht.

[9]) R. F. Post, Nucleonics, **10** (1952) 56.

[10]) D. C. Moore, Nucleonics (1955) p. 55, Special Report.

NUCLEAR INSTRUMENTS AND METHODS **8** (1960) 255–258; NORTH-HOLLAND PUBLISHING CO.

LETTERS TO THE EDITOR

IRON-FREE TOROIDAL BETA-BETA COINCIDENCE SPECTROMETER†

MELVIN S. FREEDMAN, FRANK WAGNER, JR., FRED T. PORTER, JOHN TERANDY and PAUL P. DAY

Argonne National Laboratory, Lemont, Illinois

Received 14 March 1960

The first half of a double beta spectrometer, being an iron-free version of the "sliced orange" design of Kofoed-Hansen *et al.*[1]) has been completed. The dual instrument consists of two identical, independent, "back-to-back", plane normal to the axis midway between its detector (D) and the source (S), i.e., the conductors bounding the entrance and exit to the toroidal magnetic field have mirror symmetry, and are precisely formed to have their center

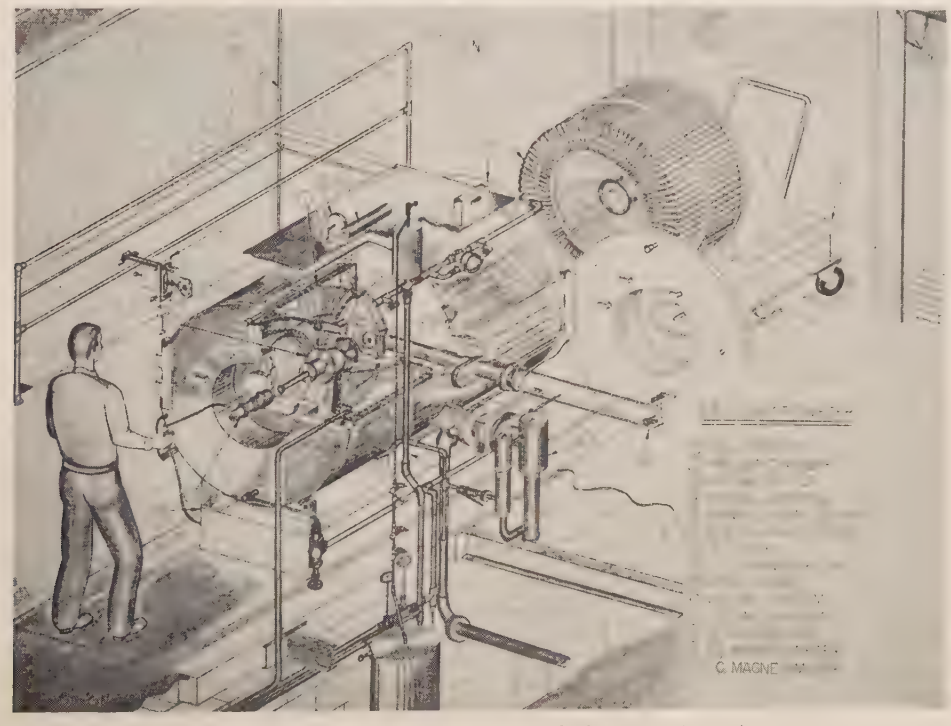

Fig. 1. Isometric projection of double beta spectrometer.
West toroidal coil shown withdrawn from vacuum chamber on coil transfer cart.

100 turn, 100 gap toroidal coils of 1 meter over-all diameter, mounted 12 cm apart in a 1.15 meter diameter, 1.6 meter long vacuum chamber, with the source midway between them on their common axis. Each coil is symmetrical about a lines lie on the focussing curve consistent with the parameter $b^{(1)} = \rho/r = p/A_0 e = 0.59$, where $H = A_0/r$. The performance of the instrument is quite sensitive to the choice of this parameter, owing to the cylindrical lens defocussing effects

† Based on work performed under the auspices of the U. S. Atomic Energy Commission.

[1]) O. Kofoed-Hansen, J. Lindhard and O. B. Nielsen, Det. Kgl. Dansk. Vid. Selsk. **25**, No. 16 (1950).

at the field boundaries[1]). Betas emitted between 30°—70° of the axis can be focussed. The open solid angle in the gaps between the conductors in the range 30°—70° is 20.2%. Distance S—D = 67 cm. E_{max} is 3.5 MeV, requiring 1150 amps at 140 kW, resulting in a maximum rise of 12° C over ambient of the iron-free-water cooled, flattened, tubular conductors ($\frac{1}{8}'' \times \frac{3}{8}''$ cross section). The current supply is a servo controlled motor generator, with series output stage consisting of 240 Delco transistors, type 2N278.

The performance results on the first toroid (transmission T, % of 4π steradians, measured with intensity calibrated sources; resolution, R, full width at half max):

Source Diam	$\frac{1}{8}''$	$\frac{1}{8}''$	$\frac{1}{8}''$	$\frac{1}{4}''$	$\frac{3}{8}''$	1 mm	1 mm
T (%)	19	16	2.8	16	18	13	1.6
R (%)	0.93	0.40	0.21	0.56	0.88	0.30	0.13

One can use the two instruments so as to add their transmissions. As they are rotationally "in phase", they can also be operated in tandem (source at usual detector position, small circular baffle at usual source position) with improved resolution and a large reduction in scattered background. For β—β coincidence studies the efficiency at $R \leq 1\%$ is improved by < 100 over existing instruments. All currents to the toroid and in the series connections between adjacent turns are circulated on coaxial leads, and the coils are constructed with a precision such that the leakage magnetic field at the source and throughout the volume of the second toroid $\leq 10^{-5}$ of the focussing field in the first. Thus 1 keV and 3 MeV betas can be focussed with negligible mutual interference. The construction is entirely non-ferrous, and the instrument is housed in a specially constructed non-ferrous building with all ferrous equipment, generators, motors, pumps, etc., located over 40 feet away from the spectrometer. A 20 foot cubical degaussing coil array surrounding the instrument enables compensation of $H_{earth} \leq 10^{-4}$ oersteds.

Baffles adjustable from outside the spectrometer:

(a) limit exterior and interior conical acceptance angles at source and detector over the range 30°—70°;

(b) intercept axial quantum radiation;

(c) continuously adjust the open width of each gap symmetrically about the gap mid plane;

(d) intercept all multiloop trajectories thus preventing transmission of ghost peaks. (Ghost peak/true peak $\leq 3 \times 10^{-5}$);

(e) select and continuously vary the azimuthal angle into each spectrometer over 360° range.

With this latter baffle β—β angular correlation measurements can be made over the angular range 45°—180° with $T \geq 1\%$. A gamma detector (3″ NaI crystal) can be inserted through a gated side port near the source enabling β—γ coincidences and angular correlation studies. α energy analysis by pulse ion chamber at the source position provides for (α, e^-) coincidence studies. Operation and recording are remote and automatized. Detectors include scintillation counters with provision for cooling the photomultipliers, (no light pipes needed) and proportional end window counters. A port and gate allow source insertion and position adjustment in 1 minute. With various detectors introduced through the side port, triple coincidences ($\beta\beta\beta$), ($\beta\beta\gamma$), ($\beta\beta\alpha$), ($\beta\beta$X) can be observed. A more detailed description of this instrument will be published later.

BANDWIDTHS OF THE EQUAL TIME-CONSTANT AMPLIFIER

J. B. S. WAUGH

Physics Division, Atomic Energy of Canada Limited, Chalk River, Ontario†

Received 8 May 1960

The use of amplifiers with upper and lower pass band limits defined by equal RC time-constants is common in those nuclear physics applications requiring the best signal-to-noise ratio. The relevant noise theory is very well known[1]) but in work on low noise ion chambers[2]) and semiconductor particle detectors[3]) a knowledge of the effective amplifier noise bandwidths was required. Explicit mention of these parameters was not found in the literature and it may be of value to note them.

Consider an ideal amplifier with a level frequency response from zero to infinity and having a voltage gain G_0. The transfer function of such an amplifier when operated with its high frequency response determined by a single (integration) time-constant T_1 and its low frequency response defined by a single (differentiation) time-constant T_2 is $G_0\, pT_1/(1 + pT_1)\,(1 + pT_2)$. When both time-constants equal T, the square of the transfer function or power gain $G(f)$ becomes $4\pi^2 G_0{}^2 f^2T^2/(1 + 4\pi^2 f^2T^2)^2$. The maximum gain occurs when $2\pi fT = 1$, thus defining f_c, the centre frequency of the pass band. The overall voltage gain at f_c is 6 db less than that of the flat amplifier. The half-power bandlimit points, $f_{0.5}$, thus occur at 9 db below the original reference and are the roots of the bi-quadratic

$$32\pi^2 f^2T^2/(1 + 4\pi^2 f^2T^2)^2 = 1.$$

Hence, $$f_{0.5} = f_c(\sqrt{2} \pm 1)$$

and the half-power bandwidth, $B_{0.5}$, is

$$2f_c = 1/\pi T\,.$$

† Present address: Research School of Physical Sciences, Australian National University, Canberra, A.C.T., Australia.

The effective noise bandwidth B_n evidently differs from the half-power bandwidth since it must be dependent on the actual noise spectral distribution in the region of the pass band. An effective bandwidth can be defined as the width in cps of a rectangular pass band which passes the same noise power. The bandwidth, B_n, so defined[4]) $= (1/G_c)\int_0^\infty G(f)\mathrm{d}f$ where $G(f)$ is the available power gain at the frequency f and $G_c = G(f_c)$ is the power gain at the centre of the pass-band, f_c. This definition supposes that the noise is white, however, if this is not so but the noise has a spectral distribution $P_n(f)\Delta f$, then a bandwidth, containing the same noise power, can be defined from f_c/k to kf_c, i.e.

$$G_0{}^2\int_{f_c/k}^{kf_c} P_n(f)\,\mathrm{d}f = \int_0^\infty G(f)P_n(f)\,\mathrm{d}f$$

where $G_0{}^2$ is the power gain of the flat amplifier

Table 1

Effective amplifier bandwidths for common noise spectral distributions

$P_n(f)$	Bandwidth $= \dfrac{k^2-1}{k}\, f_c$
f^0, shot noise	$\frac{1}{4}\pi f_c = 0.785\, f_c$
f^{-1}, flicker noise	$2f_c \sinh(\frac{1}{4}) = 0.505\, f_c$
f^{-2}, grid current noise	$\frac{1}{4}\pi f_c = 0.785\, f_c$

[1]) A. B. Gillespie, Signal, Noise and Resolution in Nuclear Counter Amplifiers (Pergamon Press, 1953).

[2]) J. B. S. Waugh, A Nuvistor Ionization Chamber Preamplifier, Atomic Energy of Canada Report, CREL-912 (1960).

[3]) J. M. McKenzie and J. B. S. Waugh, Silicon Junctions as Particle Spectrometers, Proceedings of the 7th Scintillation Counter Symposium, IRE, PGNS (1960).

[4]) S. Goldman, Frequency Analysis, Modulation and Noise (McGraw-Hill, 1948) p. 254.

assuming equal input and output impedances. Values of the resulting bandwidth, $(k^2 - 1)f_c/k$, are tabled below for the three most common types of noise distributions.

Thus for the "equal time constant amplifier", the half power or 3db bandwidth is twice the centre frequency while the effective noise bandwidth, though dependent on the noise spectral distribution, is also proportional to f_0 in the ratios given above.

The author wishes to acknowledge the assistance of R. E. Bell who read the manuscript and suggested a number of improvements.

BOOK REVIEWS

Experimental Nuclear Physics, Vol. III, Editor E. Segrè, John Wiley and Sons, Inc., New York, Chapman & Hall Ltd., London 1959.

This volume completes the book edited by Professor Segrè. The preceding volumes are already well known standard reference works in the field. The present book deals with Radioactive Decay (E. Segrè), Alpha Radioactivity (G. C. Hanna), Gamma Rays and Beta Rays (Martin Deutsch and O. Kofoed-Hansen) and, Particle Accelerators (E. M. McMillan). The Editor gives in his contribution a very elegant account of the statistical laws governing the radioactive decay and the basic experimental methods used for measurements of decay constants. G. C. Hanna's chapter on Alpha Radioactivity is comparable in scope and magnitude to the recent Handbuch der Physik article by Perlman and Rasmussen. These two surveys of alpha radioactivity will certainly for a long time remain the standard sources of reference. Hanna's paper is perhaps somewhat easier to follow and can be recommended as an introduction into the field. The following two chapters deal with gamma and beta decay. The latter has been revised and brought up to date since the parity nonconservation was discovered. It contains the basic theory and a fairly detailed account of the experimental methods. The chapter on gamma decay on the other hand seems to the reviewer in certain parts somewhat outdated. The compilation of material for this chapter was finished already 1955. For this reason some of the statements in this chapter are no longer valid. But the authors have made several interesting comments and called attention to certain problems worth future studies. The last chapter by Professor McMillan gives a review of the development of particle accelerators from the early days in 1926 when the acceleration of electrons to about 400 keV was achieved by means of high voltage X-ray tubes and up to the CERN and Brookhaven 30 GeV strong focussing machines. The author has managed to cover this vast field in only 150 pages.

It is not necessary to recommend this volume to the readers. T. R. GERHOLM

The Isotope Index, July 1959, International Edition, Editor: J. L. Sommerville, Scientific Equipment Co, Indianapolis 19, Indiana, $ 5.50.–. This handy booklet is a complete guide to the isotopes, containing information concerning U.S. A.E.C. licensing procedures, isotope supplies, availability, prices, catalogue numbers etc. of labelled compounds, standard sources and sources for radiographic and therapeutic use. Those interested in the industrial and medical applications of labelled compounds of radioactive and stable isotopes will find this Isotope Index very useful. T. R. GERHOLM

NUCLEAR INSTRUMENTS AND METHODS 8 (1960) 259–260; NORTH-HOLLAND PUBLISHING CO.

NEWS ITEMS

ACCELERATOR CONFERENCE

High Voltage Engineering Corporation has organized an accelerator conference to be held in Amsterdam October 4–6, 1960. The conference report will be published in our journal at an early date.

The conference program is the following:

Tuesday, October 4 - Nuclear Physics

Chairman: Prof. H. BRINKMAN,
University of Groningen, The Netherlands

Resonance Reactions—Prof. P. M. ENDT, *University of Utrecht, The Netherlands*
Energy-Angle Distribution of Positrons from a Thick Target Irradiated with Fast Electrons and
Spectrum and Intensity of Photons from Positron Annihilation in Flight—Prof. L. KATZ, *University of Saskatchewan, Saskatoon, Canada*
Coulomb Excitation—Dr. T. HUUS, *Institute for Theoretical Physics, Copenhagen, Denmark*
Experiments using Ultra-Fast Pulse Techniques—Dr. G. GOLDRING, *The Weizmann Institute, Rehovoth, Israel*
Nuclear Lifetimes—Dr. E. COTTON, *Centre d'Etudes Nucléaires de Saclay, Gif-sur-Yvette (S & O), France*
Injectors—Staff member of *Frascati, Italy*

Wednesday, October 5 - Particle Research

Chairman: Prof. H. H. STAUB,
University of Zürich, Switzerland

The Tandem Electrostatic Accelerator—Dr. P. ROSE, *High Voltage Engineering Corporation, Burlington Mass., U.S.A.*
Current Experimentation with the Tandem at the Chalk River Laboratories—Dr. H. GOVE, *Atomic Energy of Canada Ltd., Chalk River, Canada*
Advanced Methods for Nuclear Reactions Research—Dr. K. W. ALLEN, *United Kingdom Atomic Energy Authority, Aldermaston, England*
Polarized Ion Sources—Prof. R. FLEISCHMANN, *University of Erlangen, Germany*
Millimicrosecond Pulsing—Mr. R. CONNOR, *High Voltage Engineering Corporation, Burlington, Mass., U.S.A.*
Recent Advances in High Power Microwave Electron Accelerators for Physics Research—Mr. J. C. NYGARD, *High Voltage Engineering Corporation, Burlington Mass., U.S.A.* and Dr. R. F. POST, *University of California, Livermore, U.S.A.*

Thursday, October 6 - Physics and Radiation Research

Chairman: Prof. K. SIEGBAHN,
University of Uppsala, Sweden

High Intensity Neutron Research—Prof. K. LÜCKE, *Institut für Algemeine Metallkunde, Aachen, Germany*
Reactor Physics with Pulsed Neutron Sources—Dr. K. BECKURTS, *Institute of Neutron Physics, Karlsruhe, Germany*
Isotope Separation—Prof. J. KISTEMAKER, *Laboratorium voor Massaspectrografie, Amsterdam, The Netherlands*

Chairman: Prof. A. CHARLESBY,
Royal Military College of Science, Shrivenham, England

The Use of Electron Bombardment in Solid-State Research—Dr. P. BARUCH, *Ecole Normale Superieure, Paris, France*
Photoactivation and Photoneutron Activation Analysis—Dr. J. W. OTVOS, *Shell Development Company, Emeryville, California, U.S.A.*
High Energy Radiation for Research in Biochemistry and Microbiology—Dr. W. HUBER, *Stanford University, U.S.A.*
Development of Radiation Process Applications—Dr. S. H. PINNER, *B.X. Plastics Limited, England,* and Mr. W. H. T. DAVISON, *Tube Investment Research Laboratories, England.*
Research in Radiation Chemistry — Speaker not known
Future Accelerators: Intense Sources for Processing—Mr. D. A. TRAGESER, *High Voltage Engineering Corporation, Burlington Mass, U.S.A.*

For all information apply to *Mr. Nathan Tufts, Jr.*, High Voltage Engineering Corporation, Burlington, Mass., U.S.A.

SEMINAIRE INTERNATIONAL/INTERNATIONAL SEMINAR

LE CALCUL ANALOGIQUE APPLIQUE A L'ETUDE DES PROCESSUS CHIMIQUES

ANALOGUE COMPUTATION APPLIED TO THE STUDY OF CHEMICAL PROCESSES

Bruxelles 21–22–23 Nov. 1960

Organisé par/Organized by

Institut Belge de Régulation et d'Automatisme

Sous les auspices de/Sponsored by

l'Association Internationale pour le Calcul Analogique et l'Applications Committee of the International Federation of Automatic Control

The papers to be presented will be grouped under four headings:

I. Simulation of kinetic and thermal problems,

II. Simulation of chemical reactors,

III. Automatic control,

IV. Methods of operational research in the chemical industry.

Intending authors are asked to inform the Seminar Secretariat as soon as posible of their desire to present a paper. The address of the Secretariat is 43, Rue de la Science, Brussels 4, Belgium.

Spotlight on Industry

This section appears each month and features various happenings of interest in the nuclear industrial world and objective information on products of the nuclear manufacturers. It is offered entirely as a service and all nuclear manufacturers are cordially invited to submit clearly objective and descriptive material on their endeavours and product developments for consideration for use in this section.

NO TUBES, NO TRANSISTORS IN A NEW AUTOMATIC VOLTAGE REGULATOR

Ad. Auriema, Inc., Exporters, 85 Broad Street, New York 4, N.Y., U.S.A.

This new model 650 from Tel-Instrument consists of a closed loop servo system which automatically controls a continuously adjustable autotransformer. Designed specifically for industrial or laboratory use to control power line voltage variations with accuracy and speed, it may also be used to obtain a continuously variable voltage from 0 to 130V AC or 0–230V. It is particularly useful in areas where the line voltage is subject to wide fluctuations.

The model 650 features: no tubes, no transistors, no mag-amps; no warm-up time required; no waveform distortion; over 50–70 cps range operation; 0.5% voltage regulation; independent of load and power factor; available as bench or rack models, 105–125 volts or 210–230 volts.

Higher powered units, delivering up to 30kVA single phase, or 90 kVA three phase operation, DELTA or WYE connection, are available with the 600 series.

ROTATING OBJECT THERMOMETER

Gelman Instrument Company, 106 North Main Street, Chelsea, Michigan

This thermometer allows measuring surface temperature without actual contact of the probe with a surface. Temperatures of processing rollers and drums can be accurately measured without introducing errors due to friction.

It consists of a resistance sensing head and a battery operated temperature indicator. In use the probe is positioned about 0.003 inch from the surface to be measured. Conduction losses of the surface heat the sensitive resistance element. Errors which would be introduced by conduction losses only are automatically compensated by means of a built in parabolic reflector behind the element.

The temperature indicating unit is small enough to be held in the operators hand. It operates from a single flashlight battery and indicates temperature directly on a calibrated dial. The thermometer can be used up to 450° F.

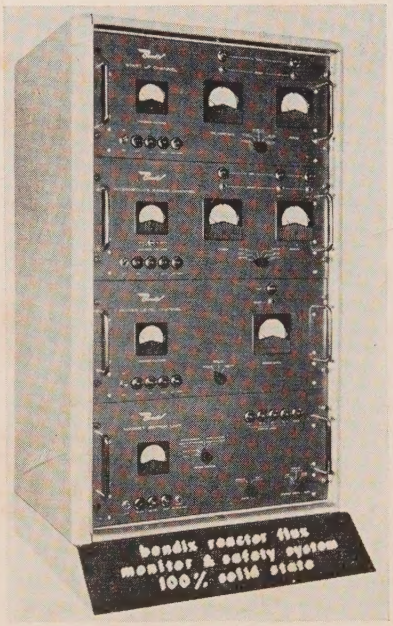

ELECTRONIC SAFETY SYSTEM TO GUARD ATOM POWER PLANT

Bendix International Division, The Bendix Corporation, 205 East 42nd Street, New York 17, N.Y., U.S.A.

A transistorized "electronic brake" for controlling the power of a nuclear chain reaction will be constructed for the Atomic Energy Commission's new Pathfinder Atomic Power Plant at Sioux Falls, S.D.

The unit, called a "reactor flux monitor and safety system", will automatically and continuously measure the number of neutrons—or

atomic energy output—of the reactor from the start of its chain reaction through the full cycle of operations. Any time the energy output starts to exceed normal levels the system will automatically shut down the reactor in a fraction of a second.

Not only the amount of energy output, but also the rapidity with which it is built up at any time, are "sensed" by this system, and if the reactor's human supervisors do not take indicated control methods when too-rapid built-up is taking place, the system automatically shuts it down. It literally "feels the pulse" of a nuclear reaction, by measuring neutrons, or sub-atomic particles, emitted in the atom-splitting process.

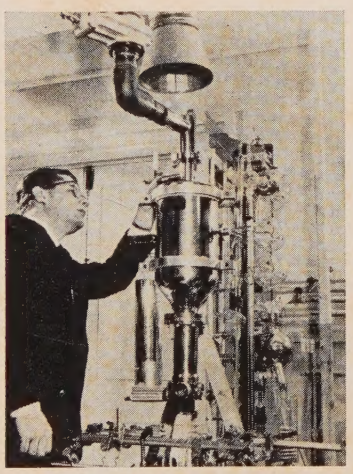

Photo courtesy National Bureau of Standards, Washington, D.C.

5 WINDOW HELIUM RESEARCH DEWAR FOR LOW TEMPERATURE CHEMISTRY

Hofman Laboratories, 5 Evans Terminal, Hillside, N.J., U.S.A.

Helium-nitrogen research dewars with new high levels of thermal efficiencies are now available. This Hofman dewar is a 2-liter, stainless steel vessel with highly efficient radiation shielding and features five windows mounted in the helium reservoir. Four quartz windows are mounted on the side at 90° angles and one on the bottom. These ports provide convenient viewing and measurement of the spectra of light emitted by free radicals trapped in solids.

MINIATURIZED MOTOR INTRODUCED

A.W. Haydon Company, 232 North Elm Street, Waterbury, Connecticut, U.S.A.

A miniaturized motor, no longer than a cigarette filter, and designed to allow the direction of rotation to be established by electrical control alone, is announced.

Designated as the 42100 Series Commercial 60-cycle AC Timing Motor, this five-ounce device was designed for applications where reliability, performance and space are of prime consideration. Currently being used in many applications including the company's own commercial programmers, long-life repeat cycle timers, time delay relays, elapsed time indicators, stop clocks, and other custom designed timers, the motor provides extremely fast starting and stopping, eliminating prestarting and clutching in many applications.

Length of these motors is only $\frac{7}{8}$ inch, making them the shortest motors available, the company claims, with no sacrifice in running torque, nominally specified as 30 ounce-inches. Available in voltages ranging from 6 to 230 volts at 20 mA maximum, the unit's rotor speed is 300 rpm with output speeds of 300 rpm to $\frac{1}{6}$ rph. Direction of rotation is optional and established solely by electrical control, thereby eliminating the need for noisy troublesome mechanical devices with limited life. Maximum temperature rise is only 40° C, while power input is stated at 2.5 W max. (All specifications stated at a frequency of 60 cps. 25 and 50 cps. versions are also available.)

The manufacturer stated that two basic gear trains are available to meet various requirements, with output torque independent of gear train material. The standard gear train has brass wheels and steel pinions, while the optional hard steel gear train will carry up to three times normal load, thereby obtaining greater usable torque. The standard shaft is $\frac{1}{8}$ inch diameter by $\frac{3}{8}$ inch long. A large number of variations to the standard shaft are offered and special shafts can be supplied on demand.

Additional applications for this light weight motor are in chart drives, control equipment, and any application requiring an accurate time base or source of rotary timing power.

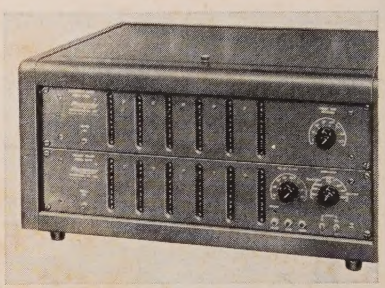

SCALER AND CRYSTAL CONTROLLED TIMER COMBINATION

Hamner Electronics Corp., Princeton, N.J., U.S.A.

The instrument, which consists of Hamner's N-803 Timer and N-276 Scaler, permits data print-out in many flexible modes of operation as follows:

Preset count: 15 settings from 10 to 500 000 counts.

Preset time: 15 settings from 1 to 50 000 seconds.

Combined preset time and count: any of the time or count settings may be used simultaneously with the system stopping when the first preset event occurs.

Data print-out: both scaler and timer provide "staircase" outputs, for operation of a digital printer. A binary coded decimal (1–2–2–4) output can also be provided for operation of Data Handline Equipment.

Automatic recycling: The system will recycle automatically, if desired, following occurrence of a preset event and data print-out. In this case, print-out can be cumulative or cyclical. Both print-out and automatic recycling can be used in any mode of operation.

The Scaler and Timer can also be used independently. They feature high levels of stability and high speed of operation.